3-24-2016

Investigation into Active Spanwise Camber Deformation on the Lateral Stability and Roll Control of the X-56A Compared to Conventional Ailerons

Eric T. Yerly

Investigation into Active Spanwise Camber Deformation on the Lateral Stability and Roll Control of the X-56A Compared to Conventional Ailerons

THESIS

Eric T. Yerly, Captain, USAF

AFIT-ENY-MS-16-M-249

DEPARTMENT OF THE AIR FORCE
AIR UNIVERSITY

AIR FORCE INSTITUTE OF TECHNOLOGY

Wright-Patterson Air Force Base, Ohio

AFIT-ENY-16-M-249

Investigation into Active Spanwise Camber Deformation on the Lateral Stability and Roll Control of the X-56A Compared to Conventional Ailerons

THESIS

Presented to the Faculty

Department of Aeronautics and Astronautics

Graduate School of Engineering and Management

Air Force Institute of Technology

Air University

Air Education and Training Command

In Partial Fulfillment of the Requirements for the

Degree of Master of Science in Aeronautical Engineering

Eric T. Yerly, BS

Captain, USAF

March 2016

AFIT-ENY-16-M-249

Investigation into Active Spanwise Camber Deformation on the Lateral Stability and Roll Control of the X-56A Compared to Conventional Ailerons

Eric T. Yerly, BS

Captain, USAF

Committee Membership:

Lt. Col. A. M. DeLuca, PhD
Chair

J. J. Joo, PhD
Member

D. L. Kunz, PhD
Member

AFIT-ENY-16-M-249

Abstract

This research compares the stability and roll characteristics of an X-56A using AFRL's Variable Camber Complaint wing technology to actively change wing camber compared to conventional ailerons deflected at set angles. An analysis of the stability and roll characteristics was modeled using a 3-D vortex lattice theory simulation, and that data was compared to wind tunnel testing to verify and validate the model results. Wind tunnel data was collected using 19 inch 3-D printed scale models with wings fabricated with a pre-determined percentage of camber deformation, as well as models with fixed aileron deflections. The full span model changed camber from the original airfoil 5% between the root and tip; the 1% camber model changed camber a total of 5% starting from the root, scaled at 1% per foot; and the quick camber change model changed camber 5% from the root over a scale adjusted 2 foot span.

Wind tunnel testing was performed at a Reynolds number range from 30,000 to 150,000. Testing indicated at high speeds and low angles of attack, the camber deformed wings produced a roll moment and roll rate equivalent to, or greater than conventional ailerons. At larger angles of attack and low forward speeds, roll reversal and early wing stall were encountered due to the decreased camber. Because of early onset stall, the camber deformed wing had a lower lift coefficient with increased drag. The camber deformed models did not result in aerodynamic moment instability; however, they did demonstrate a decrease in roll and pitch stability. The 3-D model predicted accurate

trends in roll and stability, but could not model viscous effects due to the inviscid nature of the simulation. Manual skin friction corrections yield more accurate drag results, increasing the ability for Tornado to model the behavior of the X-56A.

Acknowledgments

This monumental accomplishment could not have been feasible without the numerous people who stood behind me and supported me though each step. I would like to thank my advisor Lt. Col. Anthony DeLuca for his guidance throughout this entire process. The gentle but firm hand always pushing me to perform to a higher level and believing in what I am doing and capable of doing helped make me a better engineer. I would like to give my greatest appreciation to my sponsor, AFRL, Aerospace Vehicles Directorate, especially Dr. James Joo for his ongoing encouragement and for building the VCCW and allowing me to aid in his experimentation. I would like to thank my God for always being my foundation and keeping me strong when the days became long and hard. Finally, I would like to thank my beautiful wife Emily. She is and always has been my rock and given a never ending amount of support and love throughout the long days and tiring nights working in the lab and at home. She never stopped believing in me and has always seen great things in me. I love you!

Eric T. Yerly

Table of Contents

Page

List of Figures

Page

List of Tables

Page

List of Symbols

o	Degree
L/D	Lift to Drag ratio
M	Mach number
δ_a	Aileron deflection angle
P	Roll rate (deg/s)
$C_{l_{\delta_a}}$	Aileron control power per degree aileron deflection
C_{l_p}	Roll damping derivative
b	Total wing span
U_1	Free stream velocity
q	Dynamic pressure
S	Wing planform area
α	Angle of attack
β	Sideslip angle
Λ_n	Wing sweep angle
ρ	density
ψ	Yaw angle ($\psi = -\beta$)
AR	Aspect ratio
c	Chord
Re_c	Reynolds number of the total chord length
C_f	Coefficient of skin friction
L'	Local lift
C_L	Coefficient of lift
C_D	Coefficient of drag
C_m	Pitch moment coefficient
C_n	Yaw moment coefficient
C_l	Roll moment coefficient
λ	Taper ratio (tip chord/ root chord)
Γ_n	Vortex strength
V	Velocity
N	Normal Force (Body Axis)
A	Axial Force (Body Axis)
S	Side Force (Body Axis)
P	Pitch Moment (Body Axis)
Y	Yaw Moment (Body Axis)
R	Roll Moment (Body Axis)
a	Speed of Sound
L	Lift (Wind Axis)
D	Drag (Wind Axis)

m	Pitch Moment (Wind Axis)
n	Yaw Moment (Wind Axis)
l	Roll Moment (Wind Axis)
$C_{L_{\alpha_w}}$	Wing lift curve slope
lbf	Pound force

1. Introduction

Since the Wright Brothers' first flight at Kitty Hawk and the birth of man being able to fly with the birds, the need for aerial vehicles to be able to change directions has been pivotal. The Wright Brothers first used wing warping as a means of changing the twist of a wing at the tip. This twisting caused the aircraft to bank; the more twist added, the more the aircraft would bank. When aircraft reached the extent of the ability to twist a wing due to structural limitations, ailerons were enlisted as a replacement. Ailerons were first developed in 1908 by Henry Farman as an integrated, movable component toward the end of a wing, which changes the camber and creates the same effect of banking or rolling without flexing the wing [1]. By twisting the wing, or moving the aileron, the increase in lift on one wing, and decrease in lift on the opposite wing, creates a rolling moment. At low dynamic pressures, rigid wing assumptions hold and ailerons are very effective sources of roll, as dynamic pressures continue to increase, the elasticity of the wing causes wing twist reducing or reversing aileron effectiveness [2].

1.1 Background

Changes in camber along an aircraft's span is not a new concept. Initially this was performed by having one airfoil section at the root, and a different airfoil section at the wing's tip. This camber change creates a more elliptical lift distribution without having to physically build the wing in an elliptical shape. This simplified wing construction and made building aircraft more economical. The elliptical lift distribution helps maximize the ratio of the coefficients of lift to drag by reducing the induced drag on the wing [3]. One limitation of building a fixed camber change into a vehicle, is generally the airfoils selected are maximized for the vehicles cruise condition. Conformal wings have the ability to constantly optimize wing shape as flight conditions continuously change. Taking advantage of the elasticity inherently

built into all aircraft, wing shape can be manipulated to generate a roll moment and roll rate equivalent to conventional ailerons. This has the added benefits of reduced drag from contoured surfaces, and reduced weight by eliminating heavy mechanical control surfaces and high lift devices.

Conformal wing technology is the capability to control shape changes in flight with the purpose of increasing efficiency, versatility, and mission performance [4]. Similar to a birds' ability to constantly adjust its feathers in flight at a wide range of speeds, wing morphing is capable of this same natural state [4]. The Mission Adaptive Wing (MAW) was the first to build on this idea with the capability to modify wing sweep, leading and trailing edge deflection, camber, and twist to optimize flight performance at all speeds, eliminating leading edge slats and trailing edge flaps [5]. As flexible skin technology continued to take shapimprovee, the Smart Wing used shape memory alloy materials capable of smooth contoured flexible control surfaces as the start of roll control surface elimination. To further this development, camber deformation of an entire cross sectional airfoil, capable of deformation along the wing's entire span, which alters the lift distribution and generate a rolling moment. This was investigated by Martindale et. al. through spanwise morphing on a Citation V business jet. The development of this technology is being pursued for weight savings by eliminating heavy mechanical devices and complex geometries, while shape memory alloy technology is not suitable for large scale operation.

1.2 Research Motivation

The Air Force Research Laboratory (AFRL), located at Wright Patterson AFB, has developed a new wing rib capable of achieving specified camber profiles with minimal error in the mold line with a single actuator. This new rib has been applied to a new wing called the Variable Camber Compliant Wing (VCCW). This new wing has a fully enclosed contour which

alters camber 6% from a NACA 2410 to NACA 8410 profile. The VCCW has six independent deformable ribs capable of spanwise camber deformation to modify an aircraft's lift distribution. Application of the VCCW for future application is to be applied to the joint venture Lockheed Martin Skunkworks and AFRL X-56A as seen in Figure 1. The X-56A was originally designed as a flutter suppression platform. Two wings are available for the X-56A UAV; a flexible wing, and a rigid wing.

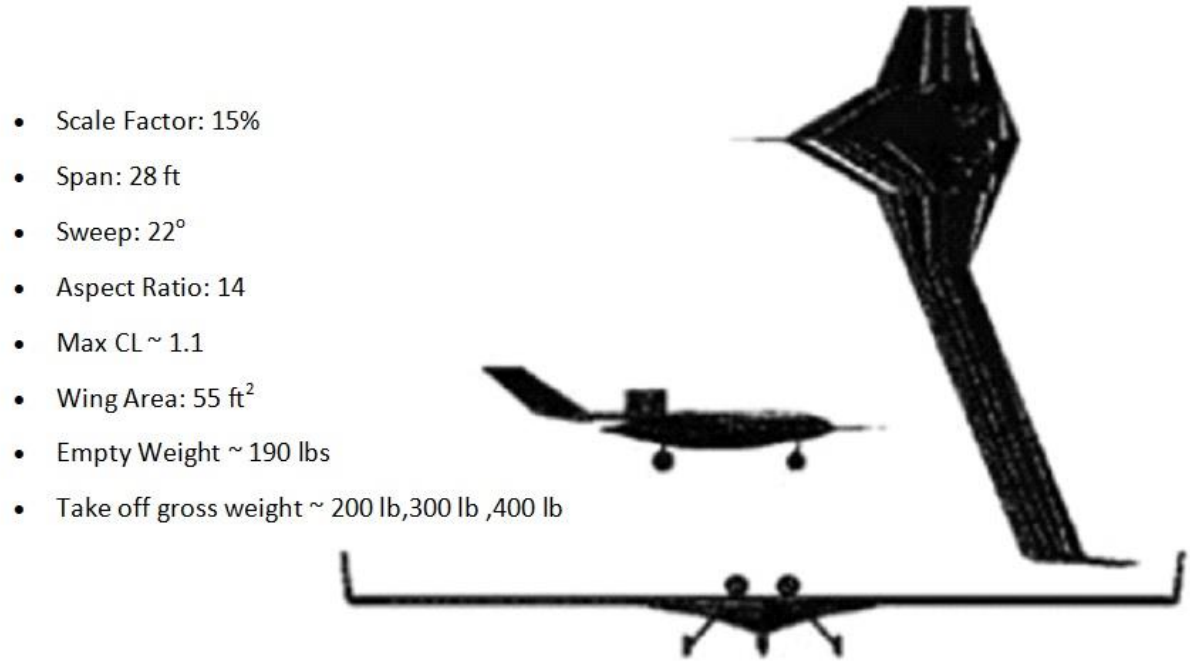

Figure 1. X-56A UAV flying wing dimensions.

The X-56A is a UAV flying wing configuration. Due to the lack of a horizontal stabilizer, the X-56A uses a reflexed airfoil to generate an adverse pitching moment to counteract the moment produced by the lift generated by the wing. The reflexed airfoil has a 1.4% maximum camber and 10% maximum thickness on a 24in chord length. AFRL is investigating replacing the conventional stiff wing which utilizes ailerons for roll authority, with a flexible wing that is capable of deforming the aircraft's wing camber along the span. Tests will be performed on an X-56A simulation model and 3-D printed wind-tunnel models to answer the following questions:

1. Can camber deformation produce an equivalent or larger rolling moment and roll rate than conventional ailerons at fixed deflection angles?
2. Does camber deformation cause adverse effects or instabilities in roll, pitch, or yaw stability?
3. Can Tornado be used as an accurate simulation tool to predict the behavior of camber deformed aircraft?

1.3 Research Objectives and Brief Methodology Description

In order to prove the effectiveness of the new camber-deforming wing compared to that of a conventional wing with ailerons, the following research objectives and methods have been developed to characterize the use of this wing on a new aircraft type. The initial feasibility study using 2-D Strip Theory of a swept wing aircraft will prove that spanwise camber deformation is capable of producing a large enough rolling moment to be comparable to ailerons. Next, models will be built in the MATLAB based computer program TORNADO. This program utilizes Vortex Lattice Theory along with a complete aircraft model to create a wholistic view of the rolling moment as lift, drag, and pitch moment change with speed and angle of attack. The camber deformed models will be compared to models with aileron deflections at $\pm 5^{o}$, 10^{o} and 15^{o}. To validate the TORNADO models, 3-D models will be built for use in AFIT's low speed wind tunnel equipped with a 31in by 44in test section. Each wind tunnel model will match the model built in TORNADO for an accurate comparison.

In summary, as wings become more flexible and speeds continue to increase, the need for roll control will continue to grow. Camber deforming wings, like the VCCW, show potential for aircraft to generate a rolling moment comparable to conventional ailerons with increased performance benefits. These benefits include smooth lift distributions, decreased drag, and lower

bending loads at the root and on the wing spar. Over time, these benefits will result in cost savings in fuel consumption and part longevity. Ultimately, wings like the VCCW and MAW will allow for aircraft to maximize performance for all flight conditions in real time through the use of computer systems linked to the wings for the most efficient aircraft possible.

2. Literature Review

The Wright Flyer was the first manned aircraft to utilize conformal wings to control aircraft roll. As engine technology advanced, aircraft velocity increased which necessitated stiffer wings to prevent aeroelastic instabilities from adversely affecting flight and safety performance. With the increase in wing stiffness, wing warping disappeared as a method to control aircraft roll because the power required to manipulate the wings exceeded actuator capabilities, giving birth to the conventional aileron [6]. With new material technology and advancements in flexible conformal wings, adaptations to aircraft wings have the capability to maximize aircraft performance. Conformal wings have been shown to reduce induced drag, which increases range by reducing fuel consumption, optimize mission performance, and generate a rolling moment nearly equivalent to conventional ailerons [7]. Conformal wings have the added benefit of a reduction in weight due to the elimination of the mechanical components of the ailerons and associated linkages [8]. This chapter summarizes the history of conformal wings and their uses in rolling maneuvers for aircraft.

2.1 Conformal Wing Evolution

2.1.1 Parker Variable Camber Wing

The development of today's conformal wing first began in 1920 with the development of the Parker Variable Camber Wing. Report number 77 by the National Advisory Committee for Aeronautics (NACA) outlines H.F. Parker's development and use of "sliding ribs" in the wing which were designed to broaden the upper and lower limits of the flight envelope of aircraft. The Parker Wing was constructed of wood and steel, and consisted of ribs, tension and compression linkages, two spars, a spring, and cloth outer skin as seen in Figure 2 below [9].

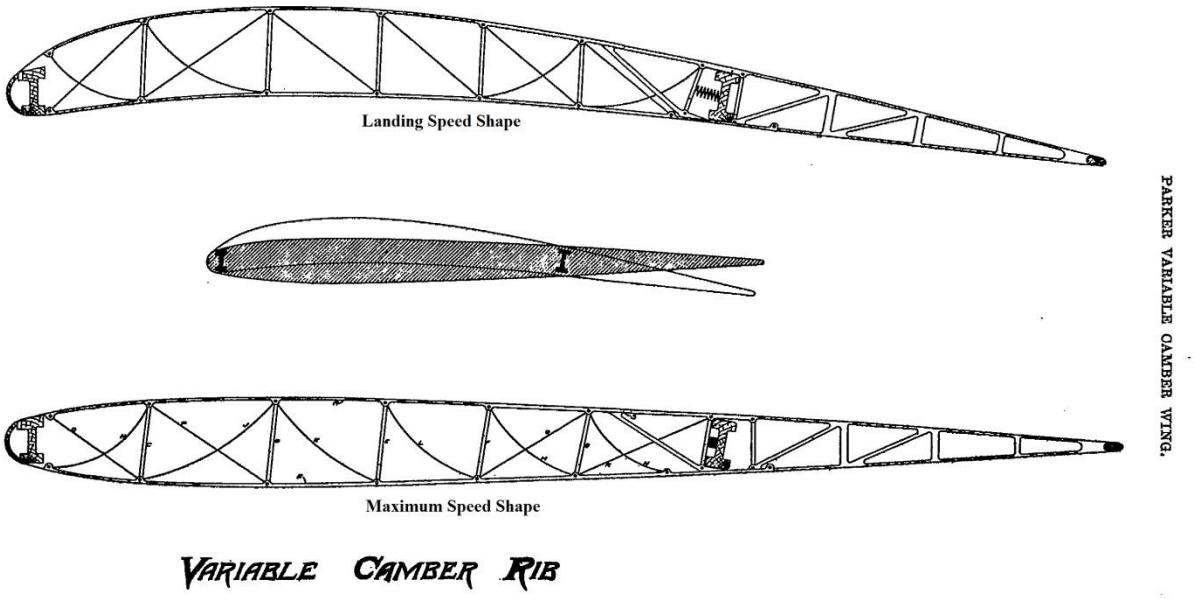

Figure 2. Cutaway of the Parker Variable Camber Wing internal rib structure in both low speed and high speed configurations. [9]

The forward spar is placed directly behind the leading edge, while the aft spar is approximately two thirds the length of the chord behind the forward spar. The spars are connected by wood channel strips and leading and trailing edge surfaces are fixed and non-variable. The center section of each rib between the spars has a flexible internal structure, which changes camber as the aerodynamic loading increases/decreases depending on flight conditions. At lower speeds, the wing rib spar is extended in the increased camber position to provide maximum lift at takeoff and landing. In high-speed flight, the aerodynamic loads caused the ribs in the wing to deform and become more streamline, which reduces drag. This streamline configuration, suitable for cruise and high-speed flight, decreased the overall drag by one-third compared to a wing with a permanently cambered wing [9]. The passive camber deformation of the wing changed the center of pressure at certain angles of attack. This resulted in instabilities in control on both stagger wing biplanes, as well as monoplanes [9].

2.1.2 Mission Adaptive Wing

Due to the need for greater technological advancements in more flexible materials, as well as mechanical devices, the next technological development in conformal wing design was not until the Mission Adaptive Wing (MAW) in 1981. "The [MAW] is defined as a wing having the ability to actively modify airfoil camber, spanwise camber distribution, and wing sweep in flight, while maintaining a smooth and continuous airfoil surface" [10[11]. The MAW was designed by the National Aeronautics and Space Administration (NASA), in conjunction with the United States Air Force's (USAF) Advanced Fighter Technology Integraion (AFTI) group. The MAW was implemented on a USAF F-111A creating a smooth, variable camber wing, which included fully enclosed leading edge slats and trailing edge flaps creating a continuous contour across the chord [12]. The leading edge slat could deflect from -5^{o} to $+30^{o}$ and the trailing edge flap could deflect from -7.5^{o} to $+25^{o}$ [11]. Unlike the Parker Wing, which allowed the entire rib to deform, the MAW's center wing box remained constant as seen in Figure 3 below.

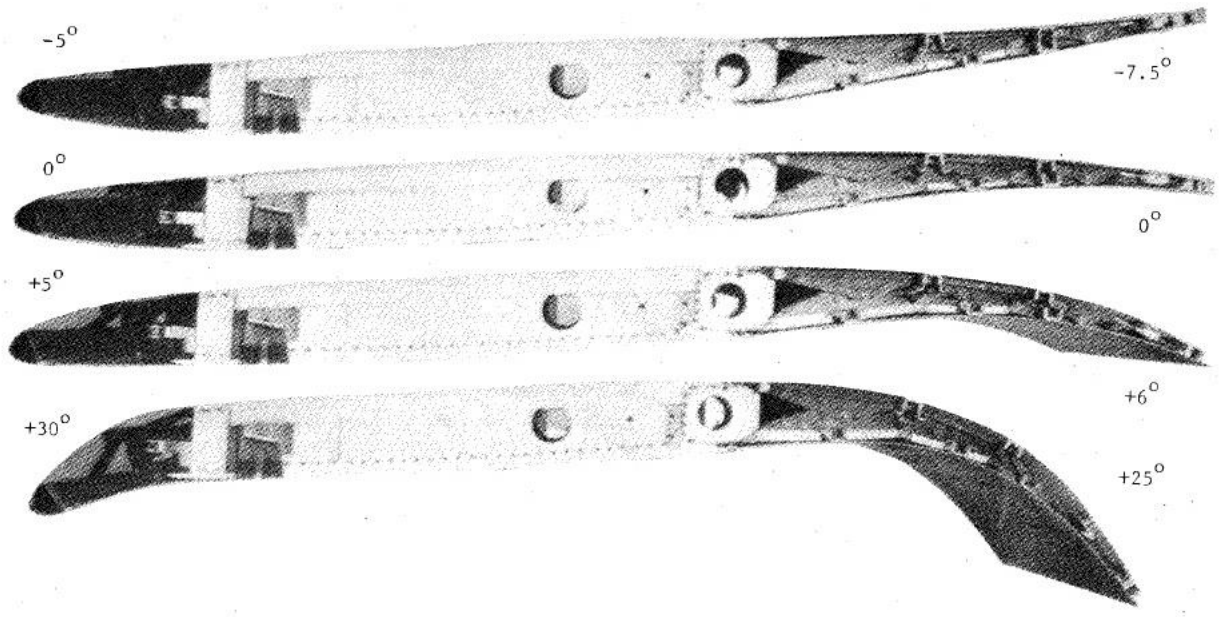

Figure 3. Leading and Trailing Edge deflections of the Mission Adaptive Wing (MAW). [11]

Camber deformation and wing twist along the span optimize the wing shape for a given speed or flight condition by modifying the leading and trailing edge shapes. The main technical issues of employing an adaptive wing with the MAW were complexity, space, and mechanism backlash, which prevented this type of wing from being employed on future aircraft [12].

2.1.3 Smart Wing

To reduce the complexity and weight penalties inherent with the MAW, AFRL and NASA designed the "Smart Wing" for use on Uninhabited Combat Air Vehicles (UCAV). This wing design has hingeless, smooth, contoured leading and trailing edge control surfaces with the ability to vary twist and camber through the use of internal torque tubes and smart wire technology. Shape Memory Alloy (SMA) based actuation allows for the leading and trailing edges to deflect, creating a smooth, continuous contour, similar to the MAW, with a low weight penalty by removing the mechanical internal linkage structure and replacing it with SMA technology. "SMA based actuation systems are ideal because of their high force and high strain capabilities" [12]. The torque tubes located in the center wing box are shown on the left in Figure 4 below with the deflection capabilities exhibited from the embedded SMA wire technology. The right image in Figure 4 shows the SMA wire contour compared to conventional trailing edge flap deflection.

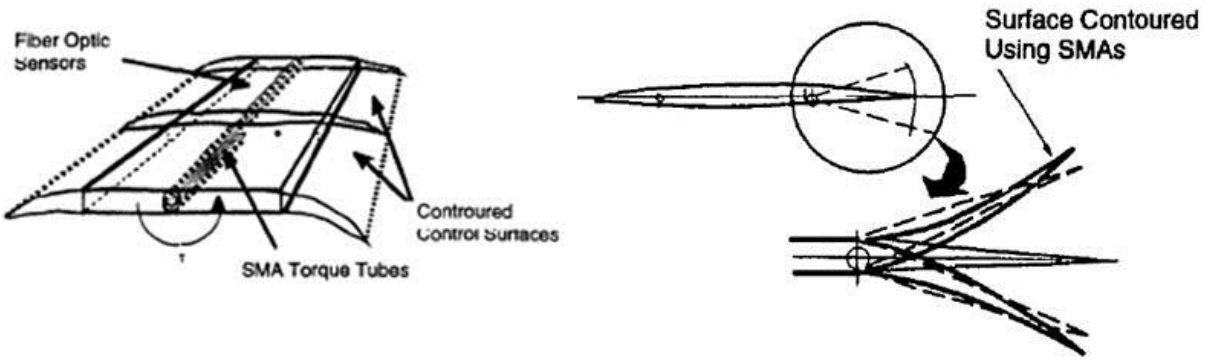

Figure 4. Smart Wing shape morphing through the use of SMA materials. [12]

Two wing models were built and tested analyzing the use of SMA against conventional control surfaces at Mach numbers between M=0.2 and M=0.4 [13]. Wind tunnel tests showed a significant improvement in pressure distribution due to delayed flow separation at the trailing edge, as well as an improvement in the overall pressure distribution resulting in a net lift increase [12]. Later tests evaluated increases in rolling moments of 8 to 12% compared to conventional aileron design [12]. Despite the performance improvements seen in wind tunnel testing, SMA limitations included bandwidth, actuation time, and scaling issues to full scale models.

2.1.4 Mission Adaptive Compliant Wing

Similar to the MAW and Smart Wing, "FlexSys Inc. under a Small Business Innovation Research (SBIR) program with Air Force Research Laboratory's Aerospace Vehicles Directorate, developed a variable geometry, trailing edge flap that can re-contour the airfoil upper and lower surface" [10]. This design was called the "Mission Adaptive Compliant Wing" (MACW), shown below in Figure 5.

Figure 5. MACW model shown installed in the AFRL Subsonic Aerodynamic Research Facility (SARL). [14]

The MACW structure deforms as a whole, capable of moving into predetermined positions with minimal force by distributing the aerodynamic loads along the entire deformable span. Unlike the MAW and Smart Wing, the MACW only moves the trailing edge surface to optimize lift/drag (L/D), decreasing the drag in order to maximize fuel savings, extend aircraft range, and decrease aircraft noise [10]. Through wind tunnel testing and instrumented flight test data, the MACW demonstrated flow separation and airfoil/wing drag minimization over a large lift range by maintaining laminar flow approximately 10% longer along the chord length [14]. The MACW's primary advantages over the MAW and Smart Wing were the low power costs, as well as minimized weight penalties to apply a compliant trailing edge surface. The primary limitation to the MACW was the need for sliding/stretchable skins to create the enclosed contour as seen in Figure 6 below.

Figure 6. Flexsys MACW trailing edge deflection and flexible transition regions. [15]

2.1.5 Next Generation Morphing Aircraft Structure

A new compliant wing capable of morphing numerous wing geometry aspects similar to the MAW is the Next Generation Morphing Aircraft Structures (N-MAS) project. N-MAS was developed by NextGen Aeronautics in 2003 as a wing morphing program capable of wing optimization. Wing optimization was achieved by modifying the aspect ratio through span and wing area morphing, as seen in Figure 7 below.

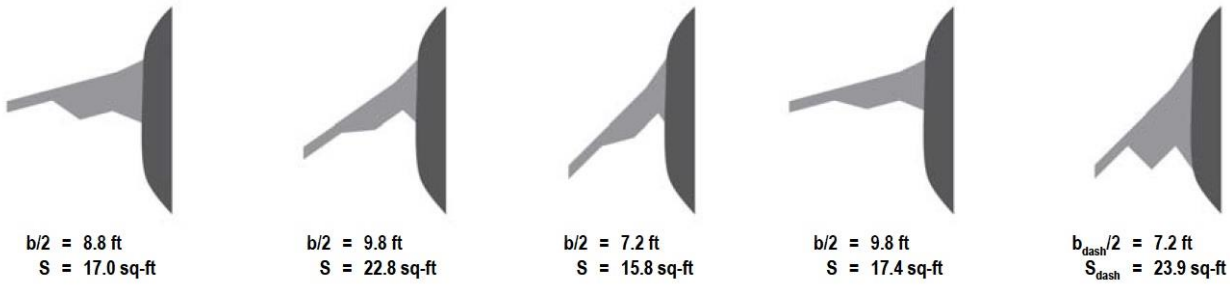

Figure 7. N-MAS wing morphing shapes. [16]

Each wing has a solid leading and trailing edge, as well as, wing tip. A flexible center structure with mult-directional reinforcements, allows the wing to deform while maintaining structural strength under aerodynamic loads [16]. Wind tunnel testing of a half-span model in the NASA Langley Transonic Dynamic Tunnel, showed over a Mach range of M=0.2 to M=0.92 and under g loads up to 2.5g, the wing could withstand the aerodynamic loads on the scale model and

demonstrate successful wing morphing under load [16]. The wing was also applied to a Remotely Piloted Vehicle (RPV) in 2005 and 2006 demonstrating a successful flight deploying the N-MAS in two configurations as shown in Figure 8 below.

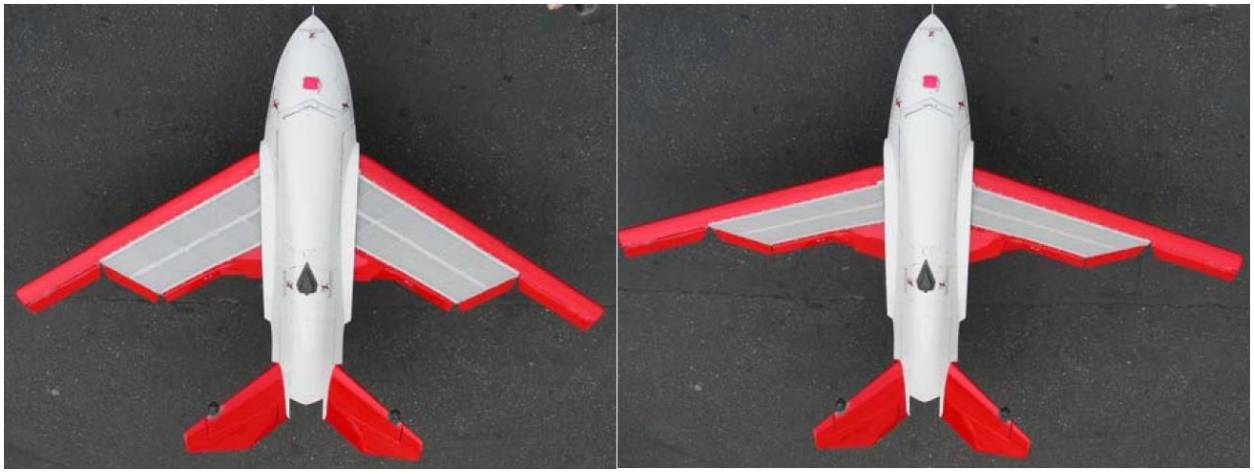

Figure 8. N-MAS application on RPV flight test. [17]

This flight test demonstrated the successful technology use of the N-MAS wing and continued stability and control while in flight.

2.1.6 Variable Camber Compliant Wing

The latest technology in smooth, variable camber compliant wings, similar to the MAW, Smart Wing, and MACW, is the AFRL Variable Camber Compliant Wing (VCCW), shown in Figure 9 below.

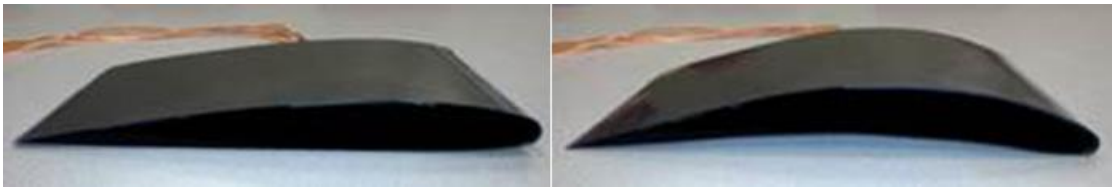

Figure 9. Variable Camber Compliant Wing in the non-deformed position (NACA 2410) left and fully deformed position (NACA 8410) right. [19]

The VCCW ribs utilize a flexible internal truss system similar to the Parker Wing, with a single actuator mounted at the maximum camber location, at 40% of the airfoil chord. The actuator incrementally changes the camber from a NACA 2410 to a NACA 8410 [19]. The camber

deformation shapes produced similar results to the prescribed NACA airfoil goal, as seen in Figure 10 below.

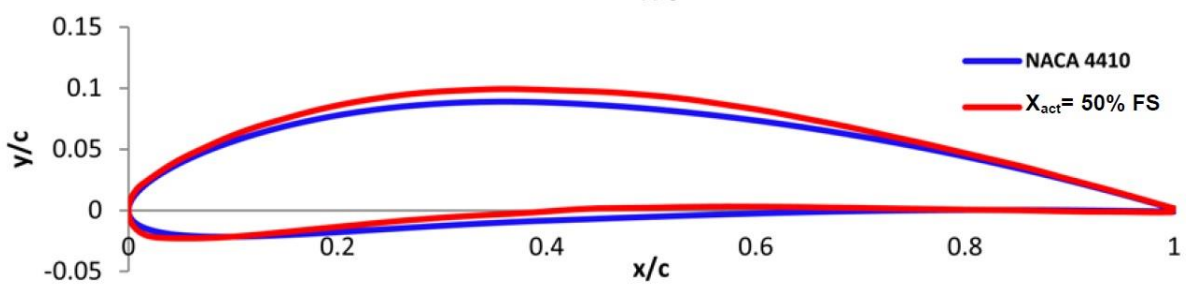

Figure 10. VCCW comparison of camber deformed profile versus NACA airfoil goal shape. [19]

The VCCW is covered in a single layer of carbon fiber, capable of transitioning through an infinite array of shapes within the prescribed 6% camber range. Six independent ribs, spaced one foot apart, create a six-foot wing with a constant two-foot chord [18]. Each rib is capable of moving independently of all other ribs. Unlike previous compliant wings, the VCCW modifies the camber shape along the span to allow a wider range of lift distribution to be achieved due to morphing shape accuracy and spanwise actuation ranges.

The aforementioned compliant wing technologies were successful major programs, only a small sampling of the programs developed, with new technologies continually evolving and entering the field. Numerous universities from around the globe are studying compliant wings for Micro Air Vehicles and passenger aircraft alike. Some capacities compliant wings are being investigated to fill include noise reduction, drag reduction, weight reduction, flutter mitigation, long loiter applications, and roll control to name a few.

2.2 Roll Control with Conformal Wing Technology

2.2.1 Conventional Roll Control

In 1903 during the Wright Brothers 59 second first flight, roll, pitch, and yaw controls were necessary to make such a monumental feat safe and successful. The main method for

manipulating the lateral (roll) stability of the Wright Flier was wing warping. Wing warping utilized cables and pulleys attached to the upper and lower outer wing, deflecting the trailing edge surface, physically moving the structure of the wing. This deflection increases or decreases the angle of attack of the wing increasing or decreasing the lift distribution, respectively, and asymmetrically manipulating the opposing wing to generate a lift imbalance between the two wings. This lift imbalance induces a rolling moment about the axis through the chordwise centerline of the aircraft. As aircraft velocities increased, lateral control became more difficult due to increased aerodynamic wing loading.

As aircraft technology advanced and wings became more rigid, ailerons offered a low power, more efficient means of roll control. Ailerons, similar to wing warping, deflect asymmetrically altering the spanwise load distribution as seen in Figure 11 below.

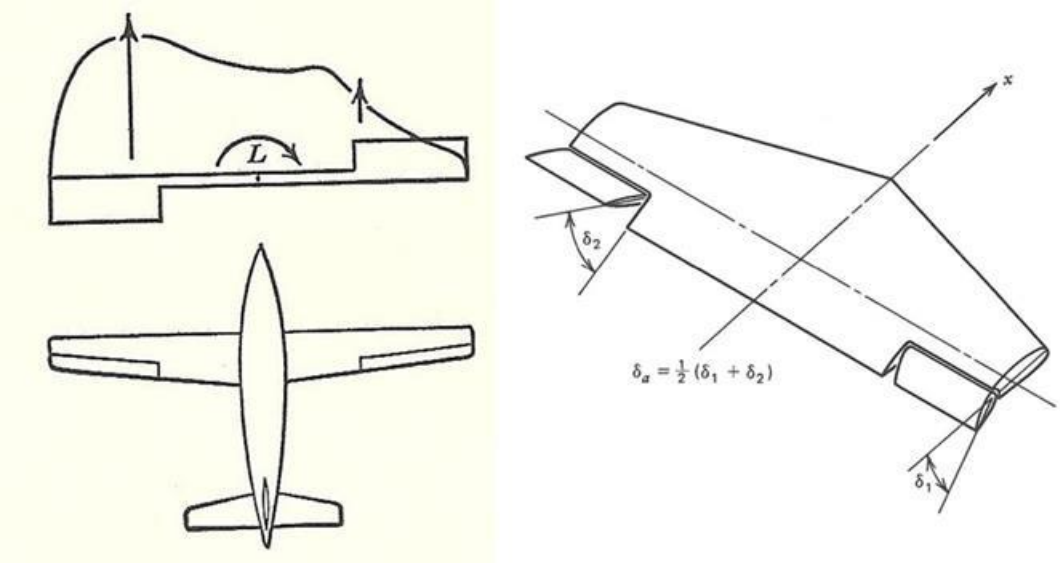

Figure 11. Spanwise loading due to asymmetric aileron deflection left, asymmetric aileron deflection and location right. [20, [21]**]**

Ailerons function by increasing lift on one wing and decreasing lift on the opposing wing and are generated by trailing edge controls deflecting a prescribed angle, altering the wing camber. The

lift imbalance between the two wings induces a rolling moment acting about the fuselage centerline, as seen in Equation 1 below.

$$M = F * y \quad \textbf{(1)}$$

"*M*" equals torque applied to the aircraft wing. "*F*" equals force applied due to lift at the airfoil aerodynamic center, a distance "*y*" from the centerline of the aircraft. The roll rate, "*P*", due to aileron deflection along with the rolling moment is derived starting from the equation of motion about the roll axis as seen below.

$$I_x * \dot{P} = L_p * P + L_{\delta_a} * \delta_a \quad \textbf{(2)}$$

$$\delta_a = \frac{1}{2}(\delta_{up} + \delta_{down}) \quad \textbf{(3)}$$

$$0 = L_p * P + L_{\delta_a} * \delta_a \quad \textbf{(4)}$$

Rearranging and solving for *P*,

$$P = -\frac{L_{\delta_a}}{L_p} * \delta_a \quad \textbf{(5)}$$

Dividing by *qSb* to non-dimensionalize ,

$$P = -\frac{C_{l_{\delta_a}}}{C_{l_p}} * \delta_a \quad \textbf{(6)}$$

$C_{l_{\delta_a}}$ is defined as the aileron control power per degree aileron deflection and C_{l_p} is the roll damping derivative. As the aircraft rolls, a vertical velocity contribution on the wing and horizontal tail is created [22]. The vertical velocity at the wing tip has a value of $\frac{P*b}{2}$ and causes

the wing tips to deflect an angle equal to the helix angle, $\Delta\alpha = \frac{P*b}{2*V}$, opposing the increase or decrease in lift generated by the aileron, as seen in Figure 12 below.

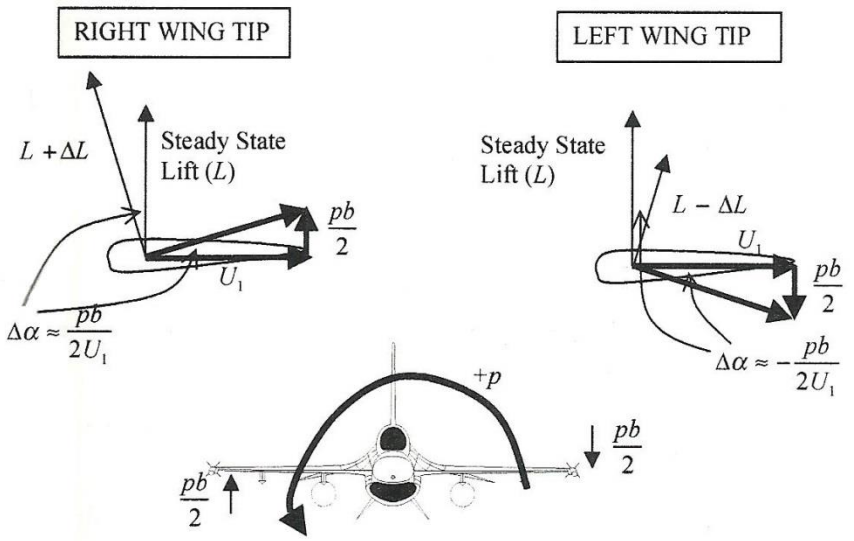

Figure 12. Helix angle induced by roll rate. [22]

The roll helix angle produced by the roll rate generated by aileron deflection and rolling moment, produces the roll damping derivative as seen in Equation 7 below.

$$C_{l_p} = {\partial L_a}\Big/{\partial \frac{pb}{2U}} \tag{7}$$

Ailerons have two major limitations which greatly affect aileron control power, deflection angle and aeroelastic effects at high speeds. Excessive aileron deflection and abrupt surface change causes a large rise in drag or loss of effectiveness due to flow separation. Along with excessive aileron deflection, ailerons can lose effectiveness due to aeroelatic effects at high speeds. When aircraft speeds exceed the region of rigid wing assumptions, the elastic effects of the structure allow wing twist to occur. This twist reduces the rolling moment created by the aileron until

complete lateral control is eliminated. At high enough speeds, reversal can occur, as shown in Figure 13 below [20, [**23**].

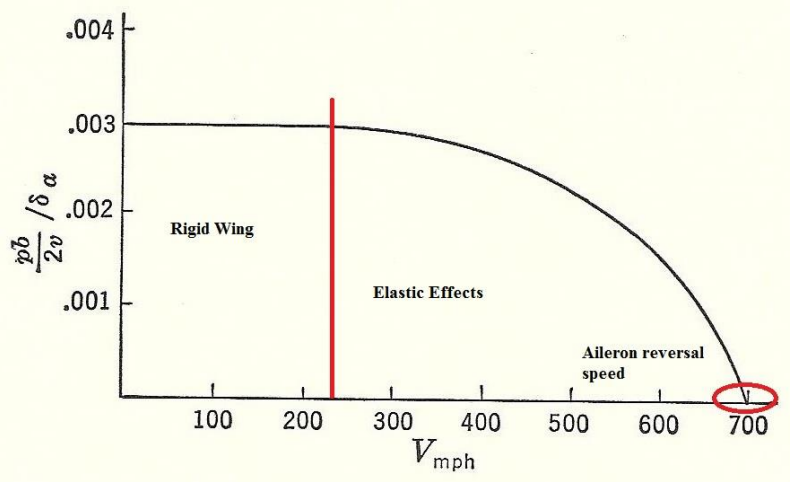

Figure 13. Loss of aileron control effectiveness per degree due to wing twist from aeroelastic effects. [20]

One method to counteract effects of increased speeds or aeroelastic effects is the use of spoilers.

Spoilers were first investigated by NACA and first used on the P-61 fighter aircraft [20]. Spoilers work in a different manner than ailerons. When activated, the spoiler raises into the free stream creating a rolling moment by spoiling the lift on one wing section, as seen in Figure 14 below [20].

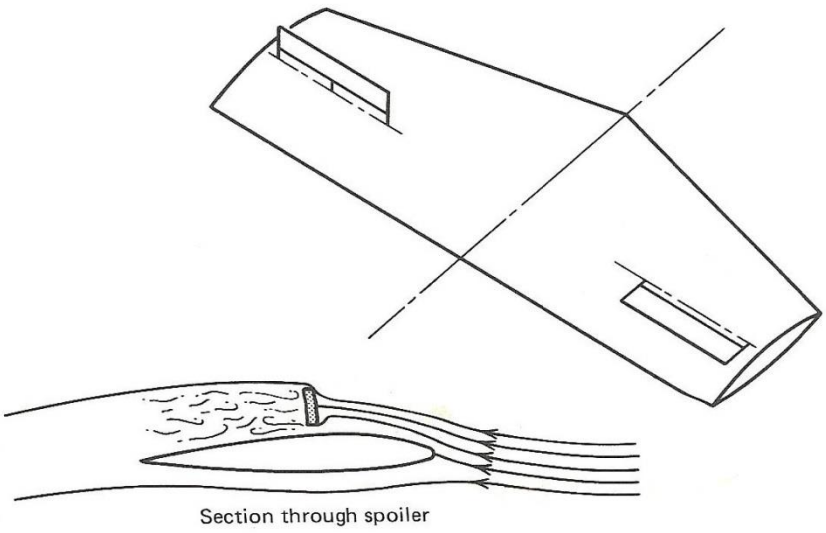

Figure 14. Wing spoiler deflection and flow separation. [21]

The loss in lift on the wing causes a lift imbalance between the wings, generating a rolling moment about the fuselage centerline. Spoilers are traditionally placed approximately 70% of the wing chord [20]. As the spoilers are moved toward the leading edge, their effectiveness at disrupting the airflow increases but causes an increased lag in roll capability [20]. Figure 15 below shows traditional spoiler placement chordwise and spanwise on the wing.

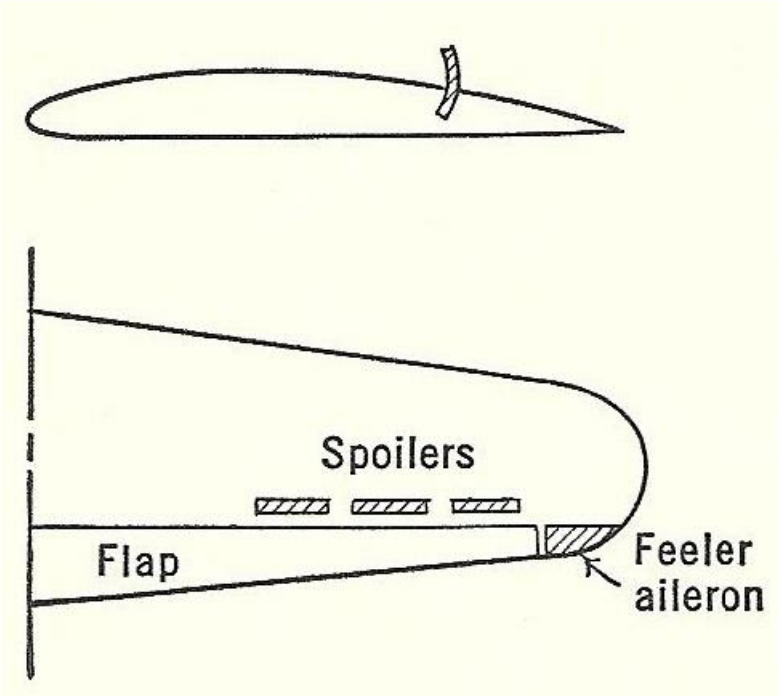

Figure 15. Wing spoiler location. [20]

Spoilers provide the benefit of generating a rolling moment without adverse yaw, unlike ailerons, and have low aerodynamic hinge moments. Despite these benefits, spoilers are limited by decreased roll rate and large drag rise during use.

2.2.2 Compliant Wing Roll Control

Through the use of flexible technology and the conformal wing, alternate methods of producing roll moments have evolved since the Wright Brothers used wing warping to roll their aircraft. Of the numerous compliant wing applications capable of generating a rolling moment, several examples utilizing flexibility within a wing to remove conventional mechanical controls,

such as ailerons and flaps, including conformal trailing edge surfaces, camber and twist modification, and camber only modification were discussed. One example is Khot, Eastep, and Kolonay (1997) evaluated the ability of a flexible wing to vary both camber and twist along the spanwise and chordwise directions to generate equivalent roll rates compared to a rigid wing with conventional control surfaces. The model utilized "Fictitious Control Surfaces" (FCS) to provide the control forces and model the twist and camber in ASTROS [2]. The steady state roll rate was determined by the trim equation for a steady rolling aircraft. The roll coefficient with respect to aileron deflection was replaced with the stability derivative for the ith aerodynamic panel with respect to the angle of attack of the given panel describing both twist and camber as seen in Equation 8 below [2].

$$qSb[\sum_{i=1}^{n} C_{M_{\alpha_i}} \alpha_{R_i} + C_{M_p} \frac{pb}{2V_o}] = 0 \quad \textbf{(8)}$$

Solving for the roll rate *P* per Equation 9 below.

$$p = -\frac{2V_o \sum_{i=1}^{n} C_{M_{\alpha ii}} \alpha_{R_i}}{bC_{M_p}} \quad \textbf{(9)}$$

This technique was evaluated at specific Mach numbers *M*=0.85, and *M*=1.2 and selected roll rate of 90 deg/s, varying the dynamic pressure from 5psi to 50psi [2]. Both the conventional rigid wing with ailerons, as well as the elastic wing with active twist and camber, were compared. For all dynamic pressures at *M*=0.85, the elastic wing maintained a constant roll rate, while the rigid wing with ailerons generated an equivalent roll rate up to 15psi with increasing losses of up to 5 deg/s in roll rate as dynamic pressure increased to 50psi as seen in Figure 16 below [2].

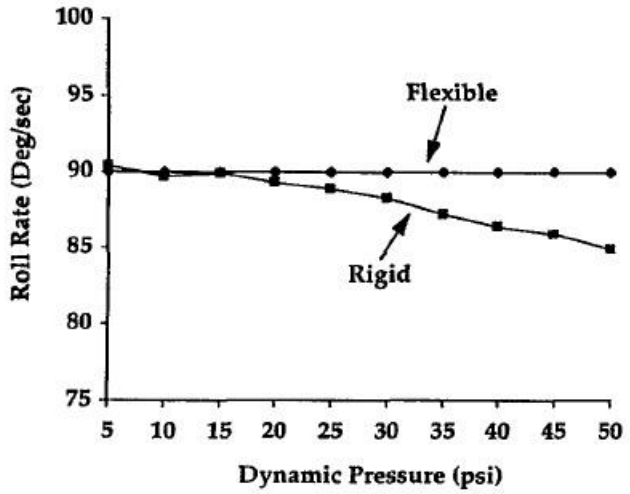

Figure 16. 90 deg/s roll rate comparison between flexible wing camber and twist and rigid wing with ailerons. [2]

This concluded that conformal wings can generate an equivalent or better roll rate, especially at high dynamic pressures where ailerons become less effective. The strain energy required to deform the flexible wing ranged between 8.72 in-lbs to 107.95 in-lbs [2]. Alternately, the flexible wing at M=1.2 generated a lower roll rate at all dynamic pressures than the rigid wing while the strain energy required to deform the wing was nearly three times the amount at M=0.85 [2]. Through the use of SMA technology like that of the Smart Wing, elastic camber and twist may be achieved [2].

Another method of morphing wings to generate a roll moment is through the use of conformal trailing edges. Sanders, Eastep, and Forster (2003) showed conformal control surfaces produce an increase in lift coefficient of approximately 40% and a more negative pitching moment compared to conventional control surfaces [6]. This result was shown through analytical models compared to wind tunnel data between conformal control surfaces, with smooth contour shape,s and conventional ailerons, which allow for discontinuities in the flow from the sharp angle at the attachment hinge. The comparison between conformal surfaces and conventional

surfaces at two flap-to-chord ratios is presented below in Figure 17 showing the smooth pressure changes at the hinge locations by conformal control surfaces.

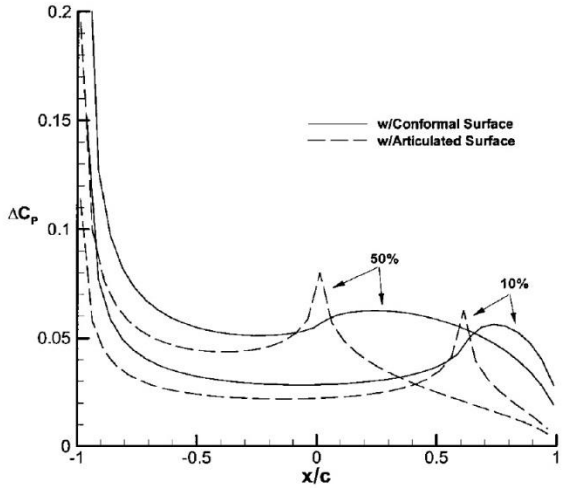

Figure 17. Pressure distribution over airfoil at two flap-to-chord ratios: 10% and 50%. [6]

In addition to analyzing pressure, lift, and moment for each control surface, roll rate was also analyzed per Equation 10 below where β equals aileron deflection.

$$P = -\left(\frac{C_{l_\beta}}{C_{l_p}}\right)\left(\frac{2U}{b}\right)\beta \quad \textbf{(10)}$$

Testing found that roll rate at three flap-to-chord ratios each produced a larger peak roll rate on the order of 25 to 30% when using conformal control surfaces [6]. This roll rate increase was due to the increase in total lift [6]. The peak roll rate occurred at a lower dynamic pressure for the conformal control surfaces than the conventional control surfaces, as seen in Figure 18 below, as a result of the increased pitching moment [6].

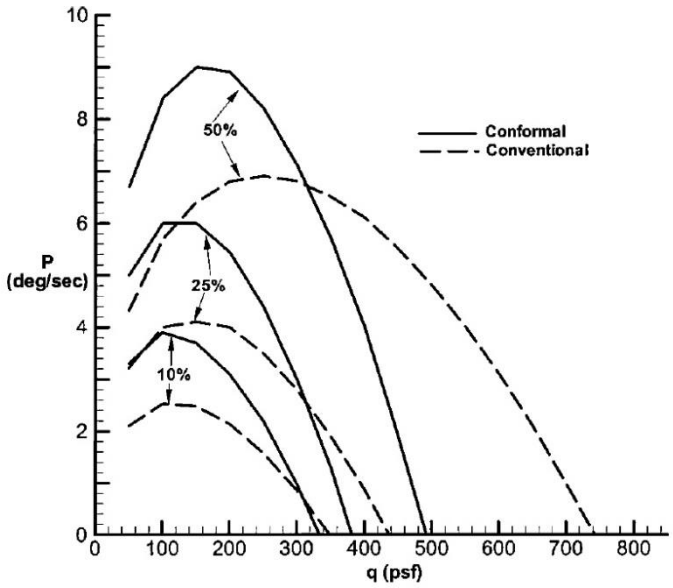

Figure 18. Comparison of roll rate and dynamic pressure for a flexible wing with flap-to-chord ratios of 10%, 25%, and 50%. [6]

Conformal control surfaces on flexible wings showed an increase in lift, pitching moment, and roll rate due to the smooth flow contour at the hinge locations. Low rate applications, such as takeoff and landing, and concepts involving multiple control surfaces may be ideal for conformal control surfaces due to roll reversal occurring at decreased dynamic pressures compared to conventional control surfaces on flexible wings [6].

Similar to the use of conformal trailing edges, spanwise camber deformation is another version of conformal wing design used to generate a rolling moment. Camber deformation varies lift along the wing span through the use of a flexible inner structure and either sliding or stretchable outer skin. One such example was performed by Martindale, Law, and Pedro (2010), in which camber deformation was applied to a Cessna Citation V business jet to generate a roll moment. The model was designed in Tornado, a MatLab based, Vortex Lattice Method solver and compared to published data from Cessna. The Cessna Citation V has a modified NACA 23014 airfoil at the root and 23012 airfoil at the tip [24]. Camber modification in Tornado was

modeled by modifying the mean camber line equation for a NACA five digit airfoil through the addition of multipliers and an actuation variable which yields a smooth, continuous camber change along the chord [24]. Spanwise camber was applied to each wing by further modifying δ_k and adding the parameter δ_p as the roll rate actuator, specifying the camber change value. The main wing camber deformation ranged from 0% to +5% camber deformation on the right wing and 0% to -5% camber deformation on the left wing as seen in Figure 19 below.

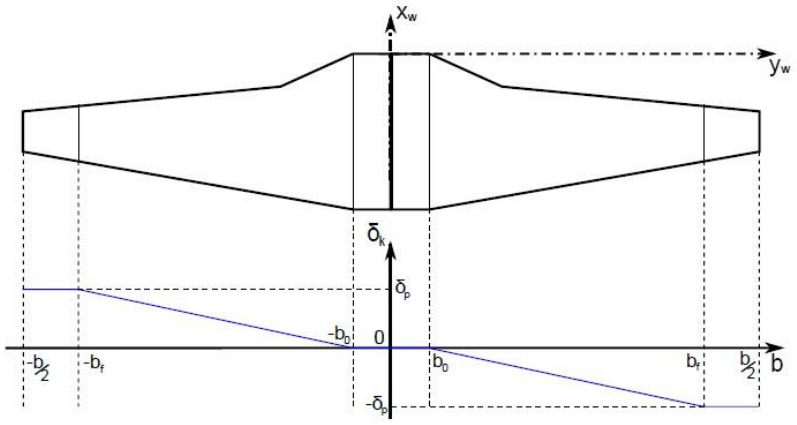

Figure 19. Spanwise camber deformation on Cessna Citation V main wing. [24]

The camber deformation started from zero at the wing root, because the root is more structurally rigid, and varied linearly toward the tip [24]. Applying this form of camber deformation showed that lift distribution could be altered to mimic conventional ailerons, by producing a rolling moment comparable to a $\pm$ 10^o aileron deflection [24]. This study also showed that Tornado produces results comparable to published data and is an effective tool for analyzing camber deformation [24].

Similar to Martindale et. al. using wing flexibility to deform camber, Previtali and Ermanni (2012) evaluated the use of the belt-rib airfoil, in conjunction with compliant wing technology, to evaluate aerodynamic and roll performance [25]. The belt-rib is composed of a

flexible, unstretchable outer structure (belt) married to an internal stiffening system with flexible joints and bonded to the airfoil skin as seen in Figure 20 below [25].

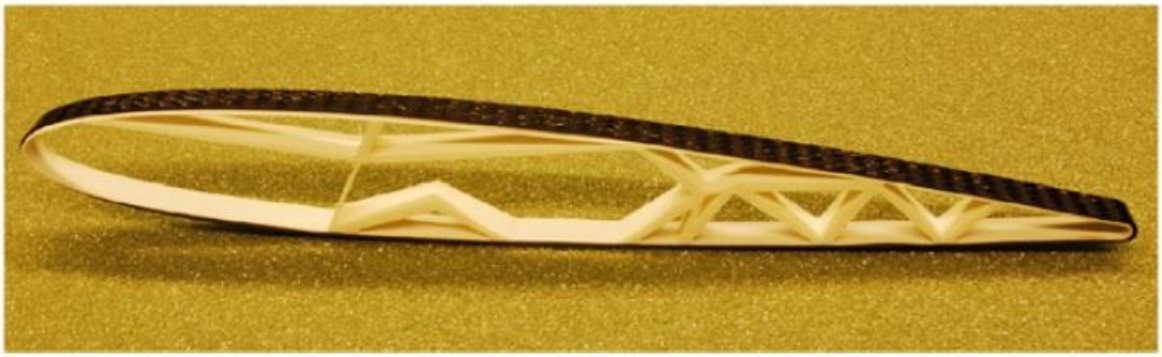

Figure 20. Belt rib internal and external structure. [25]

Previtali et. al. (2012) showed an increase in lift could be achieved through the use of the belt-rib concept with a flexible outer wing skin. With the change in lift generated by the actuation of the ribs, an evaluation of the rolling moment was performed using a Cessna 172 model, morphing the airfoil from a NACA 0012 to NACA 2412 and NACA 3412, as well as the belt-rib shape profile, compared to conventional ailerons. According to Figure 21 below, the rolling moment generated using an antisymmetric NACA 3412 profile can produce a comparable, or higher, rolling moment versus conventional ailerons deflected 15^{o}.

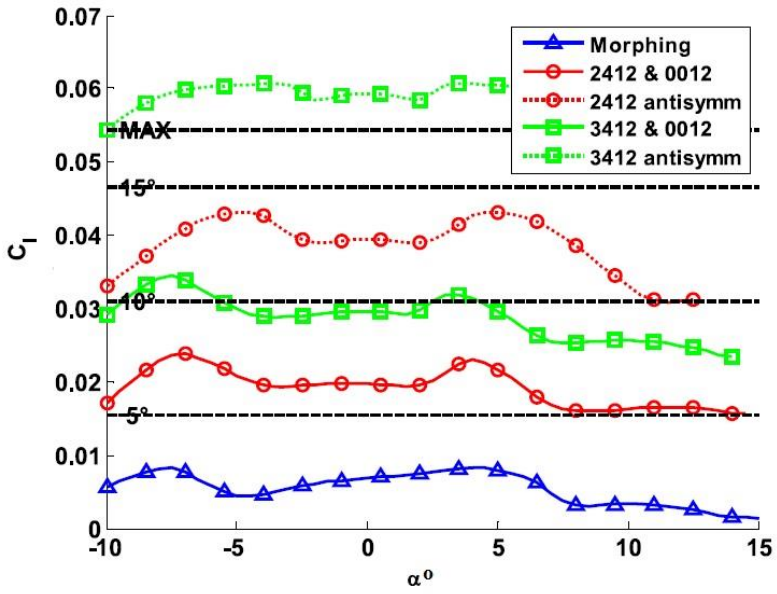

Figure 21. Rolling moment coefficient compared to angle of attack for various wing camber configurations at a Reynolds number of 700,000. [25]

The belt-rib, when morphed, produced the lowest roll moment coefficient due to limited shape morphing capability, as seen by the bottom line denoted with triangles in Figure 21 above. Although, the belt-rib actuation profile was found to need refinement, the study proved that camber deformation alone could produce an equivalent rolling moment compared to conventional ailerons [25].

AFRL's VCCW, described previously, uses the same technique of varying the lift profile by camber deformation capable of inducing a rolling moment, similar to the work done by Martindale et. al. The VCCW, has the ability to deform spanwise and chordwise camber, using linear actuators built into the ribs coupled with a non-sliding skin [19]. It is a lightweight option which can be produced full scale, generating actuating power capable of camber deformation under aerodynamic loads without a large power draw from the host aircraft's power supply [19]. To test the full-scale production model, tests were performed in the AFRL vertical wind tunnel up to 50knots, as shown in Figure 22 below.

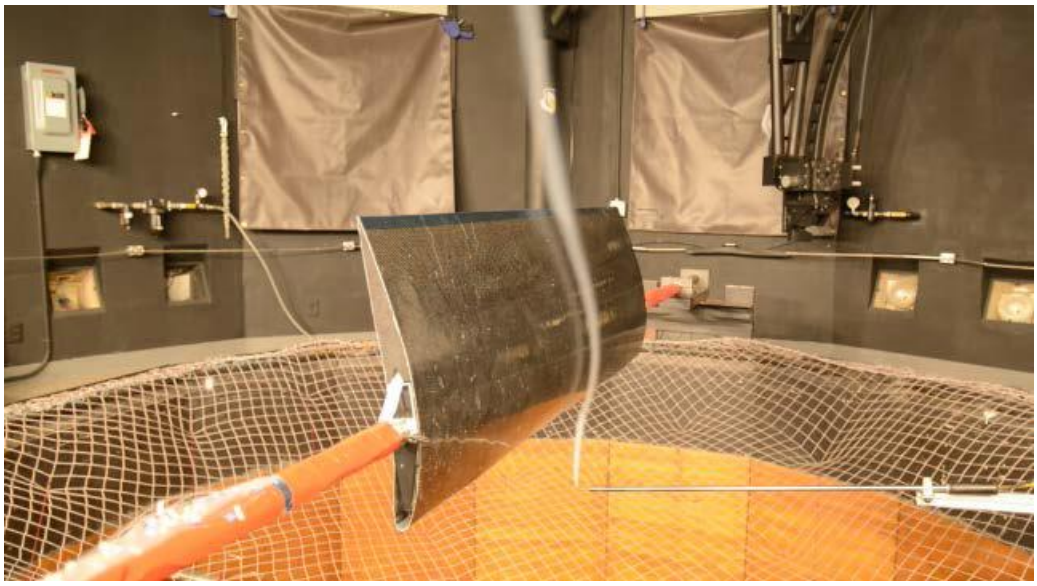

Figure 22. VCCW installed in the vertical wind tunnel, suspended by end plates. [18]

The wind tunnel tests consisted of pressure data, oil flow visualization, and 3D Digital Image Correlation (DIC). Pressure sensors were located on the upper and lower surfaces as shown in Figure 23 below.

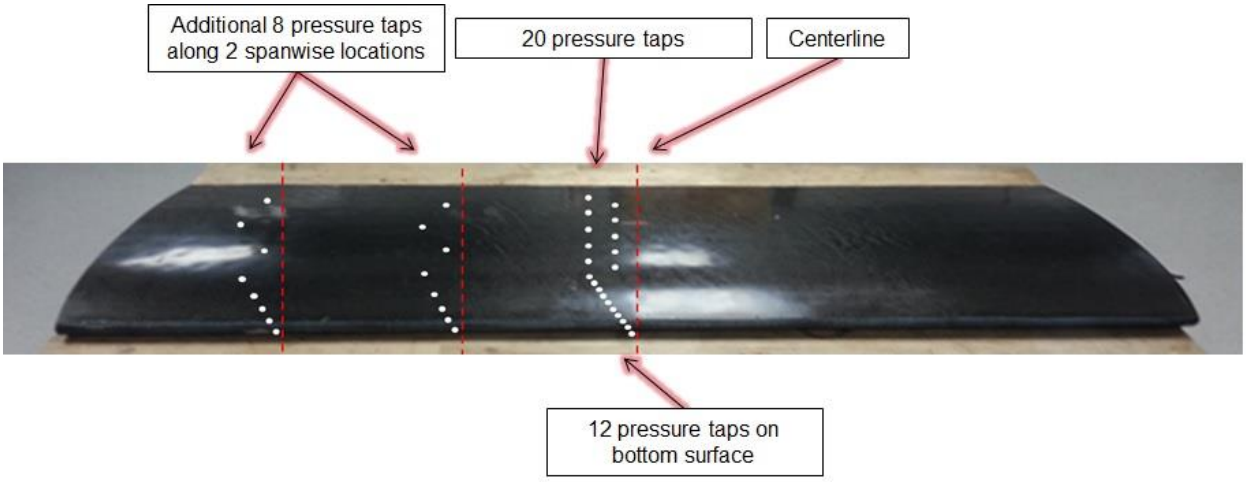

Figure 23. VCCW pressure port placement and location. [18]

Wind tunnel testing showed that increasing the profile camber of the wing resulted in a near matching increase in section lift coefficient compared to the NACA four digit airfoils the VCCW was mimicking. Pressure data and oil flow visualization showed that the flexible skin deformed during testing, resulting in premature flow separation. XFLR5 predictions calculated using the

viscous 2-D data along the six foot span, concluded a spanwise camber deformation could shift the lift distribution inboard or outboard with the change in camber. AFRL is continuing testing on the various capabilities and applications of this conformal wing.

2.3 Application of the VCCW

To transfer this proof of concept technology to a USAF application, the VCCW's 1% camber deformation per foot concept was applied to the Lockheed Martin (LM) X-56A Unmanned Ariel Vehicle (UAV). The X-56A was originally designed to perform high risk flight tests for active aeroelastic control technologies to mitigate flutter in flexible wings. The active flutter suppression system was designed to mitigate Body Freedom Flutter (BFF) to increase the speeds of flexible wing aircraft. This LM program produced a 75% increase in BFF speed as a result of their flutter suppression system [26]. The X-56A has the ability to integrate multiple data acquisition and instrumentation systems with the capability to change wings and tail designs of future UAV platforms as seen in Figure 24 and Figure 25 below.

Figure 24. X-56A removable outer wings between rigid and flexible. [27]

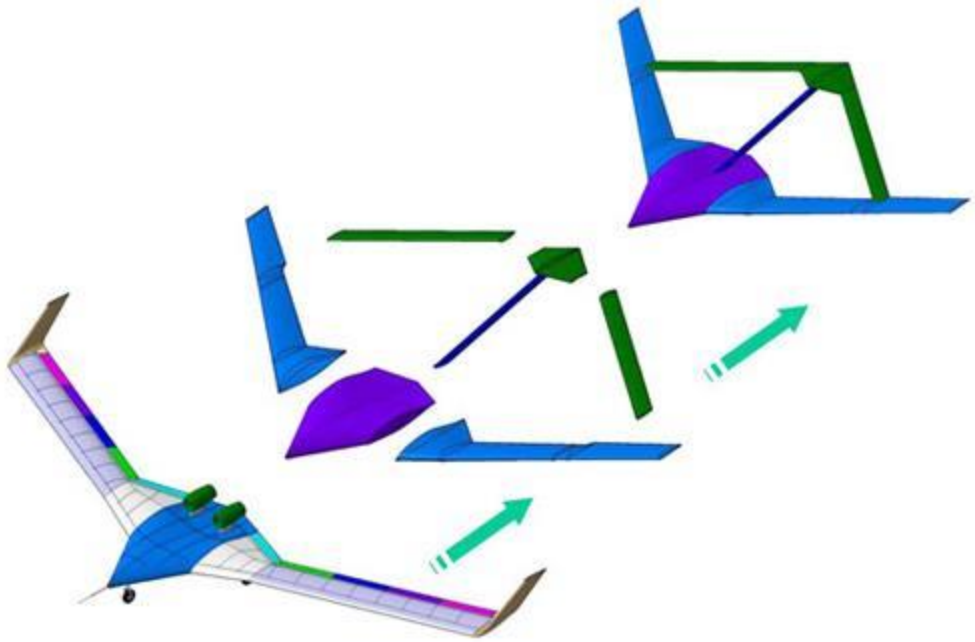

Figure 25. X-56A reconfigurable wing and tail geometry concept. [28]

The geometry properties of the X-56A are defined in Table 1 below.

Table 1. X-56A geometric properties. [29]

Wing Span (b)	28ft
Wing Sweep (Λ_n)	22^o
Aspect Ratio (AR)	14
Planform Area (S)	$55ft^2$
Chord (c)	2ft

For longitudinal pitch control, a reflexed airfoil is applied to the outer wing section of both the rigid and flexible wings using the above geometric properties. The airfoil used on the X-56A is a custom reflexed airfoil which has a concave curve in the upper mold line of the airfoil. This concave curve is aft of the maximum camber chordwise location toward the trailing edge. Figure 26 below shows the X-56A's custom reflexed airfoil compared to a conventional NACA 2410 airfoil.

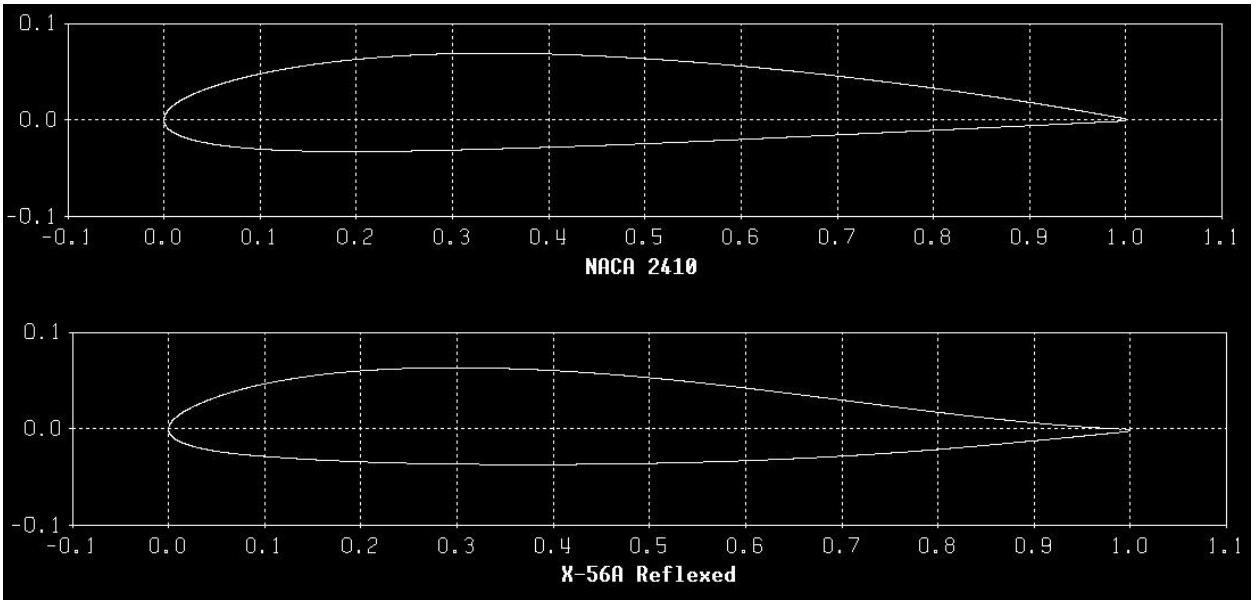

Figure 26. NACA 2410 versus X-56A outer wing airfoil.

The X-56A has a flight envelope extending to approximately 150knots (173mph) and has five sets of control surfaces for maneuvering and BFF control as seen in Figure 27 below.

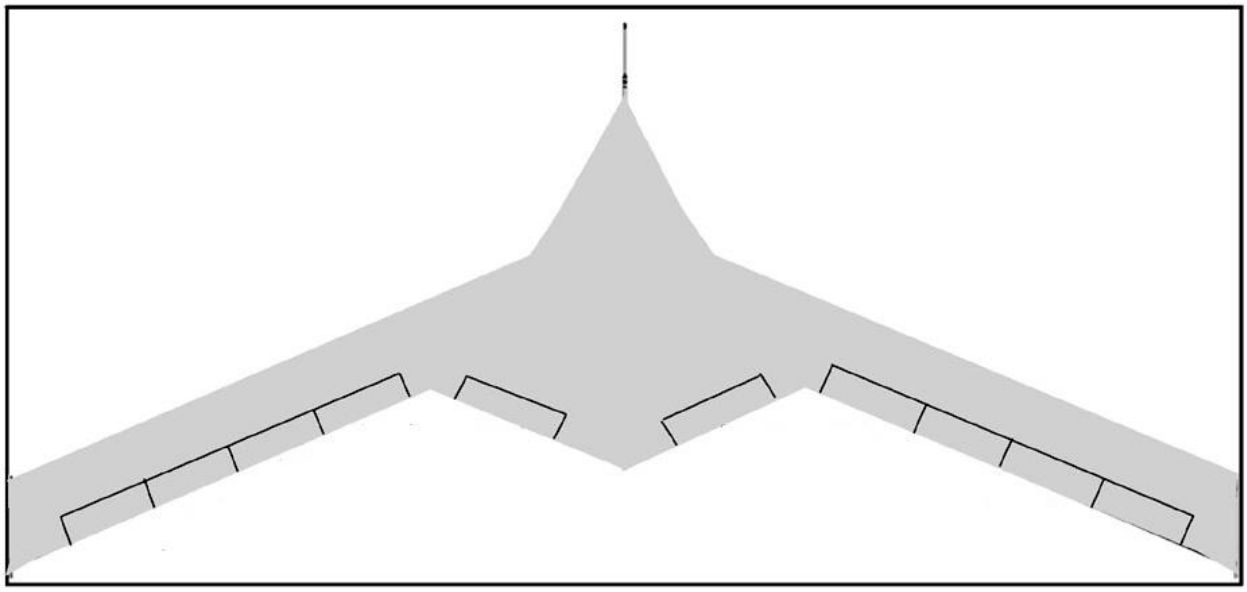

Figure 27. Control surface locations X-56A. [30]

AFRL selected the X-56A due to the availability of technical data and drawings and the X-56A's unique ability to change the outer wing sections between rigid and flexible. The goal of this project was to conduct research on roll control capabilities of a flying wing aircraft with

reflexed airfoil and large sweep angle with asymmetrically camber deformed wings compared to conventional ailerons. The next two chapters of this thesis outline the testing that was completed on scale models by simulation and performing wind tunnel testing at speeds ranging from 30mph to 130mph corresponding to a Reynolds number ranging between 30,000 and 150,000. The scaled X-56A stability and roll control are compared against the conventional ailerons deflected at set angles using the outboard ailerons located in Figure 27 above.

3. Methodology

This chapter describes the methodology used to compare aircraft roll and stability characteristics of an X-56A with the AFRL VCCW wing technology set to three camber deformation configurations compared to conventional ailerons deflected at set angles. The roll and stability characteristics of the X-56A were analyzed using two dimensional (2-D) Strip Theory as a feasibility study, low speed wind tunnel testing of 3-D printed models, and compared to simulated models in the Vortex Lattice Theory program, Tornado. Wind tunnel data was collected using 3-D printed scale models with fixed camber deformed wings, and fixed aileron deflections. The results from the testing described in this chapter will provide a more complete understanding of the VCCW's capabilities, and describe the behavior of a flying wing with a reflexed airfoil and high swept wings when applying camber deformation compared to conventional aileron application.

3.1 SolidWorks Model Manipulation and Separation

The X-56A model was selected as the test platform to employ the VCCW as a form of roll control to study the effects of eliminating ailerons. The original SolidWorks® and Finite Element Analysis (FEA) model was provided by AFRL as a complete X-56A aircraft without the engines, control surfaces, and landing gear. The solid body model was dissected to discern the airfoil geometry of the outer wing. The airfoil geometry was found by creating a plane in SolidWorks® at the joining location where the end plate met the tip of the outer wing, then the end plate was removed leaving the wing tip exposed. The outer mold line of the X-56A's custom reflexed airfoil was initially plotted manually using the snap feature in SolidWorks® to apply 292 reference points. These outer mold line reference points were heavily concentrated at the leading edge radius and the upper surface's trailing edge reflex to most accurately capture the geometry.

The reference points were separated from the rest of the X-56A solid body model and copied to a new part file within SolidWorks®. The airfoil geometry was saved as an IGES file, outputting the individual X, Y, and Z coordinates. The original data points used the model reference coordinate system, where the X direction ran along the chord line of the wing, the Y direction ran along the span, and Z direction was the vertical component. The IGES coordinates were input into Excel, and the Y coordinate was removed from the file leaving only the X and Z coordinates, which denoted the chord length and thickness locations respectively. These (X, Z) coordinate pairs created a two-dimensional representation of a cross-sectional view of the wing.

Figure 28. X-56A full scale airfoil coordinates

Modification of the original X-56A airfoil camber geometry was accomplished using Xfoil. To input the airfoil geometry into Xfoil, and to modify the size of the airfoil while keeping the original mold line aspect, the airfoil was non-dimensionalized along the chord ranging from zero at the leading edge, to a chord length of one at the trailing edge as shown in Figure 28 above. To non-dimensionalize the airfoil, the leading edge reference point was subtracted from each X coordinate and divided by the total chord length of 24in. The Z position coordinates were non-dimensionalized similarly by subtracting the leading edge Z reference point from each subsequent Z coordinate and divided by the chord length. This procedure produced an X location array from zero at the leading edge location, to one at the trailing edge location.

To modify the airfoil geometry, the airfoil reference points were evenly spaced and reduced to 160 panel nodes using the PANE command. The original maximum camber of the X-56A airfoil is 0.014 or 1.4% at 26.5% chord length. The VCCW changes camber from a NACA 2410 to NACA 8410 modifying the maximum camber 6%, morphing between 2% and 8%. The maximum camber is the distance from the maximum vertical location of the mean camber line to the chord line as seen in Figure 29 below. Due to the complex airfoil geometry compared to a standard NACA airfoil, camber modification was limited to $\pm$ 5% change from the original 1.4% maximum camber. In the geometry design routine within Xfoil, the maximum camber value was modified without altering the maximum camber chordwise position. Xfoil modifies the airfoil geometry from the maximum camber input by the user. The mean camber line is modified to achieve the maximum camber modifying the outer mold line coordinates based on the mean camber line equation stored within Xfoil based on the maximum thickness.

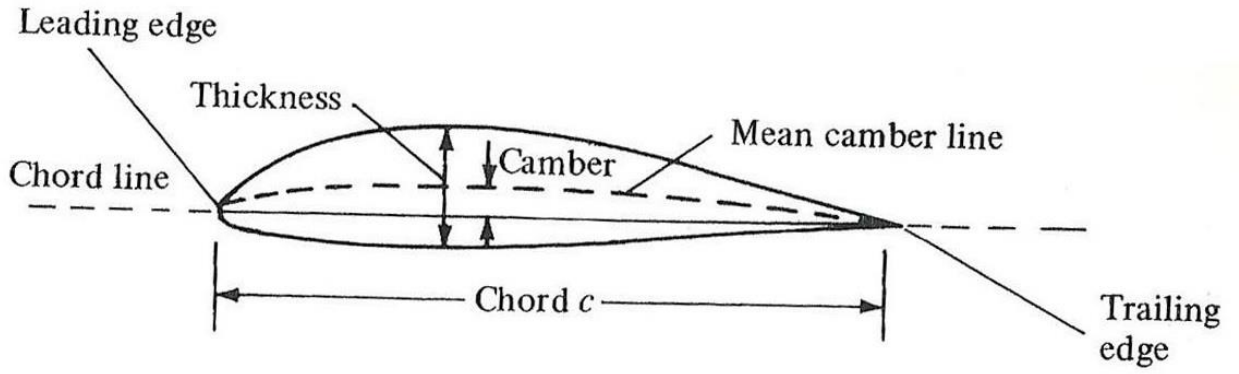

Figure 29. Airfoil geometry definitions. [3]

The outer mold line coordinates were positioned based on the maximum thickness and mean camber line. By keeping the maximum thickness constant, the upper and lower outer mold line Y value placement remained constant in relation to the mean camber line. The maximum camber

was adjusted ± 0.25% to ± 5% camber change to a final maximum camber value of 6.4% or 0.064 , and -3.6% or -0.036 as seen in Figure 30 below.

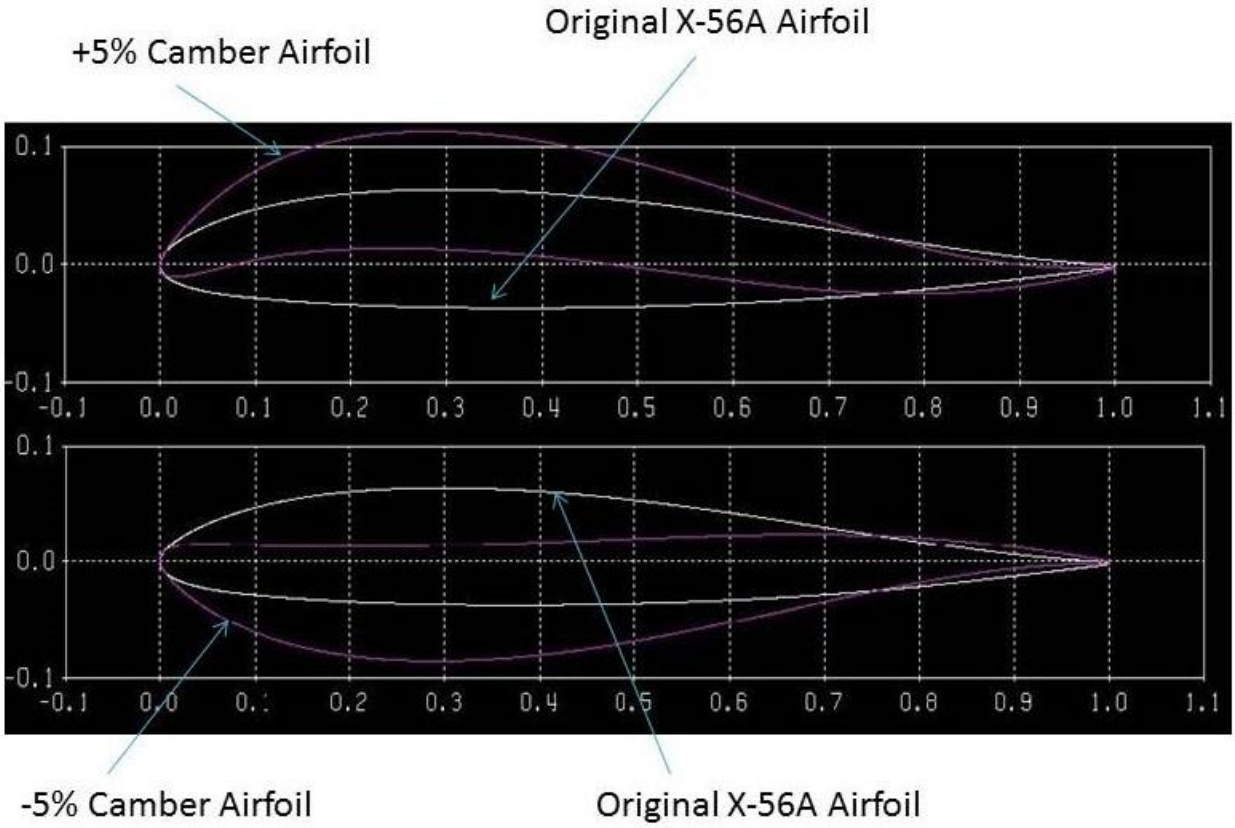

Figure 30. Xfoil camber deformation ± 5% compared to stock X-56A airfoil. 6.4% camber (top), -3.6% camber (bottom).

3.2 Low Reynolds Number Flow

Low Reynolds numbers (Re) were analyzed due to the small model size and small chord length. The full scale X-56A operates in a Reynolds number range around $1.5x10^6$ which is in the normal range of personal aircraft and UAV's. The scale models presented operate in a much lower range where flow behavior becomes more difficult to characterize with changes in speed due to viscous effects.

Reynolds number is defined as the ratio of inertial forces to viscous forces. The Reynolds number is greatly affected by the fluid in which the object is moving, the speed of the object or flow around the object, and the size of the object in the flow. One of the main factors in model scaling comparison is Reynolds number. By matching Re, the flow behavior around the surface is considered to be the same. This can be accomplished by varying the fluid, speed, or vehicle size when comparing variations in flow conditions or scaling. At low Re, viscous forces are large compared to the inertial forces. Viscous forces act on an object in a thin layer of air between the free stream air and the object surface, called the boundary layer, and is one of the largest differences between scaled models and full sized aircraft [31]. "It cannot be expected that a model wing, even one made to exact scale from a full sized prototype, will behave in exactly the same way as its larger counterpart" [31]. Within the boundary layer, two types of flow can be observed, laminar and turbulent flow. As seen in Figure 31 below, at low Re (below 200,000), the flow is mostly laminar, due to wing geometry, surface smoothness, speed of the flow, and the distance along the surface. As the air moves around an object, the Re can change, transitioning the flow from laminar to turbulent [31].

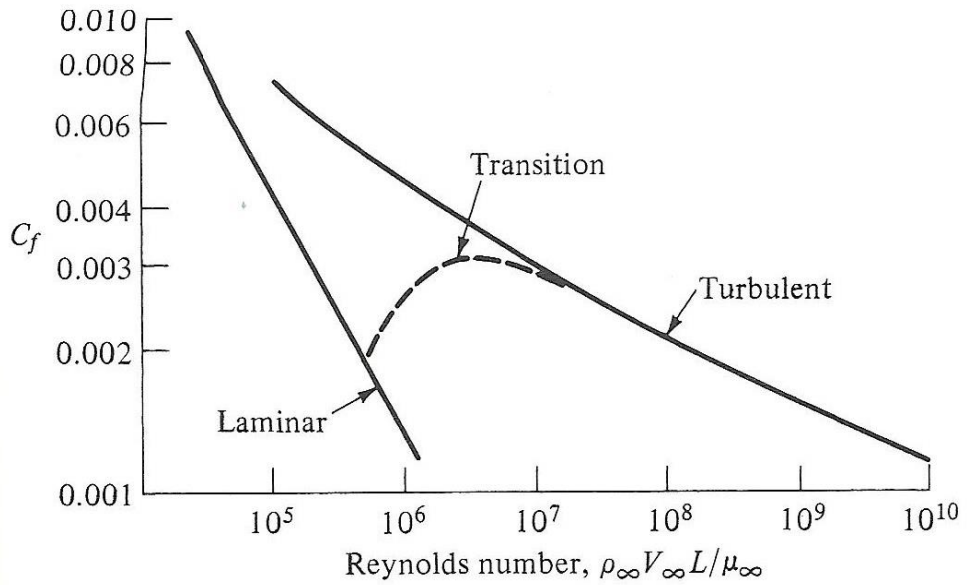

Figure 31. Coefficient of friction versus Reynolds number showing transition regions. [32]

Laminar flow, has a thin boundary layer, and considerable less skin friction drag than turbulent flow [31]. Skin friction drag is the drag encountered by the flow within the boundary layer as it interacts with the skin surface. The laminar and turbulent flow skin friction coefficients for both sides of a flat plate can be approximated by Equations 11 and 12 below [32].

$$C_f Laminar = \frac{2.656}{\sqrt{Re_c}} \quad \textbf{(11)}$$

$$C_f\ Turbulent = \frac{0.148}{{Re_c}^{0.2}} \quad \textbf{(12)}$$

The smooth movement of the layers directly above the zero flow at the surface reduces the skin friction drag. Turbulent flow has a larger boundary layer, with a steep transition from the zero velocity point at the skin surface to the free stream velocity, as seen in the right image of Figure 32 below.

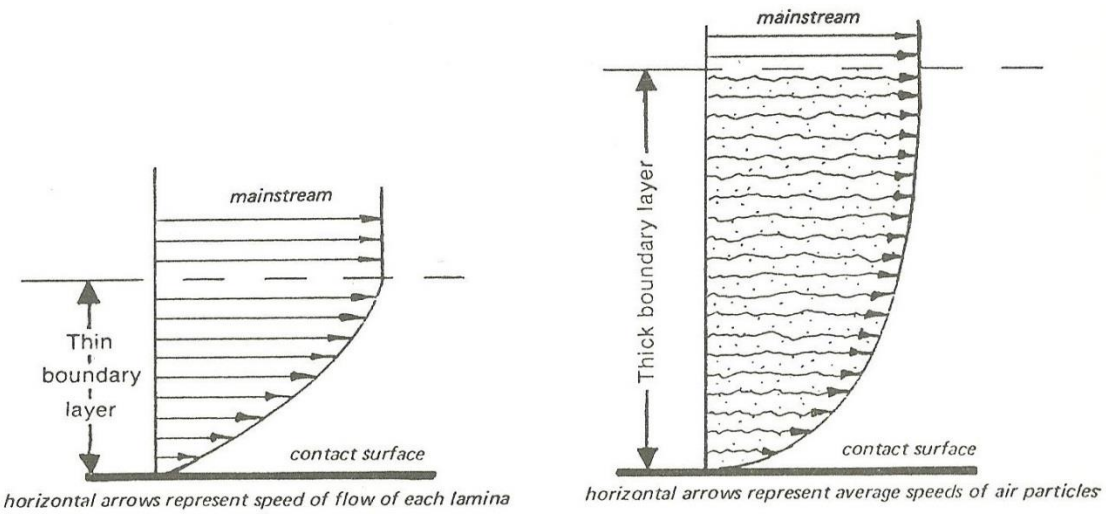

Figure 32. Laminar (left) and turbulent (right) boundary layer thickness and profile. [31]

The larger number of particles and increased speed near the surface causes increased skin friction drag while increasing the momentum of the flow as shown in Figure 32 above, and Equations 11 and 12 above for the same Re [31]. Along with the increase in speed, as the flow becomes turbulent, the profile drag increases due to the boundary layer thickness increasing causing the main airstream flow to accommodate to the additional boundary layer thickness, as seen in Figure 33 and Figure 34 below [31].

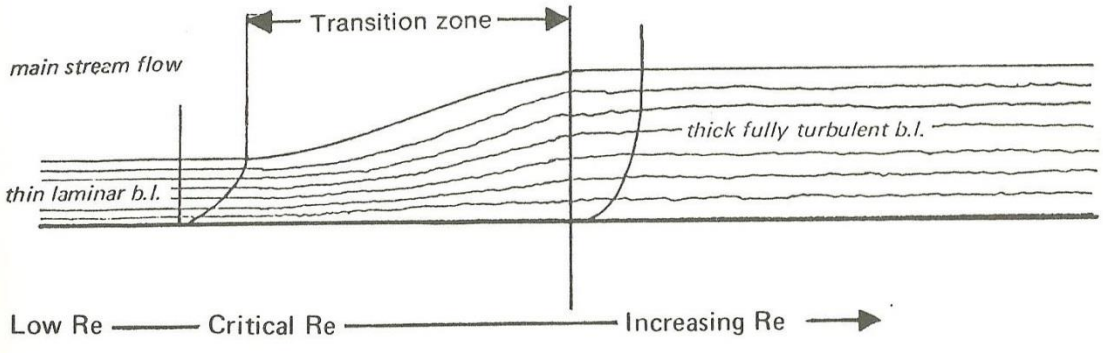

Figure 33. Boundary layer transition from laminar to turbulent with increasing Re. [31]

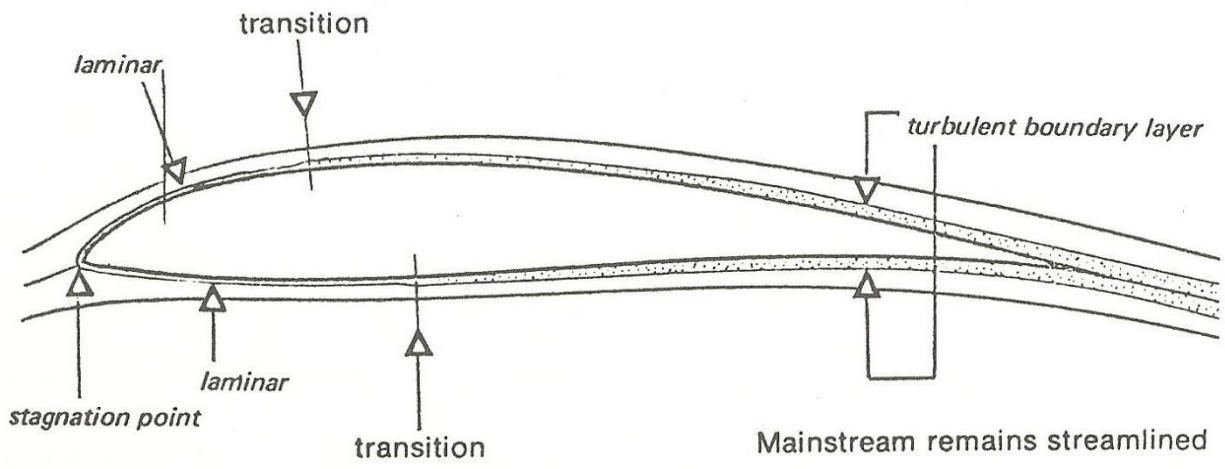

Figure 34. Flow transition over upper and lower outer surfaces. [31]

The critical Re which defines the flow regime, dependent on the location along the airfoil surface, can be increased or decreased depending on numerous factors including leading edge radius, surface roughness, and angle of attack.

As the flow moves over the upper and lower surfaces, the flow velocity along the upper surface increases, causing a decrease in pressure as described by Bernoulli's Principle. Aft of the point of minimum pressure, the flow begins to decelerate as the pressure begins to rise, and the velocity decreases while moving toward the trailing edge of the airfoil. This deceleration causes the subsequent boundary layer flow to slow causing the slower moving laminar flow to stop [31]. The barrier caused by the stagnant air causes the flow to lift from the surface, and the boundary layer continues to slow, causing a laminar separation bubble over a length of the chord [31]. Over the region of the laminar bubble, either turbulent flow reattachment or separation occurs. Turbulent reattachment is dependent on the pressure distribution gradient aft of the laminar separation bubble; due to the increased thickness and faster speeds within the turbulent boundary layer, the flow has enough energy to reattach to the skin without separation [31]. If the pressure gradient is too severe, or as the angle of attack continues to increase moving the

minimum pressure location towards the leading edge, the energy in the flow may not be sufficient for the turbulent flow to reattach causing the laminar separation bubble to burst. As the laminar separation bubble bursts, the mainstream flow is forced away from the wing and flow separation ensues resulting in aerodynamic stall. Both the lift and drag characteristics can be affected by the flow characteristics and pressure distribution at low Reynolds numbers in the critical Reynolds number region. These performance measures can cause detrimental pitch and roll performance, as well as overall poor flight characteristics. The size of the laminar separation bubble causes loss in lift over a large portion of the airfoil, in some instances, as much as 40% loss [31]. Figure 35, Figure 36, and Figure 37 below demonstrate critical Reynolds number regimes and pressure distribution over the chordwise length of the airfoil.

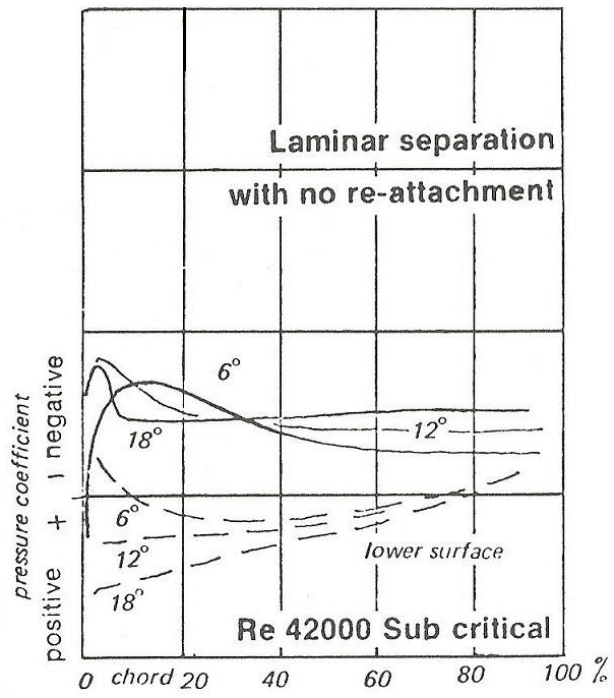

Figure 35. Airfoil chordwise pressure distribution along airfoil span for subcritical Reynolds number. [31]

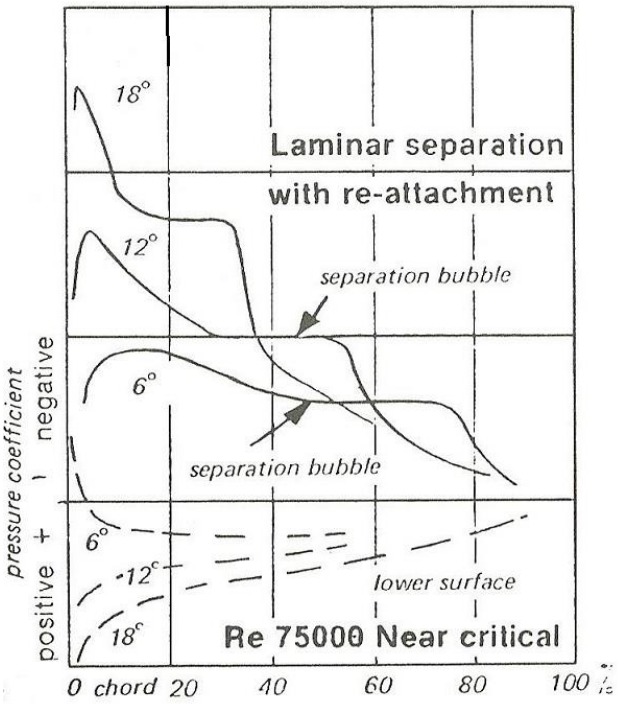

Figure 36. Airfoil chordwise pressure distribution along airfoil span for near critical Reynolds number. [31]

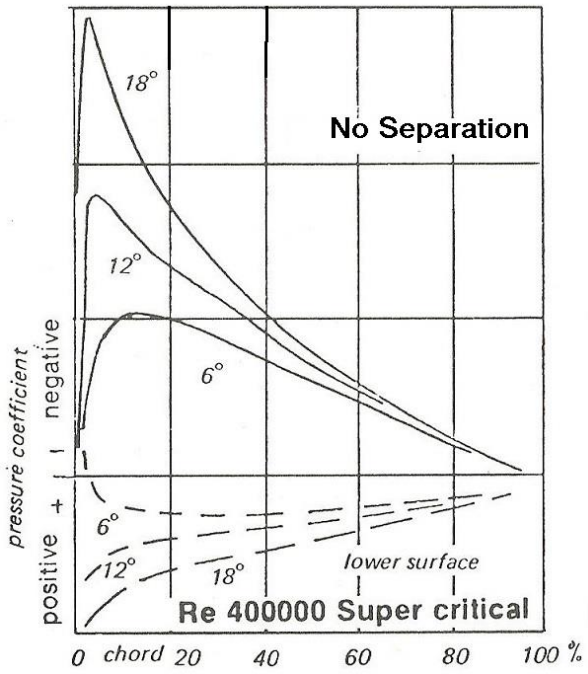

Figure 37. Airfoil chordwise pressure distribution along airfoil span for critical Reynolds number. [31]

The Reynolds number range of the scale X-56A models operate within the regime of 50,000 to 200,000. In this range, especially near Re = 50,000, the flow after the laminar separation bubble does not have sufficient time to reattach or reattaches near the trailing edge. The decreased attachment region greatly affects the lift and drag performance of the airfoil [33]. As the speed and Re increases, the laminar separation bubble decreases, allowing turbulent reattachment over a larger region of the airfoil and ultimately increasing the lift acting on the airfoil.

To increase the aircraft's performance at in low Re flow, reduction of the laminar separation bubble along the airfoil span allows for larger chordwise attachment regions. A small leading edge radius and small camber will cause a quick transition from laminar to turbulent. A quick transition to turbulent flow along with the combination of, increased speed and thin profile geometry, can improve the aircraft's performance [31, [**33**]. Changes in camber or aileron deflection requires more energy in the flow after the minimum pressure location to allow for flow reattachment. In this case, surface imperfections could cause a "trip" from laminar to turbulent, allowing the flow to stay attached over a longer span.

3.3 2-D Strip Theory Feasibility Study

Prior to building the wind tunnel and Tornado models, a feasibility study was performed on the model configuration to determine if roll moments produced by camber deformation result in a moment equivalent to conventional ailerons. Strip Theory was utilized for a simple 2-D case modeling only the outer wing sections, neglecting the center fuselage and winglets. Strip Theory analysis was performed on the full sized aircraft and scale models using viscous Xfoil data for the stock and deformed airfoil geometries. The airfoils used were 0% camber change at each

wing root, and ± 5% camber change at the appropriate wing location per the model being analyzed. The aileron models were analyzed using fixed lift values, neglecting the transitions between wing sections as seen in Figure 38 below.

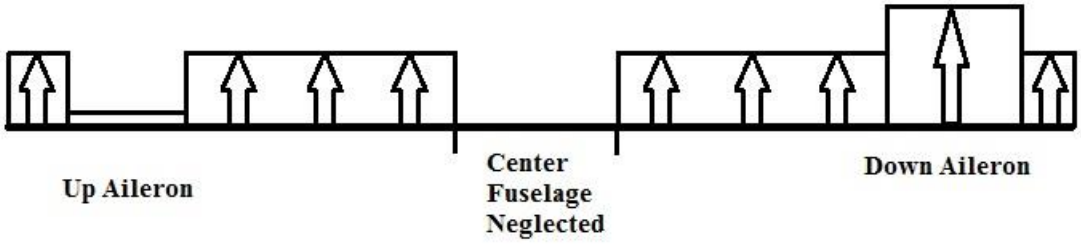

Figure 38. Strip Theory aileron lift distribution.

The governing equations for the rolling moment created by the lift imbalance between the two wings are shown below in Equations 13 to 17 [20].

$$Moment = \int_{-b}^{b} L' * y \, dy \tag{13}$$

L' equals the incremental lift on the wing, q equals the dynamic pressure, and c equals the incremental chord. Due to Strip Theories incremental nature, the chord is used instead of the planform area and integrated to allow for chordwise and spanwise changes in length.

$$L' = C_L q c \tag{14}$$

$$Moment = qc \int_{-b}^{b} C_L y dy \tag{15}$$

Due to the sweep of the outer wings, y was replaced with $\bar{y}\cos(\Lambda_n)$ [23].

$$y = \bar{y}\cos(\Lambda_n) \tag{16}$$

$$Moment = qccos(\Lambda_n)\int_{-b}^{b} C_L \bar{y} d\bar{y} \tag{17}$$

The lift profile generated through spanwise camber change varied linearly from 0% camber change to ± 5% camber deformation on each wing. The integral is the area under the lift profile varying spanwise, this was solved by breaking the wing into simple geometric shapes. Each lift distribution generates a moment about the centerline of the aircraft and the total moment is the sum of the individual moments produced. This approximation of the lift profile is shown below in Figure 39.

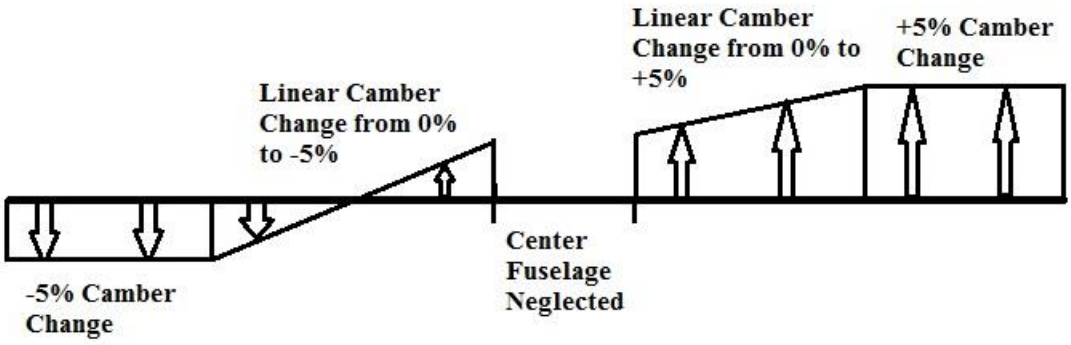

Figure 39. Strip Theory linear change with camber (1% camber deformation per foot shown).

Each X-56A model was analyzed under the flight conditions shown in Table 2.

Table 2. Full scale and scale model flight conditions

Model	Alt (ft)	Density (slug/ft^3)	Viscosity (lbs/ft$^{2)}$	Dynamic Pressure (slug/ft)	Velocity (ft/s)	Reynolds #	AoA (deg)
Full Scale	10,000	0.00176	3.53x10-7	25.07	168.78	1,657,800	0
Scale Models	Sea Level	0.00238	$3.62x10^{-7}$	16.38	117.33	87,105	0
Scale Models	Sea Level	0.00238	$3.62x10^{-7}$	30.97	161.33	119,770	0

A single speed was analyzed pertaining to the full scale model to verify the results obtained in similar papers, as seen in Eastep et. al's paper, and to determine the maximum aileron deflection angle to compare camber deformation against. Due to the small length of the scaled models' wing chord, Strip Theory analysis was also performed in small scale due to the low Reynolds number of the wing. The 2-D data was used to visualize the low Reynolds number flow and pressure distribution due to the geometric changes on each cross section of the wing for potential flow separation and transition regions. The viscous solutions in Xfoil were obtained using an Ncrit value of nine for a turbulence intensity level corresponding to 0.070% and 500 iterations. The aileron deflection cases analyzed were $\pm 5^o$, $\pm 10^o$, and $\pm 15^o$ at the full scale model flight conditions, and $\pm 5^o$ and $\pm 10^o$ at the scaled flight conditions. The $\pm 15^o$ aileron model was not analyzed due to nonconvergence of the solution in Xfoil.

3.4 Wind Tunnel Model Descriptions

The wind tunnel models used in this experiment were 3-D printed scaled models of the joint Lockheed Martin (LM) and AFRL X-56A UAV. Each model was a scaled replica of the X-56A with camber variations made to the outer wing sections to be compared to a conventional

aileron configuration. The X-56A's outer wings were modified as shown in Figure 40, Figure 41, and Figure 42 below. The maximum camber deformation was limited to $\pm$ 5% due to the small leading edge radius and reflexed airfoil. The first deformed model had a gradual camber change along the full outer wing span of each wing as shown in Figure 40 below. The right wing changed camber from 0% camber deformation at the root of the outer wing to +5% camber deformation at the tip, and -5% on the opposite wing. The second model, implemented the VCCW's 1% camber change per foot, starting from 0% change at the root, varying the original X-56A airfoil linearly to $\pm$ 5%, then maintained a $\pm$5% camber deformation to the tip as shown in Figure 41 below. The third model, was an experimental model, which changed camber quickly from 0% camber deformation to $\pm$ 5% camber deformation over a two-foot section based on the full scale aircraft to attempt to generate the maximum roll moment as shown below in Figure 42. The comparison models were the stock configuration of the X-56A with removable ailerons. The ailerons were fixed at $\pm$ 5^{o}, $\pm$ 10^{o}, and $\pm$ 15^{o} deflection angles. Originally, four models were printed, the three camber deformed models described above, and one model with three sets of interchangeable ailerons. Through the course of testing, the aileron model was reprinted twice due to structural failure during wind tunnel testing resulting in three total aileron models being used.

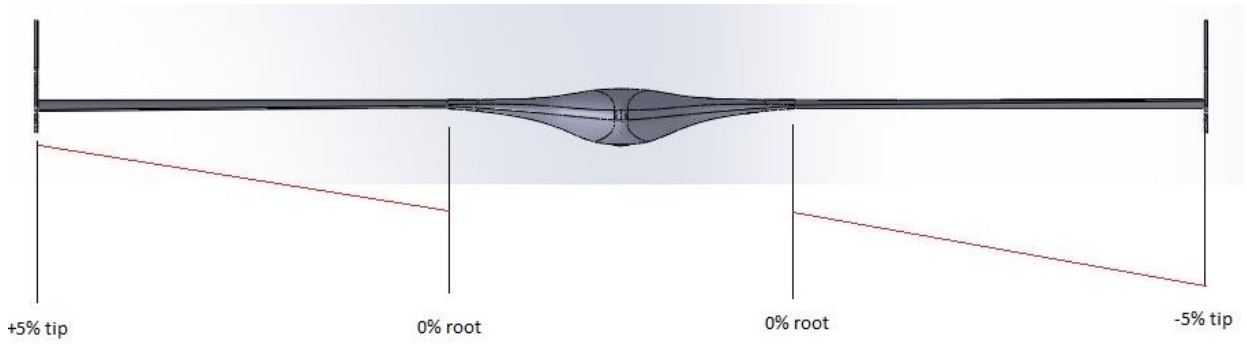

Figure 40. Gradual camber change along the full span model of the X-56A outer wing.

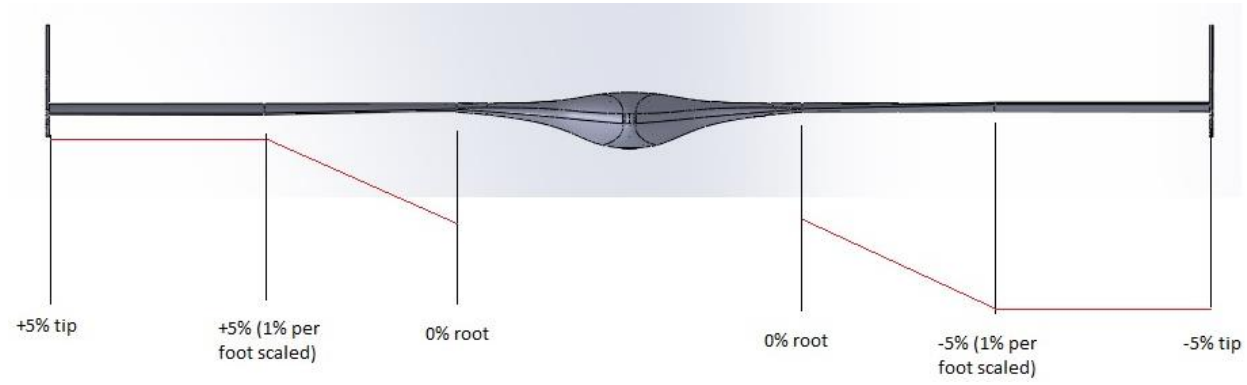

Figure 41. 1% camber change model, varying camber 1% per foot over the span holding max camber (±5%) to each wing tip.

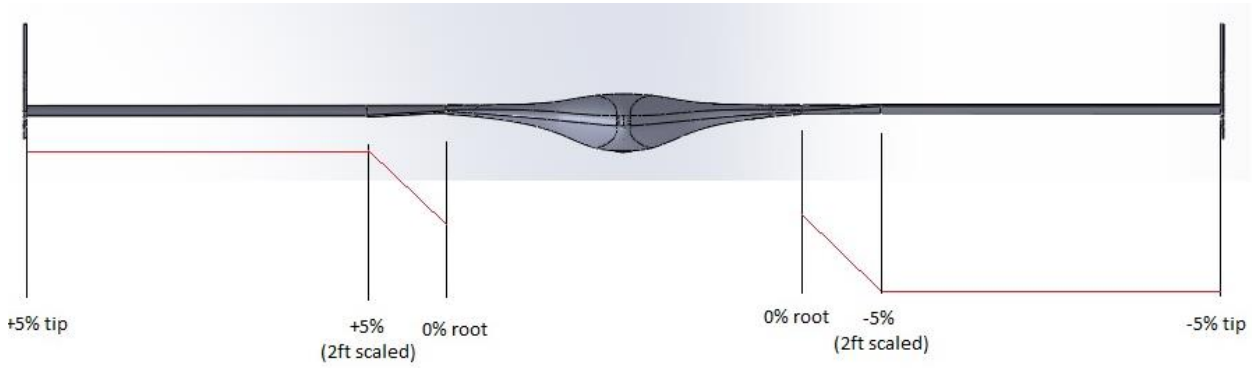

Figure 42. Quick camber change model, varying camber from 0% to 5% over a two-foot section holding 5% camber to each wing tip.

Table 3 below describes the geometric properties of each model.

Table 3. Specific geometric properties of each model.

Area (S)	25.79 in^2
Span (b)	19 in
Wing Thickness (t)	0.1357 in
Max Camber Location (x)	27% of chord
Max Thickness Location $\left(\frac{t}{c}\right)$	30% of Chord
Chord (c)	1.357 in
Mean Aerodynamic Chord (M_{AC})	2.307 in
Sweep Angle (Λ_n)	22^o
Aspect Ratio (AR)	14

The locations of the specific geometry values outlined in Table 3 are shown in Figure 43 below.

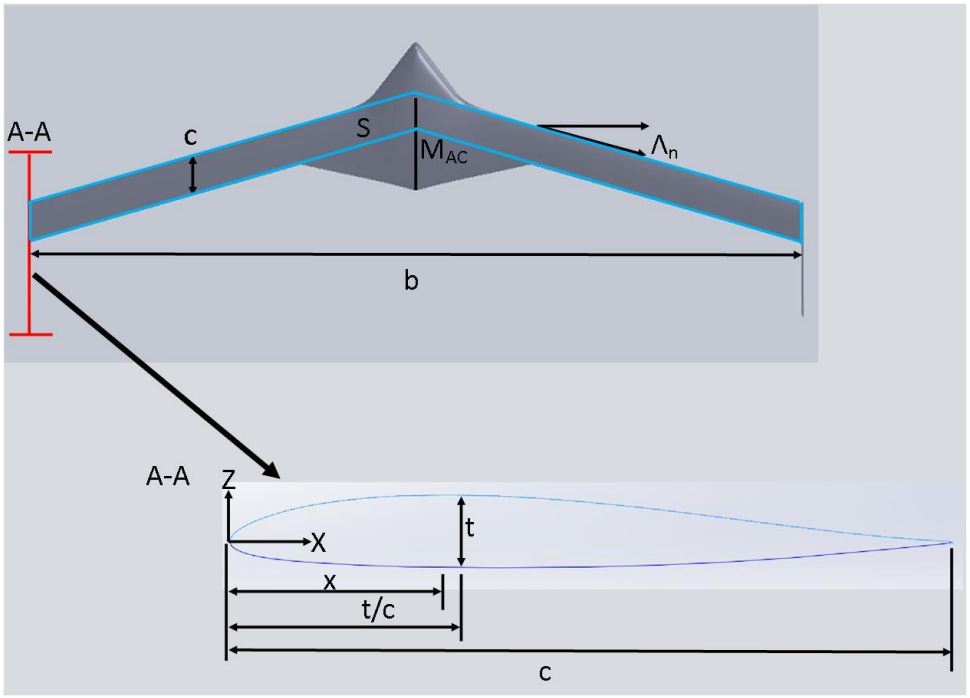

Figure 43. X-56A model geometry property locations

The planform area (*S*) is found by projecting the shadow of the model onto a 2-D surface in SolidWorks® and determining the total area. The wing span (*b*) is the tip-to-tip distance of the model. To match AFRL's VCCW configuration, the maximum thickness (*t/c*), and camber location (*x*) is held constant. The root chord (*c*) is the distance across the airfoil from the tip of the leading edge radius to the tip of the trailing edge in a straight line in the direction of the oncoming flow. The aspect ratio (*AR*) is the measure of the span squared divided by the area. The mean aerodynamic chord and its location are solved from the following Equations [21] :

$$M_{AC} = \frac{2}{S}\int_0^{\frac{b}{2}} c^2 dy \tag{18}$$

$$\frac{x}{c} = \frac{(1+2\lambda)(1+\lambda)}{8(1+\lambda+\lambda^2)}[ATan(\Lambda_n) + 4n\frac{1-\lambda}{1+\lambda}] \tag{19}$$

3.5 Wind Tunnel Model Design and Construction

A blend of SolidWorks® and Microsoft Excel was used to create each model. Each model assembly used the stock winglet and center fuselage with modified right and left outer wings. The outer wings were created by inputting the original outer wing geometry as the root section of each wing and altering each modified data point of the airfoil geometry to accommodate the 22^o wing sweep angle at a $1/24^{th}$ reduced scale, due to the non-dimensionalization of the chord. Xfoil's camber modification program holds the leading and trailing edge locations constant while raising or lowering the outer mold line coordinates to correspond with the change in the mean camber line. The VCCW uses a spar located at the maximum camber location, which the leading and trailing edge coordinates rotate about [19]. To move each Y coordinate from the Xfoil

coordinates to the spar location, the coordinates were raised or lowered 0.01in with each ±1% camber adjustment from the original airfoil geometry. Excel was used to lower the +5% camber -0.05in, and raise the Y coordinates for the -5% camber modification +0.05in. This Y coordinate linear transformation aligned the maximum camber location vertically with the original airfoil geometry along the span of the wing. The spanwise airfoil placement was accomplished through a linear X coordinate transformation to build the 22^{o} sweep. The non-dimensionalized camber deformed airfoils were shifted aft according to the specifications of the wing model being built as seen in Figure 44 below.

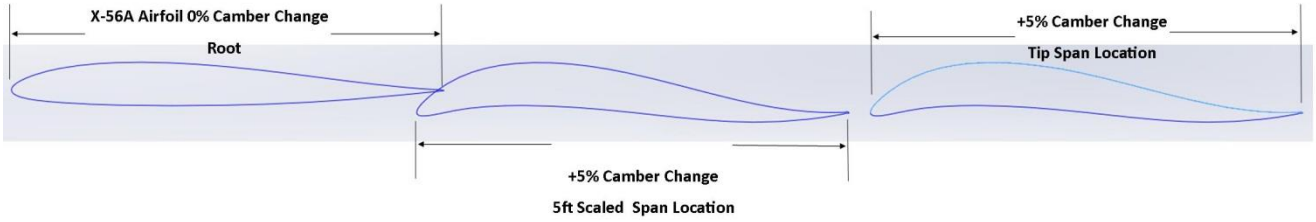

Figure 44. Airfoil coordinate shift.

Each wing tip airfoil was shifted aft with respect to the amounts shown in Table 4 below.

Table 4. X coordinate shift of each airfoil based on airfoil location to sweep wings 22^{o}. Tip places 5% camber change airfoil at wingtip, 5ft scaled to place the 5% camber change airfoil on the 1% camber deformation model, and 2ft scaled to place the 5% camber change airfoil on the quick camber change model.

Spanwise Location	Tip	5ft scaled	2ft scaled
X Coordinate Modification	1.99 in	0.94 in	0.37 in

After the X coordinates were shifted aft of the root airfoil, planes were placed at the spanwise location necessary for airfoil placement as seen in Figure 45 below.

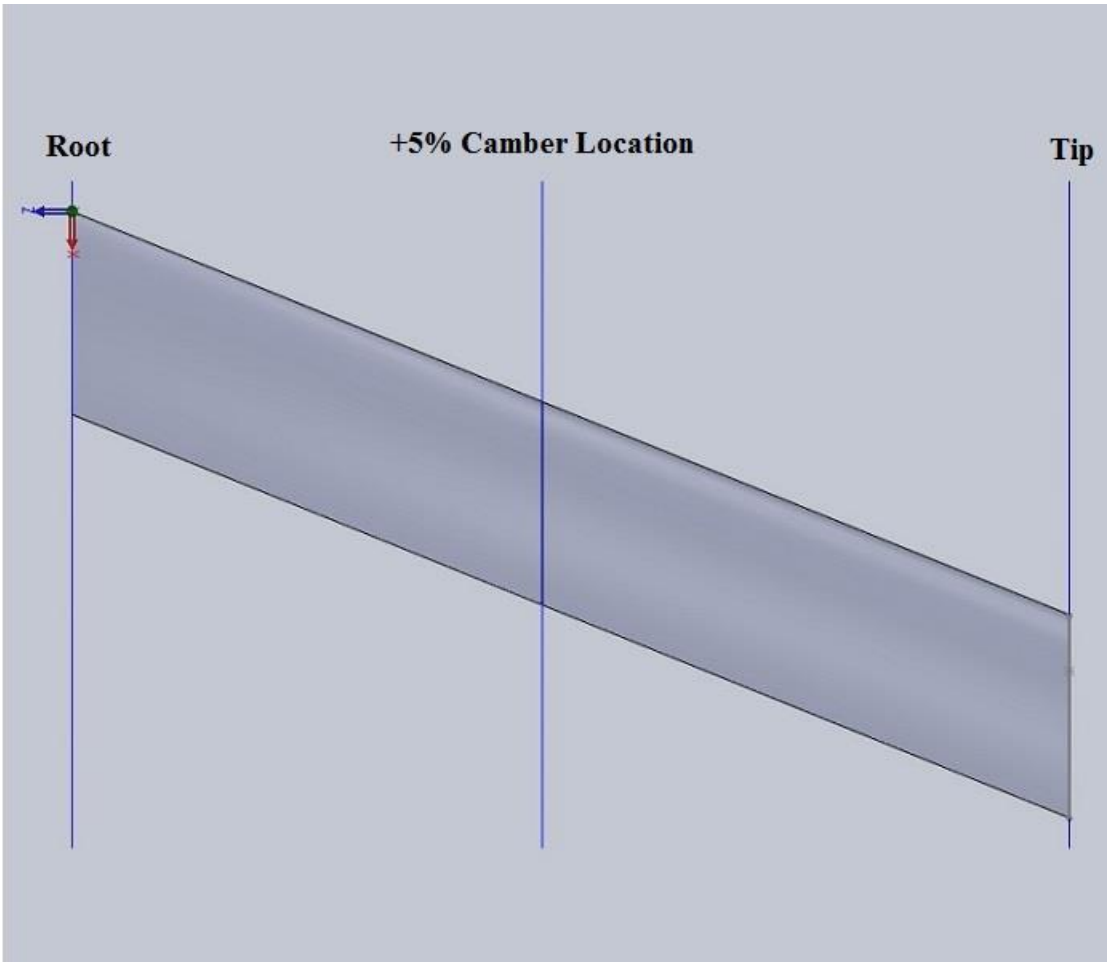

Figure 45. Right wing plane placement for 1% camber change model.

The planes were placed at 4.92in for the tip airfoil, 2.32in for the 5ft scaled airfoil, and 0.93in for the 2ft scaled airfoil. “Convert entities” was used to transfer each airfoil to the appropriate plane along the span. A reference line connecting each airfoil at the maximum camber location was placed to guide the loft function used to build the 3-D structure and outer skin.

Each wing was scaled up by a scale factor of 1.357 to change from the $1/24^{th}$ scale non-dimensionalized wing size to the 19in wing span model size at $1/17.68^{th}$ scale of the full sized aircraft. Equations 20 and 21 below were used to find the model scale and scale factor.

$$Model\ Scale = \frac{Actual\ Wing\ Span}{Wind\ Tunnel\ Model\ Span} \quad \textbf{(20)}$$

$$Scale\ Factor = \frac{Chord}{Model\ Scale} \quad \textbf{(21)}$$

The full scale X-56A wing span is 28ft (336in), and the wind tunnel model was scaled down to 19in, which was the maximum the Objet Eden 500V 3-D printer could accommodate to maximize production speed, model accuracy, and strength due to the printing orientation. After scaling each wing, the winglets and center fuselage section were scaled to fit the 19in span model and then mated together. Each aircraft model center fuselage had a mounting bulb to allow the models to mount to the balance. The bulb had an outer diameter of 0.91in, and inner diameter of 0.51in centered on the rear vertex of the center fuselage centerline. The bulb was extruded 2.35in into the fuselage with a mounting hole measuring 0.13in through the center of gravity as seen in Figure 46 below.

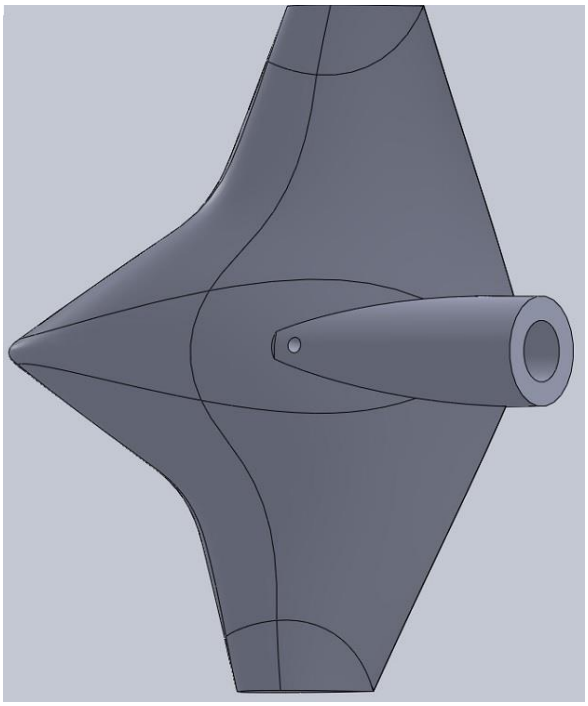

Figure 46. Center fuselage mounting bulb location and placement.

To build the aileron comparison model and the ailerons themselves, a Finite Element Model (FEM) with aileron grid points was provided for the original X-56A. These points were plotted on the SolidWorks® model for the upper and lower outboard aileron locations and connected to create an outline of the aileron. The X-56A has four aileron pairs, only the outboard ailerons were analyzed to generate the largest rolling moment, it was assumed the additional ailerons remain fixed at the wing's trailing edge. Figure 47 and Figure 48 show the aileron grid points plotted as lines in the outer aileron wing station, as well as the cut-away aileron section from the model.

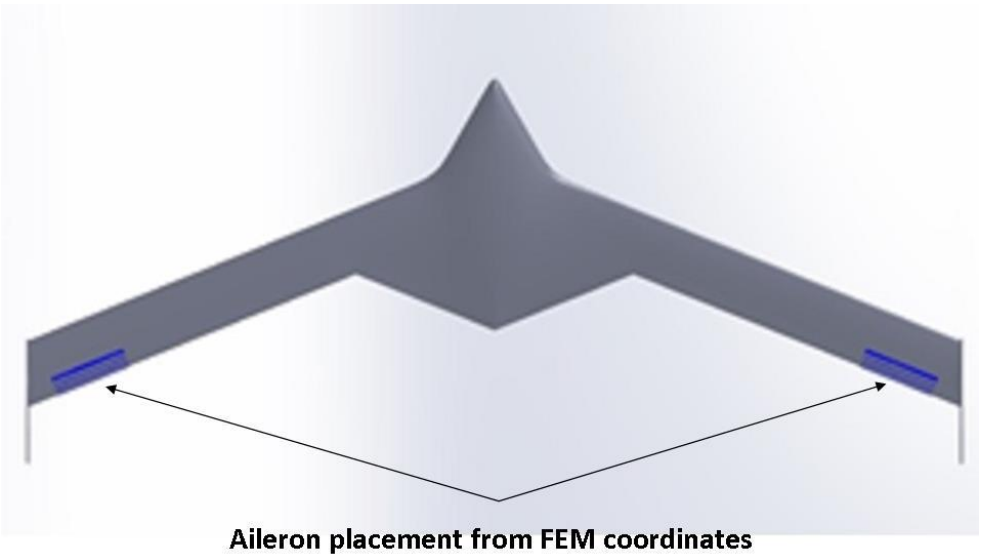

Figure 47. X-56A outer aileron location markers.

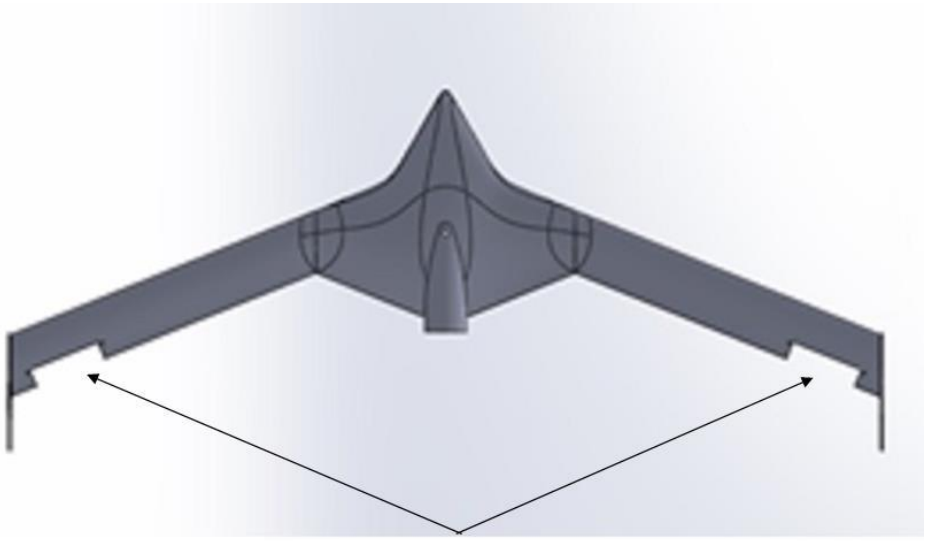

Figure 48. X-56A outer aileron cut-away.

After the aileron section was removed, a clearance of 0.002in was created on the model wings for the ailerons to ensure sufficient clearance. An alignment pin was installed on the ailerons to assist aligning the aileron edges with the wing surface. Each pin extended 0.11in from the side of

each aileron, and was 0.03in wide. Each pin was rotated $\pm 5^{o}$, $\pm 10^{o}$, and $\pm 15^{o}$ for a matching pair of symmetric ailerons, as seen in Figure 49 below.

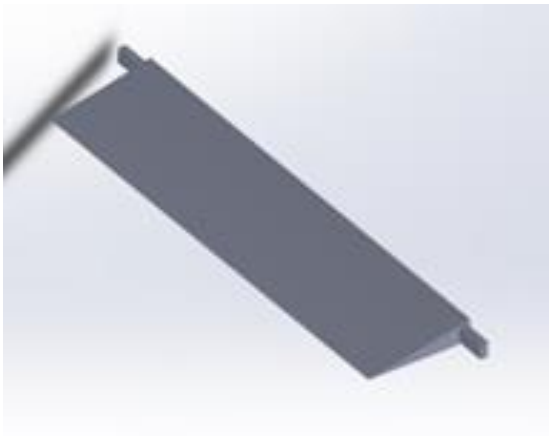

Figure 49. X-56A aileron with alignment pins positioned at 5^{o} trailing edge down.

All six aircraft models were printed on the Stratasys Objet Eden 500V as stated above. The Objet printer has a printing surface of 19.3in long x 15.4in wide x 7.9in tall, can print to a maximum size of 25.9in diagonally with a maximum resolution of 600 dpi, and minimum layer thickness of 0.0006in. The printing substrate was SUP705 support material, and the printing material was Veroblue RGD840. The model drawings were in .STL format and were printed as a single, solid print object, which required no assembly and maximized structural rigidity. The models were washed to remove the support material and remaining residue. After the support material was removed, 100-grit sand paper was used to remove printing striations and grooves to smooth out the rough surface without removing the key characteristics of the reflexed airfoil shape. Sanding was followed by #0 steel wool to further smooth the finish, and finally #0000 steel wool was used to reduce any remaining marks not addressed by the previous steps. These final stages were performed to reduce surface roughness and minimize manufacturing induced skin friction drag on the aircraft. After the aileron models were cleaned and prepped for use, the ailerons were installed by inserting the alignment pin into a slot recessed into each wing. The

aileron angle was calculated using geometry due to the small size of the ailerons, and verified with dial calipers by measuring from the trailing edge (TE) solved for in Equations 22 and 23 below.

$$\text{Sin}(\text{Aileron Angle}) = \frac{\text{Vertical TE Displacement}}{\text{Aileron Length}} \quad \textbf{(22)}$$

$$\text{Vertical TE Displacement} = \text{Aileron Length} * \sin(\text{Aileron Angle}) \quad \textbf{(23)}$$

Each aileron was glued on three sides, both top and bottom of the aileron. Table 5 below describes the aileron angle and vertical distance from the trailing edge.

Table 5. Model aileron deflection angle and trailing edge vertical displacement.

Aileron Deflection	5^o	10^o	15^o
Trailing Edge Displacement	0.033 in	0.066 in	0.099 in

3.6 Tornado Model Simulation

Simulation of the X-56A allows users to make modifications to the aircraft's geometry with quick computing time, and drastically reduced cost while allowing the user to view potential changes to the vehicle's stability and flight characteristics. Tornado was selected as a simulation model because it is a MATLAB based open software tool and allows for ease of use which yields close coherence with experimental data. Tornado was completed in 2000 as a Master's thesis from the Royal Institute of Technology, and is a linear, inviscid, aerodynamic solver utilizing the Vortex Lattice Method (VLM). The original goal of Tornado was to determine if VLM could be used in real time applications such as an aircraft simulator, where it would supply the aerodynamic force model for the simulation scenarios better than look-up tables [34]. VLM was selected to model the X-56A due to low Mach values ($M < 0.3$) which

ensure incompressible flow, swept wings, change in camber both spanwise and chordwise, and vertical stabilizer winglets which must be modeled to account for directional stability of the aircraft. According to Anderson (2007), due to the wing sweep and aspect ratio of the X-56A, classical lifting-line theory is inapplicable.

For inviscid, incompressible flow, VLM models each wing (main wing, vertical and horizontal stabilizers, etc.) as a series of lifting surfaces configured in a grid pattern in the spanwise and chordwise directions. By superimposing a finite number of horseshoe vortecies of different strengths on the wing surfaces, each bound vortex starts $l/4$ from the front of the panel, where *l* is the length of the panel [3]. Each panel can be considered a trapezoid, and does not have to be a square, this allows for any geometry to be modeled [3]. A point P, considered to be a control point, as seen in Figure 50 below, was placed at the $3l/4$ location from the front of each panel, and then centered spanwise on each panel. This point was used to calculate the induced velocity by the single vortex through the Biot-Sevart law by treating each vortex filament independently.

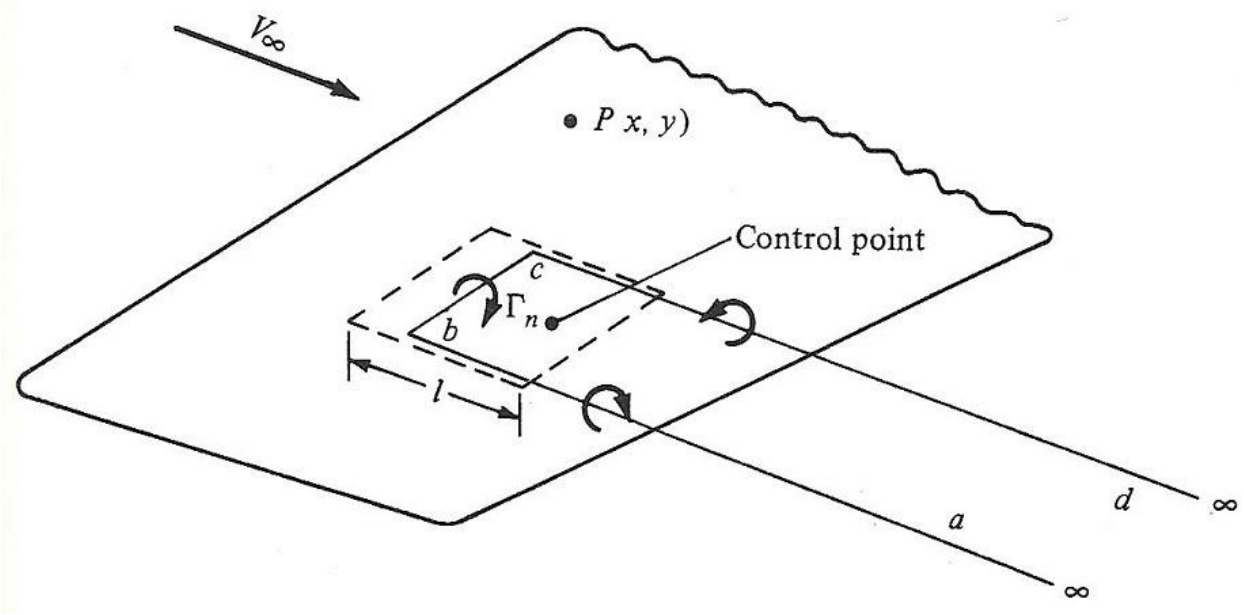

Figure 50. VLM control point location. [3]

The Biot-Sevart law solves for the incremental velocity at point P through the use of the vortex strength (Γ_n) from Equation 24 [3].

$$dV = \frac{\Gamma_n (dl\ x\ r)}{4\pi r^3} \quad \textbf{(24)}$$

Integration of the Biot-Sevart equation yields the velocity induced for a vortex segment at point P as seen in Equation 25 below [3, [**34**].

$$V = \frac{\Gamma_n}{4\pi} \frac{r_1 \times r_2}{|r_1 \times r_2|^2} \left[r_0 \cdot \left(\frac{r_1}{r_1} - \frac{r_2}{r_2} \right) \right] \quad \textbf{(25)}$$

When the flow tangency condition is applied at all the control points, a system of simultaneous equations can be solved to compute all of the Γ_n's on each panel.

$$\begin{bmatrix} w_{11} & \cdots & w_{1n} \\ \vdots & \ddots & \vdots \\ w_{n1} & \cdots & w_{nn} \end{bmatrix} * \begin{bmatrix} \Gamma_1 \\ \vdots \\ \Gamma_n \end{bmatrix} = \begin{bmatrix} b_1 \\ \vdots \\ b_n \end{bmatrix} \quad \textbf{(26)}$$

The simultaneous equations are built from the flow from each vortex through each panel (w), the unknown vortex strength (Γ_n), and the flow through each panel as determined by the angle of attack of the wing, panel angle, sideslip angle, etc. (b) as seen in Equation 26 [34].The vortex strength calculated from equation 26, was applied to the Kutta-Joukowski theorem where the force experienced on each panel is equal to the product of the fluid density, stream velocity, length of the vortex segment crossing the panel and the circulation, and has a direction perpendicular to the stream velocity, given in Equation 27 below [34, [**35**].

$$F_i = \rho V_\infty \Gamma_i l \quad \textbf{(27)}$$

These forces were used to solve for the lift and induced drag applied to each panel of the wing. The finite lift vector can be found from Equations 28 and 29, and the induced drag by Equations 30 and 31 below [35].

$$L_i = \rho V_\infty \Gamma_i \quad \textbf{(28)}$$

$$L = \sum_{i=1}^{n} L_i \quad \textbf{(29)}$$

$$D_i = -\rho w \Gamma_i \quad \textbf{(30)}$$

Where D_i is the induced drag per unit span, ρ is the density, w is the induced velocity, which was solved from the integration of the Biot-Sevart law, and Γ_i is the vortex filament strength.

$$D = \sum_{i=1}^{n} D_i \tag{31}$$

Tornado is organized in three subroutines, preprocessor, solver, and post processor. The preprocessor builds the model geometry from the user input. A lattice mesh is built before solving any forces and moments. Tornado generates the lattice mesh similar a VLM, vortex-slings are used instead of the traditional horse-shoe vortices to enable the freestream to follow the wake which allows for flapped elements. The procedure works the same way as the horse-shoe with the exception the legs of the shoe are flexible, and consist of seven, rather than three vortices of equal strength [34]. The extra four vortices occur with two vortices on the flapped panel, and two as the trailing wake as seen in Figure 51 below.

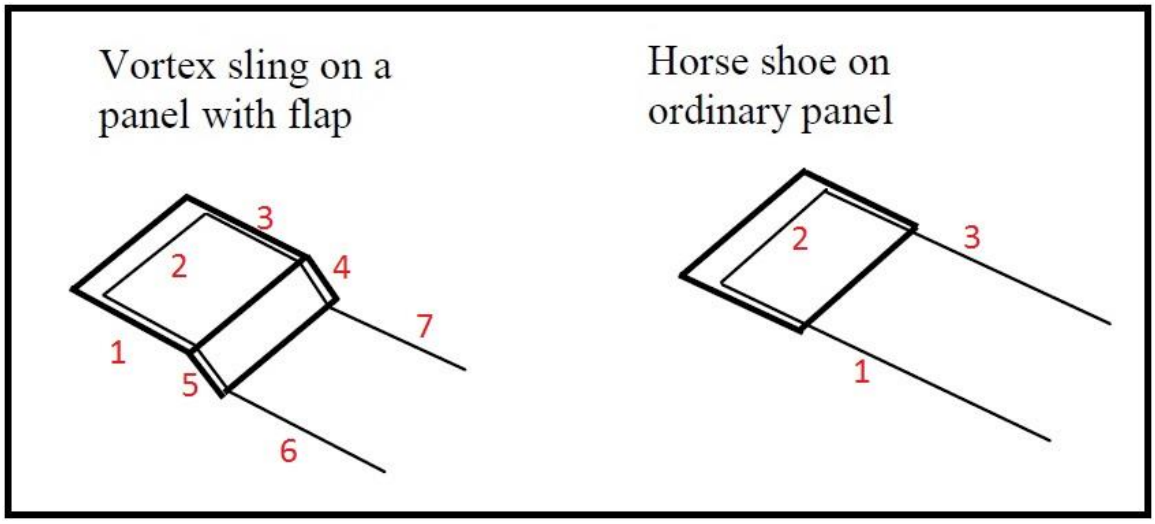

Figure 51. Tornado vortex slings (left) and typical VLM horseshoe vertices. [36]

Tornado varies from traditional VLM by aligning the panel angle with the mean camber line so the unit normal is perpendicular to the mean camber line as seen in Figure 52 below [34].

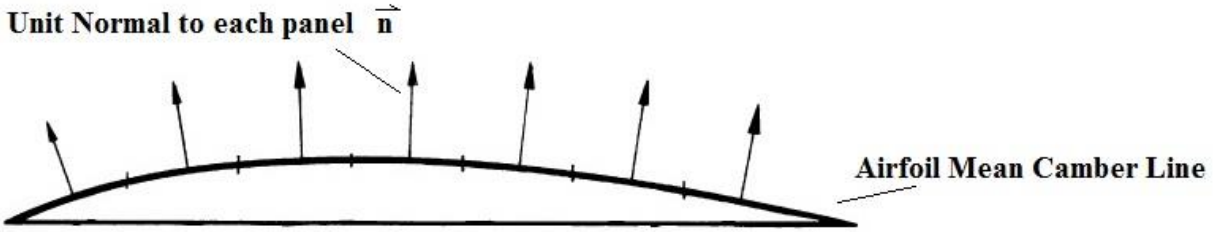

Figure 52. Tornado panel normal along the mean camber line. [34]

"The task of the solver is to convert intermediary results of the preprocessor into forces and moments" [34]. After creation of the lattice, the downwash is calculated at each vortex at all collocation points (P) created by the flow field vortices [34]. The boundary condition is applied; no flow parallel to the panel normal [34]. The vortex strengths are computed by using Gausian elimination along with the boundary condition solving Equation 24 [34]. The final step the solver applies before the forces are solved is the inwash computed with the same method as the downwash [34]. The forces are calculated using the Kutta-Jukowski theorem, and moments are solved based on the calculated forces and their distance from the applicable rotation axis. Finally, from the forces and moments, all aerodynamic and stability coefficients are solved. The postprocessor opens the results file, sorts all data, and plots the desired data creating the final output from Tornado.

3.6.1 Tornado Model Building

Four Tornado models were built to simulate the 3-D printed wind tunnel models. Each model was built in Tornado, in meters, to the scaled model sizes including the balance mount bulb. Prior to building each model, the individual source files for the airfoil geometries were modified individually and inserted into Tornado. Each airfoil coordinate file was non-dimentionalized, and the vertical coordinates were modified to raise or lower each airfoil as

necessary, as discussed in the *Wind Tunnel Model Design and Construction* section of this chapter. The non-dimensional vertical displacement is calculated by Equation 32 below.

$$nondimensional\ vertical\ displacement = \frac{Dimensional\ vertical\ displacement}{chord\ length} \quad \textbf{(32)}$$

Each center fuselage airfoil cross section and outer wing airfoil was shifted vertically along the Z axis by 0.000254m (0.01in) per 1% camber change. Each model outer wing camber change varied from 0% change at the root to $\pm$5% change along the span by $\pm$0.25% increments. Each airfoil vertical shift was referenced to the outer wing root airfoil.

The conventional aileron model was built using Tornado's built in geometry tool. The aircraft is modeled by mirroring about the XZ plane with the ailerons configured anti-symmetrically to allow each aileron to move opposite one another. The aileron model was built with two horizontal or vertical lifting surfaces ,"wings," the first being the center fuselage and outer wings, and second being the winglets placed at the wing outboard tip 0.0107m below the Z reference point to ensure proper winglet placement above and below the outer wing. The first wing was built with ten sections, seven for the center fuselage and three for the outer wing. The center fuselage and outer wings were built using the design parameters as seen in Table 6 below.

Table 6. Aileron model geometric properties for each panel.

Panel Number	Panel Span (m)	Flapped	Taper	Sweep (^{o})	Dihedral (^{o})
1	0.0051	0	0.9544	41.98	0
2	0.0051	0	0.9323	52.43	0
3	0.0042	0	0.8611	36.03	0
4	0.0144	0	0.7122	48.61	0
5	0.0144	0	0.7934	21.1	0
6	0.0144	0	0.7967	11.63	0
7	0.0144	0	0.7475	11.31	0
8	0.1173	0	1	22	0
9	0.0373	1	1	22	0
10	0.0145	0	1	22	0

The "flapped" panel in panel nine is 0.03734m in span with a flap (aileron) equating to 28.76% of the chord or .2876. The reference point and center of gravity were moved to the same location after building the model using the SolidWorks® model center of mass location (.0775m, 0m, -.003401m referenced from the nose of the aircraft, and moved to the outer wing reference line). The winglets were built similarly to the center fuselage, utilizing airfoil geometry extracted from the SolidWorks® models at the winglet upper tip and outer wing attachment chord. The winglet and outer wings were built using the geometric design parameters as seen below in Table 7.

Table 7. Winglet geometric properties per panel.

Panel Number	Panel Span (m)	Flapped	Taper	Sweep (^{o})	Dihedral (^{o})
1	0.0048	0	1.2254	-38.29	90
2	0.0058	0	1.9081	-70.23	90
3	0.0132	0	0.6446	56.31	90
4	0.0229	0	0.7103	42.66	90

Each camber deformed model was built with three, "wings". The first "wing" consisted of the outer wings and center fuselage, the second and third, "wings," are the individual winglets. Each model was built in the positive Y direction in Tornado to ensure the spanwise and chordwise velocity vectors were pointing in the proper position. The left outer wing was constructed first, building from tip to root where each taper ratio was

$Taper\ Ratio = \frac{Root\ chord\ length}{Tip\ chord\ length}$. Each taper ratio was equal to one or larger with a negative sweep angle. After the centerline of the aircraft was reached, the taper ratio was solved as $Taper\ Ratio = \frac{Tip\ chord\ length}{Root\ chord\ length}$ with positive sweep angles. Spanwise airfoils were placed every quarter of a percent change from 0% camber change to $\pm$ 5% camber change. Each winglet was built using Table 7 above from the aileron model. Each outer wing was sized with respect to Figure 53 below, and each inboard panel was divided into four panels to account for the 0.25% camber changes.

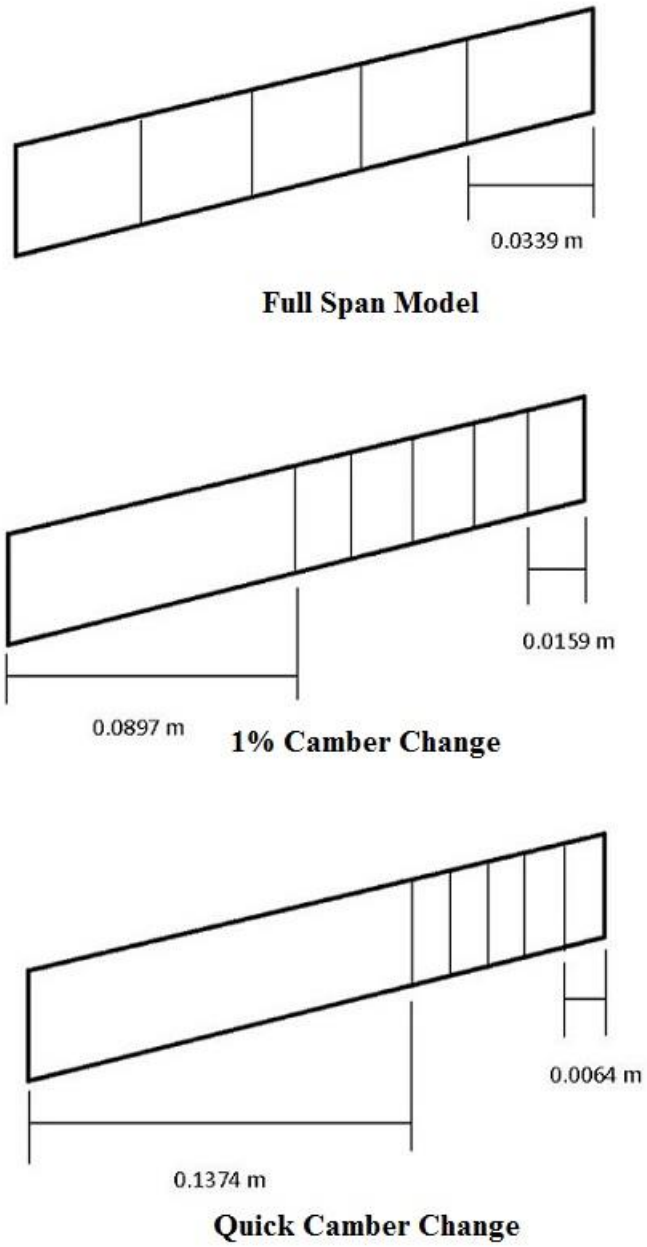

Figure 53. Camber deformed wing panel sizes.

After building each model, the reference point was moved to the center of gravity (-0.0578m, 0.2414m, -0.003401m moved from the left outboard wingtip leading edge). Each model was divided into spanwise and chordwise panels. Each chordwise section was divided into 15 segments to account for the camber change geometry. The spanwise segments were divided

based on the span length of each panel. Table 8 below outlines the segment values based on span.

Table 8. Number of panels based upon panel span.

Panel Span	Spanwise Panels
0 to 0.00127m	2
0.00127m to 0.0508m	3
0.089662m	10
0.137414m	15

Each model can be seen in Figure 54 through Figure 57.

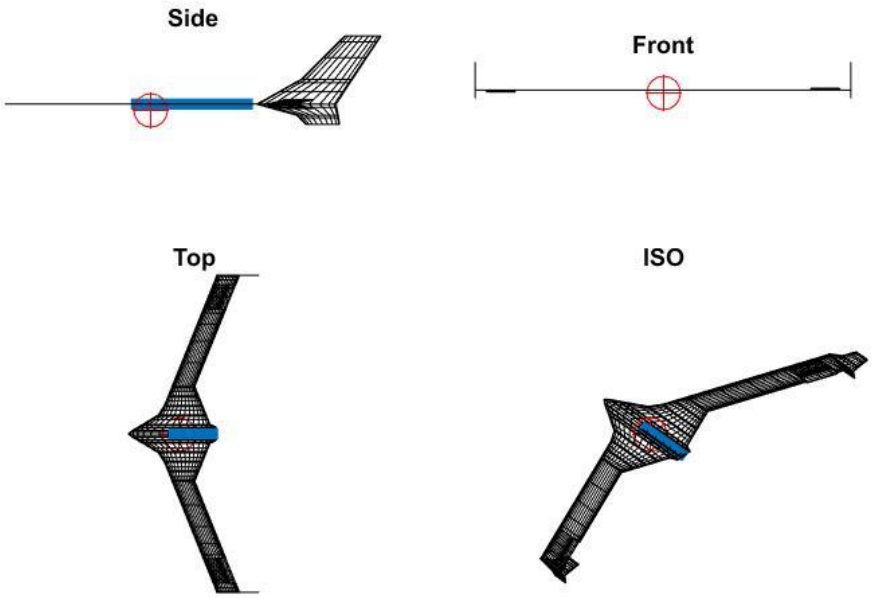

Figure 54. 15° aileron Tornado model (isometric view).

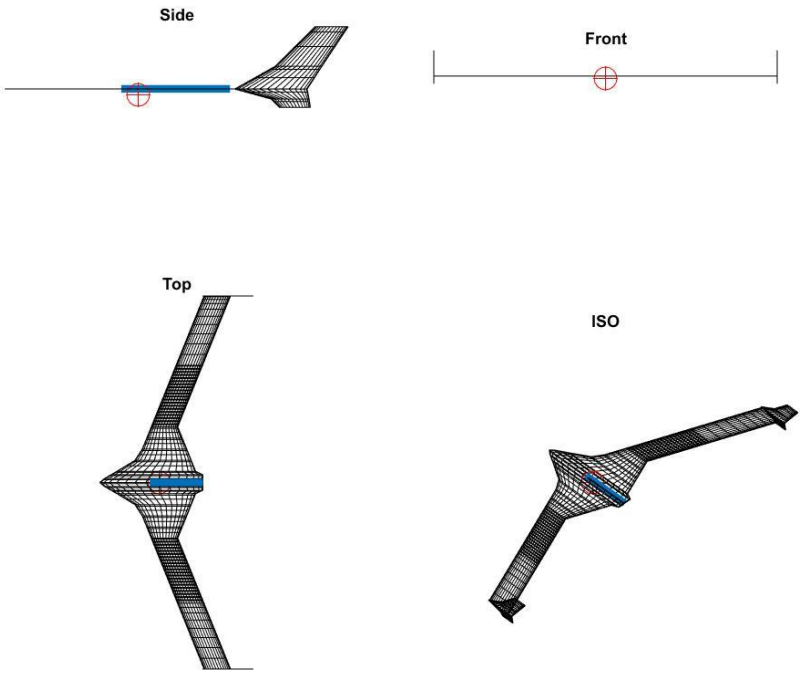

Figure 55. 1% camber deformed Tornado model (isometric view).

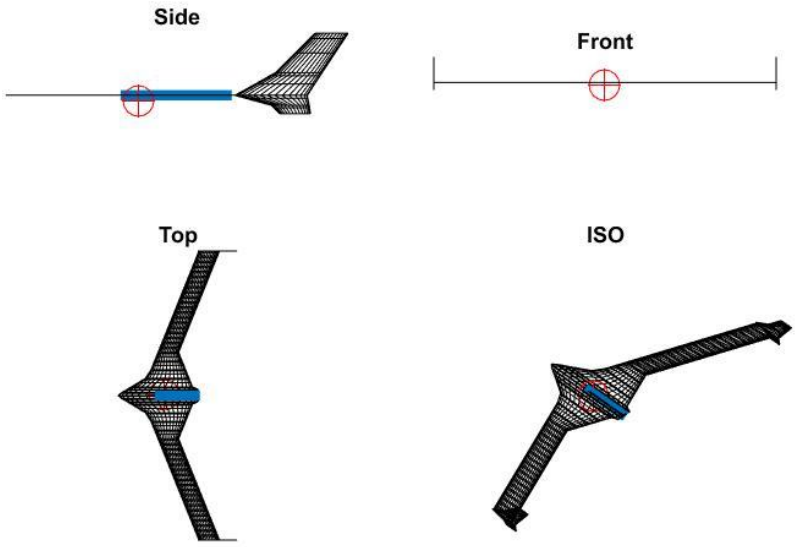

Figure 56. Full span Tornado model (isometric view).

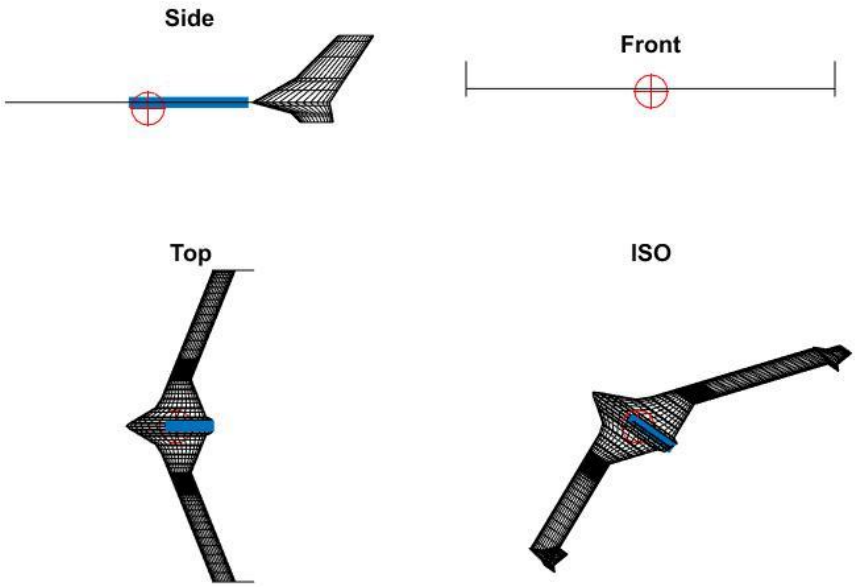

Figure 57. Quick camber change Tornado model (isometric view).

3.6.2 Tornado Simulation

Tornado utilizes geometric files which consist of the model geometry input by the user and state files which consist of flight condition data such as altitude, velocity, aircraft attitude, etc. to process and compute the desired data. The geometric files were created per the methods discussed in the previous section, then input into the program. Each state file consists of the following user defined inputs for the initial flight condition: airspeed (m/s), angle of attack (radians), sideslip angle (radians), roll rate (rad/s), pitch rate (rad/s), yaw rate (rad/s), pitch acceleration (rad/s), yaw acceleration (rad/s), altitude (m), density (kg/m3), and if a Prandtl-Glauert correction factor was used. The state file modeled the aircraft in straight and level flight modifying the state file for each run by looping through each of five sideslip angles, -6^{o}, -3^{o}, 0^{o}, 3^{o}, $6^{o,}$ and the angle of attack was initially set to 0 rad while looping through each of three speeds: 30mph, 80mph, and 130mph. Three speeds were analyzed due to the inviscid nature of

Tornado; neglecting Reynolds number effects, speed does not affect the coefficient value output. The Prandtl-Glauert correction factor neglected due to each model operating at a Mach<0.3. An alpha sweep was performed ranging the angle of attack from -5^o to $+15^o$. The linear region for the X-56A extracted from the wind tunnel analysis is approximately between -2^o to $+5^o$, to which Tornado's analysis was applied. Tornado's outputs included a [6x9] matrix of results for each angle of attack. These values included: C_L, C_D, C_C ,C_l, C_m, C_n, $C_{x,}$ C_Y, and C_Z. Each stability derivative was also output as a function of alpha (α), beta (β), roll rate (*p*), pitch rate (*Q*), and yaw rate (*R*).

Alpha sweeps were run for each speed and sideslip angle generating a [9x6x21] matrix for each speed and sideslip angle. Each test was conducted with the full angle of attack range conducted in the wind tunnel ranging from -5^o to 15^o later extracting only the linear region. This matrix block was reduced, keeping the first column of aerodynamic coefficients, removing the stability derivatives and building a single [9x21] matrix. This output was compared to the wind tunnel data comparing the linear range from -2^o to 5^o angle of attack.

3.7 Wind Tunnel Testing

Wind tunnel testing was performed with the 3-D printed models described above to validate the Tornado simulations. All wind tunnel testing was conducted in AFIT's low-speed wind tunnel. The tunnel was manufactured by the New York Blower Company, powered by an ACF/PLR Class IV fan, and controlled by a Siemens Adjustable Frequency Controller with a Toshiba EQP III motor [37]. The low speed wind tunnel is an open-loop configuration drawing air through a 122in wide, 111in high, and 70in deep opening. The inlet section feeds air into a

converging section, which is attached to the test section, and exhausted 90^{o} upwards into the ceiling as seen in Figure 58 below.

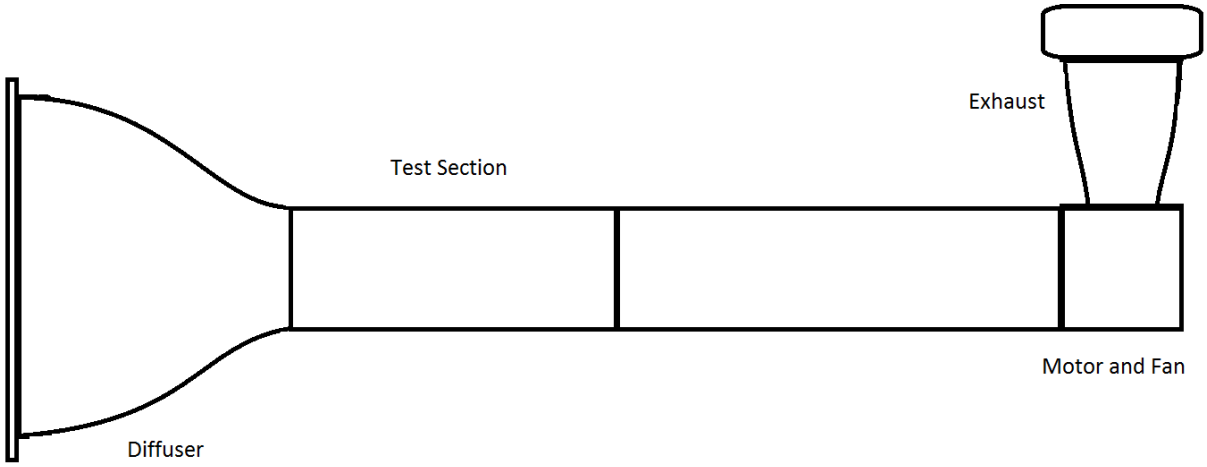

Figure 58. AIFT open-loop wind tunnel diagram showing diffuser, test section, and exhaust section.

The test section measures 31in high, 44in wide, and 72in long [37]. Each side of the test section is fitted with Plexiglas doors to access and install test articles and force balances, as well as a yaw table mounted below the test section which protrudes through the floor of the tunnel. The X-56A span-to-tunnel width ratio equation is given in Equation 31 below:

$$span\ to\ tunnel\ width\ ratio = \frac{b}{w} \tag{33}$$

Where b is the model wing span and w is the width of the test section. The tunnel test section width is 44in and the model wing span is 19in. This equates to a span-to-tunnel width ratio of $0.432 \approx 0.43$, where the general rule of thumb is $\frac{b}{w} \leq 0.8$ [37, [**38**].

The 3-D printed models were attached to the AFIT-3 50-lb_f, six degree of freedom (DOF) balance manufactured by Modern Machine and Tool Company. The balance contains three

internal strain gauges, and is accurate to 0.04% of full capacity, which is approximately 0.02-lb_f. Table 9 below lists the maximum forces and moments, along with the percent accuracy for each direction and overall resolution.

Table 9. Maximum AFIT-3 balance load, % accuracy, and resolution in each of the six degrees of freedom.

Force/Moment	Load	% Accuracy	Resolution
Normal Force	50 lb_f	0.04	0.02
Axial Force	25 lb_f	0.1	0.025
Pitch Moment	50 in-lb_f	0.12	0.06
Roll Moment	15 in-lb_f	0.1	0.0255
Yaw Moment	25 in-lb_f	0.11	0.025
Side Force	25 lb_f	0.07	0.015

The AFIT-3 balance is 0.5in in diameter, and is 2.525in from the balance tip to the moment center. The center mounting hole used for model attachment is 0.150in from the balance end and 2.375in from the moment center, as seen in Figure 59 below.

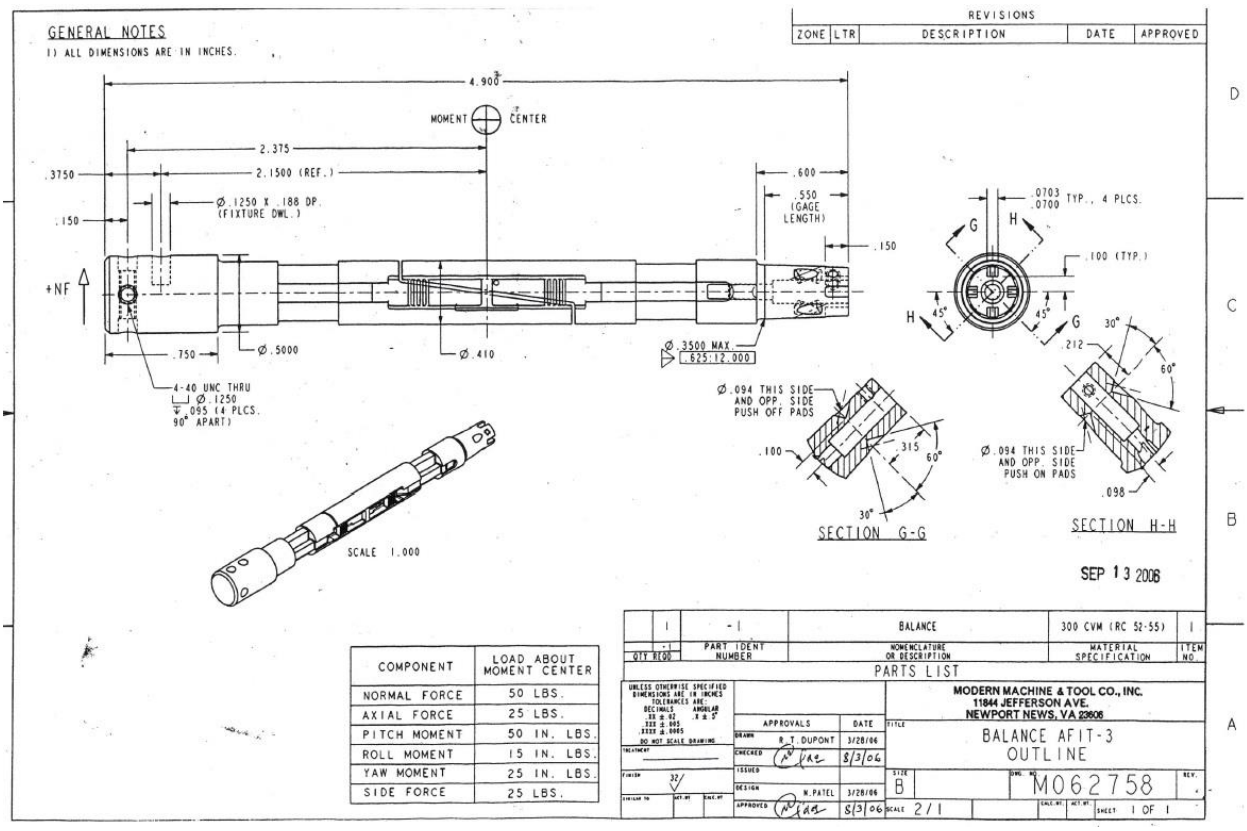

Figure 59. AFIT-3 balance dimensions.

The controller converts the analog strain gauge output to a digital signal. It then amplifies and refines the signal with a low pass filter, and converts it from voltage changes to forces and moments, through a lab view conversion, and stores the data to a PC [37]. The balance is attached to an automated sting mounted below the test section. The sting can modify the test article's angle of attack and yaw angle automatically from the controller. The angle of attack limits are -20^{o} to $+30^{o}$, and the sideslip angle limits are -60^{o} to $+60^{o}$ [37]. The balance and tunnel reference frames follow the convention as shown in Figure 60 below.

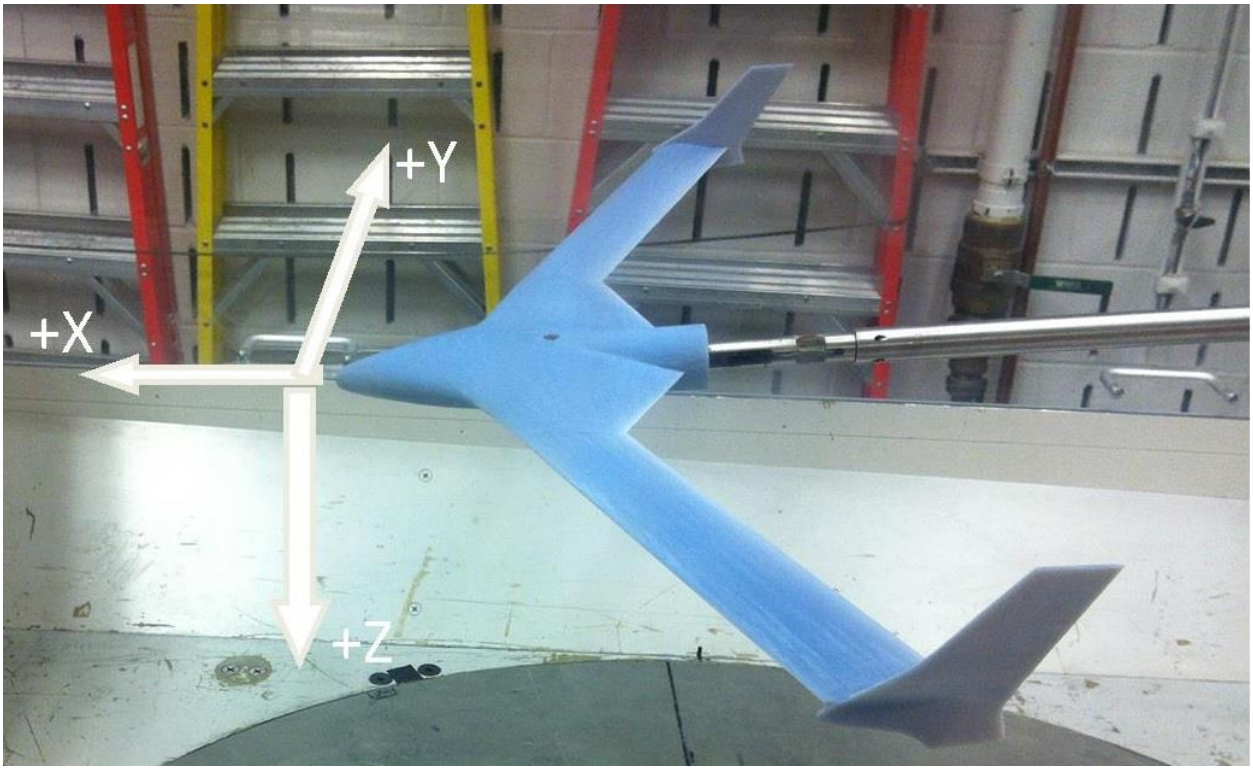

Figure 60. Body axis reference frame.

+X is the direction pointing toward the wind tunnel opening through the centerline of the balance. +Y is the direction out the right side of the balance, and +Z points down through the tunnel floor. The forces and moments measured about the balance center use the following sign convention: +N measured upwards along the –Z axis, +A measured along the –X axis towards the rear of the tunnel, +S measured along the –Y axis. Each moment follows the right hand rule through each of the positive X, Y, and Z axes.

3.7.1 Wind Tunnel Test Procedure

The AFIT-3 balance was calibrated using a calibration jig supplied by the manufacturer. The calibration block was fitted to the balance and leveled with a digital inclinometer. Calibrated weights ranging from 10grams to 1000grams were used to test linearity and accuracy of the

balance, and the lab view conversion factors output through the PC for the given loading configuration as seen in Figure 61 below.

Figure 61. Calibration block with weights, testing axial force component.

Figure 62 shows the calibration articles used for each of the six balance components.

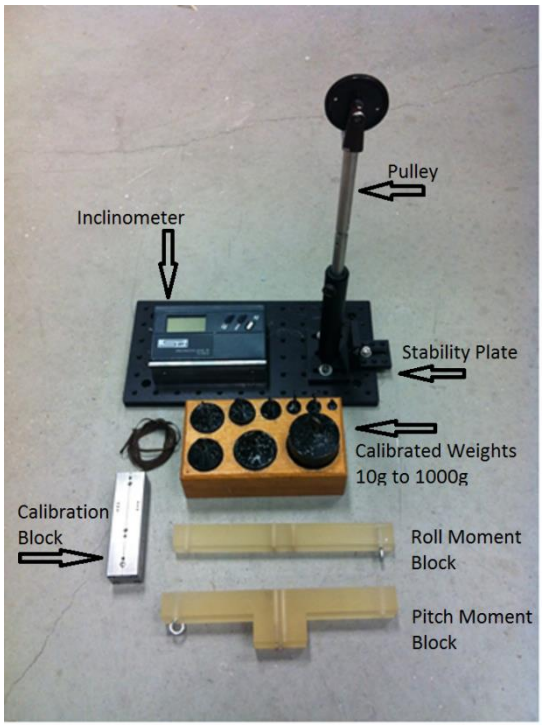

Figure 62. Calibration setup.

The X-56A models were mounted to the balance using a set screw and a mounting bulb designed into the aft section of the center fuselage. The screw mounting hole on the model was placed through the model's center of gravity, which was calculated by SolidWorks® to minimize center of gravity adjustments. Figure 63 shows an X-56A model mounted to the balance and sting inside the wind tunnel test section.

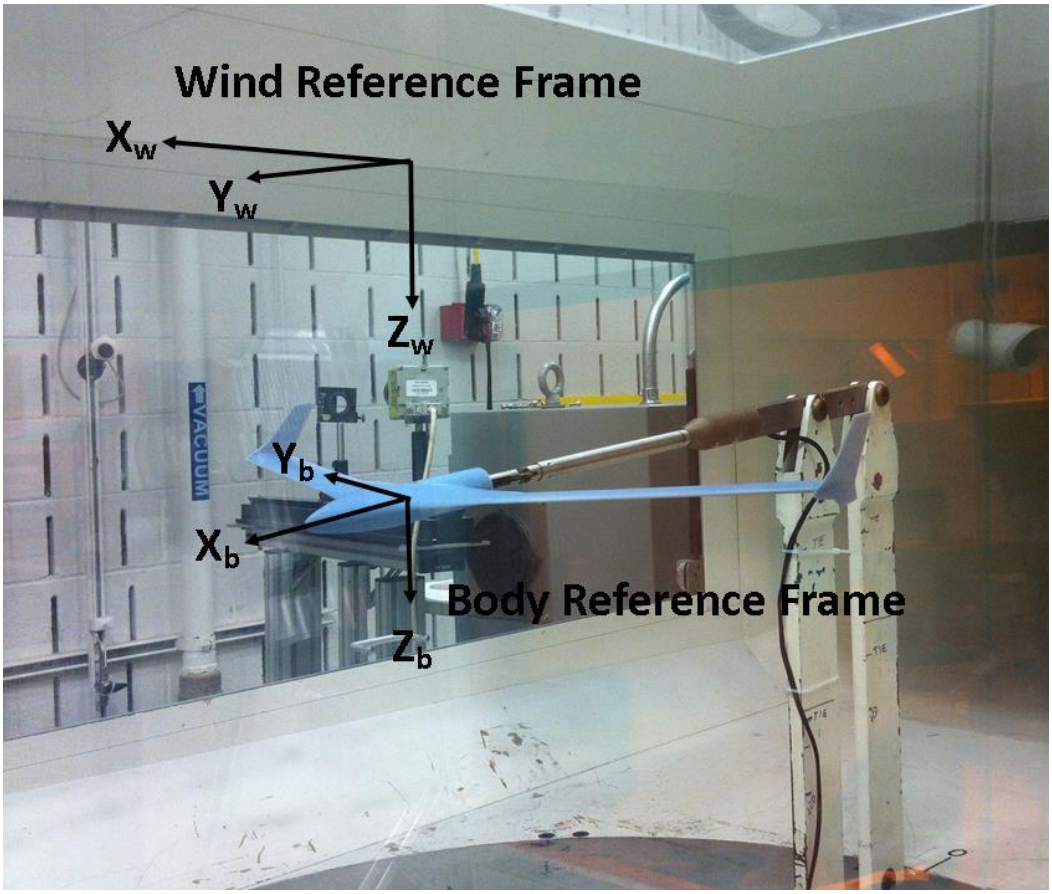

Figure 63. X-56A model mounted to AFIT-3 balance at -5° angle of attack.

Each model was tested across three parameters: sideslip angle (β), velocity (V), and angle of attack (α). Before each wind tunnel run, a tare file was created to capture the effect of the model's mass on the balance at every angle of attack and at each sideslip angle with the tunnel off. This data was used to remove the static weight change on the axial force sensor, which alters

the drag coefficient [37]. The model was placed on the sting, tared to remove the static weight at zero α, and the angle of attack was varied from -8° to +20° for sideslip angles of -6°, -3°, 0°, +3°, +6°. A positive angle of attack is indicated by a nose up attitude, and positive sideslip angle is indicated by a nose right attitude.

For each test run, the sideslip angle was set to one of the five previously stated angles. The wind tunnel velocity was set to an initial speed of 30mph, and the angle of attack was set to -5°. Working in 10mph increments, the wind tunnel velocity ranged from 30mph to 130mph and angle of attack was varied from -5° to +15° in one degree increments. Table 10 below details the test matrix for each model.

Table 10. Test matrix for each model.

		Velocity (mph)										
		30mph	**40mph**	**50mph**	**60mph**	**70mph**	**80mph**	**90mph**	**100mph**	**110mph**	**120mph**	**130mph**
Sideslip Angle (β)	**-6°**	α -5° to +15°	α -5° to +15°	α -5° to +15°	α -5° to +15°	α -5° to +15°	α -5° to +15°	α -5° to +15°	α -5° to +15°	α -5° to +15°	α -5° to +15°	α -5° to +15°
	-3°	α -5° to +15°	α -5° to +15°	α -5° to +15°	α -5° to +15°	α -5° to +15°	α -5° to +15°	α -5° to +15°	α -5° to +15°	α -5° to +15°	α -5° to +15°	α -5° to +15°
	0°	α -5° to +15°	α -5° to +15°	α -5° to +15°	α -5° to +15°	α -5° to +15°	α -5° to +15°	α -5° to +15°	α -5° to +15°	α -5° to +15°	α -5° to +15°	α -5° to +15°
	3°	α -5° to +15°	α -5° to +15°	α -5° to +15°	α -5° to +15°	α -5° to +15°	α -5° to +15°	α -5° to +15°	α -5° to +15°	α -5° to +15°	α -5° to +15°	α -5° to +15°
	6°	α -5° to +15°	α -5° to +15°	α -5° to +15°	α -5° to +15°	α -5° to +15°	α -5° to +15°	α -5° to +15°	α -5° to +15°	α -5° to +15°	α -5° to +15°	α -5° to +15°

3.7.2 Data Analysis

Each data point was held for approximately 20 seconds up to 80mph, while at 90mph and higher, each point was held for 10 seconds due to the increased loads placed on the wings. Data was read into the computer through LabView and output to Microsoft Excel. The data rate of 20

seconds and 10 seconds corresponded to approximately 36 rows and 18 rows respectively, yielding a collection rate of approximately 1.8Hz from Equation 34 below.

$$Data\ Rate(Hz) = \frac{\#\ of\ rows}{Collection\ Time} \tag{34}$$

During data collection of tare and test files, intermediate data points were collected as the model was traversed between angles of attack. These data points were removed by a separate MATLAB code. The final data output consisted of the following parameters: α, β, V_∞, N, P, A, S, Y, R, temperature, pressure, and time; where N, A, and S correspond to the normal, axial, and side force, respectively; and P, Y, and R correspond to the pitch, yaw, and roll moments, respectively. The force and moment data correlate to the output from the moment center, and was later transferred to the aircraft's center of gravity.

After all data was collected and extraneous data points were removed, the data and tare files were read into a separate MATLAB code, originally written by Capt. DeLuca, and later modified by Lt. Gebbie to use the AFIT-3 balance, the code was modified for the X-56A 3-D printed models. Modifications for use with the AFIT-3 balance included the matrix of sensitivities and interactions between the strain gauges provided by the manufacturer. The data reduction code followed the process outlined in the Master's Thesis by DeLuca (2004) [37]. The legacy code read in the vehicle mass, room temperature, barometric pressure, tare files, and data files. The code was then modified to remove any tail effects and pitching moment corrections. The original code was written for a single speed and sideslip angle, varying only angle of attack during a test run. Modifications were made to run the function for multiple speeds and sideslip angles. The code contains calculations and corrections for the model specifics and solid body blockages. The code also accounts for coordinate transformations from the wind reference frame

to the body reference frame, and then finally transfers the data from the balance moment center to the center of gravity of the model. Output data consisted of the following parameters: M, Re, q_∞, U_∞, α, β, C_L, C_D, C_l, C_m, C_n, and C_Y. Each of the previously listed non-dimensional parameters use Equations 35 to 42 below to non-dimensionalize each parameter from the collected dimensional value.

$$M = \frac{U_\infty}{a} \tag{35}$$

$$Re = \frac{\rho U_\infty c}{\mu} \tag{36}$$

$$C_L = \frac{L}{q_\infty S} \tag{37}$$

$$C_D = \frac{D}{q_\infty S} \tag{38}$$

$$C_Y = \frac{Y}{q_\infty S} \tag{39}$$

$$C_l = \frac{l}{q_\infty Sc} \tag{40}$$

$$C_m = \frac{m}{q_\infty Sc} \tag{41}$$

$$C_n = \frac{n}{q_\infty Sc} \tag{42}$$

The roll rate was approximated from the wind tunnel data described above. The equation for roll rate was derived from the equation of motion about the roll axis, due to the lack of ailerons, Barlow (2010) approximates the roll rate given by Equations 43 to 46.

$$P = \frac{2V}{b}\frac{C_l}{C_{l_p}} \tag{43}$$

Nelson (1998) solves C_{l_p} with the following equation,

$$C_{l_p} = -\frac{4C_{L_{\alpha_w}}}{Sb^2}\int_0^{b/2} cy^2\, dy \tag{44}$$

Due to the sweep angle of the wings, *y* transforms to the sweep coordinate system by the following equation:

$$y = \bar{y}\cos(\Lambda_n) \tag{45}$$

Where $\bar{y}$ is the spanwise location along the sweep line, and Λ_n is the sweep angle of the outer wing. Therefore, the roll moment coefficient due to roll rate becomes:

$$C_{l_p} = -\frac{4C_{L_{\alpha_w}}}{Sb^2}\int_0^{b/2} c(\bar{y}\cos(\Lambda_n))^2\, d\bar{y} \tag{46}$$

$C_{L_{\alpha_w}}$ was approximated from the linear region of the CL vs α lift curve slope. The roll rate was calculated for each speed and angle of attack. C_{l_p} is constant for each aircraft, and the roll rate varies with C_l. Plots of the above parameters are presented in the next chapter outlining the stability and roll control of the X-56A models.

4. Results

This chapter details the results of the experiments outlined in Chapter 3. The goal of this study is to provide an analysis of the capability of camber deforming wings to generate a rolling moment equivalent to, or larger than conventional ailerons. The secondary goals are to ensure that the X-56A while statically camber deformed, does not cause instabilities in pitch, roll, or yaw, as well as analyze the overall aerodynamic benefits due to camber deformation. Testing consisted of a two dimensional (2-D) feasibility study using Xfoil, scaled, static wind tunnel testing, and simulation in Tornado in low Reynolds number flows for small scale testing.

4.1 2-D Strip Theory Results

The 2-D roll analysis was performed as an initial feasibility study on the X-56A for both aileron deflections and axisymmetric camber deformed wings. The Strip Theory results analyzed the rolling moment of each model, and using a maximum aileron deflection angle of $\pm 15^{o}$. For this analysis, the aileron models tested used axisymmetric deflection angles to generate a left hand rolling moment. Table 11 below presents the feasibility study findings for the full scale X-56A with its 28ft wing span. It shows the 1% camber deformation per foot model, similar to the VCCW, and the quick camber change model, which changes camber over a 2ft span from the root, can produce a rolling moment 24% and 30% greater than a 10^{o} aileron deflection, respectively. Each camber deformed model produces a greater rolling moment at 0^{o} angle of attack than each of the aileron deflected models.

Table 11. Full Scale X-56A strip theory results

Full Scale X-56A		
Re = 1,657,800 Alt = 10,000 ft Mach = 0.156 V = 168.78 ft/s		
Models	**Angle of Attack**	**Roll Moment**
5^o Aileron Deflection	0^o	865.2 lb-ft
10^o Aileron Deflection	0^o	1646.6 lb-ft
15^o Aileron Deflection	0^o	2211.9 lb-ft
Full Span Camber Deformation	0^o	1299.7 lb-ft
1% Camber Deformation	0^o	2034.9 lb-ft
Quick Camber Deformation	0^o	2134.1 lb-ft

Xfoil's viscous solver shows the local coefficient of lift generated by the camber deformed models has a lower magnitude than either the 5^o or 10^o aileron deflected models, as seen in Table 12 below. It also shows that camber deformation can produce a larger rolling moment because the change in lift occurred over a larger span of the wing compared to the localized ailerons.

Table 12. Xfoil Coefficient of lift at Re = 1,657,800 for the full scale X-56A.

Coefficient of Lift (C_l)		Coefficient of Lift (C_l)	
X-56A Airfoil	0.048	X-56A Airfoil	0.048
-5^o Aileron	-0.2346	$+5^o$ Aileron	0.3958
-10^o Aileron	-0.4884	$+10^o$ Aileron	0.7114
-15^o Aileron	-0.7126	$+15^o$ Aileron	0.8991
-5% Camber Def.	-0.1627	+5% Camber Def.	0.3206

The camber deformation increases the coefficient of lift from the original airfoil along the entire span of the right wing, and decreases the coefficient of lift on the left wing. Unlike aileron deflection, the inboard section of each wing from the root to the aileron, remains constant and generates equivalent lift, which cancels the roll moment generation, allowing the rolling moment to be produced purely by the ailerons.

Due to the small chord length of the scaled wind tunnel models, the low Reynolds number flow behaved differently on the small scale models than the full scale aircraft. Table 13 and Table 14 show at 0^o angle of attack and varying speeds, the camber deformed models produce a rolling moment larger than the 10^o aileron deflection. The 15^o aileron deflection was not analyzed at either low Reynolds number speed due to Xfoil's inability to converge because the wind speed was too low to maintain attached flow.

Table 13. Strip theory calculation of wind tunnel model at Re= 87,105 (80mph).

1/17.68th Scale Wind Tunnel Model		
Re = 87,105 Alt = 0 ft Mach = 0 V = 117.33 ft/s		
Models	**Angle of Attack**	**Roll Moment**
5^o Aileron Deflection	0^o	0.05 lb-ft
10^o Aileron Deflection	0^o	0.10 lb-ft
Full Span Camber Deformation	0^o	0.11 lb-ft
1% Camber Deformation	0^o	0.15 lb-ft
Quick Camber Deformation	0^o	0.16 lb-ft

Table 14. Strip theory calculation of wind tunnel model at Re= 119,770 (110mph).

1/17.68th Scale Wind Tunnel Model		
Re = 119,770 Alt = 0 ft Mach = 0 V = 161.33 ft/s		
Models	**Angle of Attack**	**Roll Moment**
5^o Aileron Deflection	0^o	0.09 lb-ft
10^o Aileron Deflection	0^o	0.21 lb-ft
Full Span Camber Deformation	0^o	0.25 lb-ft
1% Camber Deformation	0^o	0.32 lb-ft
Quick Camber Deformation	0^o	0.34 lb-ft

For both speeds, the +5% camber deformed airfoils produces a lower local coefficient of lift than the original airfoil as shown in Table 15 below.

Table 15. Scale model coefficient of lift at Re = 87,105 and Re = 119,770

Airfoil	**C_L Re = 87,105**	**C_L Re = 119,770**
X-56A Airfoil	0.311	0.302
$+5^o$ Aileron Deflection	0.4191	0.414
-5^o Aileron Deflection	0.0973	0.09
$+10^o$ Aileron Deflection	0.5413	0.6282
-10^o Aileron Deflection	-0.0846	-0.0937
+5% Camber Deformed	0.2013	0.2768
-5% Camber Deformed	-0.3578	-0.3484

The Xfoil analysis shows the increase in camber causes an increase in the laminar flow region from approximately 15% chord on the original airfoil to 20% chord on the camber deformed airfoil. The laminar separation bubble forms in the reflexed section of the airfoil, and moves toward the leading edge from approximately 60% chord to 35% chord with separation at approximately 57% chord. The movement of the laminar separation bubble toward the maximum camber location increases the overall size of the laminar separation bubble with turbulent flow reattachment at approximately the 70% chord location. The separation bubble on the lower surface decreases the pressure due to flow separation with reattachment on the aft section of the airfoil. The separation bubble on the upper surface occurs at the time the lower surface is reattached eliminating the lift where the separation bubble occurs. The decreased pressure difference and laminar separation bubbles cause a loss in lift on the high camber airfoil. Figure 64 shows the difference in Pressure Coefficient *(Cp)* distribution between the original airfoil and the +5% camber deformed airfoil.

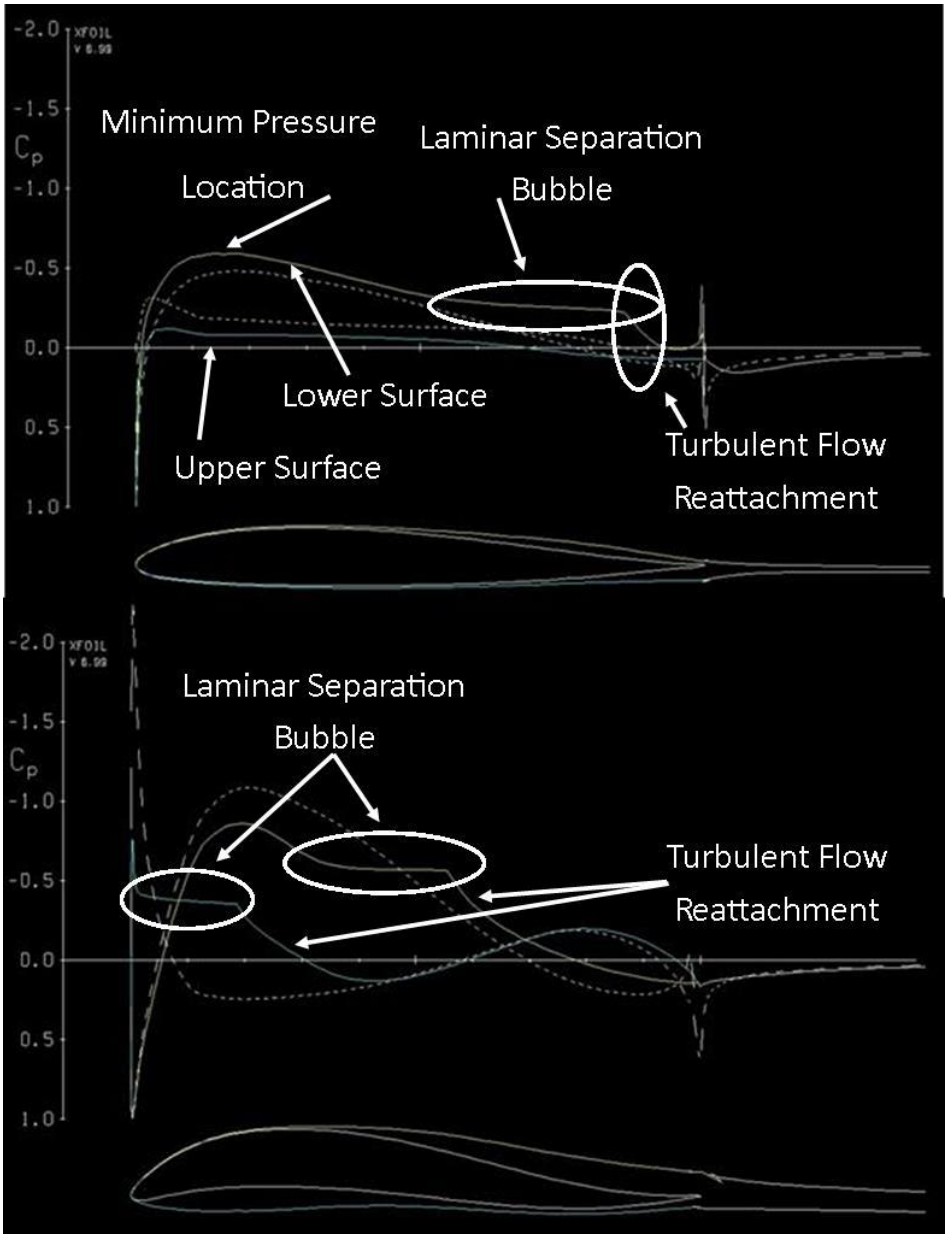

Figure 64. X-56A airfoil *Cp* distribution at Re = 87,105 0^{o} AoA. X-56A airfoil top, +5% camber deformation bottom.

As the Reynolds number increases from 87,105 to 119,770 (80mph to 110mph), the lift increases approximately 38% from 0.2013 to 0.2768. This increase was due to the minimum pressure rise which occurs with the increasing Reynolds number causing a steep pressure rise after flow separation resulting in the flow follow the wings contour more closely. Each Strip Theory

solution described above shows camber deformation alone can produce a rolling moment equivalent to, or greater than, conventional ailerons at all scales in level flight.

4.2 Wind Tunnel Findings

4.2.1 Aerodynamic Results

The following subsections will show each camber deformed model to have early stall of the left wing due to decreased camber, which reduces the stall angle of attack of that wing. Each camber deformed model also had less overall lift and larger drag due to the early wing stall. Due to these models no longer generating lift over the majority of the wing, this shows that camber deformation is not as efficient as the aileron models at generating lift at higher angles of attack, $\alpha > +5^{o}$. These subsections will also show a consistent trend of both wings on the camber deformed models stalling before one wing stalled on the aileron models.

4.2.1.1 Speed and Angle of Attack Sweeps

This section describes the results of the lift and drag changes due to aileron deflection and spanwise camber deformation. Each aileron model, as well as the baseline model, are shown by dashed lines and a character designator and camber deformed models are shown with the symbol designator shown in Table 16 below, unless plotted alone.

Table 16. Plot designator for wind tunnel models.

Wind Tunnel Model	Plot Designator
0^o Aileron	- - +
5^o Aileron	- - o
10^o Aileron	- - ◊
15^o Aileron	- - *
Full Span	◊
1%	o
Quick Camber Change	□

The full span, 1% camber change, and quick camber change wind tunnel models correspond to the models in Figure 40, Figure 41, and Figure 42, respectively, in Chapter 3. The maximum angle of attack was limited to $+15^o$ due to wing stall of the left wing. As speeds increase, the results show the linear region of C_L vs α, $-5^o < \alpha < 5^o$, remains relatively constant and unaffected by Reynolds number changes. Figure 65 below show the aircraft coefficient of lift plotted against angle of attack at varying speeds. In these two plots, the left plot shows the 15^o aileron deflected model, and the right plot shows the full span model, demonstrating similar trends in the linear lift curve slope ($C_{L\alpha}$) and maximum coefficient of lift (C_{Lmax}) that testing revealed for all wind tunnel models. Additional plots can be found in Appendix A.

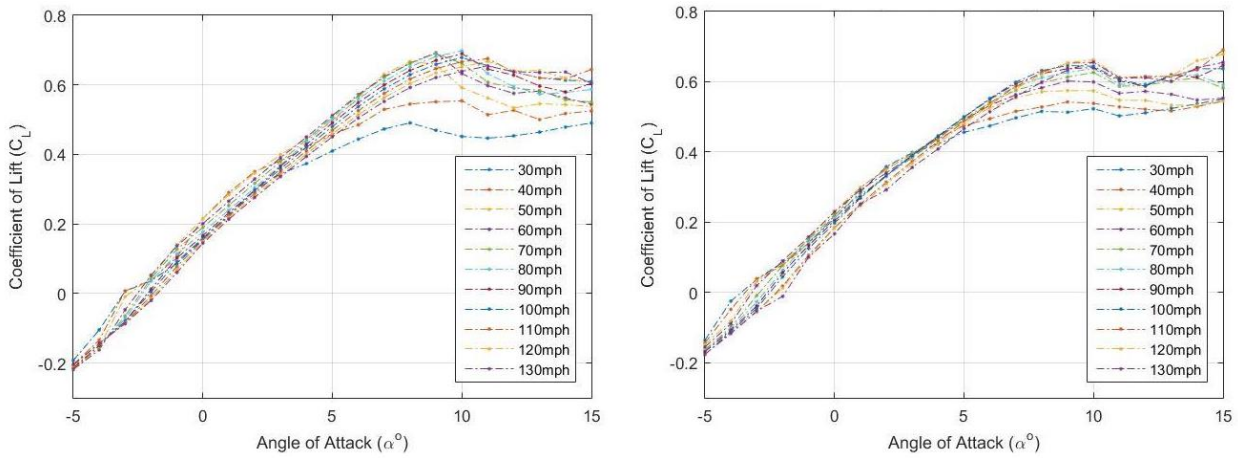

Figure 65. C_L vs α β = 0° 15° Aileron model (left) and Full Span camber change model (right) varying speed.

Testing shows a correlation between increased speed and an increased Reynolds number. This causes the maximum coefficient of lift and stall angle to increase. Due to Bernoulli's Principle, this correlation was expected since the increase in speed caused the pressure on the upper surface to decrease, which increases the pressure differential between the upper and lower surfaces, increasing the total lift on the wing. Notably, as the speed increases, the Reynolds number increases, which caused the laminar separation bubble to decrease, increasing the lift produced on the local airfoil along the span, resulting in turbulent flow reattachment along a larger length of the chord. The 30mph and 40mph speeds produced the lowest maximum coefficient of lift, and stalls approximately two degrees earlier due to lower pressure differential and early flow separation. This causes the turbulent flow to not reattach on the trailing edge which decreases the overall lift generated by the airfoil and was not due to error in the balance data which can be seen in Appendix D. Table 17 and Table 18 below show the changes in $C_{L\alpha}$ and C_{Lmax} for each model at three different mid-range speeds.

Table 17. Lift curve slope CLα at 60mph, 90mph, and 120mph for all scale wind tunnel models.

	$\Psi = 0$	$C_{L\alpha}$ (1/deg)	$C_{L\alpha}$ (1/deg)	$C_{L\alpha}$ (1/deg)	$C_{L\alpha}$ (1/deg)
	Speed	**60mph**	**90mph**	**120mph**	**Average**
Wind Tunnel Model	0^o Aileron	0.056	0.058	0.056	0.057
	5^o Aileron	0.057	0.062	0.058	0.059
	10^o Aileron	0.060	0.063	0.061	0.061
	15^o Aileron	0.062	0.065	0.062	0.063
	Full Span Camber Deformation	0.052	0.059	0.056	0.056
	1% Camber Deformation	0.057	0.060	0.061	0.059
	Quick Camber Change	0.057	0.060	0.062	0.060

Table 18. Maximum coefficient of lift at 60mph, 90mph, and 120mph for all scale wind tunnel models.

	$\Psi = 0$	C_{Lmax}	C_{Lmax}	C_{Lmax}	C_{Lmax}
	Speed	**60mph**	**90mph**	**120mph**	**Average**
Wind Tunnel Model	0^o Aileron	0.652	0.692	0.639	0.661
	5^o Aileron	0.677	0.710	0.655	0.681
	10^o Aileron	0.672	0.693	0.650	0.672
	15^o Aileron	0.692	0.689	0.652	0.678
	Full Span Camber Deformation	0.602	0.640	0.663	0.625
	1% Camber Deformation	0.565	0.602	0.626	0.598
	Quick Camber Change	0.583	0.587	0.587	0.586

Table 18 above shows the maximum coefficient of lift for the 5^o aileron deflected model is greater than the 10^o and 15^o deflected models. This is most likely due to the failure and separation of the right wing with the ailerons deflected to 10^o while testing at 120mph. The right image in Figure 66 below shows this failure; the left image shows the reprinted model which was retested at the 10^o aileron deflection. Differences in the data could be attributed to retesting the data points, differences in testing conditions such as air temperature and pressure, differences in the model surface, and minute aileron deflection differences, etc.

Figure 66. Wind tunnel aileron model before and after wing separation.

Table 18 shows a decrease in the maximum coefficient of lift between 90mph and 120mph for each aileron model. As each model underwent testing at high speeds, the high loads experienced at the tips due to the ailerons caused the wings to flex excessively as seen in Figure 67 below. This flexing increased as testing continued, and the amount of bend increased with increased aileron deflection due to the higher lift experienced by the aileron deflection.

Figure 67. Wind tunnel aileron model on AFIT-3 balance displaying wing flex above 90mph.

While testing at speeds above 80mph, this flexure caused a decrease in the projected planform area, *S*, decreasing the lift generated by the aircraft as seen in Equation 47 below.

$$L = C_l q_\infty S \quad \textbf{(47)}$$

Each camber deformed models produced overall lower maximum coefficients of lift than the aileron deflection models. This can be attributed to the decreased maximum local coefficient of lift generated by the camber change compared to the aileron deflection. Figure 68, Figure 69, and Figure 70 show the coefficient of lift versus angle of attack compared to each of the aileron deflected models at 90mph and 120mph. Two representative speeds were used to demonstrate the model behavior at the middle speed range and upper speed range. The 90mph speed represents the relative behavior of the model between 50mph and 100mph and the 120mph speed represents the relative behavior of the model between 110mph and 130mph. The 30mph and 40mph speeds were not analyzed due to the Reynolds number being below the critical Reynolds number and complete flow separation occurring on the camber deformed models at a 0^o angle of attack.

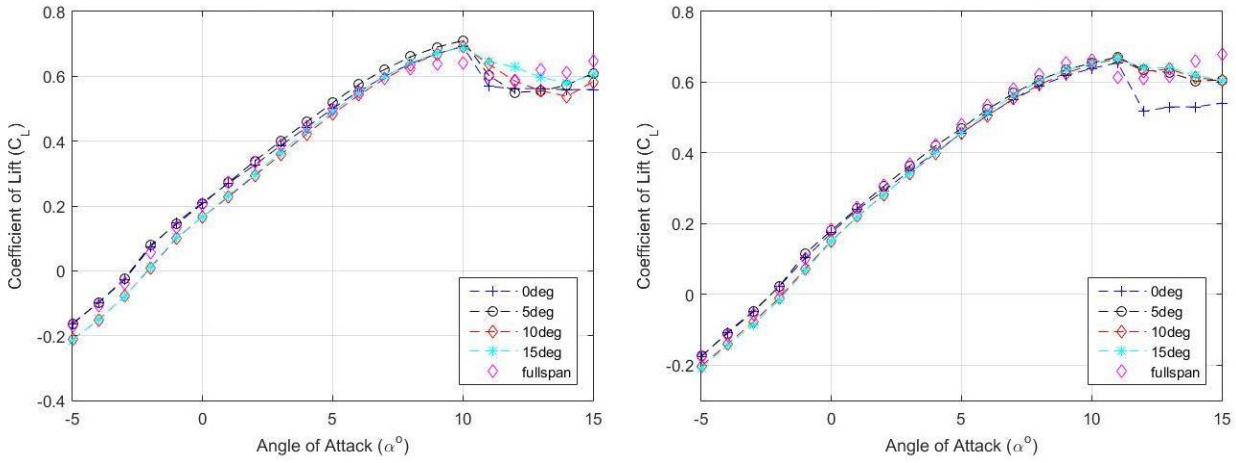

Figure 68. Full span model CL vs α β = 0^o at 90mph 9(left) and 120mph (right) compared to aileron deflected models.

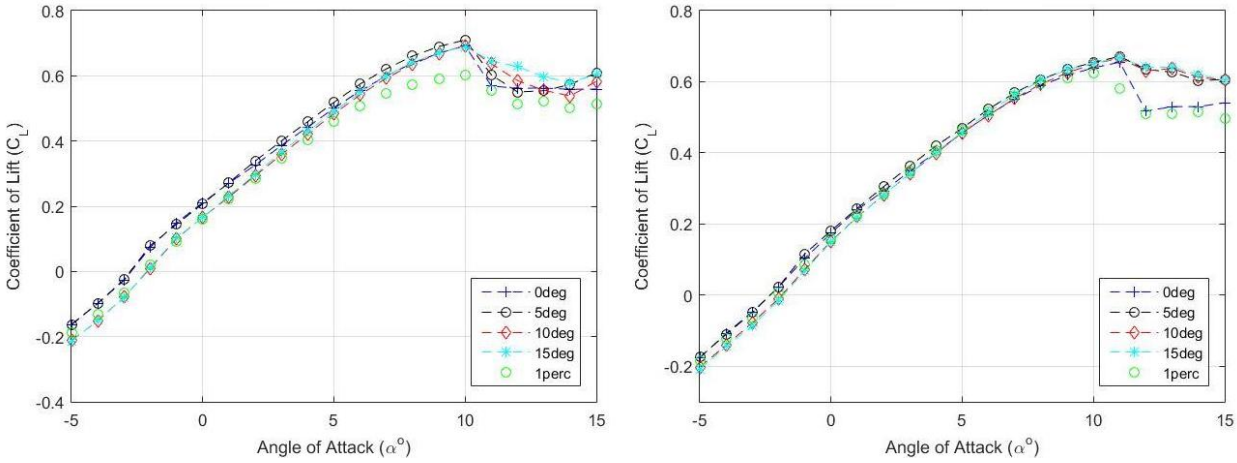

Figure 69. 1 Percent model CL vs α β = 0^o at 90mph (left) and 120mph (right) compared to aileron deflected models.

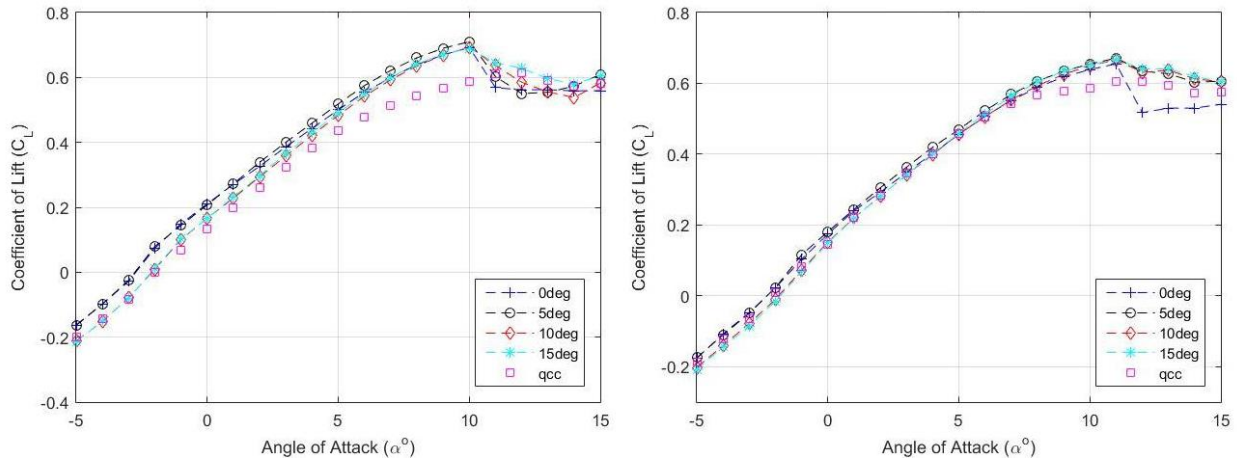

Figure 70. Quick camber change model CL vs α β = 0^o at 90mph (left) and 120mph (right) compared to aileron deflected models.

The figures above show at both speeds, the full span model produces the highest maximum coefficient of lift between the three camber deformed models. This is due to the left wing stall at approximately 6^o angle of attack reducing the total lift approaching C_{Lmax}, until the right wing stall at approximately 10^o angle of attack. The 1% and quick camber change models have a larger negative camber spanwise, causing the increased spanwise section of the wing to stall, reducing the overall lift compared to the full span model. At 120mph, the linear correlation between the camber deformed models and aileron models matches more closely and the

maximum coefficient of lift increased. The stall behavior of each of the camber deformed models also improves as seen by the decreased slope after C_{Lmax} compared to the aileron models.

Figure 71 below shows drag coefficient versus angle of attack at varying speeds.

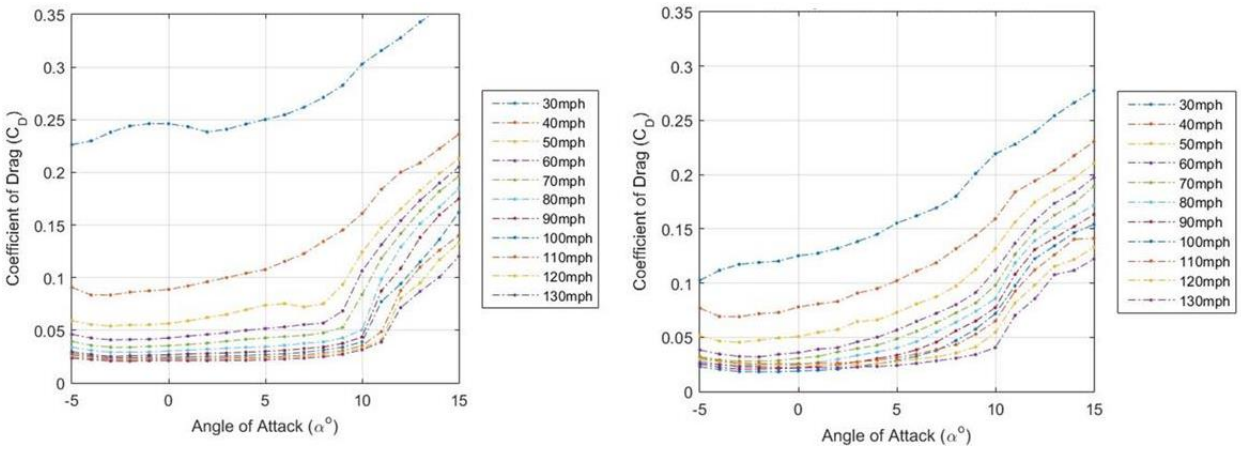

Figure 71. Coefficient of Drag (C_D) versus α varying with speed β = 0° for 15° (left) and Full Span camber change model (right).

It is evident from these two plots as speed increases, the drag coefficient decreases. At 30mph and 40mph, the drag was higher than the upper speed range due to the formation of the laminar separation bubble without reattachment. This resulted in higher drag, and is outside the range of the balance error in the axial direction. Error analysis can be found in Appendix D. The greater amount of drag on the 15° aileron deflected model at 30mph may be a combination of the separation of flow on the upper surface and the aileron deflection into the freestream acting similar to a speed break. This deflection into the freestream generates a large increase in drag and is outside the error produced in the axial direction by the balance.

Figures 72-74 show the drag plotted against the angle of attack for each camber deformed model compared to the aileron deflected models at 90mph and 120mph. Due to the gradual camber change along the wing span, the full span model produces a drag equivalent to

the aileron deflected models. The initial drag rise at approximately 6^o angle of attack is due to the negative camber wing stalling from upper wing flow separation, and the drag rise seen near 10^o angle of attack is due to flow separation and wing stall of the right wing. As speed increases, drag rise is delayed due to a slight delay in stall and flow separation. Both the 1% camber change model, and the quick camber change model produce a larger overall drag due to the increase in camber, which was expected, and is within the drag error, which can be seen in Appendix D. Since both models increase camber over a longer span of the wing, the overall drag rise was more pronounced as seen in Figure 73 Figure 74.

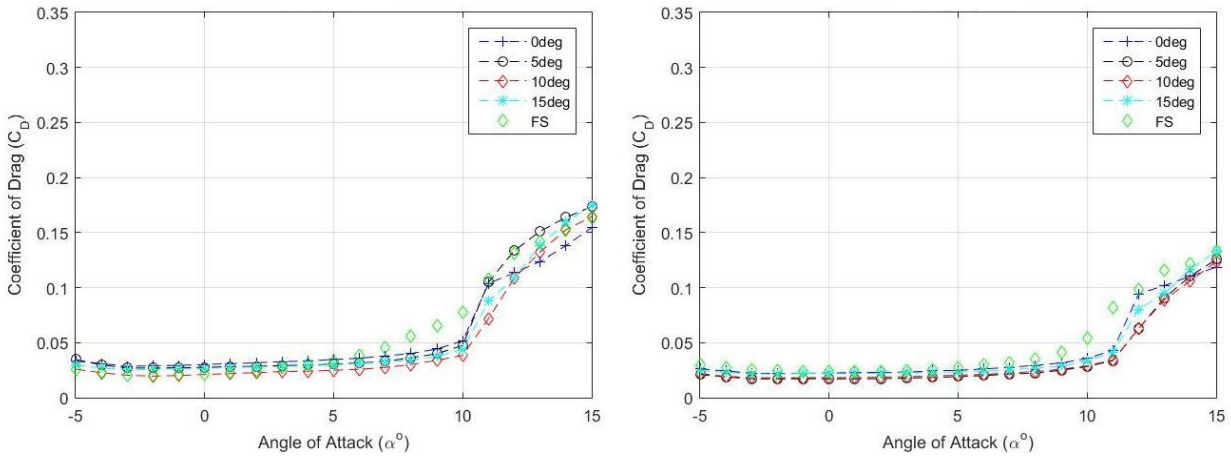

Figure 72. CD vs α β = 0^o Full Span model at 90mph (left) and 120mph (right) compared to aileron models.

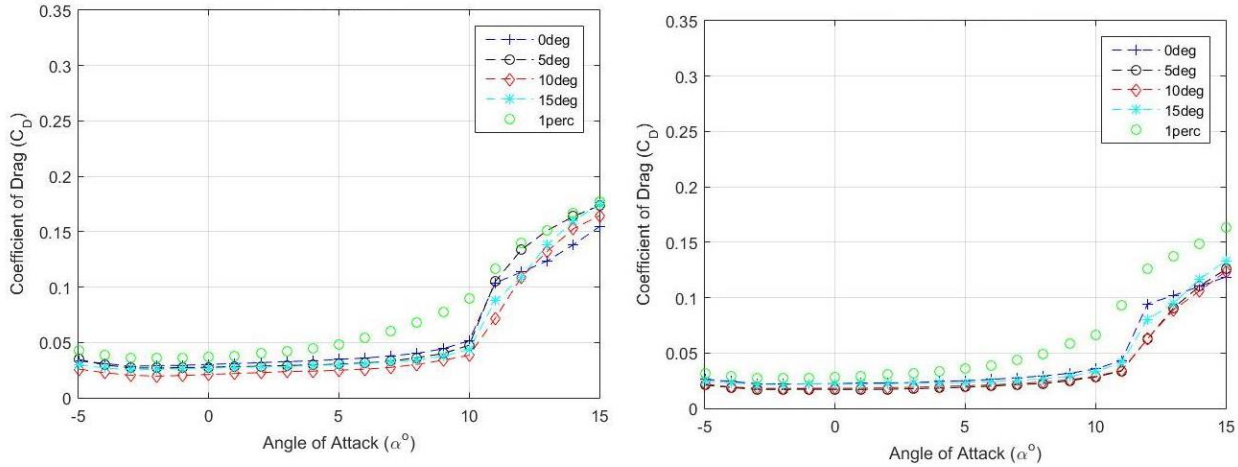

Figure 73. CD vs α β = 0° 1% camber change model at 90mph (left) and 120mph (right) compared to aileron models.

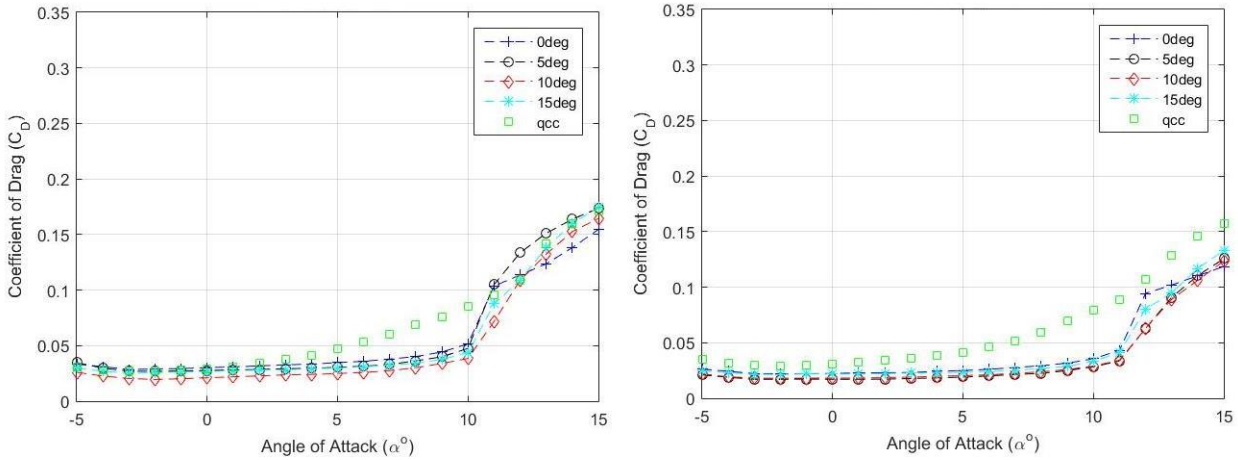

Figure 74. CD vs α β = 0° Quick camber change model at 90mph (left) and 120mph (right) compared to aileron models.

Figure 75 below shows the lift to drag ratio (C_L/C_D) compared to angle of attack at varying speeds for the 15° aileron deflection and full span models. The maximum C_L/C_D compared to angle of attack shows the most efficient angle to operate for a given flight condition. Since all models produced similar results with increases in speed, two representative examples are shown below. As speed increases, the lift to drag ratio increases, and the most efficient angle of attack increases. This increase in angle of attack occurs due to an increase in

stall speed as both speed and Reynolds number increase. Figures 76-78 below display the lift to drag ratio, and compares each camber deformed model to the aileron deflection models. Of the camber deformed models, the full span model operates at the highest efficiency with a C_L/C_D of 15 at 90mph, and nearly 20 at 120mph. The 1% camber change and quick camber change models produce nearly an equivalent efficiency of approximately 10 at 90mph. With an increase in speed, the 1% camber change model is more efficient with a C_L/C_D of approximately 14, whereas the quick camber change model has a C_L/C_D of approximately 11. These results show at small scale, none of the camber change models are as efficient as the aileron models due to the increase in drag and lower maximum lift coefficient. Although the max C_L/C_D location may be the most efficient angle at which to operate each model, other factors may be hindered while operating at these angles as seen in the following sections.

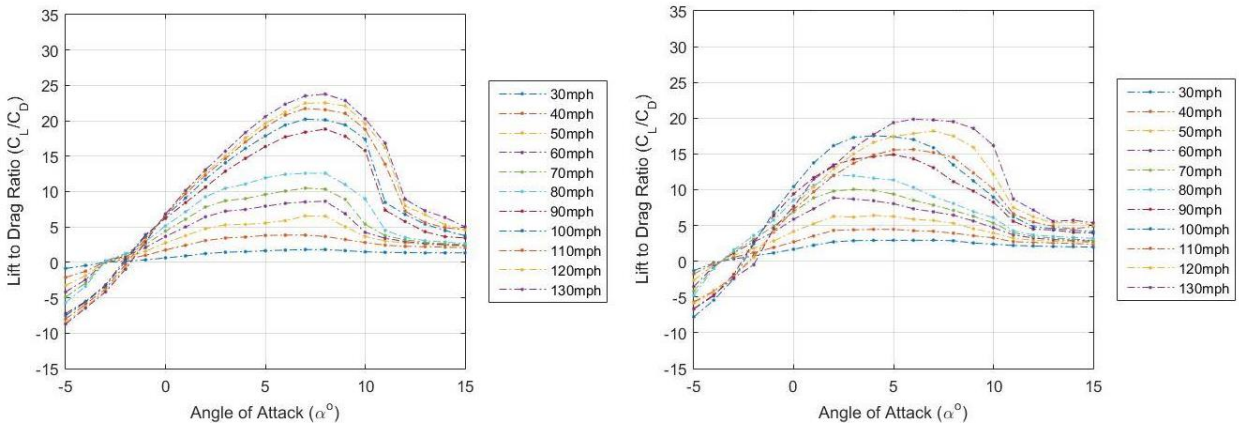

Figure 75. Lift to Drag ratio vs α β = 0° varying speed for 15° aileron model (left) and Full Span model (right).

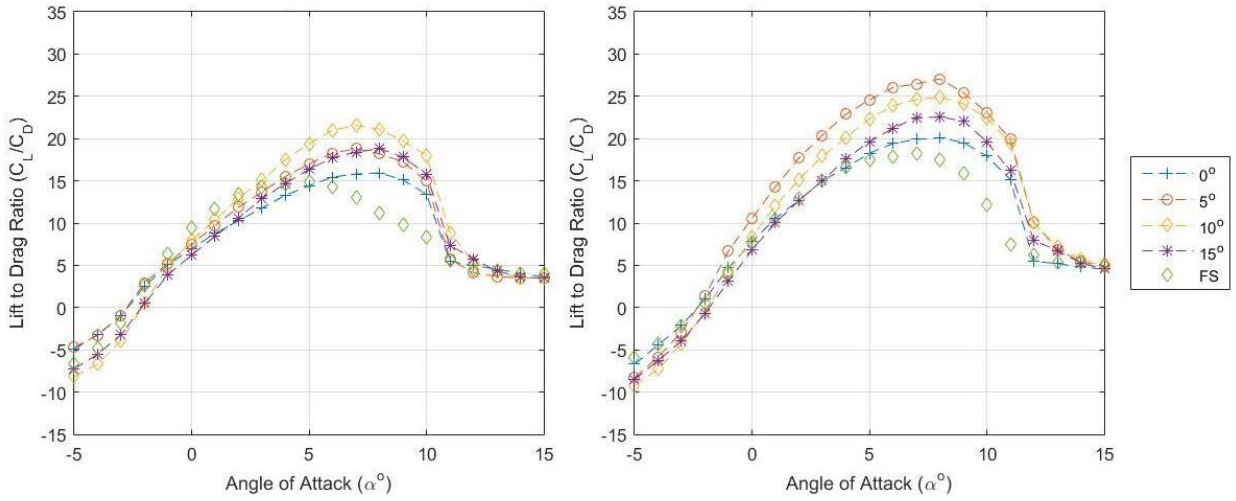

Figure 76. Lift to Drag ratio vs α β = 0° comparing Full Span model to aileron models at 90mph (left) and 120mph(right).

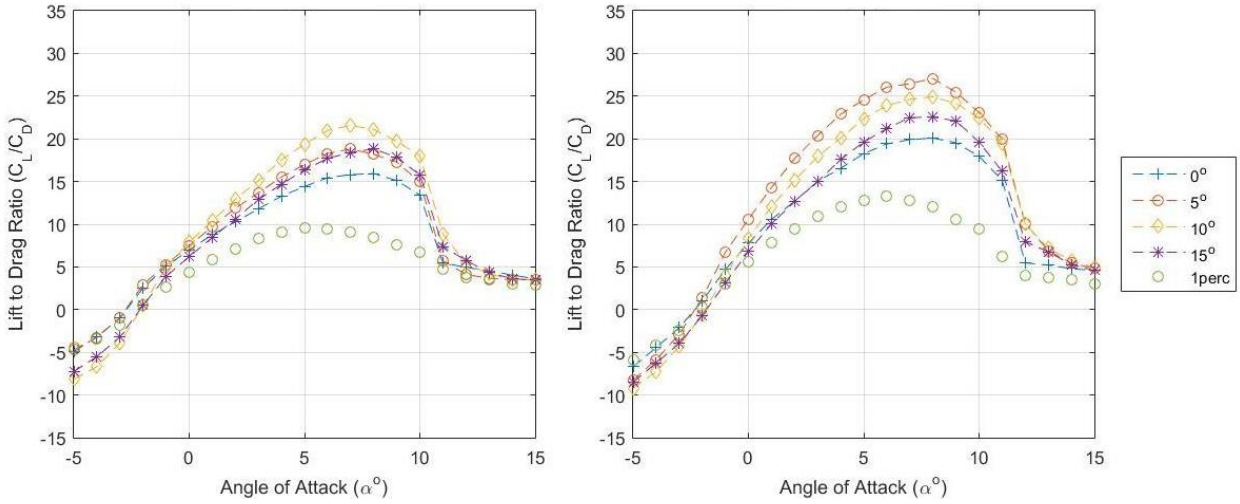

Figure 77. Lift to Drag ratio vs α β = 0° comparing 1 Percent model to aileron models at 90mph (left) and 120mph (right).

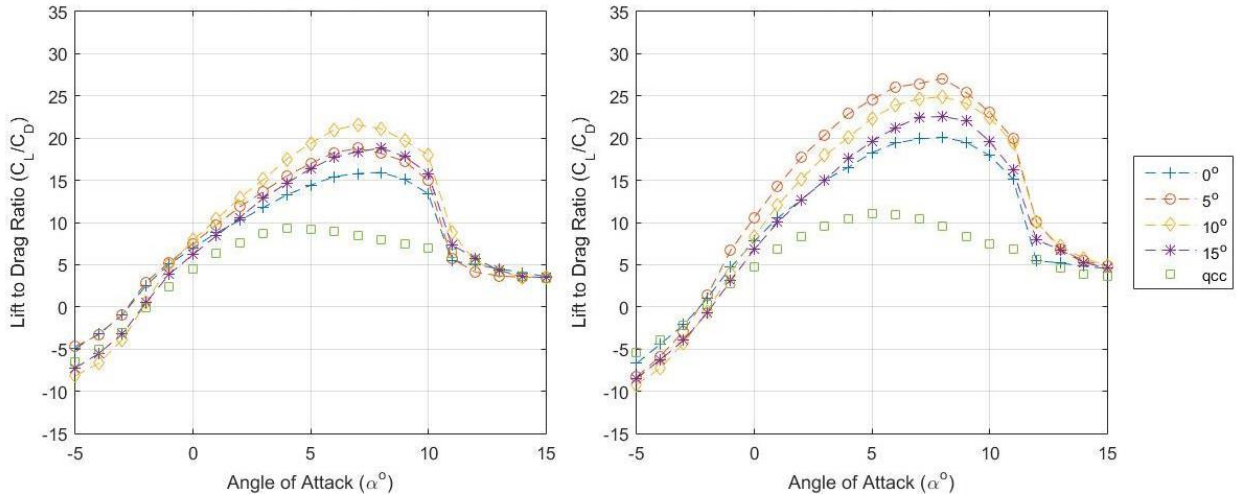

Figure 78. Lift to Drag ratio comparing Quick camber change model to aileron models at 90mph (left) and 120mph (right).

4.2.1.2 Yaw Sweeps

Unlike conventional yaw direction, due to AFIT's wind tunnel yaw orientation the yaw angle equals the opposite sign of the sideslip angle with an equivalent magnitude value of $\psi = -\beta$. Figure 79 and Figure 80 show the lift coefficient versus angle of attack, and drag coefficient versus angle of attack with varying sideslip angle at a constant speed. No appreciable change due to sideslip was noted as shown in Figure 79 and Figure 80. All plots in the following sections show the 0^o sideslip angle results unless noticeable effects were observed due to sideslip angle movement, outside of potential error.

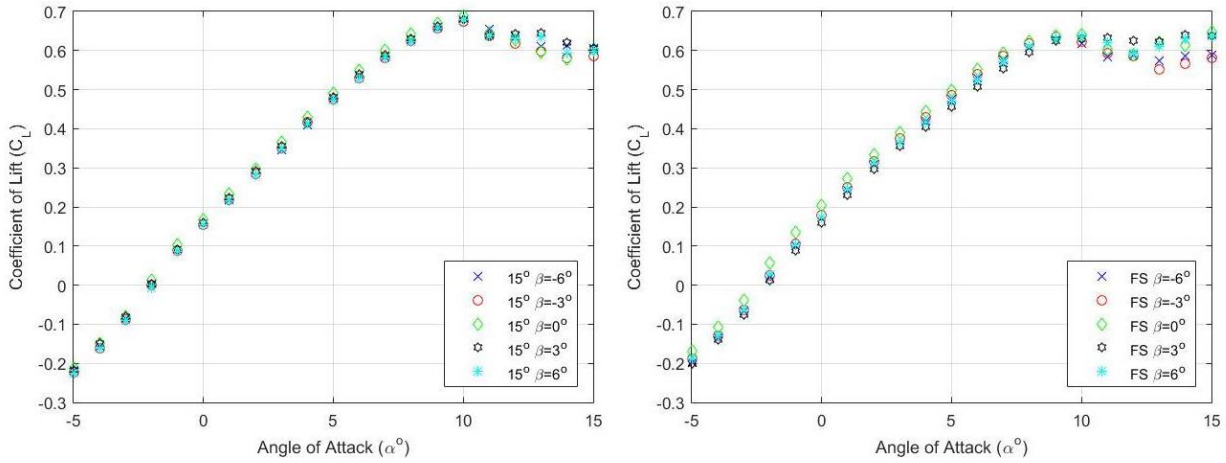

Figure 79. CL vs α 15° (left) and Full Span models (right) varying sideslip angle β at 90mph.

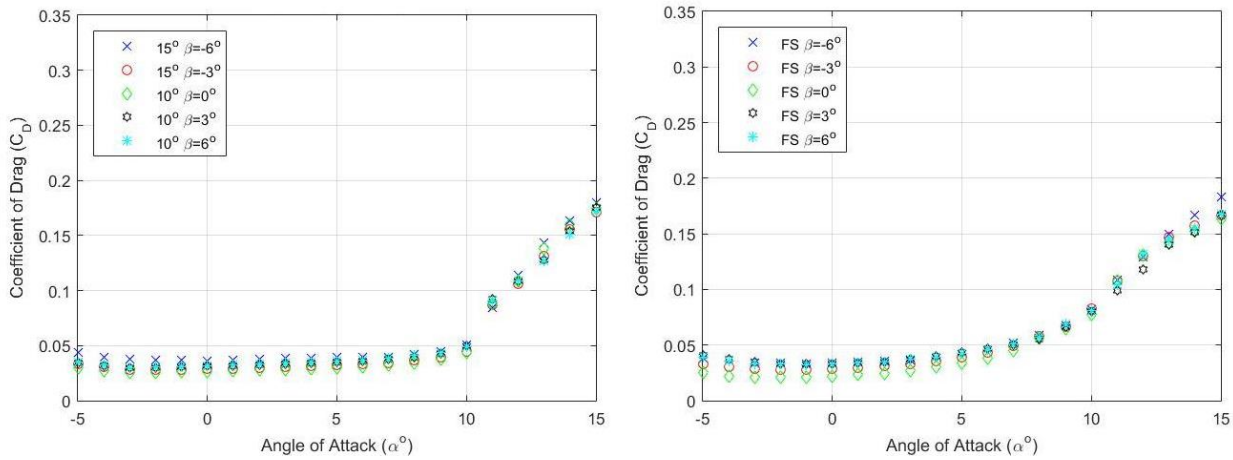

Figure 80. CD vs α 15° (left) and Full Span models (right) varying sideslip angle β at 90mph.

4.2.2 Roll Capability Results

This section discusses the roll capability of the X-56A with camber deformed wings compared to conventional ailerons deflected at three fixed angles. The comparisons between camber deformation models and conventional ailerons will analyze changes in velocity, sideslip angle, and angle of attack. To determine the effectiveness of the roll capability of each aircraft model, the roll moment coefficient and roll rate will be compared. A negative C_l in the wind tunnel reference frame is a left hand roll as indicated by the right hand rule.

Each aileron deflected model produces constant roll coefficients for all angles of attack. As discussed in Chapter 2, as speed increases, the aileron effectiveness decreases as seen in Figure 81 below. This could be attributed to one of two causes: 1) aeroelastic effects caused by aileron deflection or 2) the roll moment results were within the region of error produced by the balance.

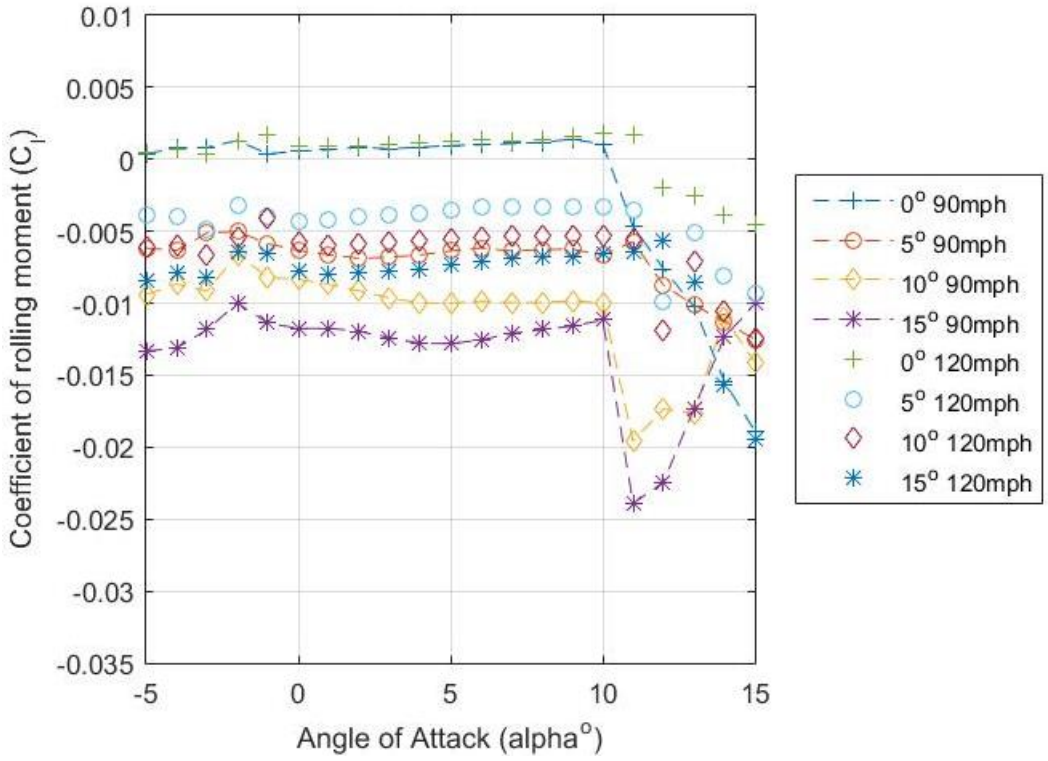

Figure 81. Roll moment coefficient (C_l) vs α $\beta = 0^o$ at 90mph and 120mph comparing aileron models.

After analysis of the data for the tested speed range from 30mph to 130mph, the roll moment coefficient varied between -0.01 and -0.006, which is within the bounds of error at all speeds. Potential aeroelastic effects could be prddominant on the wings as the torsional rigidity of the wing decreases with an increase in spanwise location. Analysis in Xfoil shows an increase in the local lift coefficient with an increase in Reynolds number. This may have lead to washout occurring if the 3-D printed material was not torsionally stiff enough to withstand the increased

pitching moment about the airfoil local aerodynamic center produced by the aileron deflection. The constant roll moment coefficient is due to the lift differential on each wing remaining constant as angle of attack increases. The constant differential comes from $C_{L\alpha}$ being equal for each wing.

Similar roll characteristics were noticed between each of the camber deformed wind tunnel models. At speeds below 110mph, the roll moment coefficient decreases with increasing angle of attack. This decrease is a result of low Reynolds number effects, the -5% camber deformation change wing changes lift at a larger rate than the +5% camber deformation change wing with increased angle of attack. Table 19 below shows $C_{l\alpha}$ produced by the +5% camber deformed airfoil and -5% camber deformed airfoil, which were determined from Xfoil predictions.

Table 19. Local airfoil lift curve slope comparing +5% camber deformation and -5% camber deformation at 80mph and 110mph.

Airfoil	$C_{l\alpha}$ 80mph	$C_{l\alpha}$ 110mph
+5%	0.0668	0.1151
-5%	0.1203	0.1073

The difference in the lift curve slope between the +5% and -5% camber airfoils causes a decrease in the rolling moment produced. The most desired effect to achieve a larger rolling moment is for the +5% camber deformation to produce a larger change in lift compared to the -5% camber deformation with increases in angle of attack. As speed increases, the change in lift on each wing with increasing angle of attack are nearly the same, which caused the roll moment to behave similar to the results seen by Privitali et. al results shown in Chapter 2. Each model shows a

decrease in roll moment coefficient with increasing angle of attack at increasing negative sideslip angles, which can be seen in Appendix B. This change was expected due to the increase in lift of the negatively deformed camber wing leading into the wind, which reduces the lift on the right wing generating a decrease in roll moment. Testing also revealed a negative yaw resulted in increased roll reversal values at mid-range speeds, and also at high speeds with sideslip angles larger than -6^{o}. Representative plots at 90mph and 120mph are in Appendix B. Roll reversal is a reversal of the expected input by the pilot, if a left roll is initiated, a right roll is experienced. At sideslip angles $\geq 0^{o}$, roll reversal does not occur.

These results align with expectation because the X-56A is not designed to operate in low Reynolds number flow or be exposed to large changes in camber, speed, or angle of attack. All of the aileron deflected models behaved in an expected manner at all speeds, while each camber deformed model behaved differently than if operating in a larger Reynolds number range.

4.2.2.1 Full Span Model

This section discusses the roll capability of the full span wind tunnel model compared to conventional aileron models. As stated above, as speed increases and the angle of attack changes, the roll moment coefficient becomes more constant. At angles of attack between -5^{o} and $+5^{o}$, the lower speeds produce a larger rolling moment, which decreases quickly with increase in angle of attack, and below 90mph, roll reversal was experienced. The roll moment coefficient versus angle of attack at varying speeds is shown in Figure 82 below. A delay in left wing stall can be seen as speed increases. The increase in left hand rolling moment indicates a stalled condition.

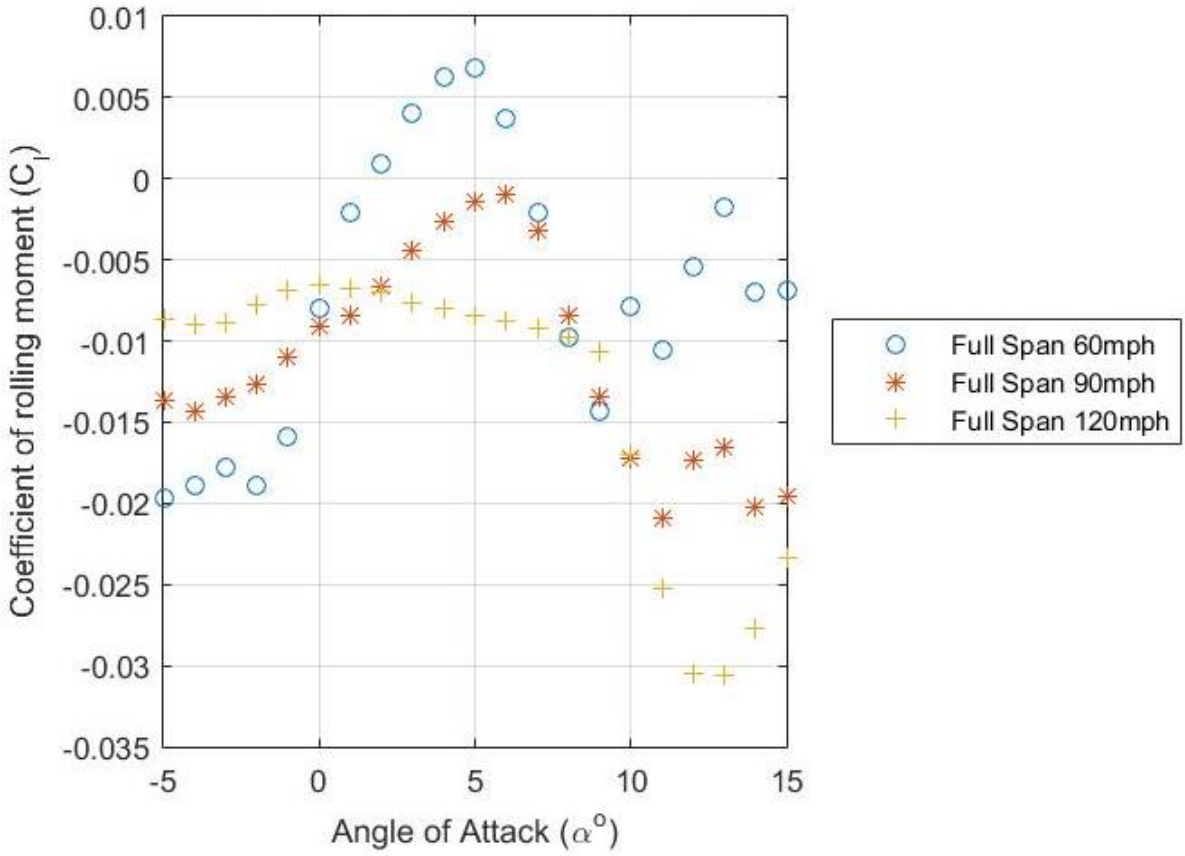

Figure 82. Full span camber model roll moment coefficient versus angle of attack β = 0° at 60mph, 90mph, and 120mph.

Figure 83 compares the conventional aileron deflected models to the full span model at 90mph and 120mph respectively. At 90mph and angles of attack below -1°, the full span model produces a rolling moment greater than the 15° aileron deflection model. Below 3° angle of attack, the rolling moment approaches zero, and produces a lower rolling moment than the 5° aileron deflected model. The increase in roll rate seen after 6° angle of attack is due to the loss of lift on the negative camber deformed wing. At speeds above 90mph in steady, level flight, at approximately 0° angle of attack, the rolling moment produced by the full span configuration is between the 10° and 15° aileron deflection. This result matches the 2-D Strip Theory discussed above.

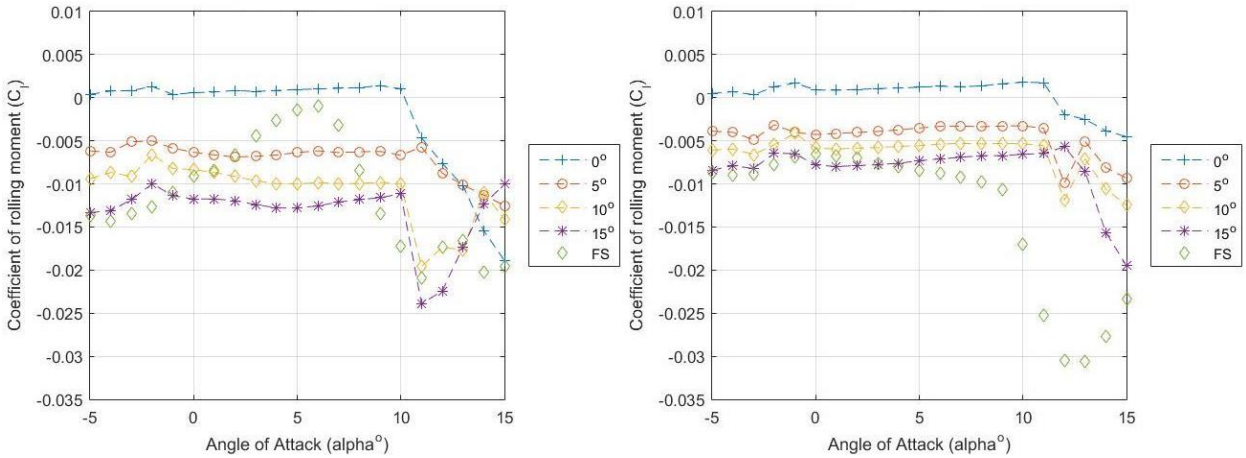

Figure 83. Roll moment coefficient versus angle of attack β = 0° for full span camber deformed model compared to conventional aileron deflection at 90mph 9 (left) and 120mph (right).

Figure 84 shows the roll rate of the full span wind tunnel model compared to each of the aileron models. Results show the roll rate of each model closely follows the roll moment coefficient seen in Figure 83 above. At 90mph, the roll rate decreases due to the decrease in roll moment coefficient. At 120mph, the roll rate decreases similar to the roll moment coefficient as expected, producing a roll rate greater than 10^o aileron deflection at all angles of attack. The increase in roll rate after 4^o and 6^o angle of attack respectively, is due to the left wing beginning to stall from flow separation. Results further indicate that in a landing, total aircraft configuration roll authority is greater than the 15^o aileron model, however, in straight and level flight, the roll rate of the camber deformed model is larger than the 10^o aileron model. While in a climbing turn, such as takeoff, the aircraft is limited to the a 5^o angle of attack with camber deformed wings prior to wing stall at speeds below 90mph. To avoid roll reversal of the camber deformed wings, the aircraft must remain at speeds above 80mph which could be detrimental in pattern flying at lower speeds. At 120mph, the full span configuration can achieve a roll rate greater than the 10^o aileron deflection shown in Figure 84 below.

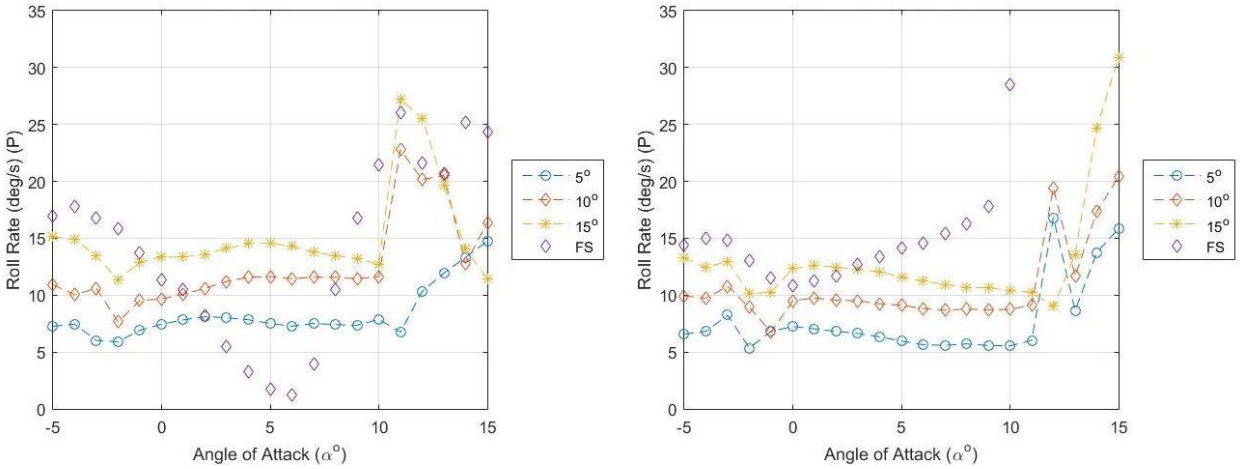

Figure 84. Roll rate versus angle of attack β= 0° comparing full span camber deformed model to conventional aileron models at 90mph (left) and 120mph (right).

Figure 85 below shows roll rate varying with dynamic pressure. Testing found that as dynamic pressure increases, the roll rate of the full span configuration closely follows the aileron models and at 0^o angle of attack in straight and level flight, conditions the roll rate of the full span model remains between the 10^o and 15^o aileron deflection angle.

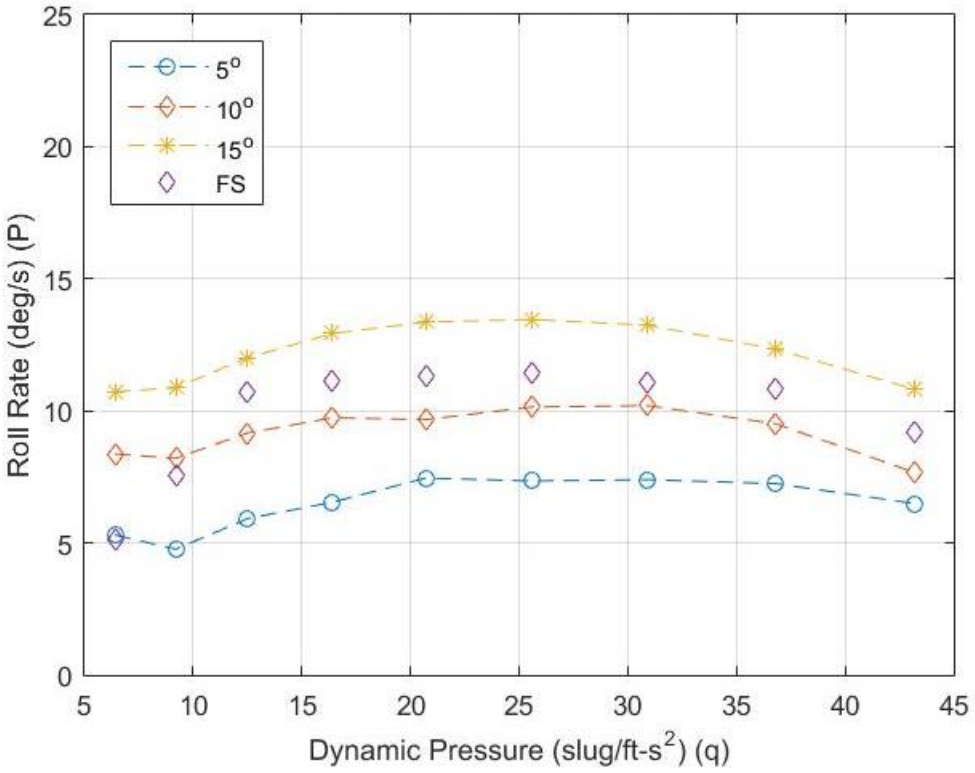

Figure 85. Roll rate versus dynamic pressure of full span camber deformed model compared to conventional ailerons at 0^o angle of attack and $\beta = 0^o$.

4.2.2.2 1% Camber Change Model

This section discusses the roll capability of the 1% camber deformed model compared to conventional ailerons. Figure 86 shows the rolling moment coefficient plotted against the angle of attack at three speeds. These results show similar patterns to the full span model. Due to the increased length of the -5% camber deformation along the span, roll reversal decreased approximately 43% compared to the full span model.

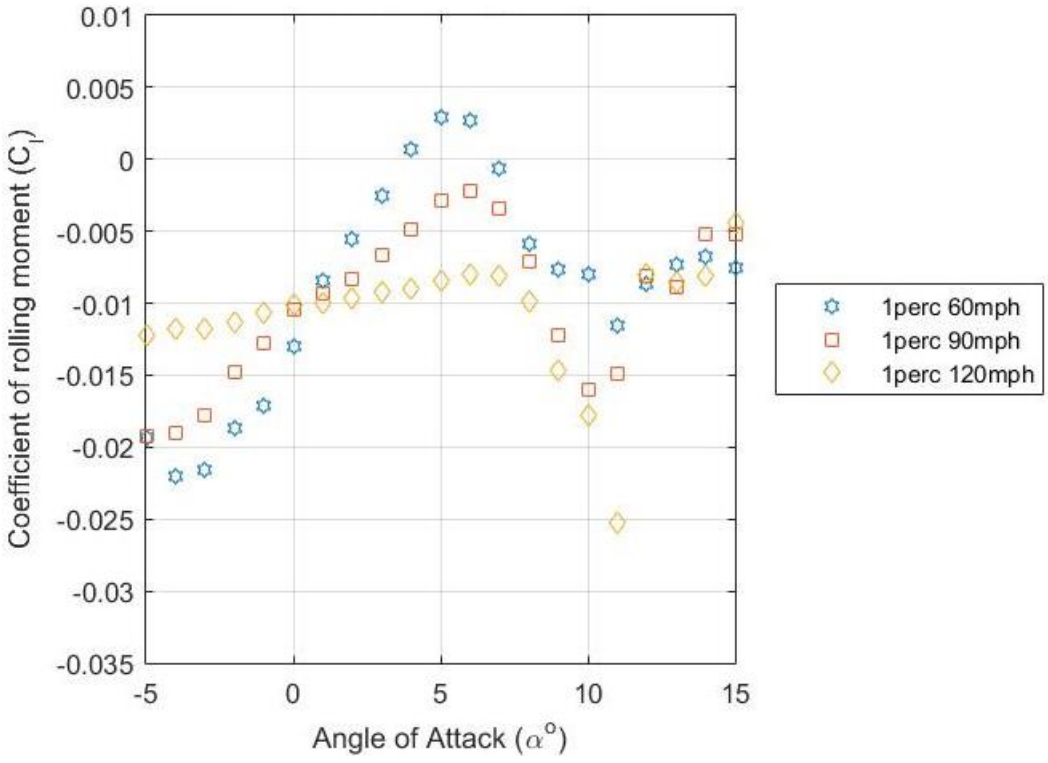

Figure 86. 1% camber change model roll moment coefficient vs α β = 0° at 60mph, 90mph, and 120mph.

Figure 87 shows the roll moment coefficient, comparing the 1% camber change model to each aileron model, while varying the angle of attack. Results show at 90mph, $C_{l\alpha}$ decreases at a larger rate and produces a larger left hand rolling moment at negative angles of attack. At a 0° angle of attack, the rolling moment is equivalent to a 10° aileron deflection, while a 5° angle of attack produces near zero roll moment. As speed increases to 120mph, the rolling moment produced exceeds the rolling moment of the 15° aileron deflection model.

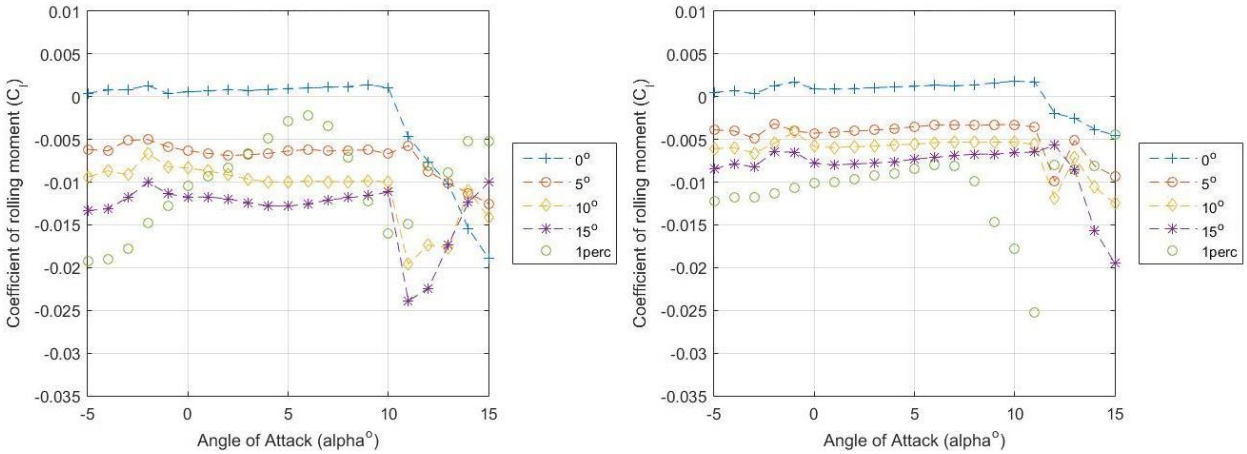

Figure 87. 1% camber change model compared to aileron deflected models rolling moment coefficient vs α β = 0° at 90mph (left) and 120mph (right).

The roll rate, shown in Figure 88, compared to the angle of attack follows the rolling moment coefficient plot. As the roll moment decreases at lower speeds, the roll rate also decreases. From -5° to +3° angle of attack, the 1% camber model produces a roll rate equivalent to a 5° aileron deflection or larger. The change in direction of the roll moment seen below is due to the negative camber wing stalling, and no longer opposing the lift on the positive camber wing. At higher speeds, the roll rate produced by the 1% camber model is larger than the 15° aileron model.

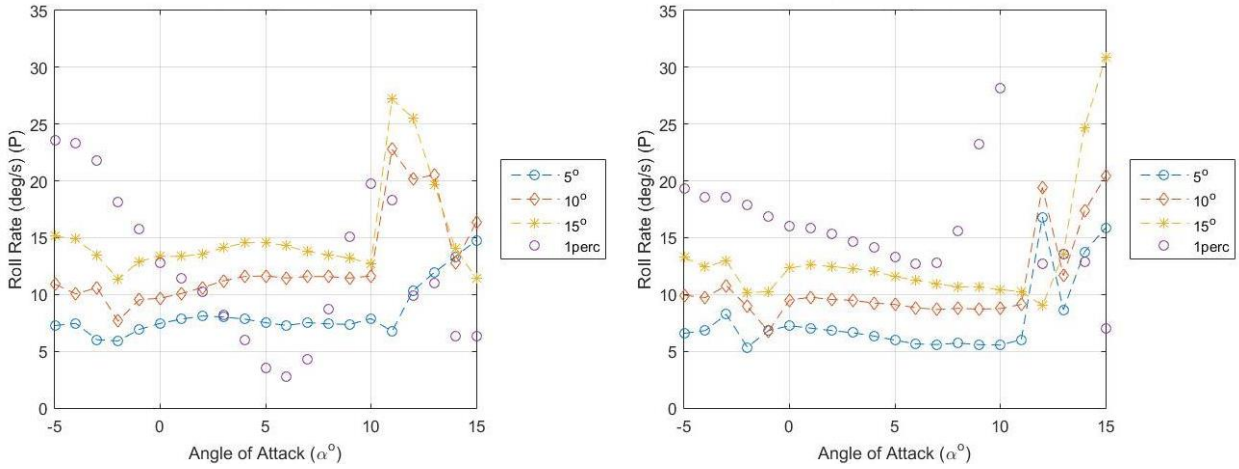

Figure 88. 1% camber change model compared to aileron deflected models roll rate vs α β = 0° at 90mph (left) and 120mph (right).

Unlike the full span model, the 1% camber deformation model, which is most similar to the ARFL VCCW design, produces an increasing roll rate compared to the aileron deflected models. In straight and level flight, the roll rate is approximately equal to a 15° aileron deflection up to a dynamic pressure of 25 slug/ft-s^2. Above 25 slug/ft-s^2, the roll rate out performs the aileron models due to the increase in lift produced by the increased camber on the right wing at higher speeds.

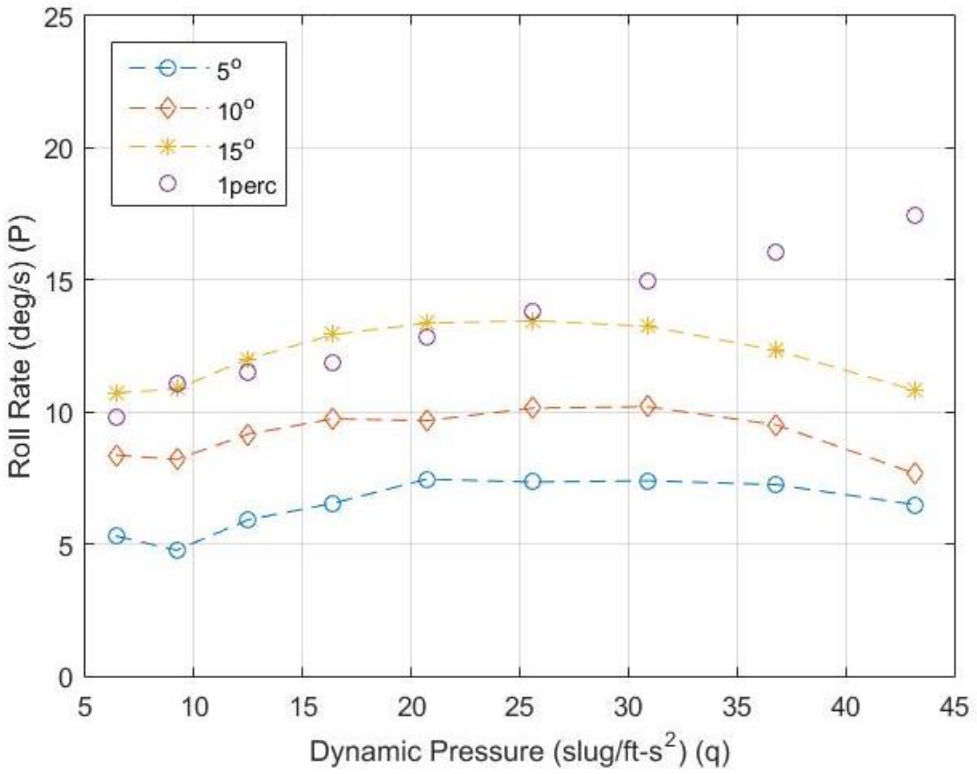

Figure 89. Roll rate vs dynamic pressure $\alpha = 0^o$ and $\beta = 0^o$ comparing 1% camber deformed model to aileron deflected models.

4.2.2.3 Quick Camber Change Model

This section describes the roll behavior of the quick camber change model compared to conventional ailerons. The quick camber change model, similar to the full span and 1% models, induces roll reversal at lower speeds in a nose up attitude, which was exacerbated with negative yaw settings. The magnitude of the roll reversal is substantially less than the other two models. While at speeds over 110mph, the slope of $C_{l\alpha}$ is greater than the other two models. Figure 90 shows the roll moment coefficient versus angle of attack of the quick camber change model at 60mph, 90mph, and 120mph. Results show at speeds above 90mph, roll reversal no longer occurs. Similar to the 1% camber change model, the roll moment at 120mph decreases at a lower rate than at lower speeds.

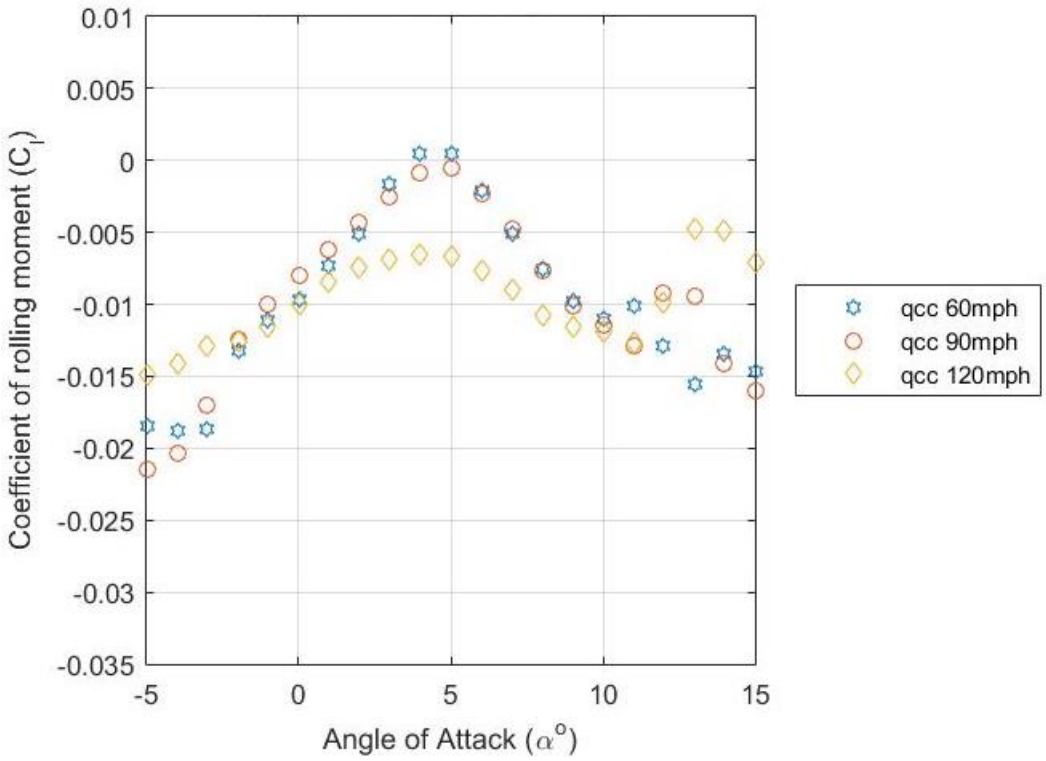

Figure 90. Roll moment coefficient vs α β = 0° at 60mph, 90mph, and 120mph for the quick camber change model.

Figure 91 shows the rolling moment coefficient, comparing the quick camber change model to each aileron model, as a function of angle of attack at two speeds. At 90mph, results indicate from -5° to 0° angle of attack, the roll moment produced is greater than or equal to the roll moment of the 10° aileron deflected model. Above 1° angle of attack, the roll moment produced is less than the 5° aileron deflected model. As speed increases, the qcc model roll moment is larger than or between that of the 10° and 15° aileron deflected models at angles of attack of $-5^o < \alpha < 1^o$ and $2^o < \alpha < 5^o$ respectively.

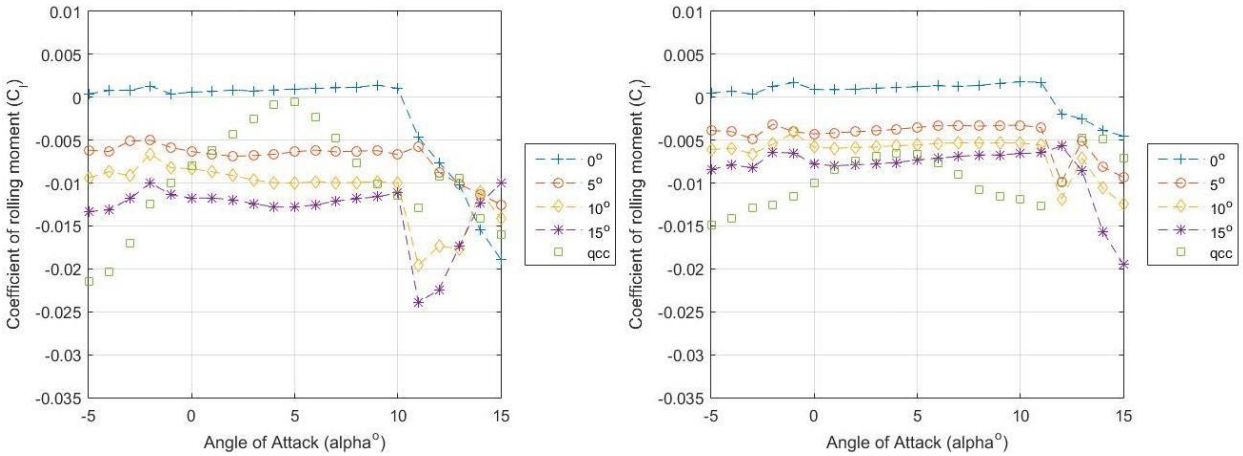

Figure 91. Quick camber change model compared to aileron models roll moment coefficient vs α β = 0° at 90mph (left) and 120mph (right).

Figure 92 details the roll rate versus angle of attack at 90mph and 120mph, comparing the quick camber model to each aileron model. The roll rate produced followed the trends of the roll moment coefficient plots, similar to the full span and 1% camber change models. At angles of attack between -5° and 1°, the roll rate was greater than the 5° aileron deflected model. At 120mph, the roll rate produced is greater than the 10° aileron deflected model.

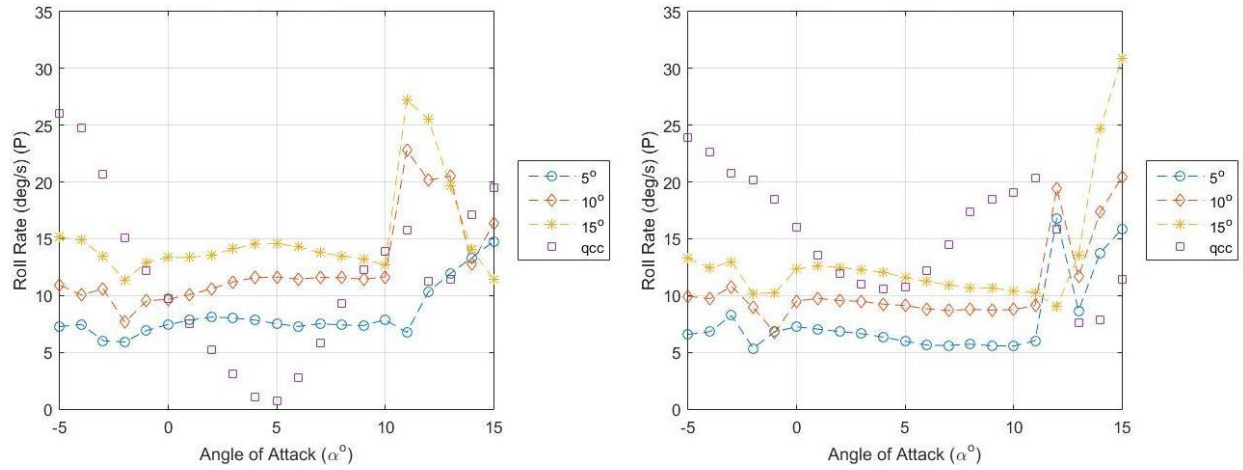

Figure 92. Quick camber change model compared to aileron models roll rate vs α β = 0° at 90mph (left) and 120mph (right).

Unlike the 1% camber change model, the quick camber model produces a roll rate initially lower than the 10° aileron deflected model. As dynamic pressure increases with speed,

the roll rate produced increases, outperforming the 15° aileron deflected model above 30 slug/ft-s^2 as seen in Figure 93.

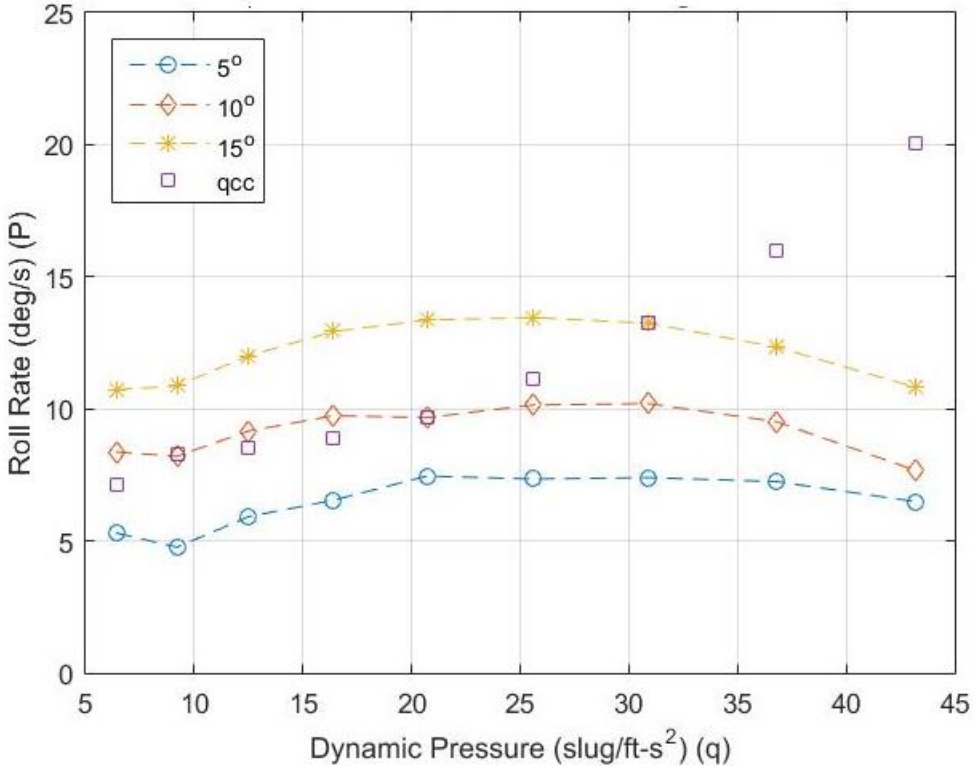

Figure 93. Quick camber change model compared to aileron deflection models roll rate vs dynamic pressure at α = 0° and β= 0°.

4.2.2.4 Final Roll Results

Comparing each of the camber deformed models at 60mph, 90mph, and 120mph shows at speeds below 90mph, roll reversal is experienced by each model given in Figure 94 below. With increased speed, each camber deformed model the lift generated on both wings produces a nearly equal $C_{L\alpha}$ and behaves more closely to the aileron models as shown above. At each speed, all three models produce similar trends in roll moment with increased angle of attack. The similar results may be attributed to the small scale of each model and balance resolution about the roll axis.

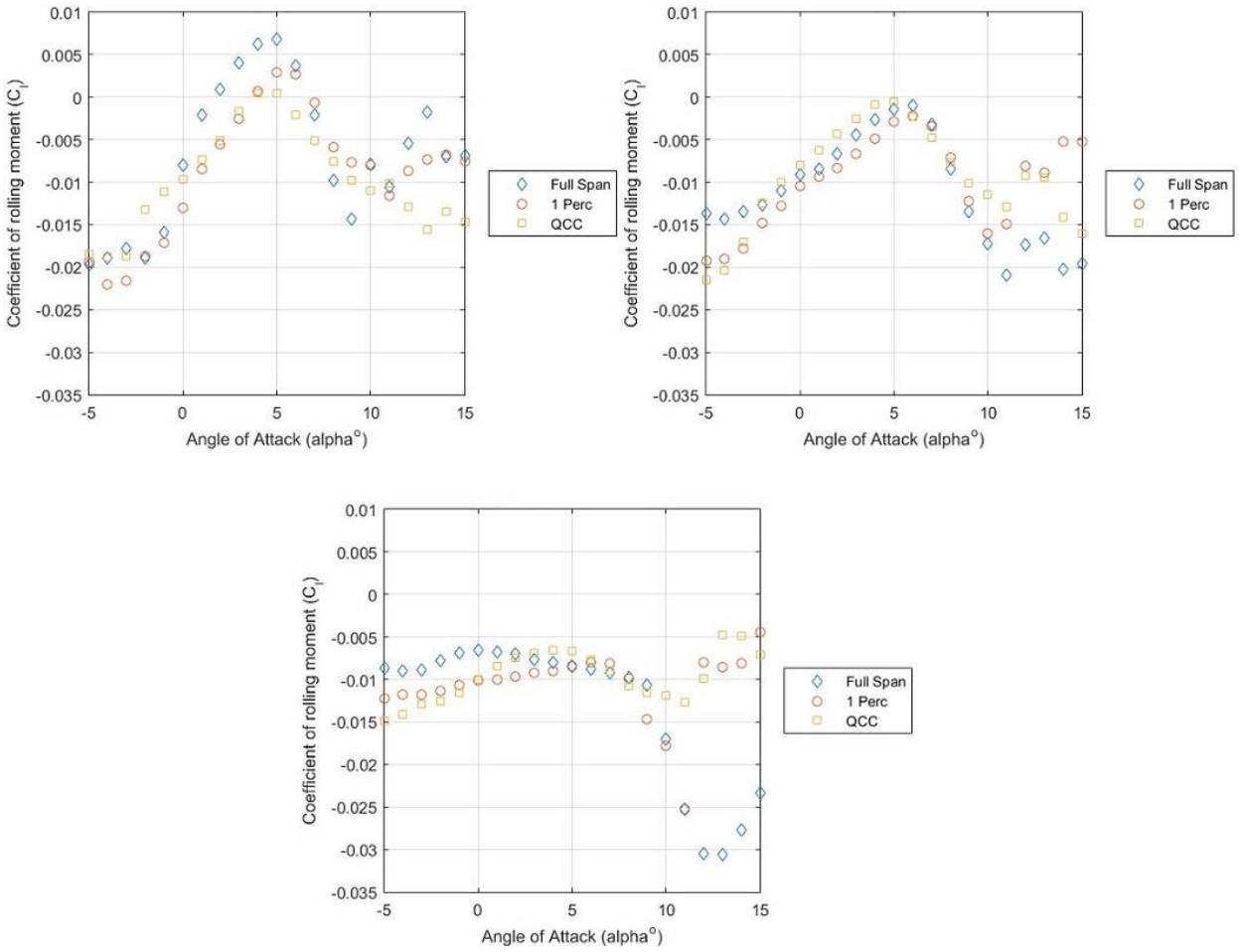

Figure 94. Roll moment coefficient vs α β = 0° for Camber deformed model comparison at 60mph (top left), 90mph (top right), and 120mph (bottom).

Figure 95 shows the 1% camber deformed model initially begins with the largest roll rate of approximately 10 deg/s and continues this trend until 110mph. At 120mph, the quick camber change model and 1% camber change model produce equivalent roll rates of approximately 16 deg/s, and the quick camber change model achieves a maximum roll rate of approximately 20 deg/s at 130mph.

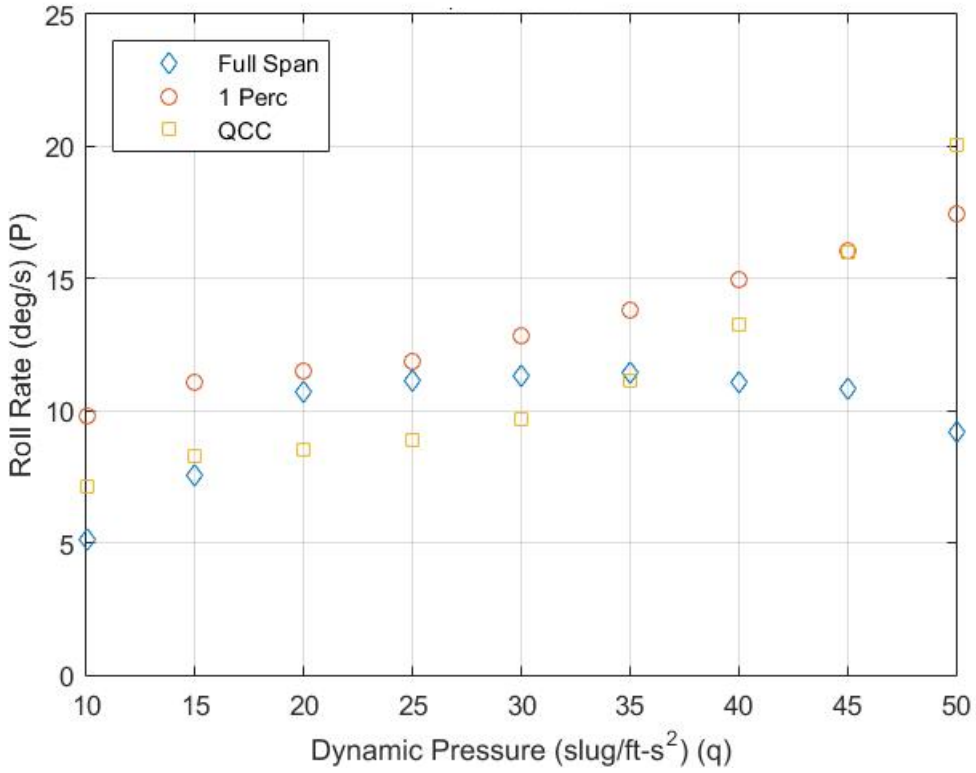

Figure 95. Roll rate vs dynamic pressure at $\alpha = 0^o$ and $\beta = 0^o$ comparing camber deformation models.

Above a dynamic pressure of 30 slug/ft-s2 (110mph), the quick camber change and 1% camber change models produce a larger roll rate at 0^o angle of attack than the 15^o aileron deflected model. Each camber deformed model produces equivalent or larger roll rates at 0^o angle of attack in straight and level flight than the 10^o aileron deflected model.

4.2.3 Aircraft Stability Results

Positive aircraft stability is the ability for an aircraft to recover from a perturbation away from equilibrium for a given flight condition. Stability occurs about each of the three aircraft axes, roll about the X axis, pitch about the Y axis, and yaw about the Z axis. Longitudinal static stability can be defined as $\partial C_m/\partial \alpha < 0$ [22]. A negative $C_{m\alpha}$ produces an aerodynamic restoring moment for a change in the angle of attack [22]. $C_{m\alpha}$ is defined as the slope of the curve of the pitching moment coefficient versus angle of attack. Lateral static stability is defined by

$\partial C_l/\partial\beta < 0$ [22]. A negative $C_{l\beta}$ produces a rolling moment which rolls away from the direction of an induced sideslip [22]. Finally, the directional static stability derivative is defined by $\partial C_n/\partial\beta > 0$ and is also called the weathercock stability derivative [22]. A positive $C_{n\beta}$ produces a yaw moment that opposes the sideslip perturbation, returning the aircraft to the original non-perturbed state [22]. Figure 96 shows the X-56A with 0^o aileron deflection is statically stable in each of the three axes. It can be seen that C_{m0}, or the pitching moment coefficient, at a 0^o angle of attack is negative for the X-56A. This value indicates that flying at a zero pitching moment requires a nose down attitude, which is expected due to the large amount of sweep in the wings. The lift generated at the aerodynamic center of each spanwise chord section is aft of the center of gravity due to the wing sweep, which produces a slight nose down pitch. As speed increases, the pitching moment coefficient decreases, decreasing the angle at which zero pitching moment occurs. $C_{m\alpha}$ remains nearly constant at varying speeds in the linear range from $-2^o < \alpha < 7^o$. $C_{m\alpha}$ varied from -0.0099 at 60mph, to -0.0074 at 90mph, and to -0.0068 at 120mph which produces a change of approximately 25% from 60mph to 90mph and 8% from 90mph to 120mph.

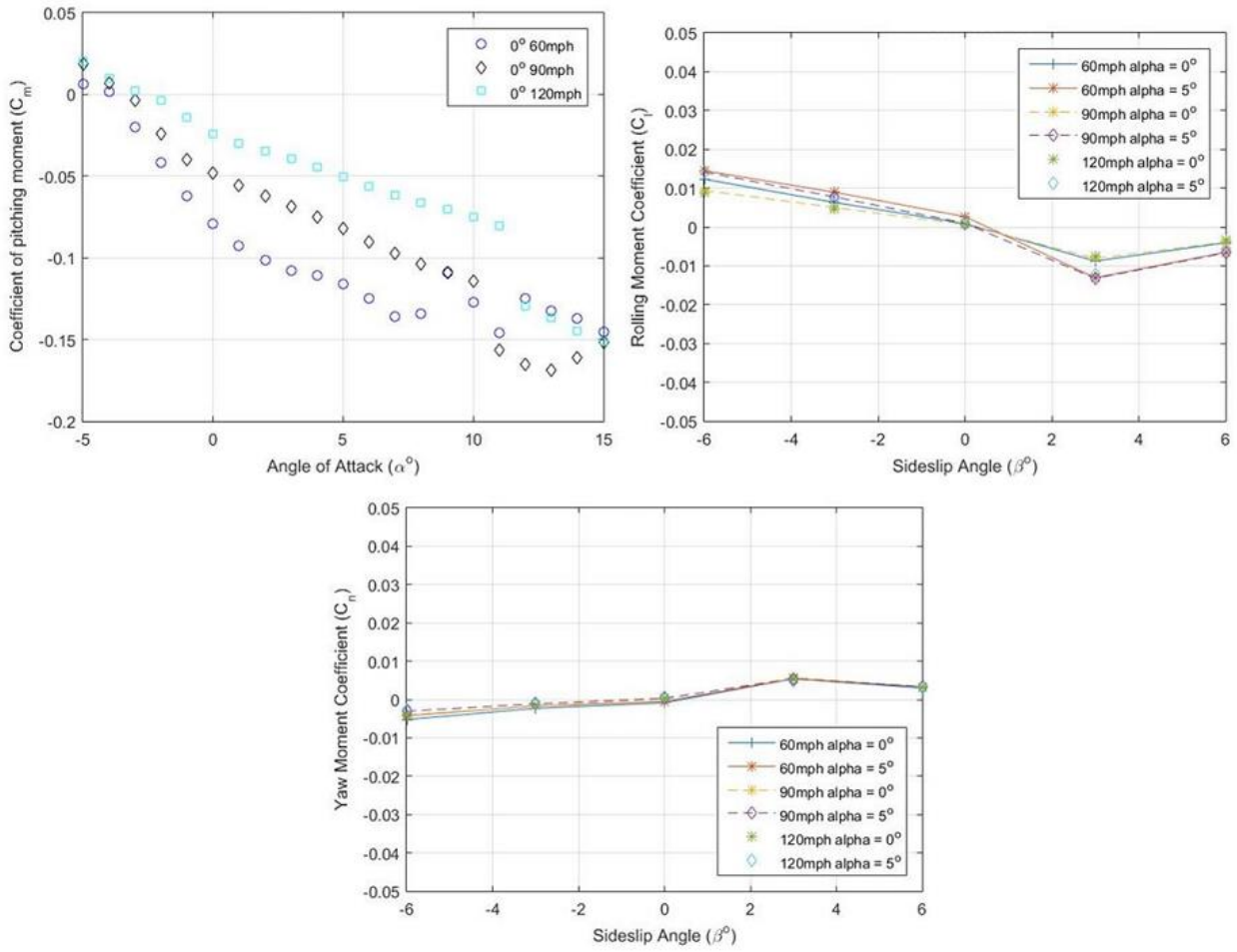

Figure 96. X-56A pitch (top left), roll (top right), and yaw (bottom) stability at 60mph, 90mph, and 120mph.

In Figure 96 above the yaw stability, shows a positive slope with a very small magnitude (0.00069). This result is due to the lack of a true vertical tail aft of the center of gravity. The vertical winglets on each wing tip produce a restoring force due to sideslip. Although the winglets do produce a restoring force, the small magnitude is due to the winglets close proximity to the center of gravity than a traditional tail. Table 20 below, details the X-56A stability derivatives at 90mph. These values varied with variations in speed, angle of attack, and sideslip angle.

Table 20. X-56A stability derivatives at 90mph.

Stability Derivative	Magnitude at 90mph
C_{m_α}	-0.0074
C_{l_β}	-0.0015
C_{n_β}	0.00069

Each model shown in the following sections, produces similar results in pitching moment with increase in angle of attack as speed increases. None of the camber deformation models cause instabilities in roll, pitch, or yaw.

4.2.3.1 Full Span Model

This section outlines the full span model stability behavior compared to conventional ailerons. Figure 97 below shows the full span model compared to each of the aileron deflected models. Testing shows that the slope of $C_{m\alpha}$ is equivalent to the aileron deflected models and the baseline model. At 7^o angle of attack the pitch moment coefficient decreases sharply due to the left wing stall, until the right wing stalls at 10^o angle of attack at 90mph. The close match in slope is due to the minimal camber change, the decrease in pitch moment is due to the flow separation from a laminar separation bubble which grows with increased angle of attack. The turbulent boundary layer does not have enough of a pressure differential to reattach, which causes separation to occur. In Figure 97, the increase in speed shows a clear pitching moment coefficient slope match without a pronounced moment decrease due to flow separation. The boundary layer has enough speed at the small scale to produce turbulent flow reattachment with

the laminar separation bubble moving closer to the minimum pressure location delaying wing stall.

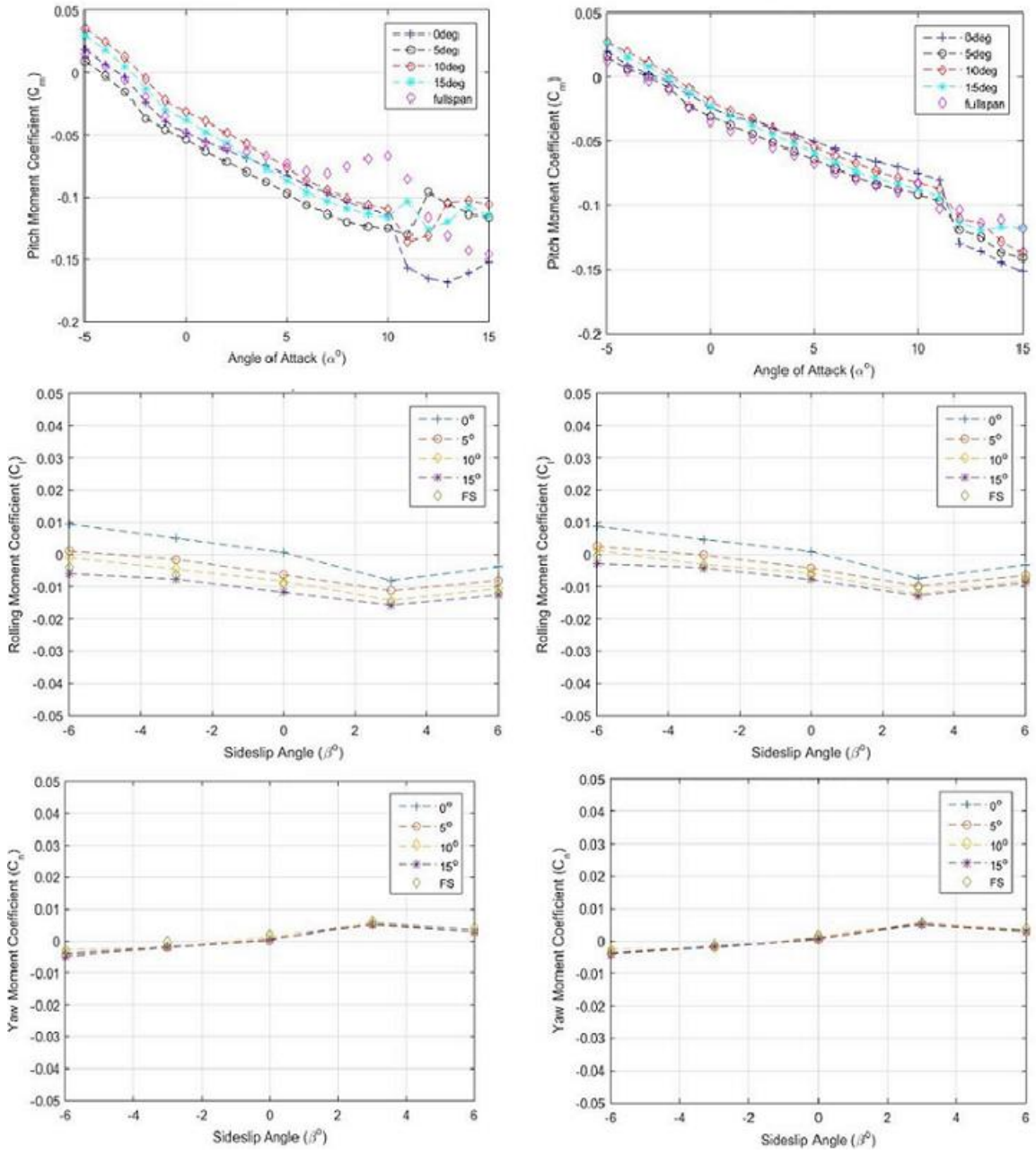

Figure 97. Full span camber change model aircraft stability in pitch (top), roll (middle), and yaw (bottom) at 90mph (left) and 120mph (right) compared to aileron models.

From Figure 97 above, C_l versus sideslip angle and C_n versus sideslip angle that the full span model does not change the stability characteristics compared to the aileron deflected models. The

variation in C_l due to both aileron deflection and camber deformation is due to an increase in lift on the right wing and decrease in lift on the left wing.

4.2.3.2 1% Camber Change Model

The following plots outline the stability characteristics of the 1% camber deformed model, similar to the VCCW, at 90mph and 120mph. Figure 98 below shows the pitch moment coefficient versus angle of attack at 90mph and 120mph. These plots show a decrease in slope, due to a loss in lift from the laminar separation bubble due to camber deformation at 90mph. At 120mph, the laminar separation bubble size is decreased and left wing stall delayed 1^o angle of attack. The variation in pitch moment is due to the increased length of the +5% camber deformation. With the decrease in $C_{m\alpha}$, C_{m0} decreases, this decrease allows the aircraft to trim in pitch at a lower negative angle of attack.

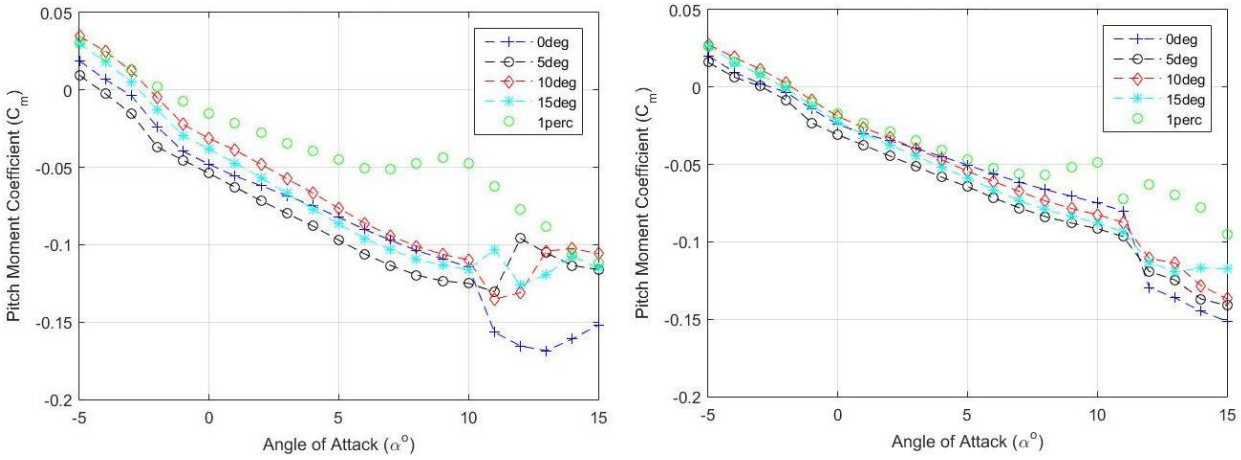

Figure 98. Pitch moment coefficient vs α β = 0^o at 90mph (left) and 120mph (right) comparing the 1% camber deformed model to each aileron deflected model.

Table 21 below shows the reduction in $C_{m\alpha}$ at 90mph.

Table 21. Pitch stability derivative comparing 1% camber deformed model to aileron deflected models at 90mph.

Wind Tunnel Model	$C_{m\alpha}$
Aileron Models	-0.0074
1perc Model	-0.0048
% Decrease	35.14%

Figure 99 below shows the change in roll moment at each sideslip angle at 90mph and 120mph at 0^o angle of attack. The 1% camber deformed model at 90 mph shows the lateral stability becoming almost neutrally stable. The neutrally stable aircraft indicates that while in a rolling maneuver, the aircraft when affected by a sideslip condition, will remain in the new attitude. Results show, increasing speed causes negligible changes in the roll stability derivative. Testing also shows that no appreciable changes in $C_{n\beta}$ is noticed, as seen in Figure 100.

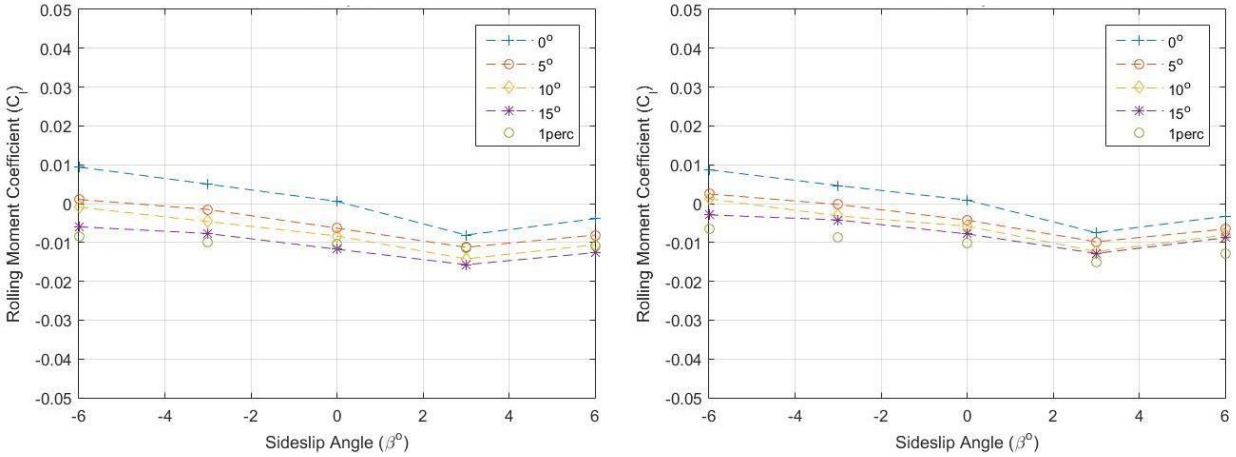

Figure 99. Roll stability derivative comparison at 90mph (left) and 120mph (right) of the 1% camber change model compared to aileron models.

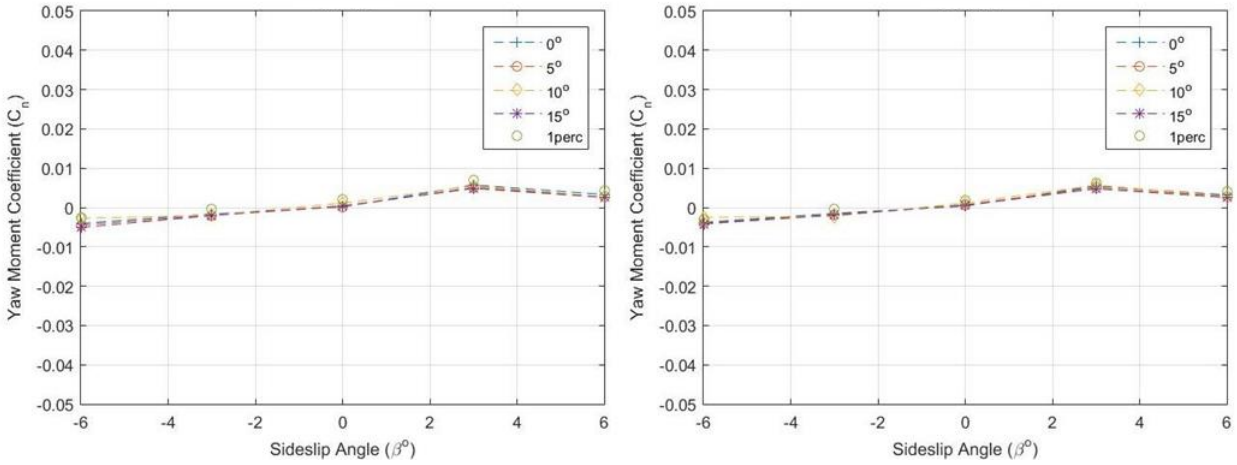

Figure 100. Yaw stability derivative comparison at 90mph (left) and 120mph (right) of the 1% camber change model compared to aileron models.

4.2.3.3 Quick Camber Change Model

This section outlines the stability characteristics of the quick camber deformed model at 90mph and 120mph. The 90mph pitch moment decreases similar to the 1% camber deformation model. $C_{m\alpha}$ of the quick camber change model decreases at a larger rate than the 1% camber change model by approximately 5% from the baseline aileron models due to the extended length of maximum camber deformation along the span as seen in Table 22 below.

Table 22. Pitch stability derivative comparing the quick camber change model to aileron models at 90mph.

Wind Tunnel Model	Cmα
Aileron Models	-0.0074
Quick Camber	-0.0044
% Decrease	%40.5

Similar to the 1% camber deformation model at 90mph, the decreased $C_{m\alpha}$ is due to the increased laminar separation bubble which decreased the lift on the wing. As speed increased, the flow separation was delayed from 5° to 6° angle of attack, as seen in Figure 101 below.

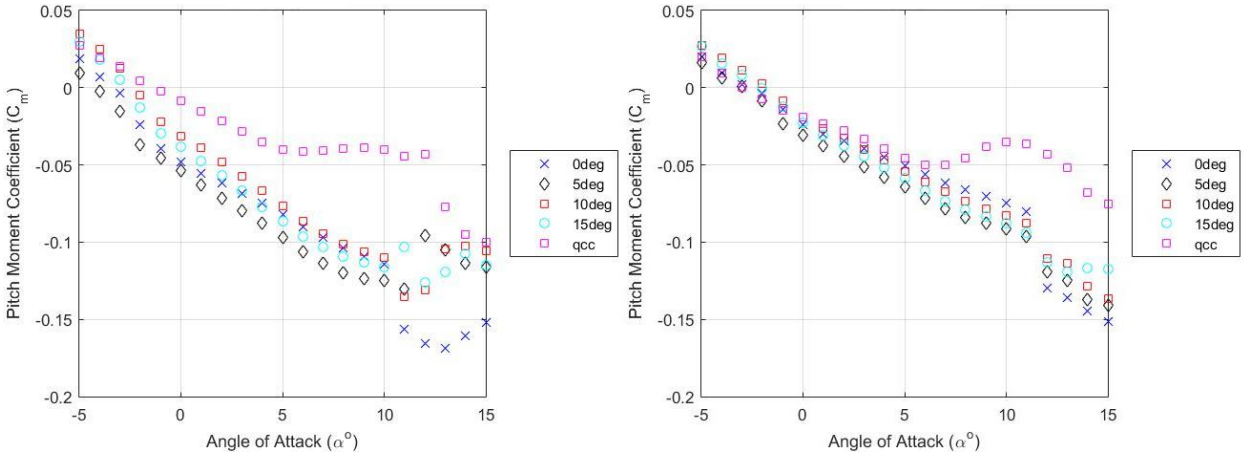

Figure 101. Pitch stability comparison at 90mph (left) and 120mph (right) of the quick camber change model compared to aileron models.

Figure 102 Figure 103 below show that, similar to the 1% camber change model, at 90mph the roll moment coefficient does not change with sideslip angle creating a neutral stability in roll.

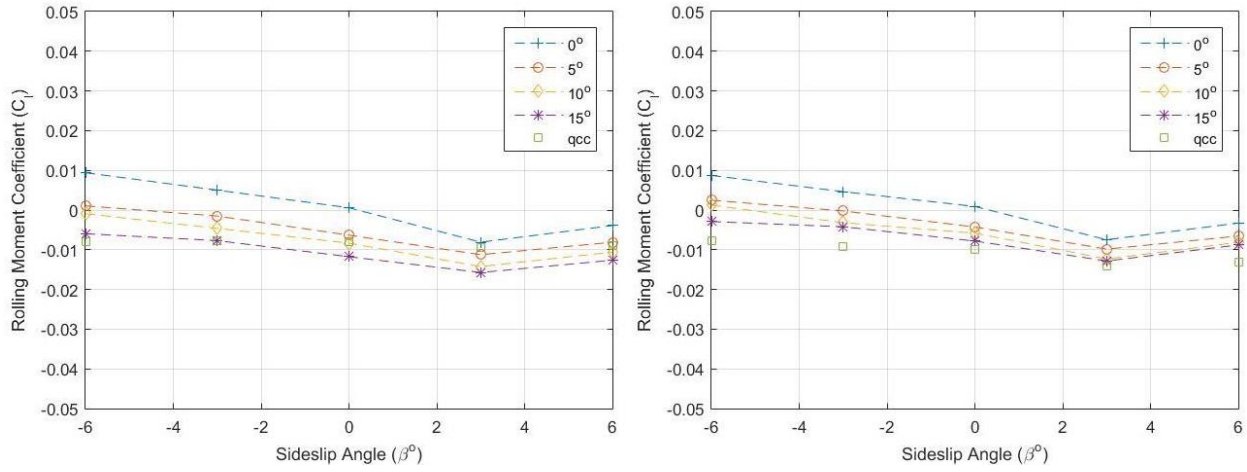

Figure 102. Roll stability comparison at 90mph (left) and 120mph (right) of the quick camber change model compared to aileron models.

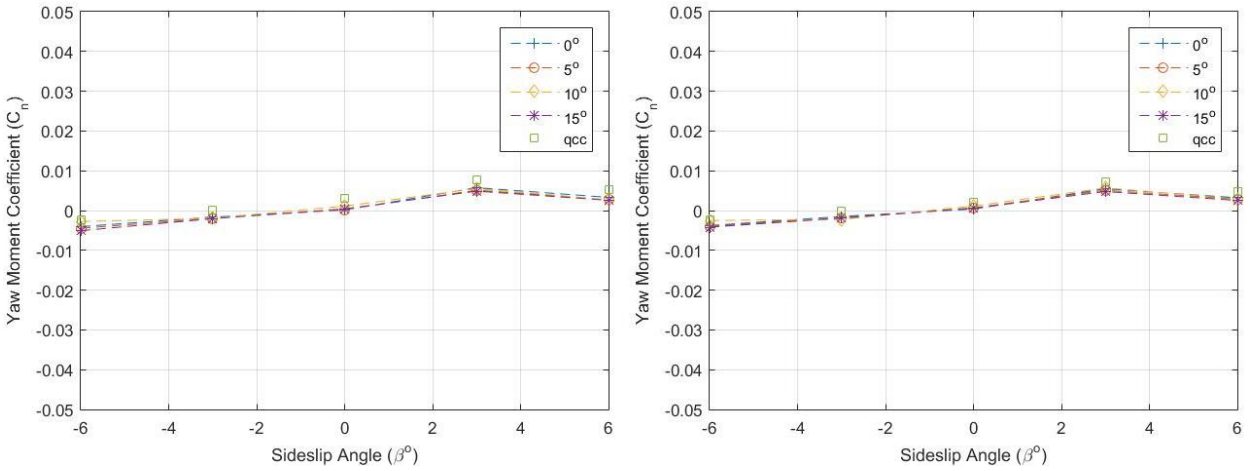

Figure 103. Yaw stability comparison at 90mph (left) and 120mph (right) of the quick camber change model compared to aileron models.

In the plots above, with increases in speed, sideslip angle, or angle of attack, the camber deformation wings on the X-56A do not cause instabilities from the baseline X-56A. Due to the low Reynolds number flow, the increased camber caused early flow separation. This is caused by the laminar separation bubble which forms due to the large curvature on the upper and lower surfaces decreasing the lift generated. This was seen most prevalently on the 1% camber deformed model and quick camber change model due to the large spanwise distance the increased camber covered.

4.3 Tornado Comparison Results

Tornado was used as an analysis tool for simple use and cost saving ability for the Air Force when considering new technology development such as camber deforming wings. Tornado uses the Vortex Lattice Method, which is an inviscid solver. Due to the low Reynolds numbers experienced by the wind tunnel models, variations in the data were expected. The trends presented are critical to ensure aircraft stability and the effectiveness of each camber deformed aircraft compared to conventional ailerons. The “inviscid” region of the lift plot was the linear

region considered from $-2^{o} < \alpha < +5^{o}$, taken from the C_L versus alpha plot in the previous sections in the aerodynamics section of this chapter. On an aircraft operating at higher Reynolds numbers, the linear region assumes the flow operating around the aircraft is attached. As Reynolds number increases, the viscous forces acting on the surface contribute less to the overall lift and drag experienced on the vehicle. At low Reynolds numbers, the viscous forces apply a large contribution, and alter the lift and drag characteristics, especially laminar separation bubbles and separation at low angles of attack and smaller dynamic pressures.

4.3.1 Tornado Aerodynamic Results

Figures 104 - 107 compare the Tornado results to experimental wind tunnel data for lift and drag at 90mph and 120mph. Results show that the lift curve slope is similar between the two tests, while the drag is significantly different due to the large viscous effect experienced by the scale models. Table 23 below compares the lift curve slope and drag values for both the wind tunnel tests and the Tornado results.

Table 23. Tornado comparison to experimental wind tunnel results at 90mph and 120mph.

Model	90mph Wind Tunnel $CL\alpha$	120mph Wind Tunnel $CL\alpha$	Tornado $CL\alpha$	Δ90mph	Δ120mph
0^o	0.058	0.056	0.081	0.023	0.025
5^o	0.062	0.058	0.080	0.018	0.022
10^o	0.063	0.061	0.079	0.016	0.018
15^o	0.065	0.062	0.078	0.013	0.016
Full Span	0.059	0.056	0.060	0.001	0.004
1 Percent	0.060	0.061	0.061	0.001	0
Quick Camber Change	0.060	0.062	0.062	0.002	0

By performing a simple friction drag calculation correction, the Tornado results are closer to the experimental results. The drag due to skin friction can be seen in Equation 48 below. The coefficient of skin friction drag, as discussed in Chapter 3, is dependent on the type of flow, laminar or turbulent.

$$D_f = C_f(\frac{1}{2})\rho V^2 S \quad \textbf{(48)}$$

The total drag can be found by the addition of the profile drag and the induced drag. Due to the small size of the models tested, the induced drag is a very small component of the total drag produced as seen in Equation 49 below.

$$D = D_f + \frac{CL^2}{\pi eAR} \quad \textbf{(49)}$$

The Oswald efficiency factor, or span efficiency factor, is solved using the following equations by Shevell [40].

$$e = \frac{1}{(\pi ARk) + \frac{1}{us}} \quad \textbf{(50)}$$

$$k = (0.38 + 57x10^{-6}\Lambda^2)C_{D_0} \quad \textbf{(51)}$$

$$s = 1 - 1.556(\frac{d_f}{b})^2 \quad \textbf{(52)}$$

In Equation 52 above, d_f equals fuselage diameter, *b* equals span, Λ equals wing sweep angle, C_{D_0} equals drag at 0^o angle of attack, and *u* equals planform efficiency factor assumed to be 0.99. The Oswald span efficiency factor is calculated to be approximately 0.98. Table 24 below shows the Drag due to skin friction, induced drag, and total drag at 0^o angle of attack and 120mph, assuming a flat plate.

Table 24. Laminar and Turbulent flow friction drag and total drag values.

Flow Type	Skin Friction Coefficient	Drag due to skin friction	Induced Drag	Total Drag
Laminar	0.0037	0.0244	0.0002	0.0246
Turbulent	0.0070	0.0462	0.0002	0.0464

By adding the drag due to skin friction to the inviscid drag output from Tornado, the total adjusted drag for each model is shown in Table 25 below. Fully laminar flow is assumed for the 5^o, 10^o and 15^o aileron deflected models adding the total drag of 0.0246 to the tornado output. Each camber change model produces larger total drag than the aileron deflected models. The complete camber deformed wing is neither fully laminar flow nor fully turbulent flow. Xfoil analysis shows at 120mph approximately 50% of the chord experiences laminar flow. The 1% camber deformed model is approximately 20% turbulent flow across the entire aircraft, and the quick camber model approximately 35% turbulent flow across the entire aircraft. These percentages of laminar and turbulent flows are multiplied by the appropriate total drag value, and added to the output from Tornado.

Table 25. Tornado drag adjustments adding skin friction.

Model	Tornado Drag	Total Drag with Skin Friction Drag	Wind Tunnel Drag
0^o	0.0006	0.025	0.022
5^o	0.0009	0.0253	0.017
10^o	0.0018	0.0262	0.018
15^o	0.0032	0.0276	0.022
Full Span	0.0009	0.0253	0.024
1 Percent	0.0013	0.0304	0.028
Quick Camber Change	0.0012	0.0334	0.031

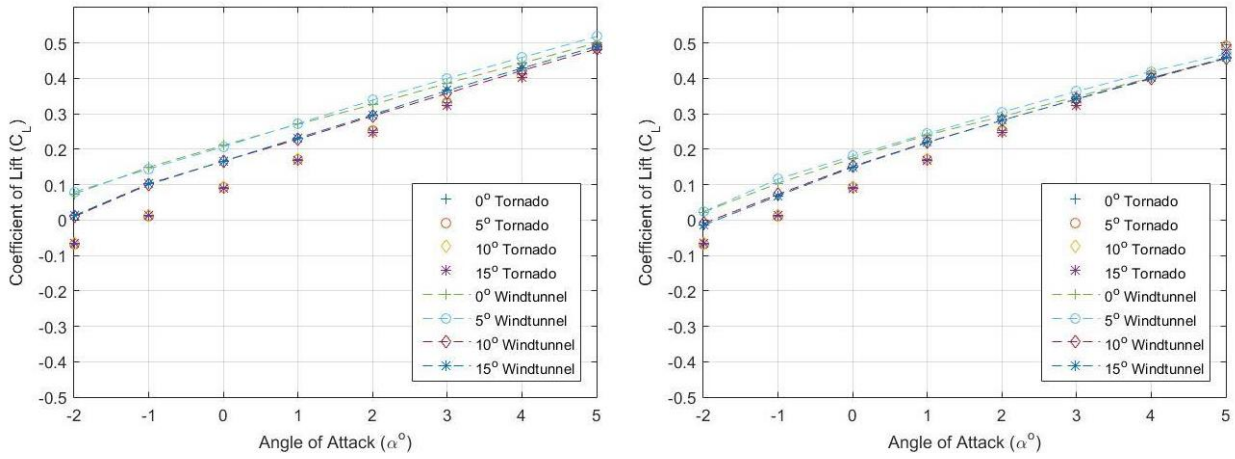

Figure 104. Tornado aileron model comparison to experimental wind tunnel aileron model data at 90mph (left) and 120mph (right) coefficient of lift versus angle of attack β = 0°.

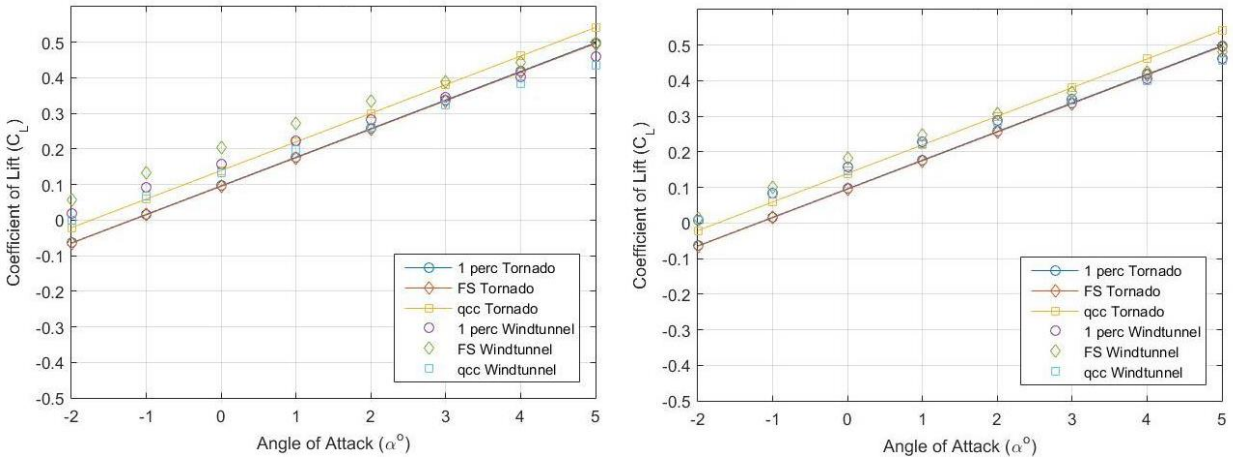

Figure 105. Tornado camber change model comparison to experimental wind tunnel camber change model data at 90mph (left) and 120mph (right) coefficient of lift versus angle of attack β = 0°.

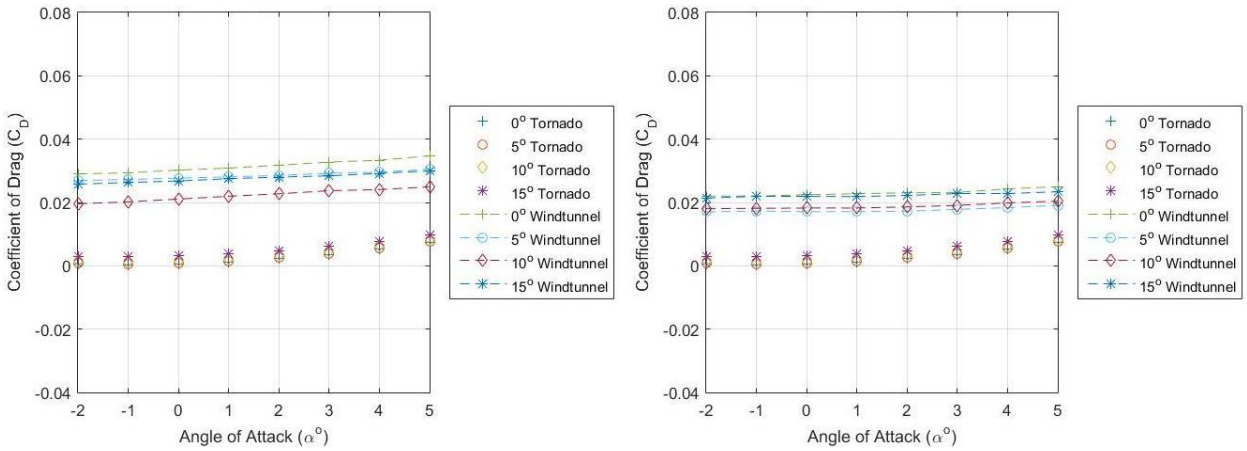

Figure 106. Tornado aileron models compared to experimental wind tunnel aileron model data at 90mph (left) and 120mph (right) coefficient of drag versus angle of attack β= 0°.

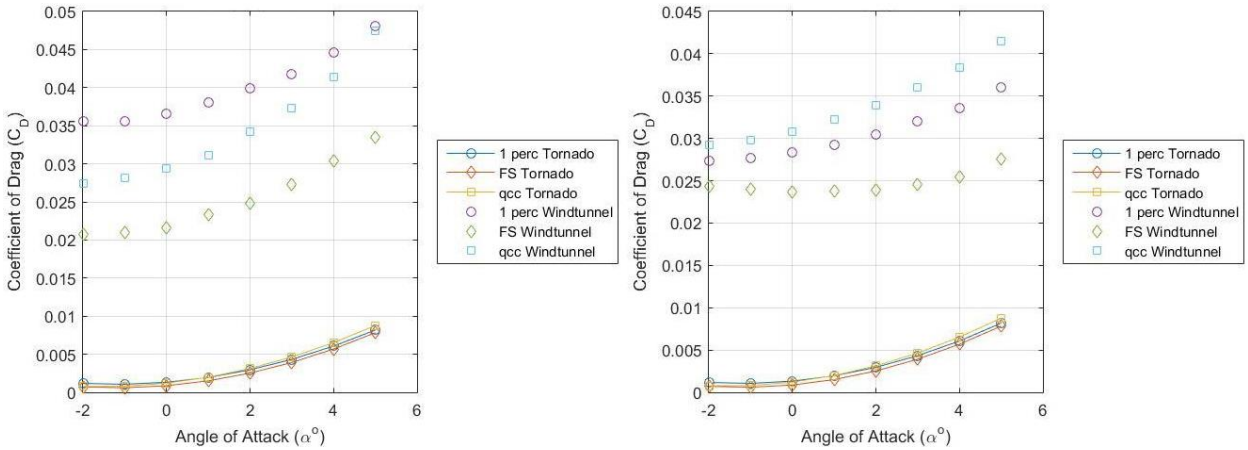

Figure 107. Tornado camber change models compared to experimental wind tunnel camber change model data at 90mph (left) and 120mph (right) coefficient of drag versus angle of attack β= 0°.

4.3.2 Roll Control in Tornado

Figures 108 and 109 compare the roll moment coefficient versus angle of attack at 90mph and 120mph between Tornado and experimental results. Results show the lift generated through the Vortex Lattice Theory affects the rolling moment coefficient. Due to the loss in lift from laminar separation bubbles, and flow separation from the low Reynolds number flow, Tornado over predicts the lift of each model, which results in approximately three times the experimental rolling moment.

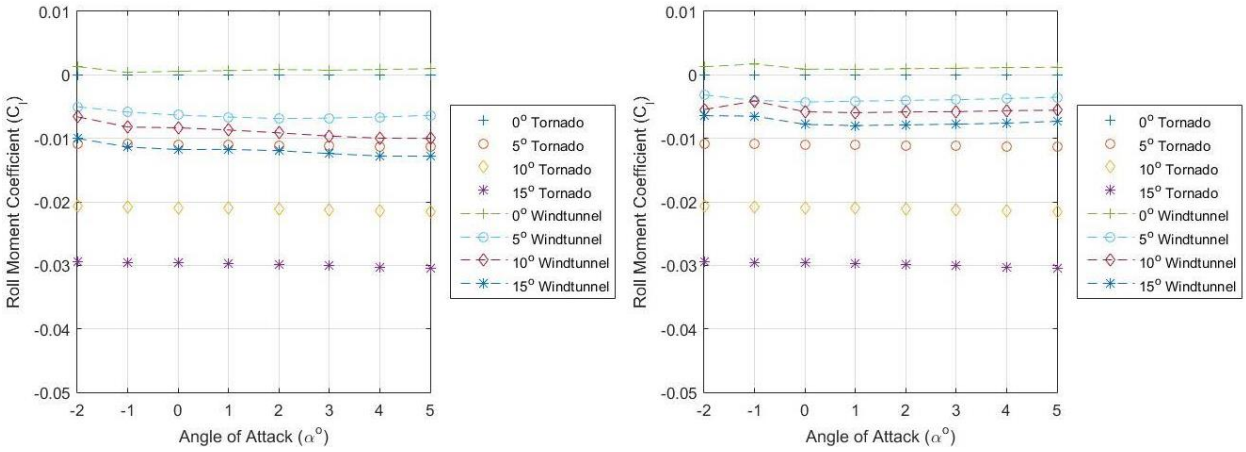

Figure 108. Tornado aileron model comparison to experimental wind tunnel aileron models at 90mph (left) and 120mph (right) roll moment coefficient versus angle of attack β = 0°.

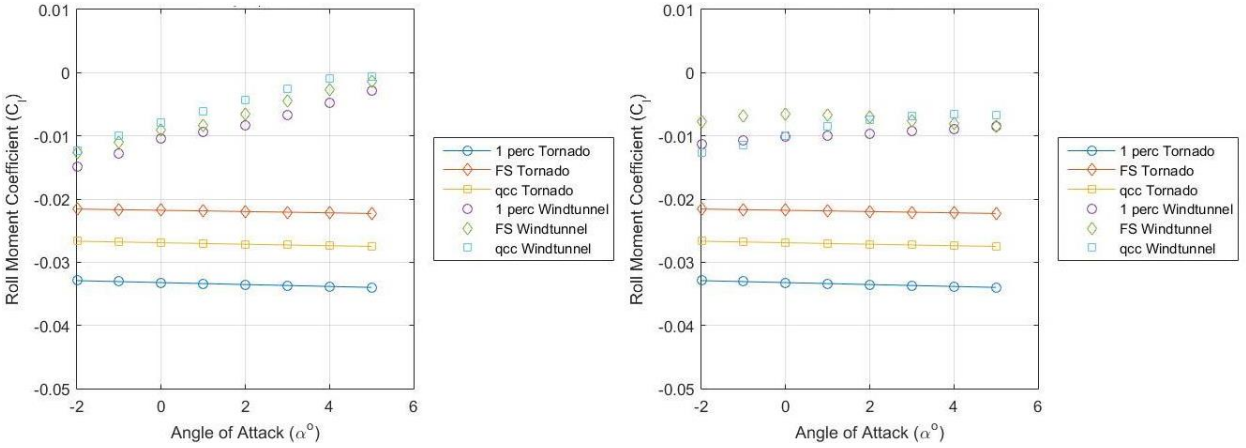

Figure 109. Tornado camber change models comparison to experimental wind tunnel camber change models at 90mph (left) and 120mph (right) roll moment coefficient versus angle of attack β = 0°.

Figure 110 below compares the tornado (left) roll moment coefficient versus angle of attack to the corresponding experimental wind tunnel data (right). Results show the 1% camber deformed model produces the largest rolling moment over the 15° aileron deflected model. Similar to the Strip Theory results, all models produce a larger rolling moment than the 10° aileron deflected model. The 120mph wind tunnel data between $2^o < \alpha < 5^o$ shows similar trend data as the Tornado results at a lower roll moment, except the full span model continues to increase after 0° angle of attack, which differs from the Tornado results.

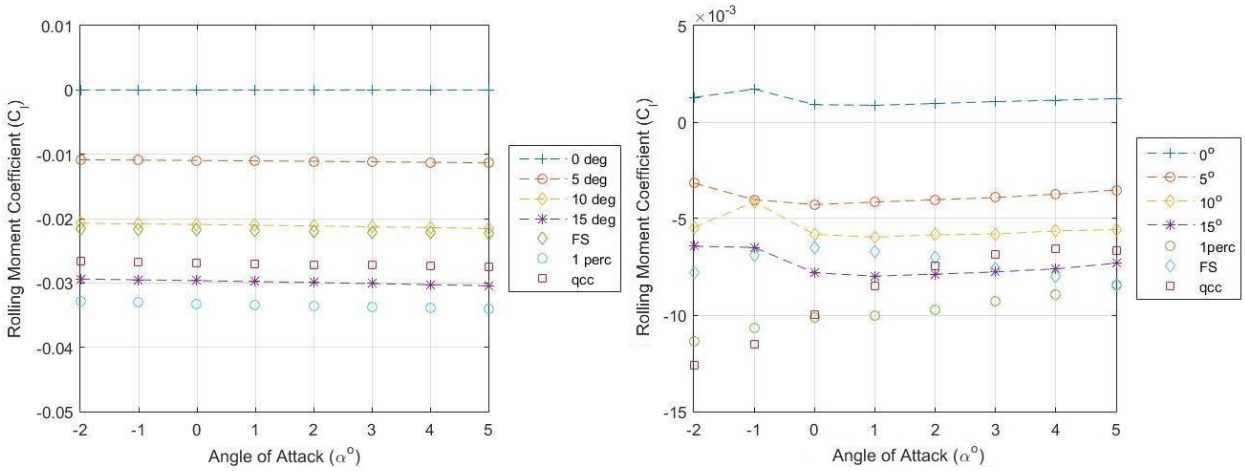

Figure 110. Tornado roll moment coefficient versus angle of attack (left) compared to experimental wind tunnel results (right)

Figure 111 shows comparisons between Tornado predicted roll rate (left) and the experimentally measured roll rate (right) plotted against angle of attack. As expected, the roll rate at 120mph is higher than the experimental data. Figure 112 shows expected results of an increase in roll rate with increasing dynamic pressure, as shown in both the Tornado prediction and in the wind tunnel results.

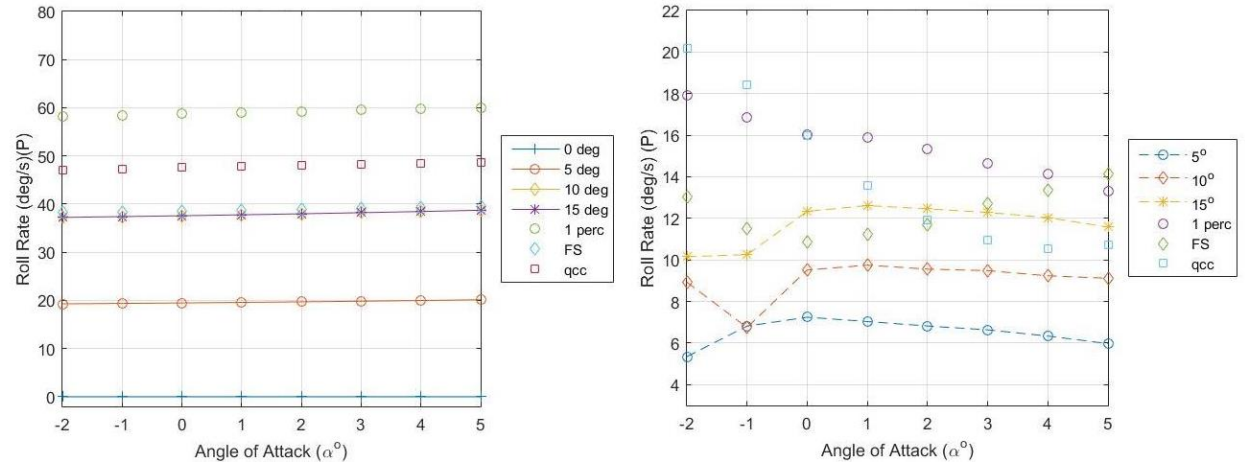

Figure 111. Tornado roll rate (left) versus angle of attack compared to experimental wind tunnel data at 120mph (right)

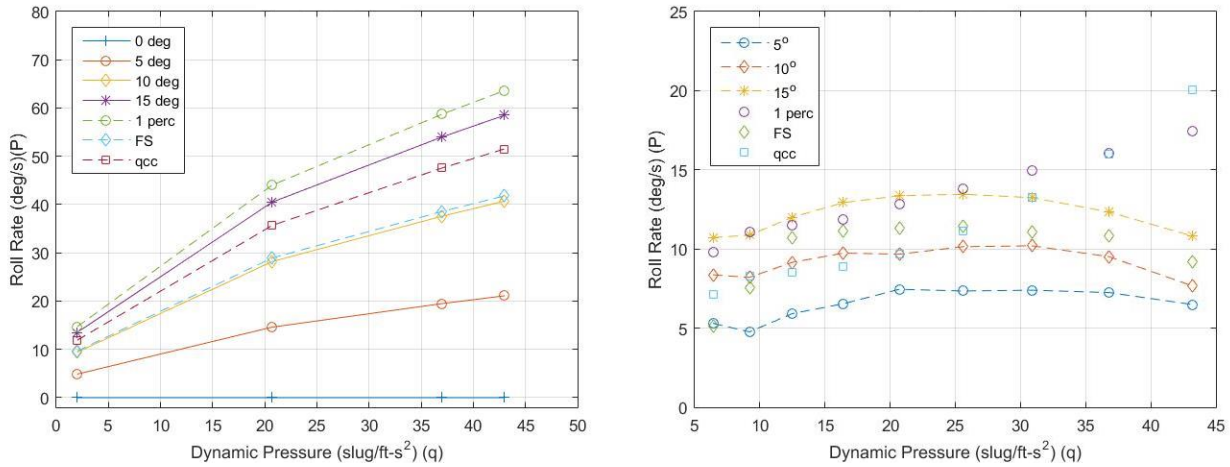

Figure 112. Tornado roll rate versus dynamic pressure (left) compared to experimental wind tunnel data (right)

4.3.3 Stability and Control in Tornado

Figure 113 through Figure 118 show the X-56A static stability comparison between Tornado and wind tunnel experimentation. The differences between the experimental and the Tornado prediction data is most likely because Tornado is only an inviscid solver. The lift distribution affected the pitch and roll moments most, producing the largest difference between the test and predicted results. Testing revealed that Tornado produces similar stability trends as the wind tunnel data, as shown in Table 26 below. The pitching moment produces the largest difference in slope. Stability trends show the model is more stable in pitch while C_{m0} tracked more closely to the wind tunnel data. The Tornado data also demonstrated that a negative angle of attack is required to produce a zero pitching moment, which is similar to what the experimental data revealed.

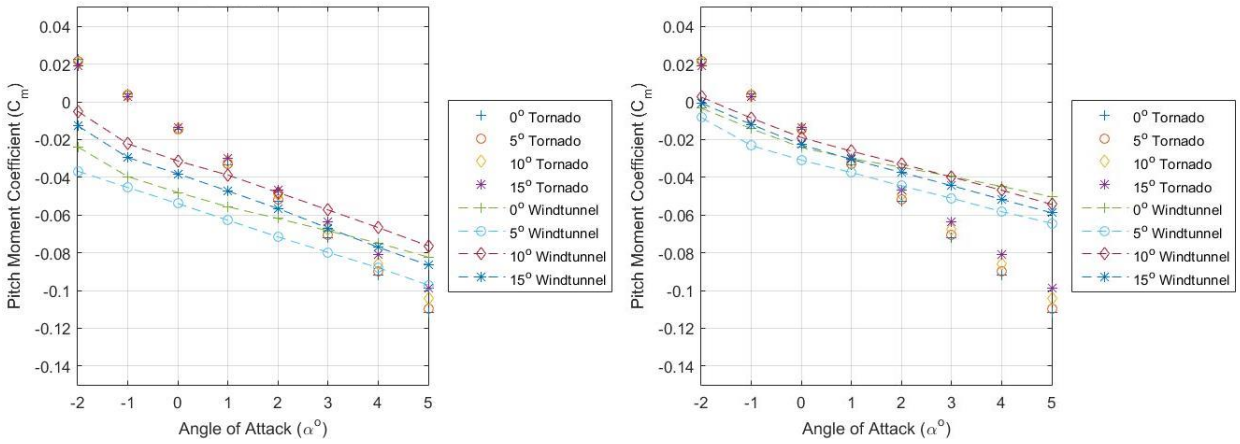

Figure 113. Pitch stability comparing Tornado results and experimental wind tunnel results at 90mph (left) and 120mph (right) for all aileron models β = 0°.

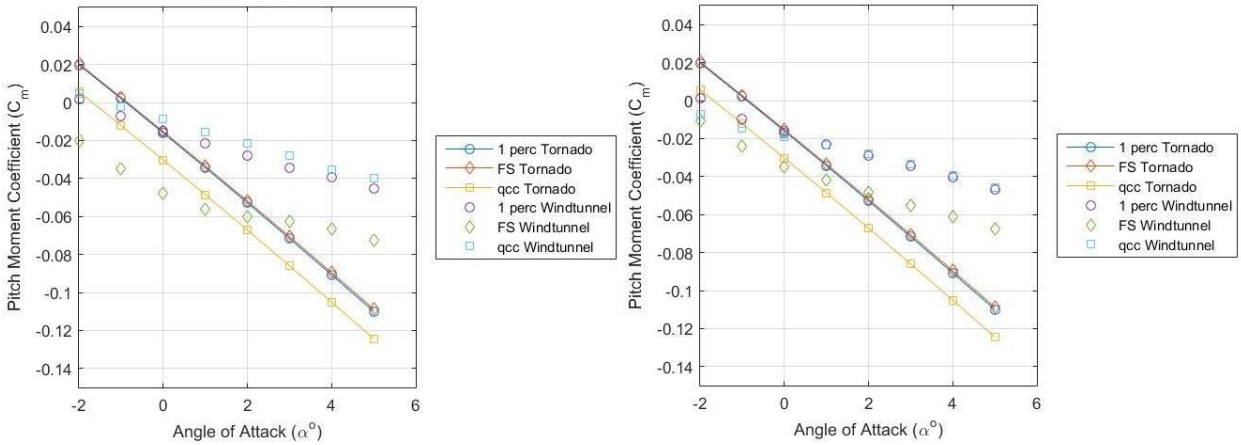

Figure 114. Pitch stability comparing Tornado results and experimental wind tunnel results at 90mph (left) and 120mph (right) for all camber deformed models β = 0°.

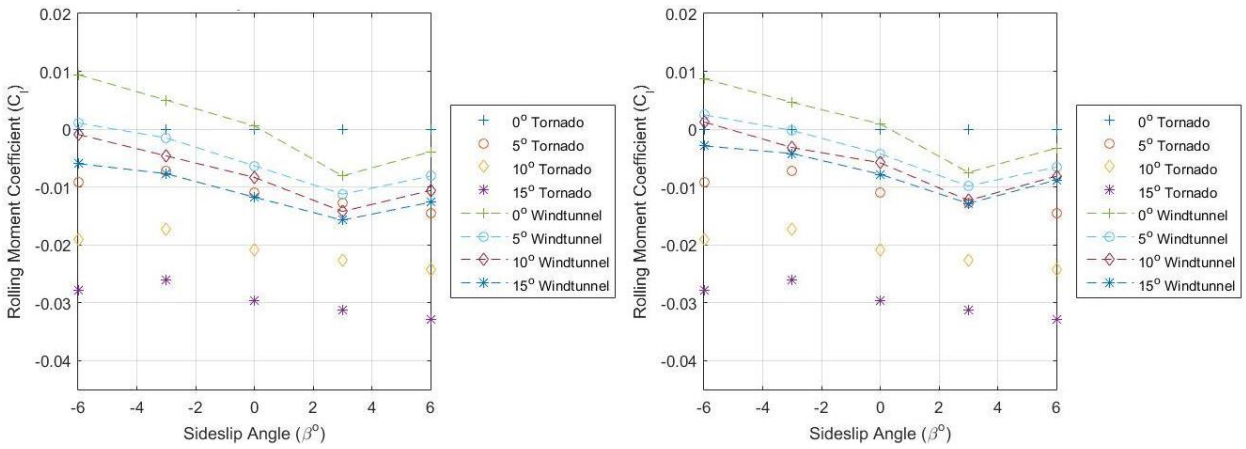

Figure 115. Roll stability comparing Tornado results to experimental wind tunnel results at 90mph (left) and 120mph (right) for all aileron models $\alpha = 0^o$.

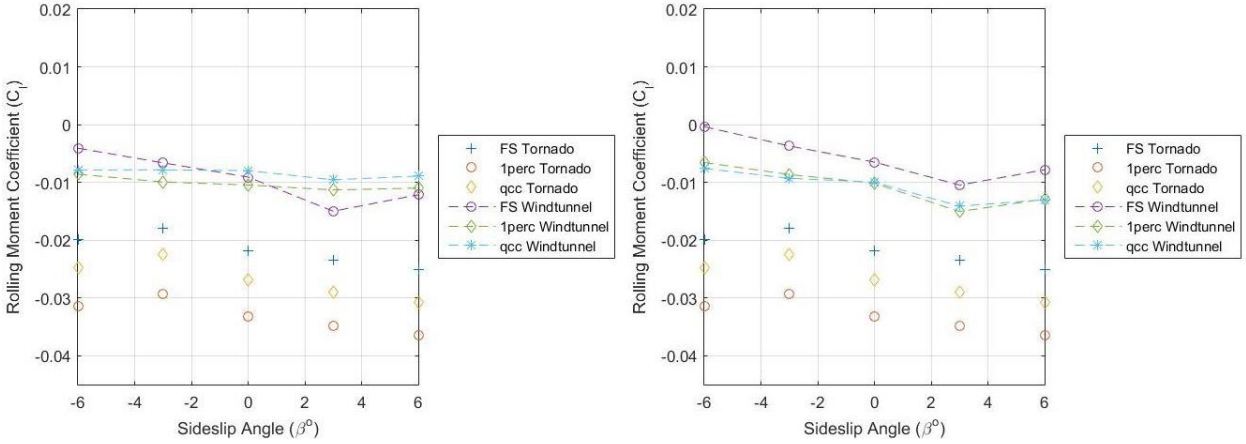

Figure 116. Roll stability comparing Tornado results to experimental wind tunnel results at 90mph (left) and 120mph (right) for all camber change models $\alpha = 0^o$.

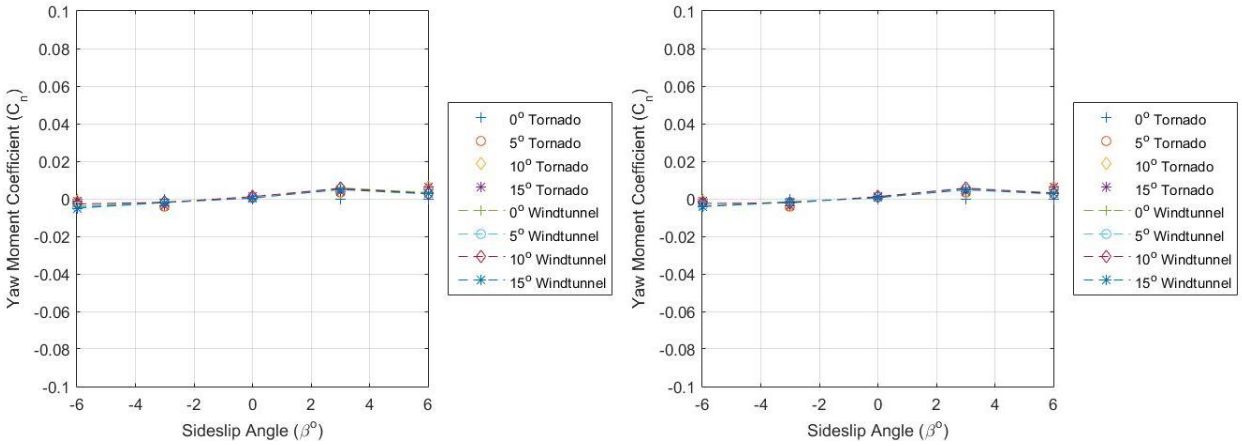

Figure 117. Yaw stability comparing Tornado results to experimental wind tunnel results at 90mph (left) and 120mph (right) for all aileron models $\alpha = 0^o$.

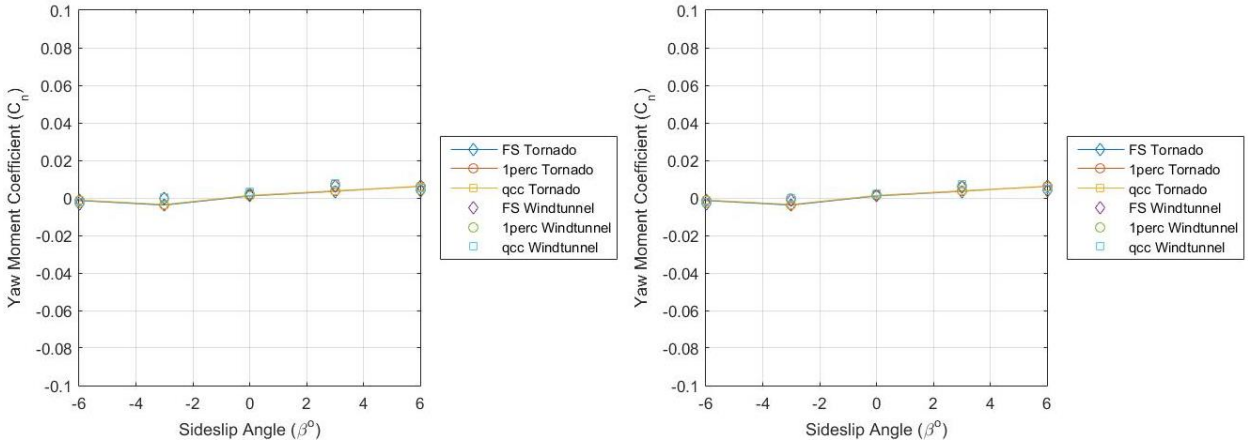

Figure 118. Yaw stability comparing Tornado results to experimental wind tunnel results at 90mph (left) and 120mph (right) for all camber deformed models $\alpha = 0^o$.

Table 26. Comparisons of the stability derivatives between Tornado and experimental wind tunnel results at 120mph for each model.

120mph β=0°									
Model	**Cmα Tornado**	**Cmα Wind Tunnel**	**ΔCmα**	**Clβ Tornado**	**Clβ Wind Tunnel**	**ΔClβ**	**Cnβ Tornado**	**Cnβ Wind Tunnel**	**ΔCnβ**
0° Aileron	-0.020	-0.005	0.015	0	-0.001	0.001	0.0007	0.0007	0
5° Aileron	-0.019	-0.007	0.012	-0.0008	-0.0008	0	0.0007	0.0007	0
10° Aileron	-0.019	-0.007	0.012	-0.0008	-0.0008	0	0.0007	0.0007	0
15° Aileron	-0.019	-0.007	0.012	-0.0008	-0.0005	0.0003	0.0007	0.0007	0
Full Span	-0.019	-0.004	0.015	-0.0008	-0.0005	0.0003	0.0007	0.0006	0.0001
1 Percent	-0.019	-0.004	0.015	-0.0008	-0.0005	0.0003	0.0007	0.0006	0.0001
Quick Camber	-0.019	-0.004	0.015	-0.0009	-0.0005	0.0004	0.0007	0.0006	0.0001

4.3.4 Tornado Results

Due to Tornado's inviscid solver, low Reynolds number flow behavior can not be accurately predicted. Tornado provides general insight into vehicle behavior and into first order stability and control for all the aileron deflected models and all the camber deformation models. The methodology of building and modeling the X-56A in Tornado matches the stability and control trends with variations in the magnitude.

4.4 Limitations

The AFIT-3 balance, as discussed in Chapter 3, can register a maximum normal force of 50lbf, axial force of 25lbf, side force of 25lbf, and a maximum pitching moment of 50in-lbf, a maximum roll moment of 15in-lbf, and a maximum yaw moment of 25in-lbf. The resolution of each force and moment reduces to a normal force of 0.02lbf, an axial force of 0.025lbf, a side force of 0.015lbf, a pitch moment of 0.06in-lbf, a roll moment of 0.0255in-lbf and a yaw moment of 0.025in-lbf. At low speeds, due to the small scale, changes in speed or angle of attack caused variations in forces and moments on the order of the balance resolution. As seen in the error analysis in Appendix D, the largest sources of error are produced in drag force, yaw moment, and roll moment due to their low overall magnitude and the balance resolution. At speeds over 80 mph, the AFIT-3 balance was required due to the increased loads in normal force and pitch moment which produced loads above the maximum load capability of the 3lbf balance.

Due to each model having been printed separately, errors in data could result from inconsistencies between each model. Final cleaning and smoothing of each model was performed by hand and variations in skin roughness, contour, etc. can cause additional inconsistencies in data as well as variations in boundary layer and trips from laminar to turbulent in alternate locations to Xfoil predictions.

The low speeds and low Reynolds number discussed previously limit the scaling capability of the X-56A models. The maximum size model matching Reynolds number at 30mph is a ¼ scale 0.5ft chord model. The elasticity of the small scale models at high speeds causes wing flex and potential aeroelastic wing twist, which may not occur on a larger scale model with

thicker wings. This testing was performed for a small scale cost effective method of testing camber deformation to generate equivalent of larger rolling moments to conventional ailerons.

Tornado's major limitation is the inviscid solver routine not capable of accurately capturing the flow physics and boundary layer phenomenon at low Reynolds numbers, even in the linear region where typically viscous affects are minimal. As discussed in the previous sections of this chapter, over predictions in lift, and under predictions in drag are produced, but can be made comparable with a simple skin friction drag calculation correction.

5. Conclusions and Recommendations

The primary goal of this research was to analyze the roll characteristics of camber deformed wings compared to conventional ailerons on the X-56A. The secondary goal was to characterize the camber deforming wings roll, pitch, and yaw stability, and to analyze Tornado's capability to model low Reynolds number flow predictions compared to experimental data as a validation. The primary and secondary goals of this thesis were accomplished.

5.1 Aerodynamics

Each peak C_L/C_D produced by the camber deformed models was lower than the aileron deflected models by as much as 57% at 90mph and 54% at 120mph. The most efficient angle of attack was found to decrease with increased spanwise camber deformation from 7^o for the full span model to 5^o for the quick camber change model compared to the aileron models at 8^o. At lower speeds, the maximum coefficient of lift was lower for each camber deformed model by as much as 17%. As speed increased, the maximum coefficient of lift of the camber deformed models increased by approximately 8%, nearly matching the aileron models C_{Lmax} of 0.7. It was found that each camber deformed model produced more drag due to flow separation, increasing by as much as 33% as spanwise camber increases, and earlier drag rise due to early onset wing stall increasing drag by as much as 130%. Overall, these results showed that the camber deformed models are aerodynamically less efficient than the aileron deflected models. The full span model is 24% more efficient than the 1 percent camber change model and 35% more efficient than the quick camber change model. The quick camber change model is least efficient with an increase in drag by as much as 24% and decrease in lift of 8% compared to the 15^o aileron model at 120mph

5.2 Roll control

Roll control characteristics were studied by analyzing the roll moment coefficient and roll rate. Due to loss of lift over the increased camber wing at low speeds, the camber deformed models had a decreasing roll moment, and roll rate as angle of attack increased. As the velocity increased, the roll moment produced by each model was similar to the scale model 2-D Strip Theory results, which generated a maximum rolling moment 37.5% larger than the 10^{o} aileron deflected model at 80mph and 38.2% larger at 110mph. It was found that the 1% camber change model produced the largest roll moment of -0.01 and roll rate of 17^{o}/s at increased Reynolds numbers. The quick camber change model produced the second largest rolling moment of -0.009 and roll rate of 16^{o}/s and the full span model produced the lowest with a roll moment of -0.006 and roll rate of 11^{o}/s. It was found that at increased Reynolds number flow, the camber deformed models can produce an equivalent or larger rolling moment and roll rate compared to conventional ailerons. In summary, these results showed the camber deformed models can produce equivalent or larger roll moments and rates than the conventional aileron models at small angles of attack or at higher speeds. In the most critical stages of flight where speeds are decreased, such as takeoff and landing, the camber deformed models are limited in nose up attitude while banking or in a climbing bank and could induce a stall or roll reversal at angles of attack $\geq 5^{o}$.

5.3 Stability

The stability and control characteristics of the camber deformed models were compared to conventional ailerons. It was found that the camber deformed wings do not cause any adverse effects to the X-56A static stability in roll, pitch, or yaw. Pitch stability is considered if

$\partial C_m/_{\partial \alpha}$ < 0, roll stability is considered if $\partial C_l/_{\partial \beta}$ < 0, and yaw stability if $\partial C_n/_{\partial \beta}$ > 0. The following stability changes due to camber deformation are noted below.

- At lower speeds, therefore lower Reynolds numbers, the camber deformed models decreased the pitch stability a maximum of 40.5% due to the increased spanwise camber deformation.
- With increased speeds, the pitch stability increased to match the original X-56A stability of -0.005 at 120mph.
- As camber deformation increases, roll stability became more neutrally stable at all tested speeds.
- Camber deformation did not have a noticeable effect on yaw stability.
- Camber deformation caused early wing stall at 5^o angle of attack, due to flow separation.
- The quick camber change model produced a 40.5% decrease in $C_{m\alpha}$.
- The 1% camber change model produced a 35.14% decrease in $C_{m\alpha}$.
- All models produced a negative C_{m0} requiring a 2^o nose down attitude to produce a zero pitching moment.

Overall, small scale testing showed camber deformation does not cause instabilities in roll, pitch, or yaw. However, it did decrease roll and pitch stability at these small scales by as much as 50% and 40.5% respectively.

5.4 Tornado

Tornado produced expected results by over predicting lift by as much as 300%, and under predicting drag results by as much as 97%. The over prediction of lift carried through to an over prediction of roll moment and pitch stability derivative (Cmα) by 200% and 79% respectively. The results of the Tornado simulation are listed below.

- Tornado matched the CLα values of the camber deformed model more closely than the aileron models as seen in Table 23 with a difference of as much as 3% compared to a 40% difference in aileron models.
- Tornado showed similar trends in data even with the over predicted lift affecting in pitch and roll.
- Roll control was over predicted by as much as 200% and did not match low speed wind tunnel results due to viscous effects. At high speeds (120mph) Tornado nearly matched the roll moment model order at low angles of attack ($0^o < \alpha < 2^o$) and matched the 2-D Strip Theory results that each of the camber deformed models produces a larger rolling moment than the 10^o aileron model.

Overall, Tornado was found to be beneficial for stability trend data such as roll, pitch, and yaw. The yaw and roll stability were modeled within 0.001, however the pitch stability, roll moment, and roll rate characteristics were found to be over predicted by as much as 200% while able to produce similar trend data.

5.5 ***Recommendations***

Due to the lack of wind tunnel testing on camber deformed aircraft compared to conventional ailerons to compare roll moment and roll rate, small scale testing proved difficult, but did provide useful results. The low Reynolds numbers experienced do not scale to the full scale X-56A, however, they do provide a representative sample of expected behaviors. To further test the benefits of camber deformation as a roll mechanism, future tests should be conducted with a larger model beginning in a Reynolds number range of 200,000 to 500,000. Some additional recommendations include:

- Large scale testing of the 1% camber change per foot model. A Reynolds number of 200,000 requires a chord length of approximately 6in, generating a $1/4^{th}$ scale model with a wing span of 84in (7ft) at 50mph.
- Computational Fluid Dynamics or modification of the Tornado code to calculate and build in viscous effects for a more accurate simulation tool.
- Analysis should be conducted to find the best spanwise camber deformation configuration per wing to generate the maximum rolling moment.
- Half span wind tunnel testing of each wing with pressure ports to have a full analysis of pressure distribution.

Appendix A: Extra CL, CD, and CL/CD Plots

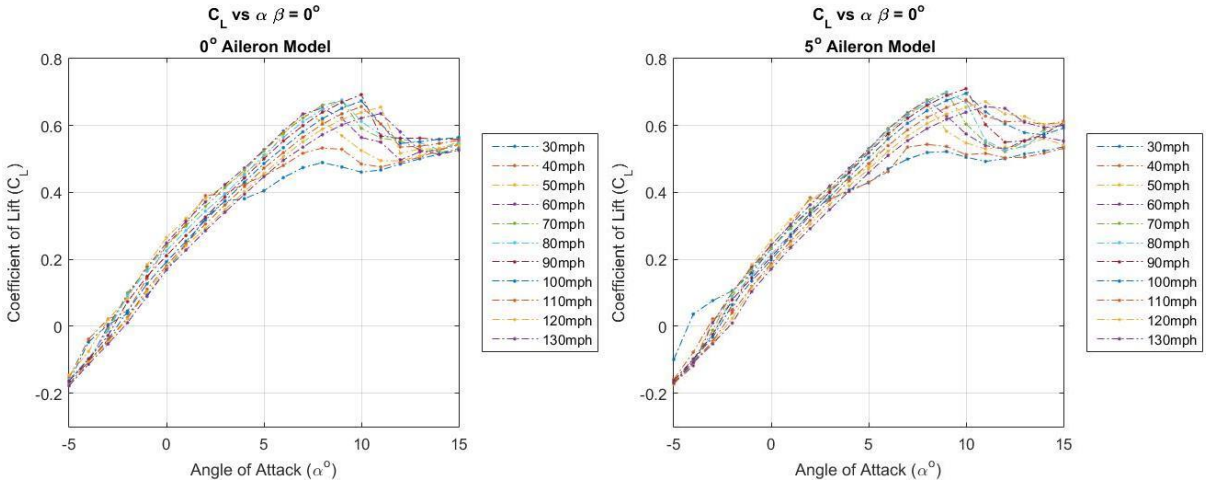

Figure 119. 0° and 5° aileron deflection coefficient of lift versus angle of attack varying speed from 30mph to 130mph.

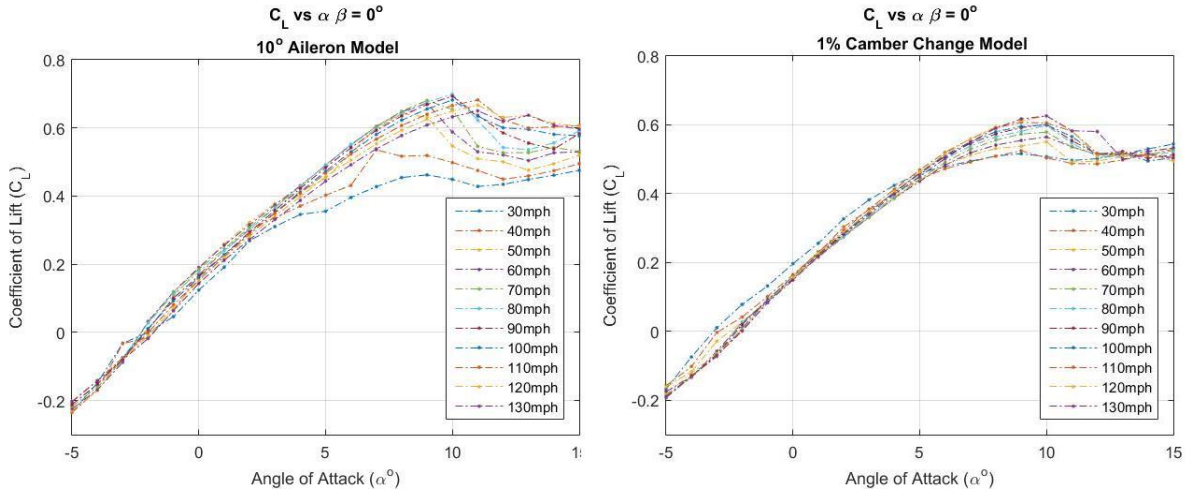

Figure 120. 10° aileron model and 1% camber change model coefficient of lift versus angle of attack varying speed from 30mph to 130mph.

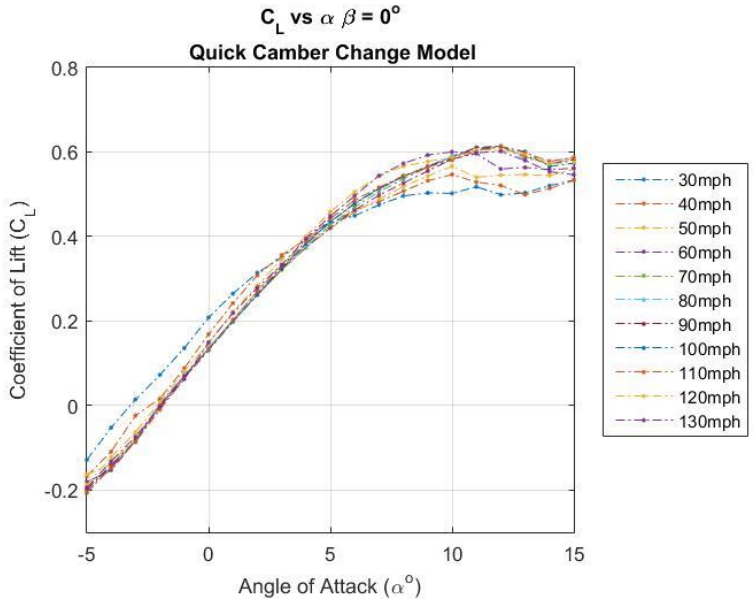

Figure 121. Quick camber change model coefficient of lift versus angle of attack varying speed from 30mph to 130mph.

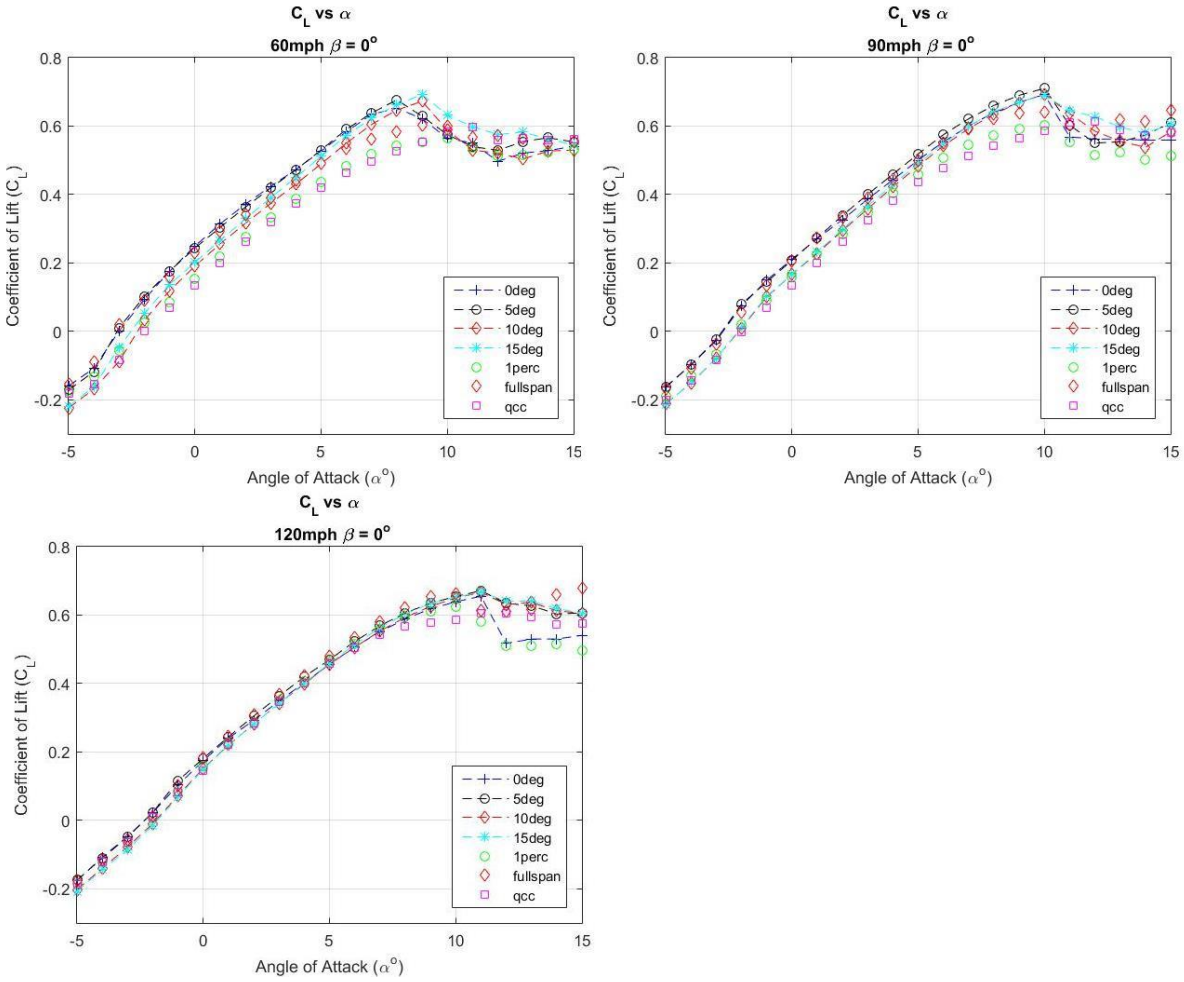

Figure 122. Comparison coefficient of lift versus angle of attack plots of all models at 60mph, 90mph, and 120mph

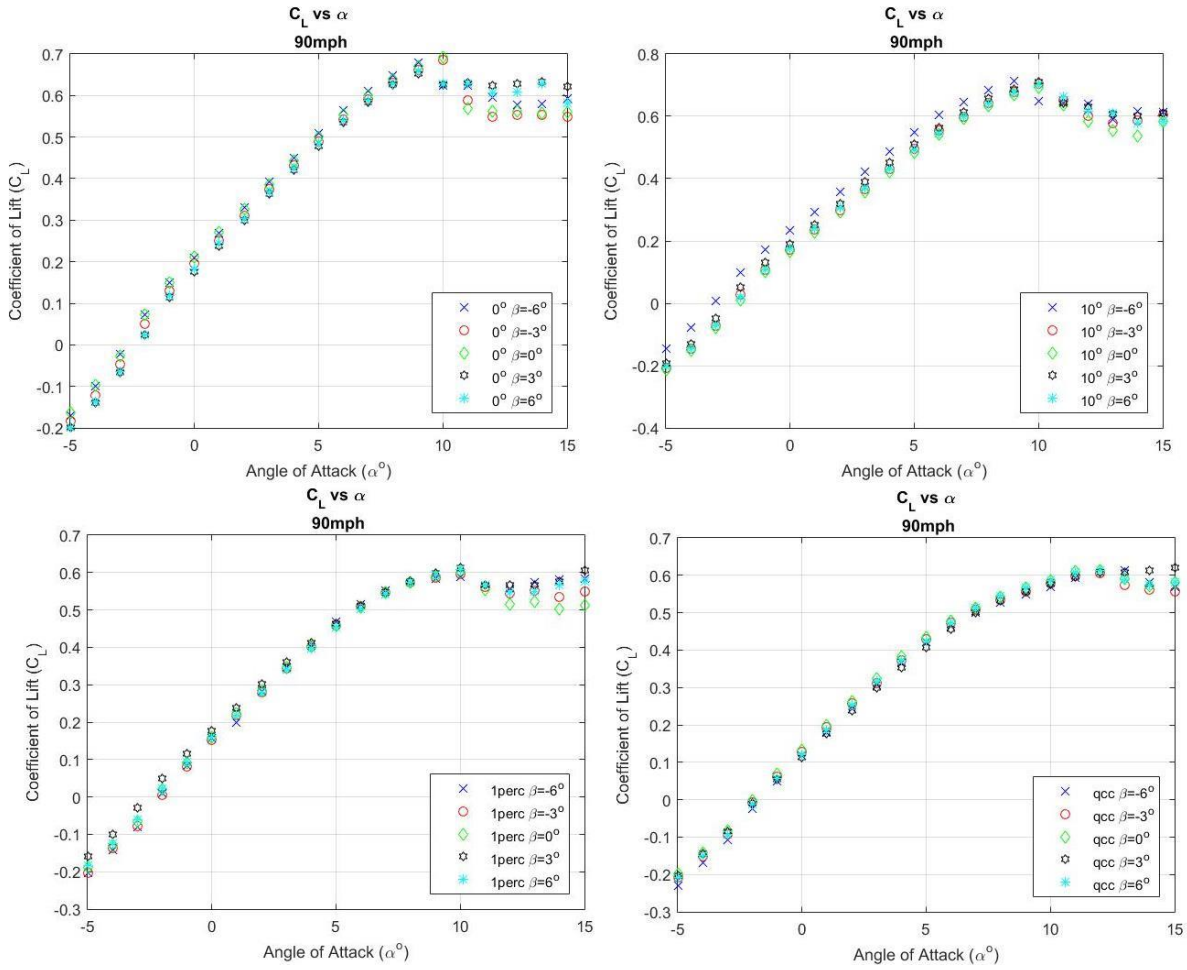

Figure 123. Additional coefficient of lift plots for each model varying sideslip angle at 90mph.

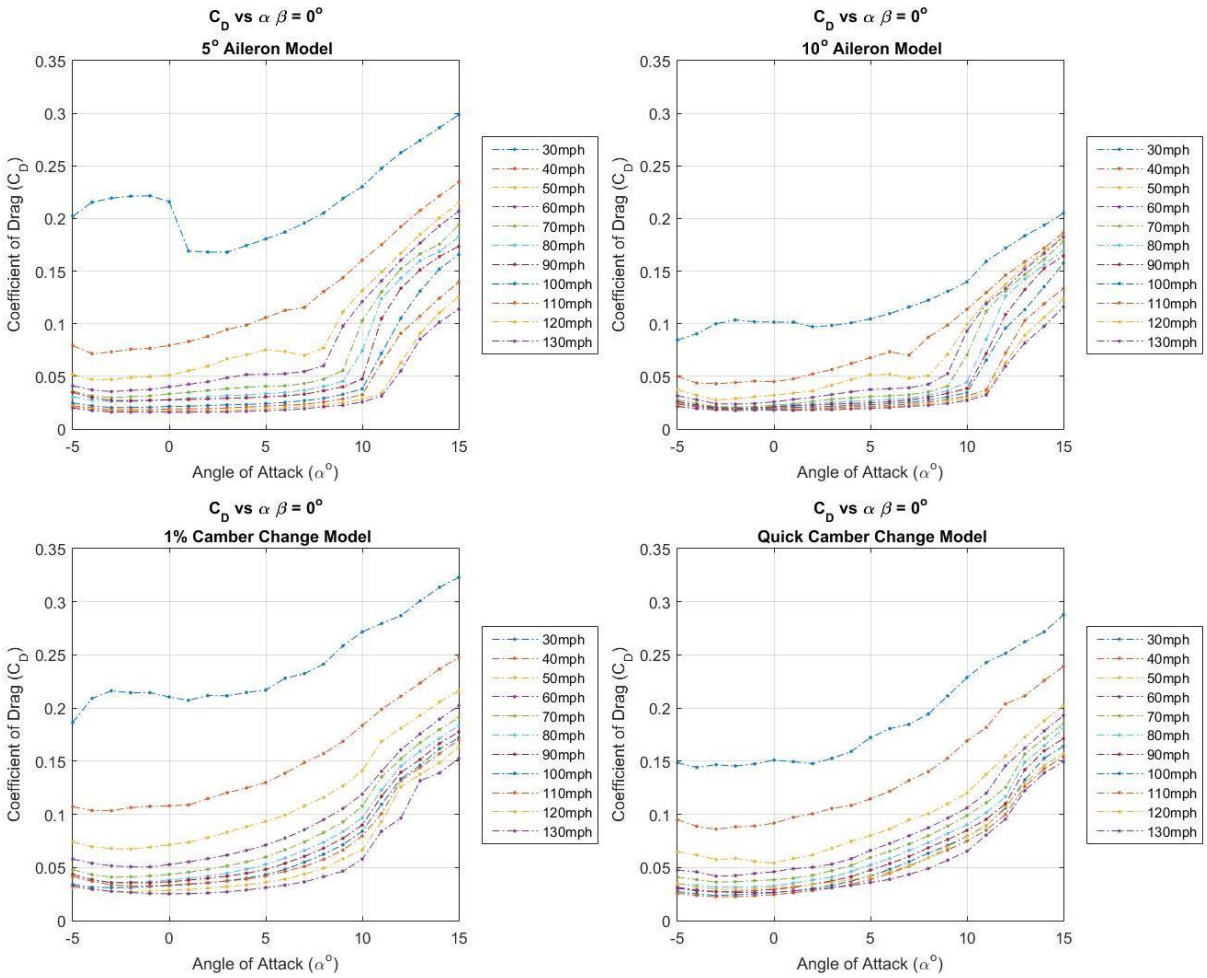

Figure 124. Additional coefficient of drag versus angle of attack plots varying speed from 30mph to 130mph.

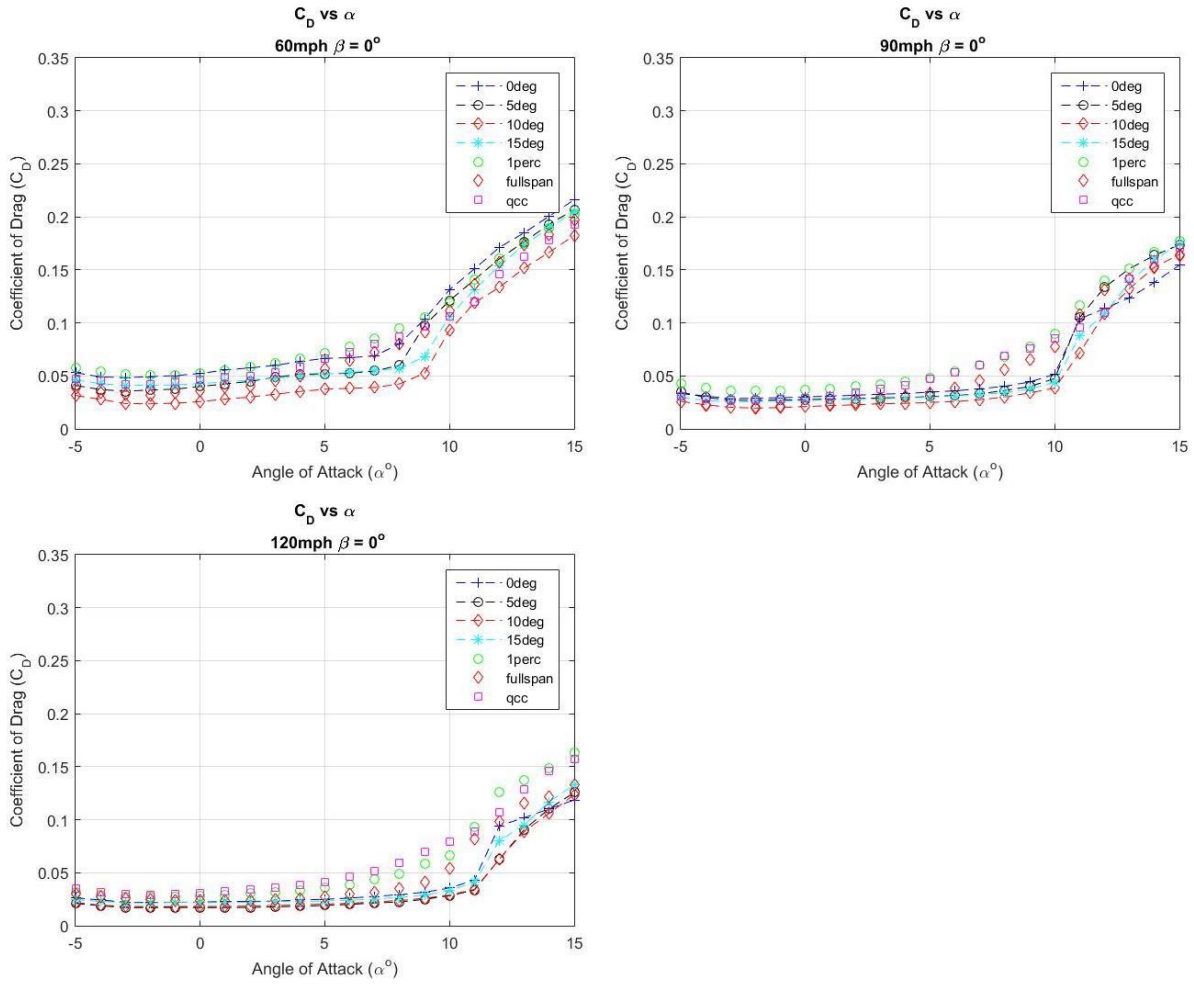

Figure 125. Coefficient of drag versus angle of attack comparing all models at 60mph, 90mph, and 120mph.

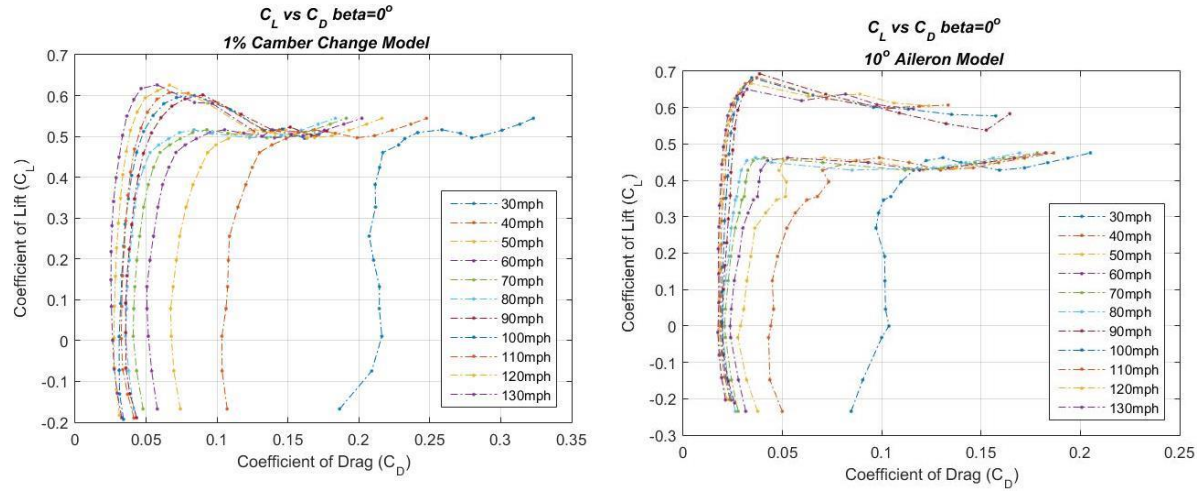

Figure 126. CL/CD plots of 1% camber deformed model and 10o aileron model showing changes in speed.

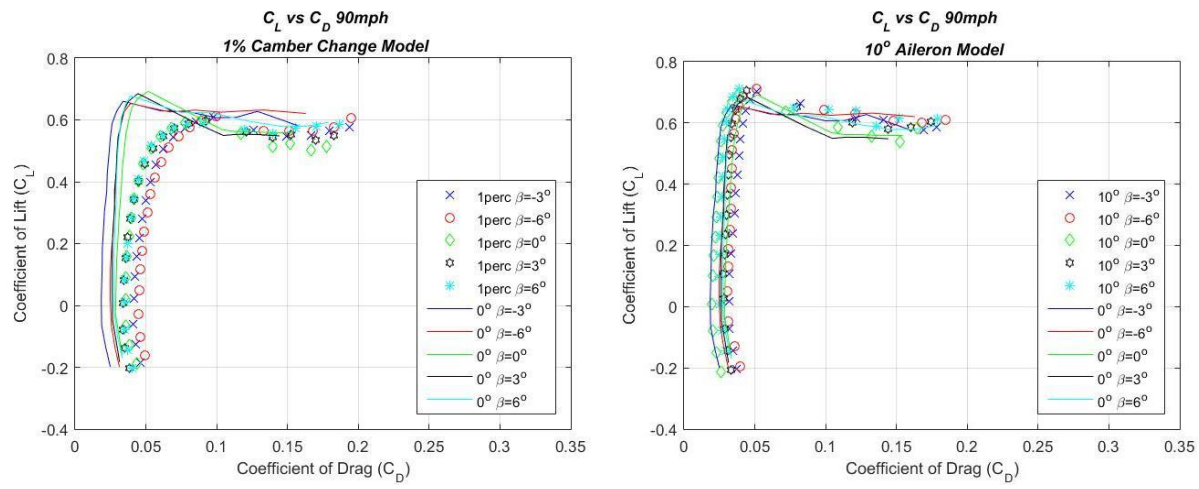

Figure 127. CL/CD plots varying sideslip angle for 1% camber change model and 10o aileron model compared to baseline model.

Appendix B: Extra Roll Plots

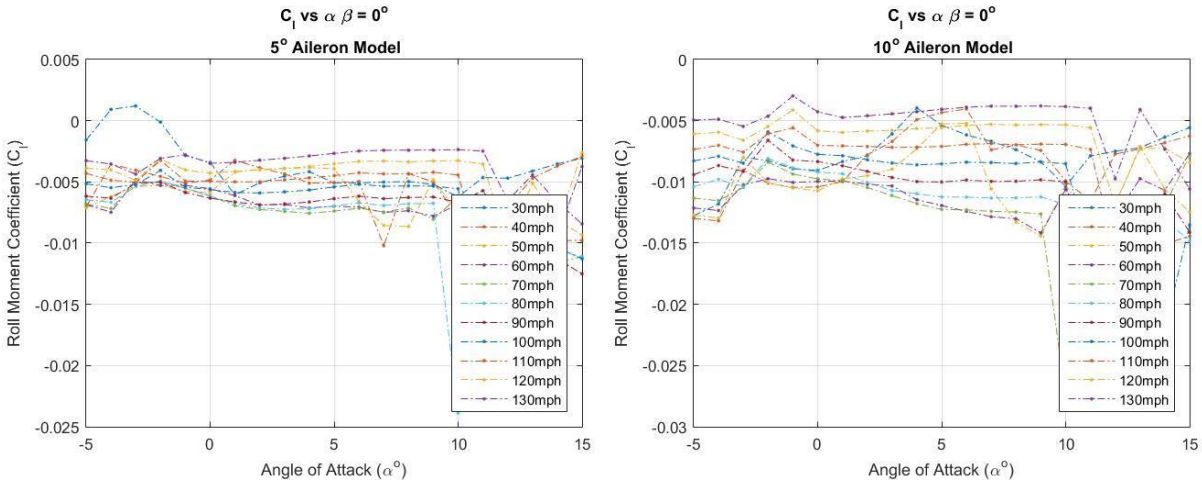

Figure 128. Roll moment coefficient versus angle of attack varying speed from 30mph to 130mph for 5° and 10° aileron models.

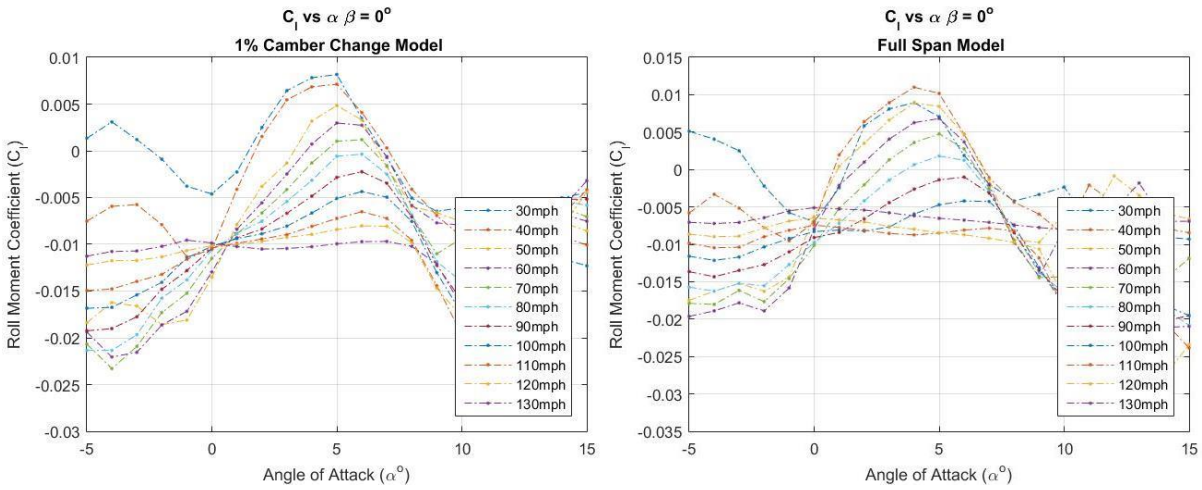

Figure 129. Roll moment coefficient versus angle of attack varying speed from 30mph to 130mph for 1% and full span camber change models.

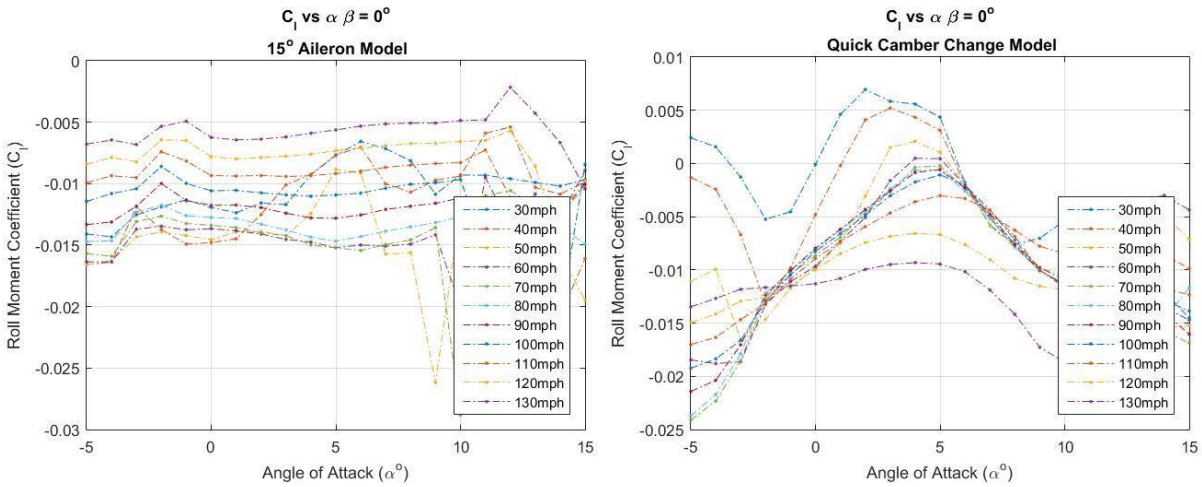

Figure 130. Roll moment coefficient versus angle of attack varying speed from 30mph to 130mph for 15° aileron and quick camber change models

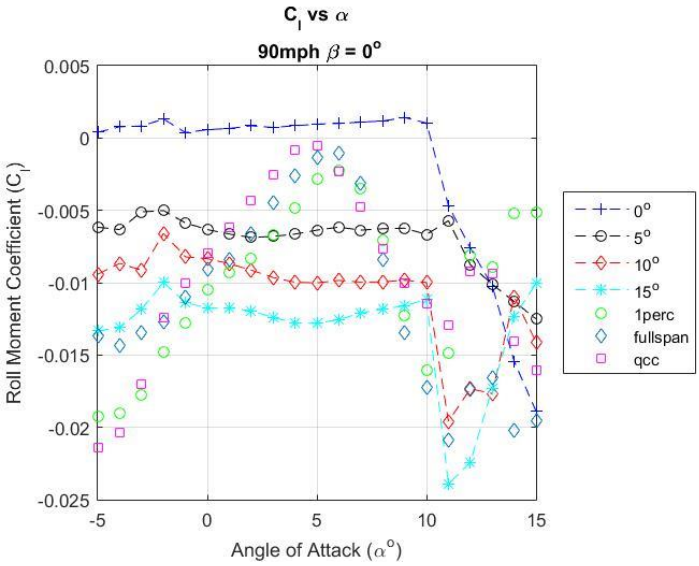

Figure 131. Comparison plot at 90mph of each model, Roll moment coefficient versus angle of attack.

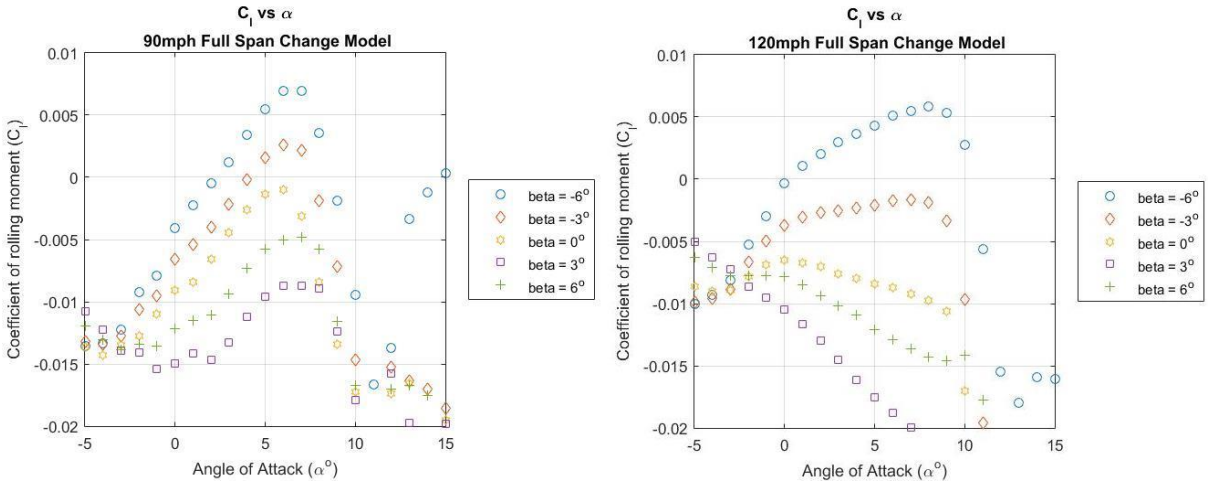

Figure 132. Full span camber change model at 90mph and 120mph varying sideslip angle showing roll moment change with angle of attack.

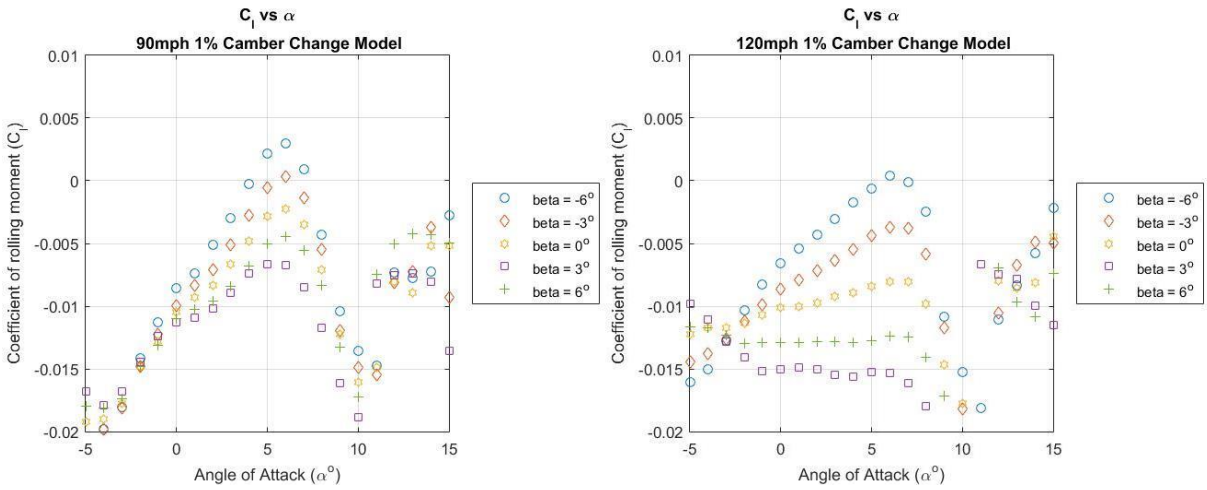

Figure 133. 1% camber change model at 90mph and 120mph varying sideslip angle showing roll moment change with angle of attack.

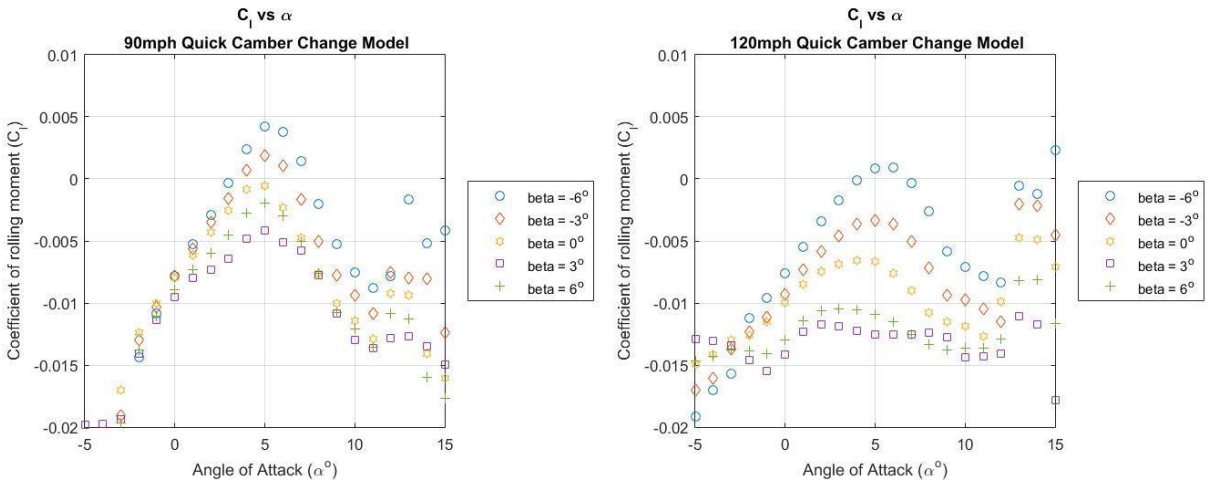

Figure 134. Quick camber change model at 90mph and 120mph varying sideslip angle showing roll moment change with angle of attack.

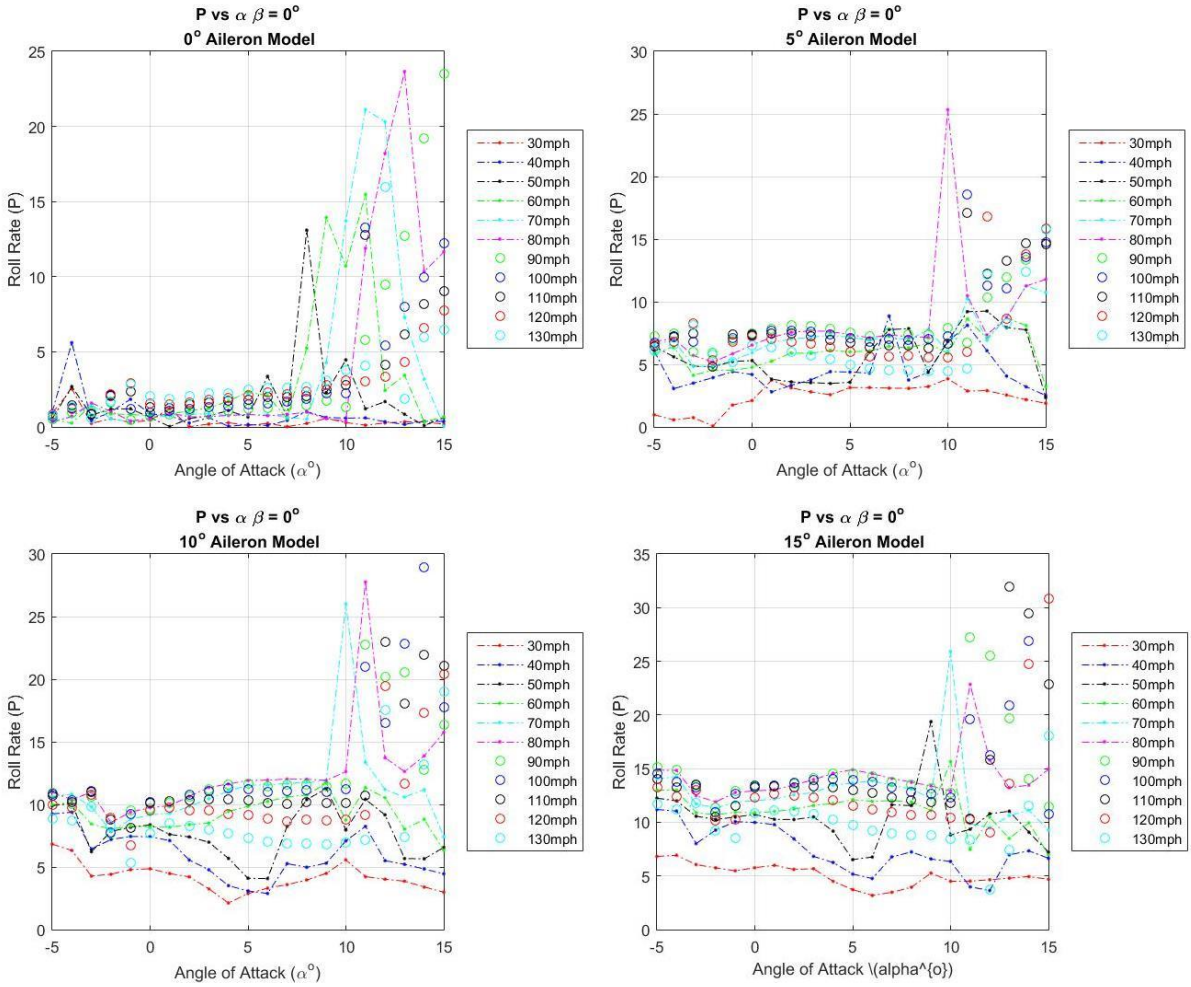

Figure 135. Roll rate versus angle of attack varying speed from 30mph to 130mph aileron models.

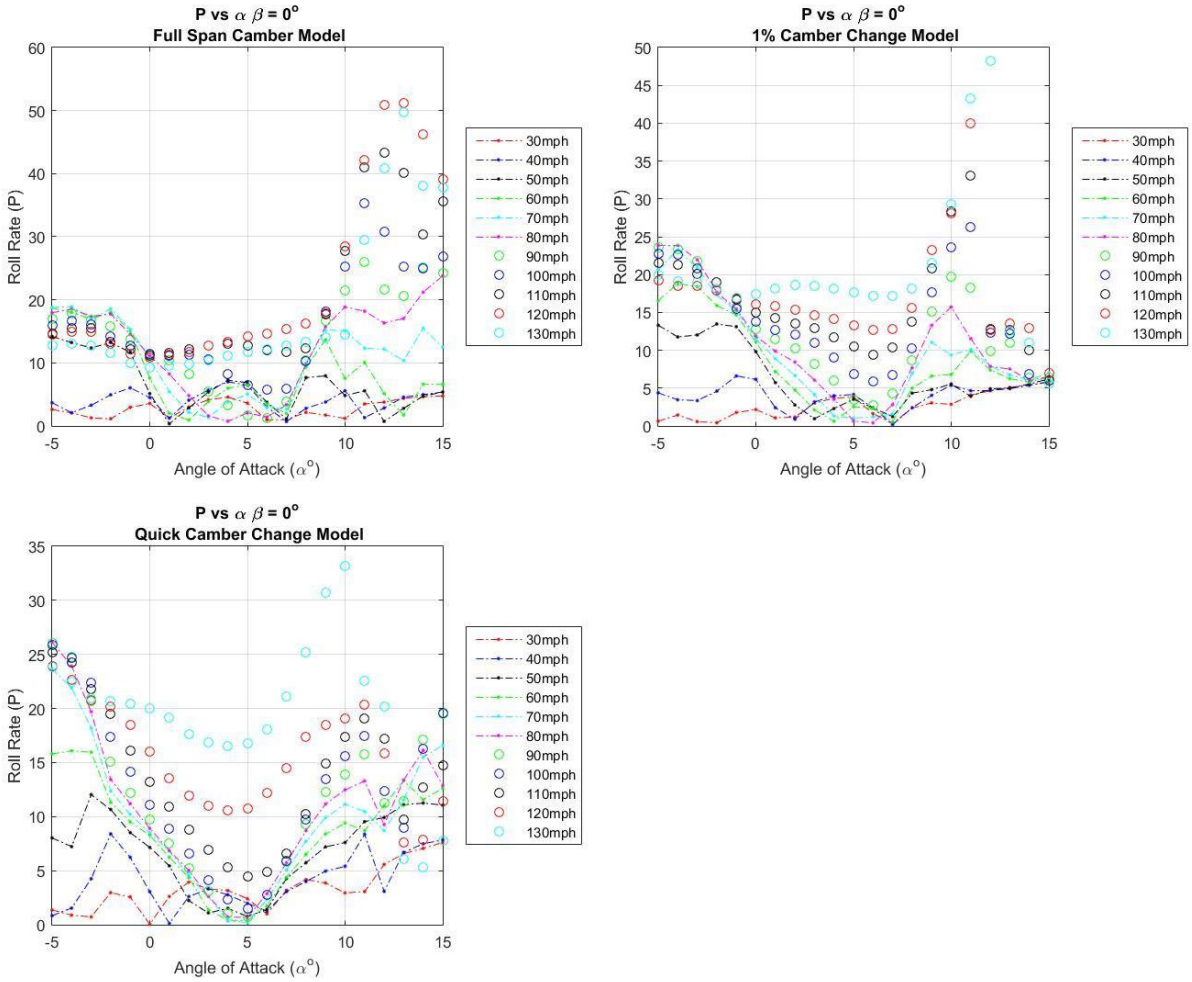

Figure 136. Roll rate versus angle of attack varying speed from 30mph to 130mph camber deformed models.

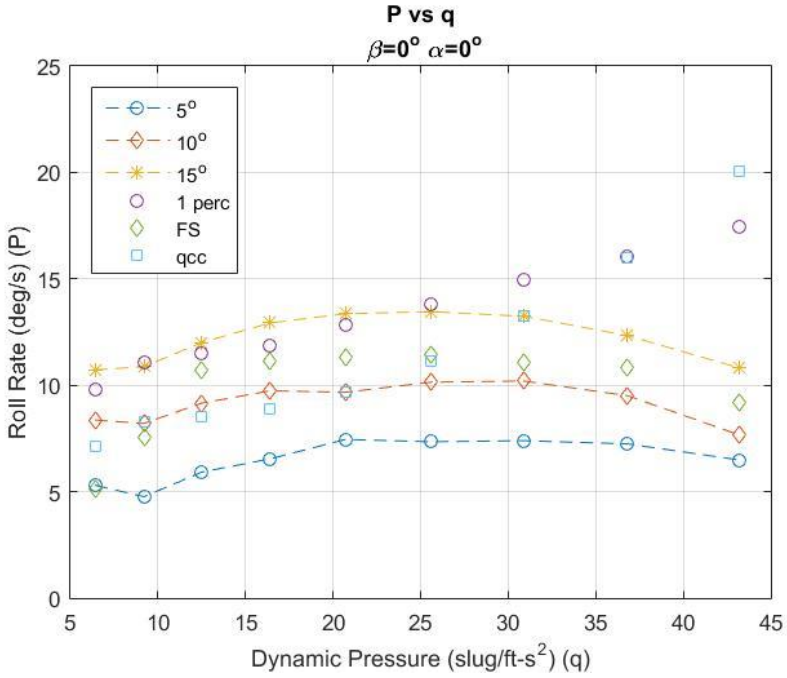

Figure 137. Roll rate versus dynamic pressure at 0^o angle of attack comparing all models.

Appendix C: Extra Stability Plots

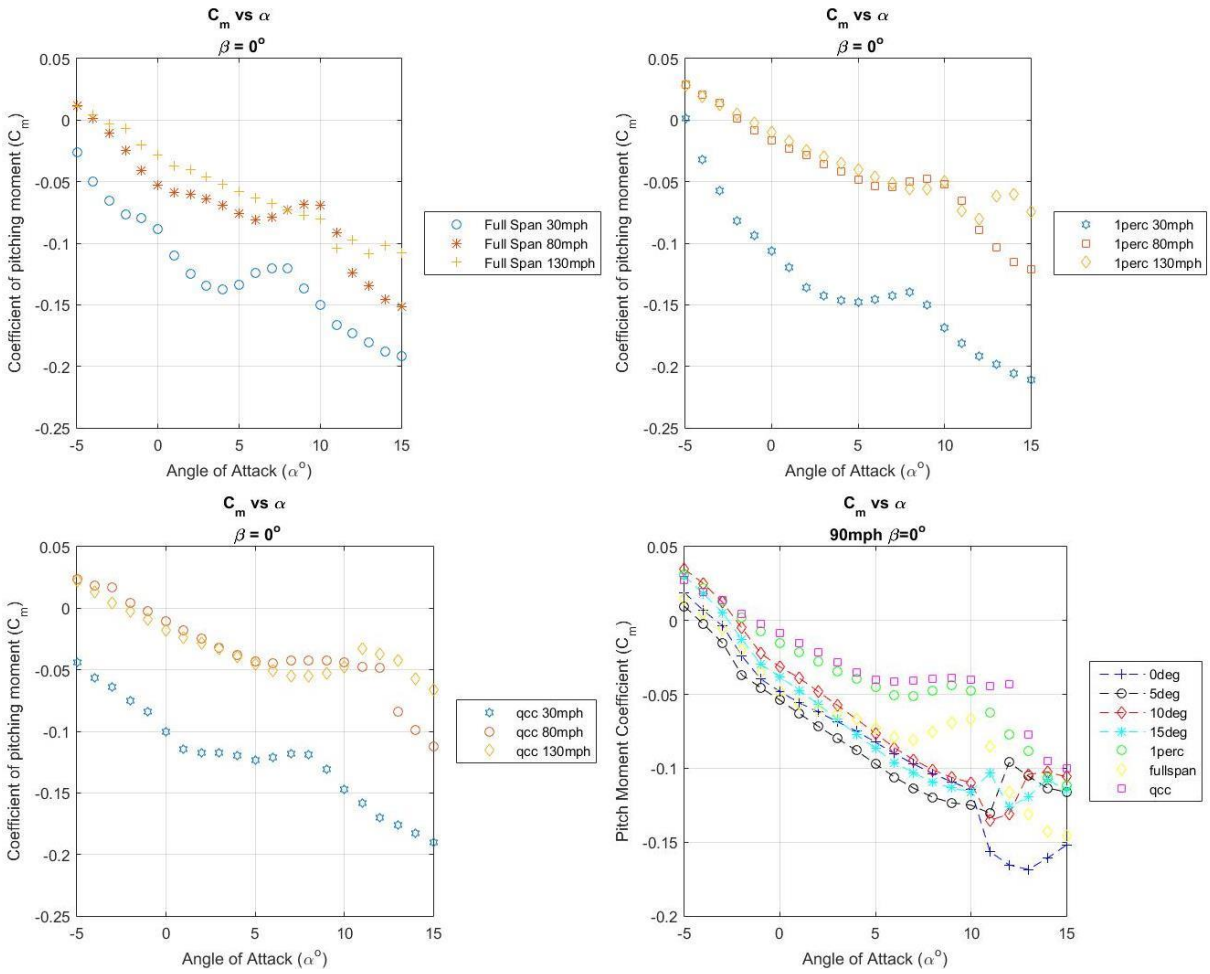

Figure 138. Pitch moment coefficient versus angle of attack varying speed.

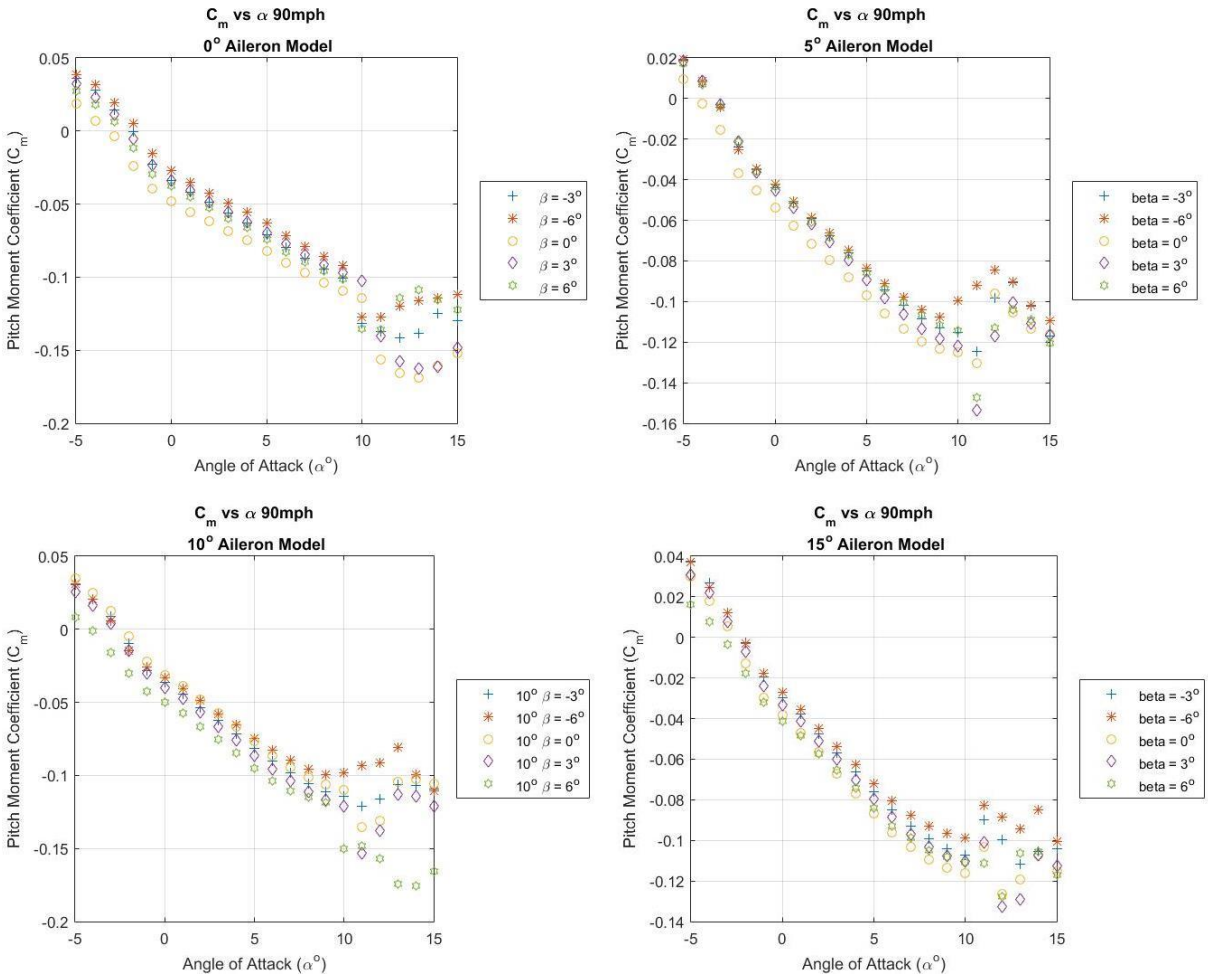

Figure 139. Pitch moment coefficient versus angle of attack varying sideslip angle aileron models.

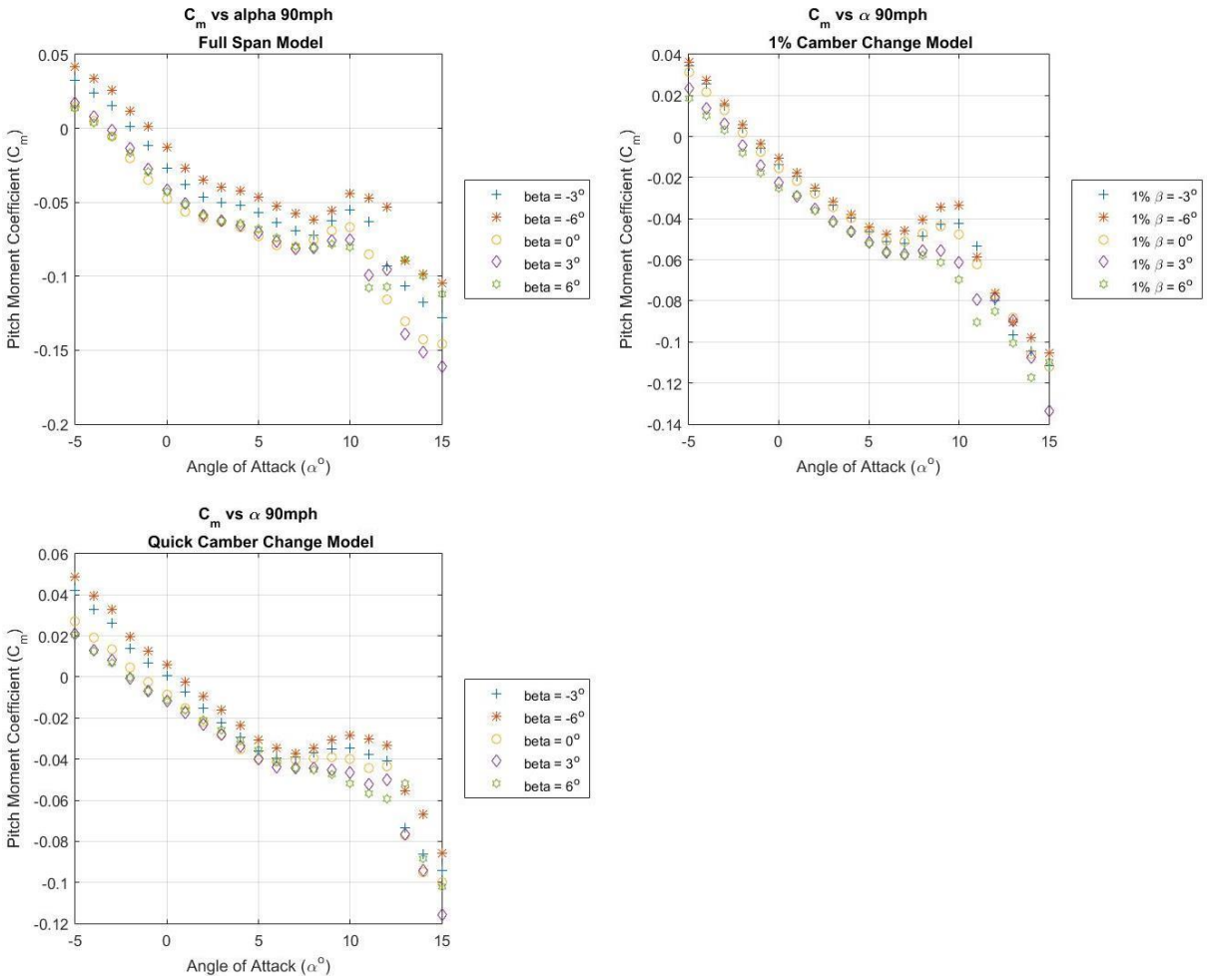

Figure 140. Pitch moment coefficient versus angle of attack varying sideslip angle camber deformed models.

Appendix D: Error Analysis

The error analysis performed was conducted for each of the six degrees of freedom calculated from the raw balance data and transformed from the balance to the wind reference frame. The six degrees of freedom analyzed were lift, drag, side force, pitch moment, roll moment, and yaw moment. Equations 53, through 58 are derived from the transformation from the balance forces and moments N, A, Y, l, m, n [38].

$$L = N\cos\theta - A\sin\theta \quad \textbf{(53)}$$

$$D = A\cos\theta\cos\psi + Y\sin\psi + N\sin\theta\cos\psi \quad \textbf{(54)}$$

$$Y = -A\sin\psi\cos\theta + Y\cos\psi - N\sin\theta\sin\psi \quad \textbf{(55)}$$

$$m = M_{cm} - (N\cos\theta - A\sin\theta)X_{cm} + (A\cos\theta\cos\psi + Y\sin\psi + N\sin\theta\cos\psi)Z_{cm} \quad \textbf{(56)}$$

$$l = l_{cm} + (-A\sin\psi\cos\theta + Y\cos\psi - N\sin\theta\sin\psi)Z_{cm} + (N\cos\theta - A\sin\theta)Y_{cm} \quad \textbf{(57)}$$

$$n = n_{cm} - (A\cos\theta\cos\psi + Y\sin\psi - N\sin\theta\cos\psi)Y_{cm} - (-A\sin\psi\cos\theta + Y\cos\psi - N\sin\theta\sin\psi)X_{cm} \quad \textbf{(58)}$$

Equations 59, through 64 are the general equations for the aerodynamic and stability coefficients used for analysis.

$$C_L = \frac{L}{qS} \quad \textbf{(59)}$$

$$C_D = \frac{D}{qS} \quad \textbf{(60)}$$

$$C_Y = \frac{Y}{qS} \quad \textbf{(61)}$$

$$C_M = \frac{m}{qSc} \quad \textbf{(62)}$$

$$C_l = \frac{l}{qSc} \quad \textbf{(63)}$$

$$C_n = \frac{n}{qSc} \quad \textbf{(64)}$$

The error for the six degrees of freedom are calculated for all variable used in each equation. Equation X demonstrates the general form of the equation for the error. The error equation is calculated by multiplying each partial derivative varied during experimentation for each coefficient by the error tolerances for each variable. This term is then squared, summed with all variables and the square root taken as seen below.

$$dC_L = \sqrt{(\partial C_L/\partial N\,\Delta N)^2 + (\partial C_L/\partial A\,\Delta A)^2 + (\partial C_L/\partial q\,\Delta q)^2 + (\partial C_L/\partial \theta\,\Delta\theta)^2} \quad \textbf{(65)}$$

The variables N, A, q, and θ were used for the coefficient of lift as the experiment altered the normal force, axial force, speed which affects the dynamic pressure, and angle of attack. Constants such as the planform area (S) and chord (c) are not altered during each experiment, therefore not built into the error. The tolerances for each variable are lifted in Table 27 below.

Table 27. Precision error tolerance for each variable.

Variable	Precision Error Tolerance
ΔN	0.02
ΔA	0.025
ΔY	0.015
Δm	0.005
Δn	0.002
Δl	0.002
Δx	0.008
Δy	0.008
Δz	0.008
Δθ	0.002
Δψ	0.002
Δq	0.001

Figure 141 and Figure 142 show the comparison of the error at 90mph for lift and drag as well as roll and pitch. The plots clearly show that the error in lift and drag are outside the balance error and the increase in drag is due to flow separation of the left wing and increased camber on the right wing. The decrease in lift at approximately 5^o angle of attack is attributed to wing stall onset by the negative camber lowering the stall angle of the outboard section of the wing. Due to the lifting body the loss in lift is not great enough to cause a dip in the CL versus angle of attack curve. The roll reversal and decrease in roll due to decreased efficiency of the increased camber wing is attributed to laminar separation bubbles and weak boundary layer attachment on the trailing edge of the increased camber wing causing the negative camber wing to increase lift at a larger rate than the right wing until wing stall at 5^o angle of attack.

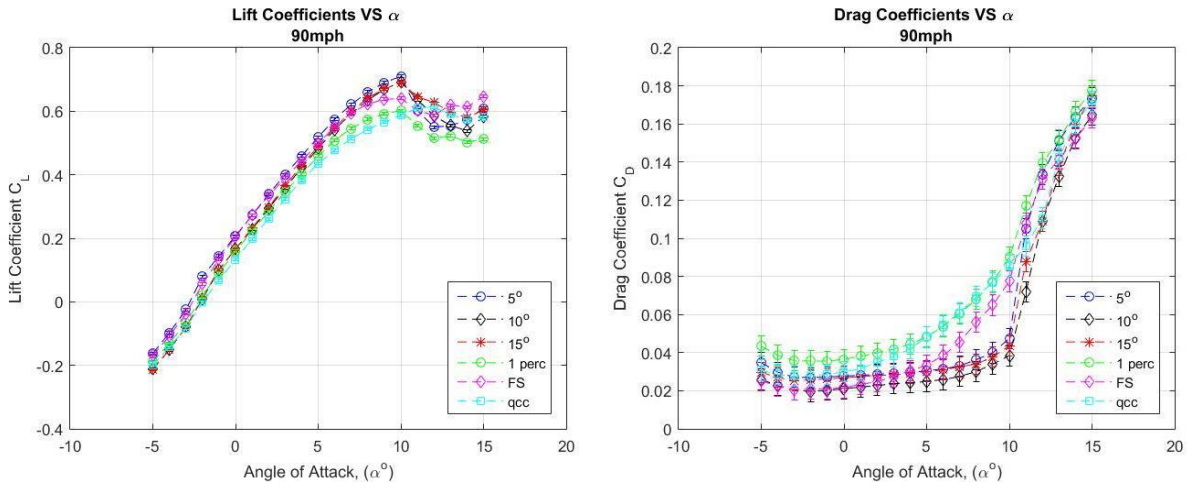

Figure 141. Lift and drag error plots comparing all models at 90mph.

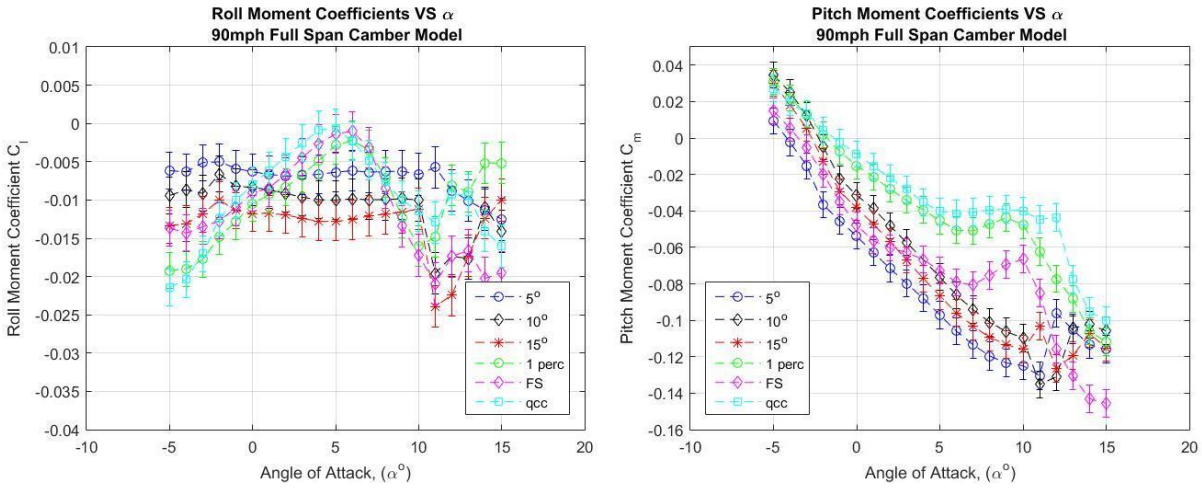

Figure 142. Roll and pitch moments versus angle of attack error comparing all models at 90mph.

Figure 143 below shows plots of the error for lift and drag on each of the models together at 120mph. The plots clearly show that the error at higher speeds is outside the error of the balance.

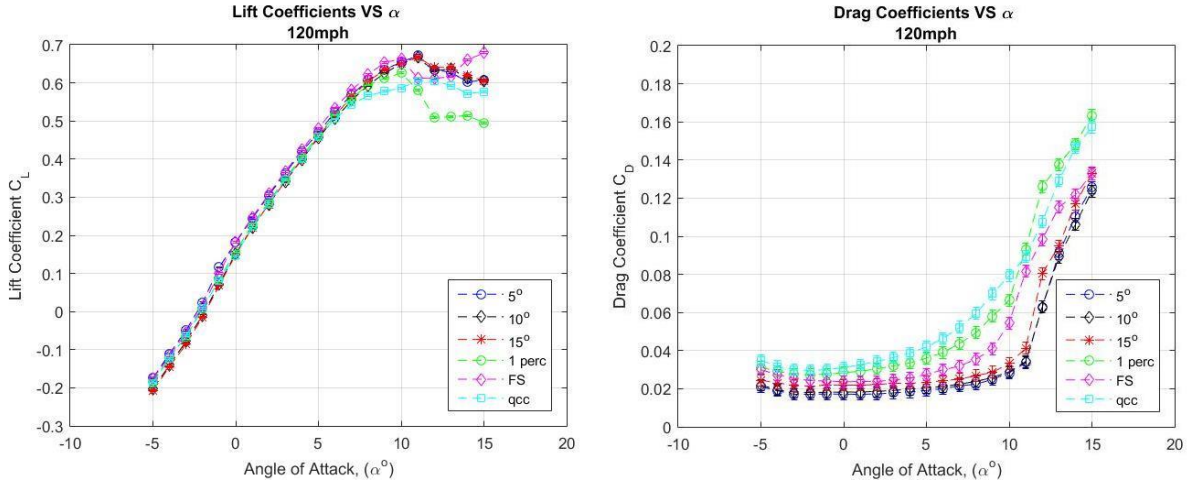

Figure 143. Lift and Drag error plots at 120mph.

Figure 144 below shows plots of the roll moment coefficient versus angle of attack, pitch moment coefficient versus angle of attack, yaw moment coefficient versus sideslip angle, and roll moment coefficient versus sideslip angle at 120mph. The plots show the yaw and roll stability plots produce large error as values approach zero. As the camber deformed models

increase spanwise camber deformation, the roll stability decreases approaching zero. The yaw stability for all models can be seen to be nearly equivalent producing a nearly neutral stability in yaw. The roll moment trends and pitch moment trends can be attributed to flow separation and laminar separation bubbles for the decrease in lift and due to the negative camber deformation, early wing stall.

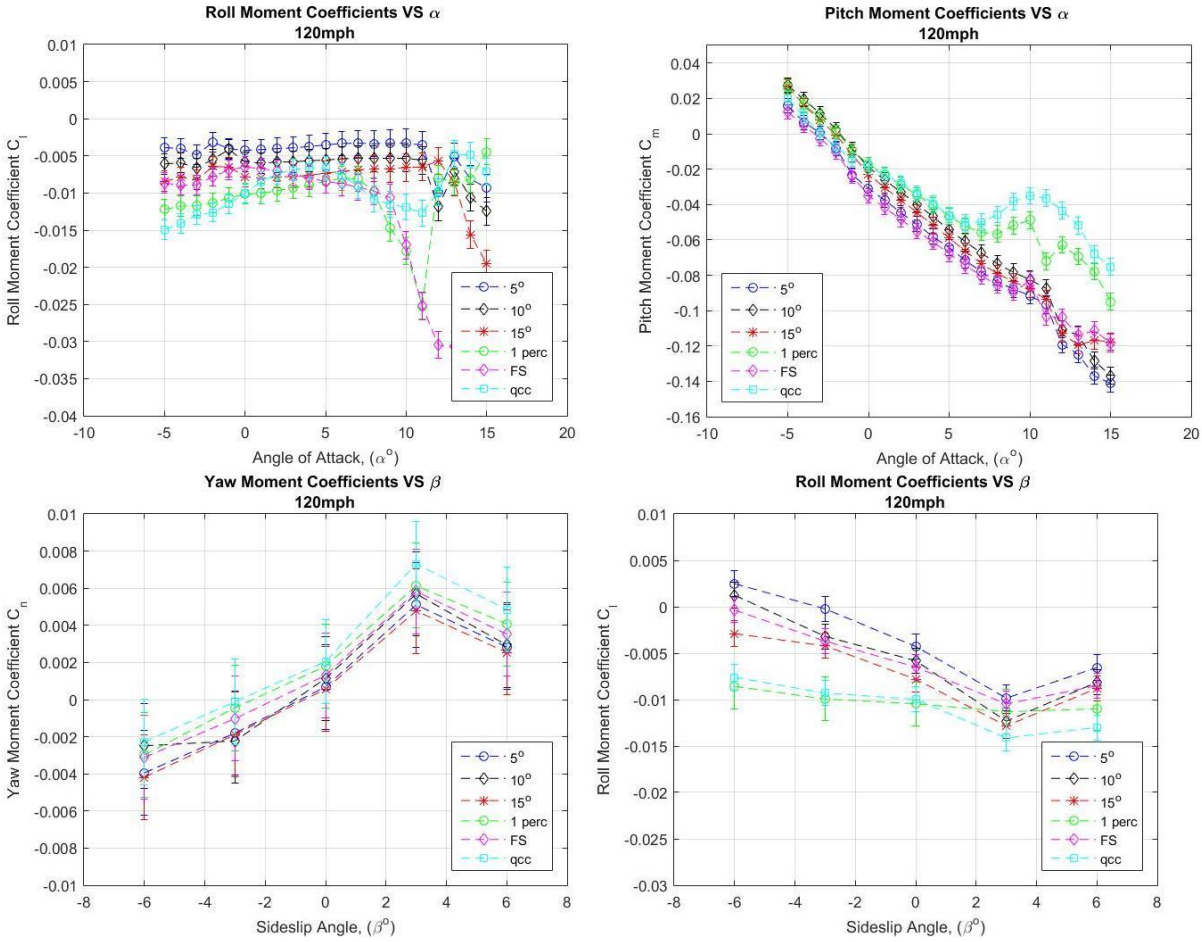

Figure 144. Roll and stability plots at 120mph comparing each of the models.

Plots from each of the sections in Chapter 4 are plotted below giving an example of the error bounds for lift, drag, pitch, roll, and yaw. The error can be seen to decrease as speed

increases due to the increase in forces and moments applied to the balance. The plots below show the 15o aileron model and 1% camber model. The error associated with lift, drag and pitching moment have the smallest error bars while the yaw moment versus sideslip angle has the largest variation in the error due to the small magnitude varying as much as 0.008. As magnitude approaches zero, the error produced by the balance increases and can be seen as noise inside the accuracy of the balance in a given degree of freedom direction.

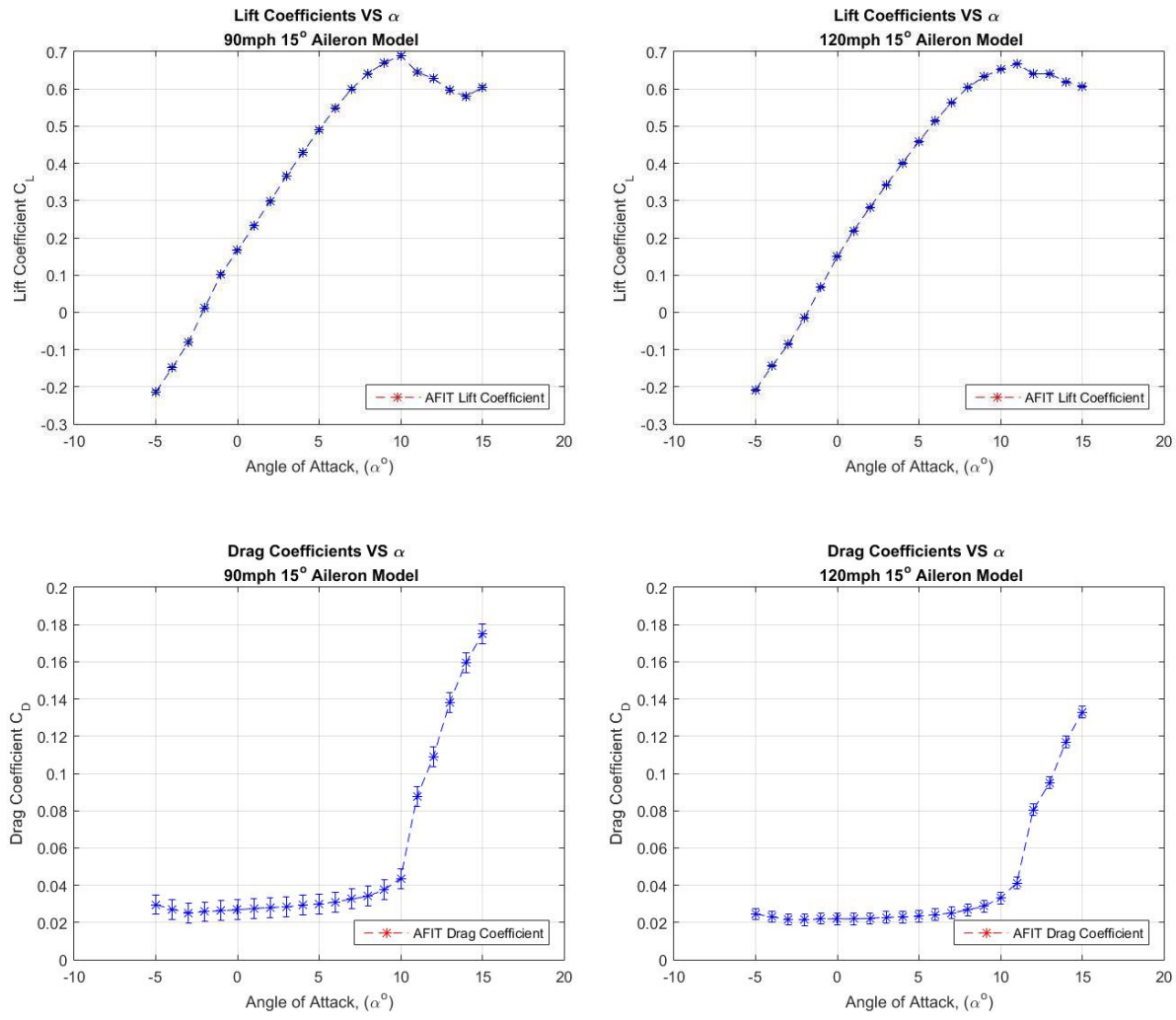

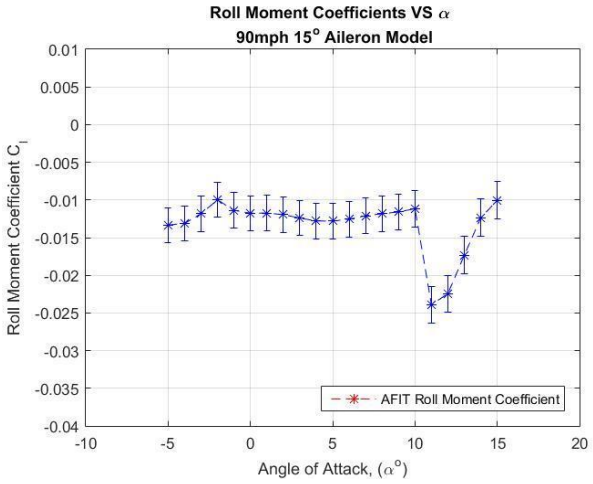
Roll Moment Coefficients VS α
90mph 15° Aileron Model
Roll Moment Coefficient C_l
Angle of Attack, (α^o)
AFIT Roll Moment Coefficient

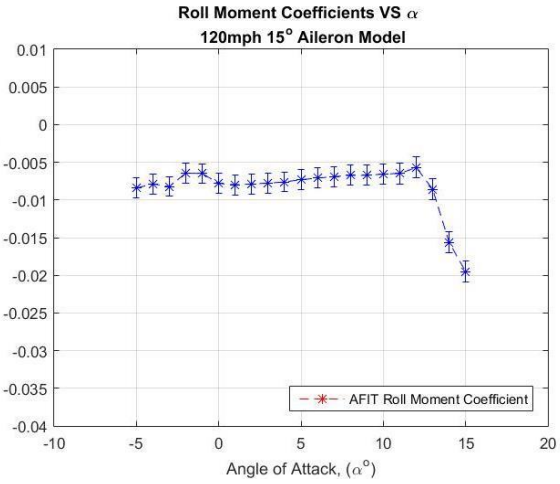
Roll Moment Coefficients VS α
120mph 15° Aileron Model
Angle of Attack, (α^o)
AFIT Roll Moment Coefficient

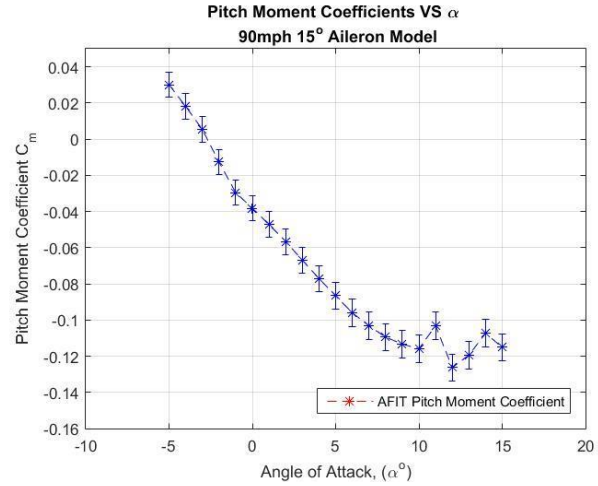
Pitch Moment Coefficients VS α
90mph 15° Aileron Model
Pitch Moment Coefficient C_m
Angle of Attack, (α^o)
AFIT Pitch Moment Coefficient

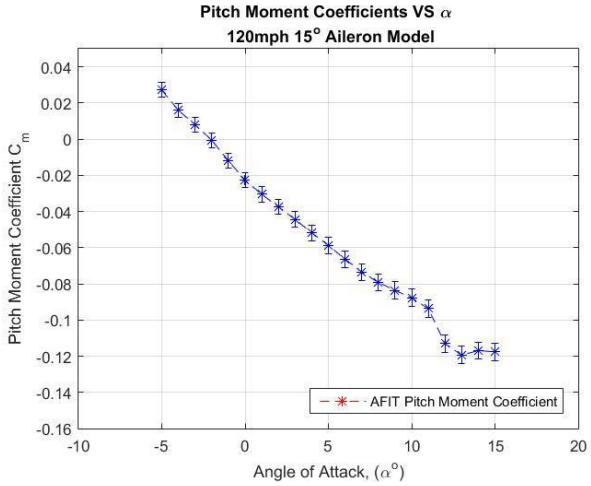
Pitch Moment Coefficients VS α
120mph 15° Aileron Model
Pitch Moment Coefficient C_m
Angle of Attack, (α^o)
AFIT Pitch Moment Coefficient

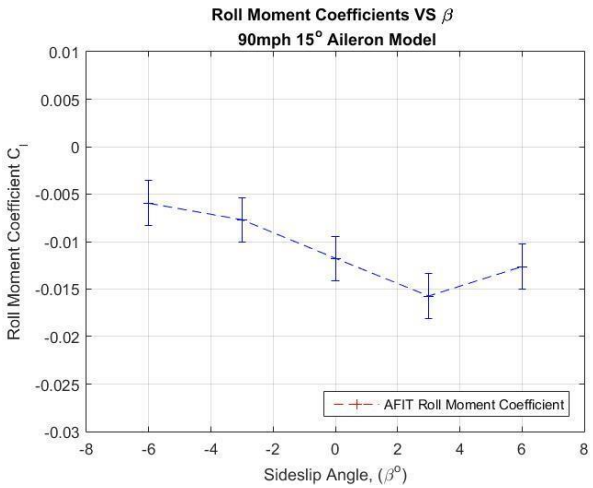
Roll Moment Coefficients VS β
90mph 15° Aileron Model
Roll Moment Coefficient C_l
Sideslip Angle, (β^o)
AFIT Roll Moment Coefficient

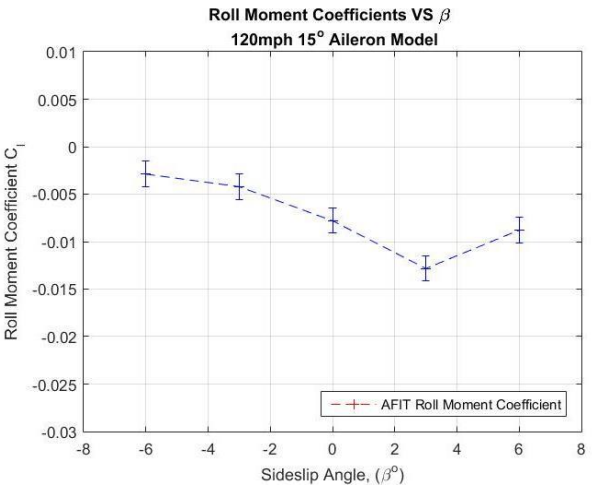
Roll Moment Coefficients VS β
120mph 15° Aileron Model
Roll Moment Coefficient C_l
Sideslip Angle, (β^o)
AFIT Roll Moment Coefficient

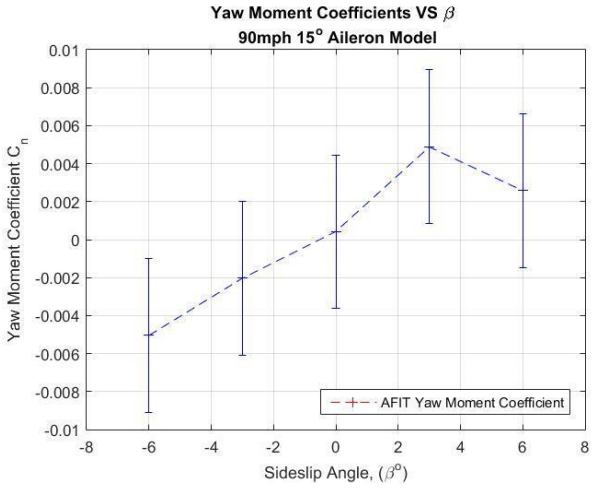
Yaw Moment Coefficients VS β
90mph 15° Aileron Model
Yaw Moment Coefficient C_n
Sideslip Angle, (β^o)
AFIT Yaw Moment Coefficient

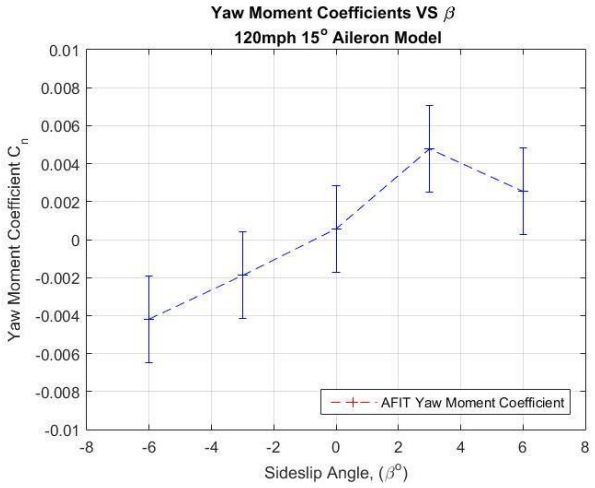
Yaw Moment Coefficients VS β
120mph 15° Aileron Model
Yaw Moment Coefficient C_n
Sideslip Angle, (β^o)
AFIT Yaw Moment Coefficient

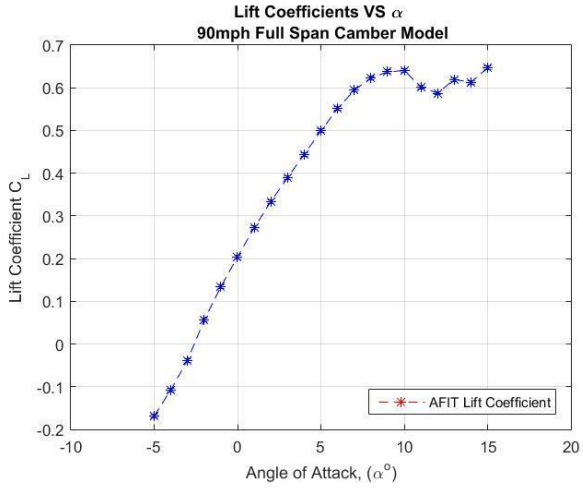
Lift Coefficients VS α
90mph Full Span Camber Model
Lift Coefficient C_L
Angle of Attack, (α^o)
AFIT Lift Coefficient

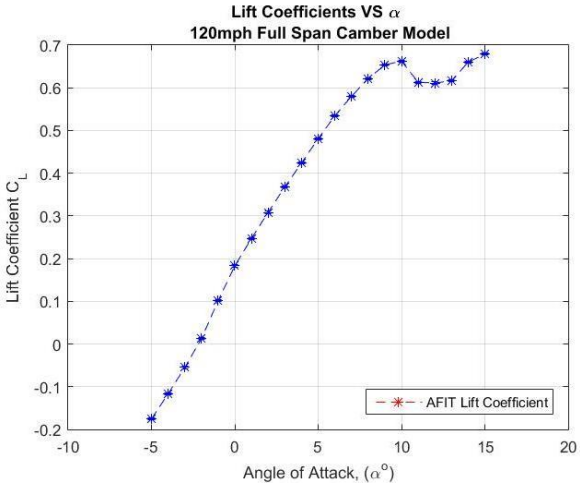
Lift Coefficients VS α
120mph Full Span Camber Model
Lift Coefficient C_L
Angle of Attack, (α^o)
AFIT Lift Coefficient

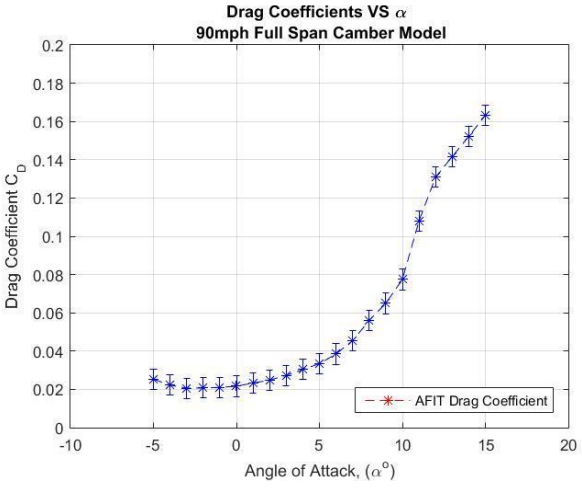
Drag Coefficients VS α
90mph Full Span Camber Model
Drag Coefficient C_D
Angle of Attack, (α^o)
AFIT Drag Coefficient

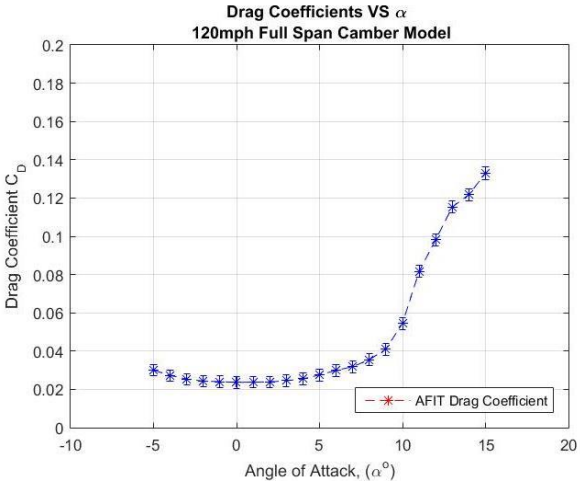
Drag Coefficients VS α
120mph Full Span Camber Model
Drag Coefficient C_D
Angle of Attack, (α^o)
AFIT Drag Coefficient

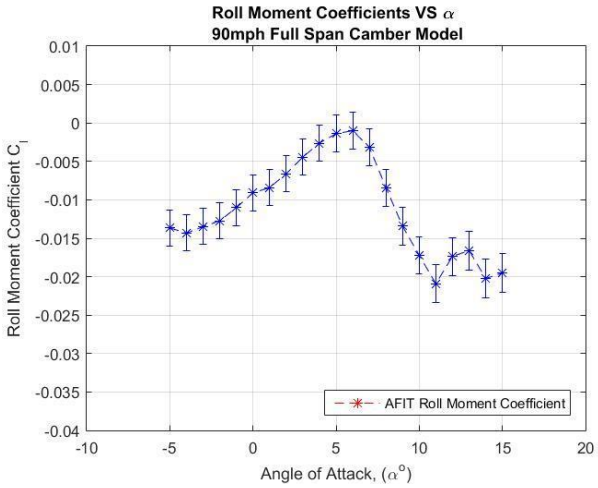
Roll Moment Coefficients VS α
90mph Full Span Camber Model
Roll Moment Coefficient C_l
Angle of Attack, (α^o)
AFIT Roll Moment Coefficient

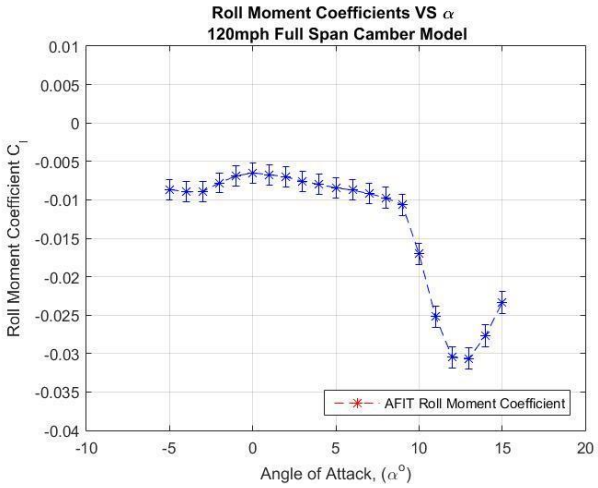
Roll Moment Coefficients VS α
120mph Full Span Camber Model
Roll Moment Coefficient C_l
Angle of Attack, (α^o)
AFIT Roll Moment Coefficient

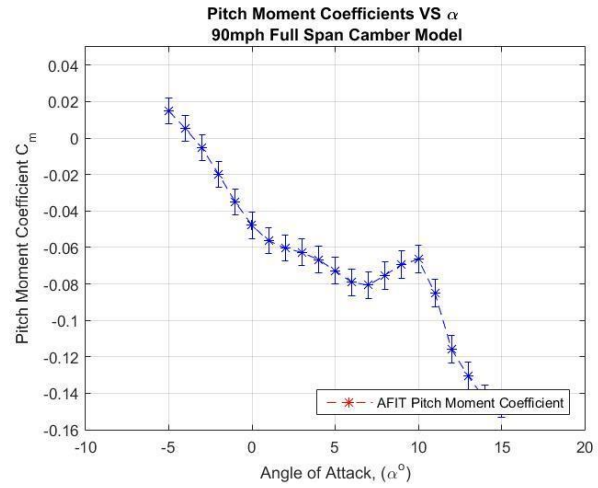
Pitch Moment Coefficients VS α
90mph Full Span Camber Model
Pitch Moment Coefficient C_m
Angle of Attack, (α^o)
AFIT Pitch Moment Coefficient

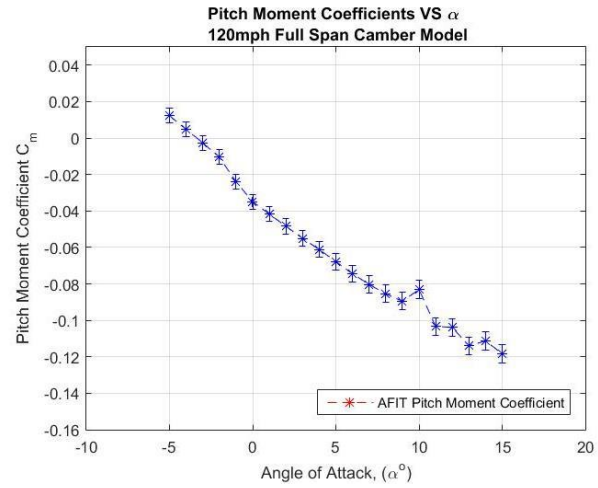
Pitch Moment Coefficients VS α
120mph Full Span Camber Model
Pitch Moment Coefficient C_m
Angle of Attack, (α^o)
AFIT Pitch Moment Coefficient

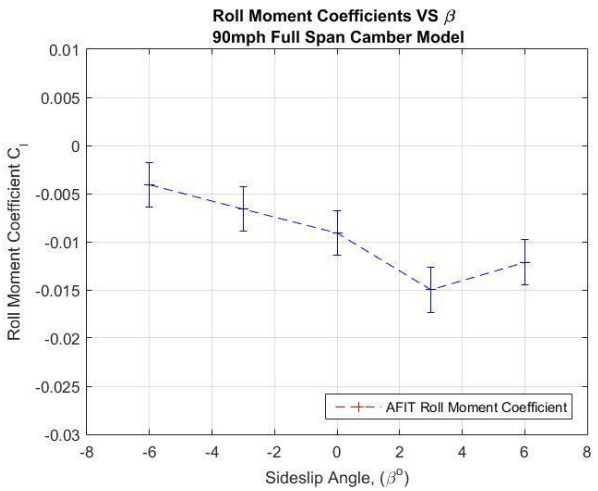
Roll Moment Coefficients VS β
90mph Full Span Camber Model
Roll Moment Coefficient C_l
Sideslip Angle, (β^o)
AFIT Roll Moment Coefficient

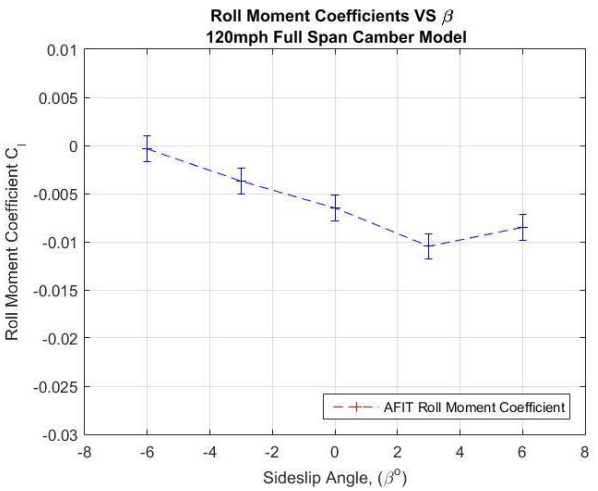
Roll Moment Coefficients VS β
120mph Full Span Camber Model
Roll Moment Coefficient C_l
Sideslip Angle, (β^o)
AFIT Roll Moment Coefficient

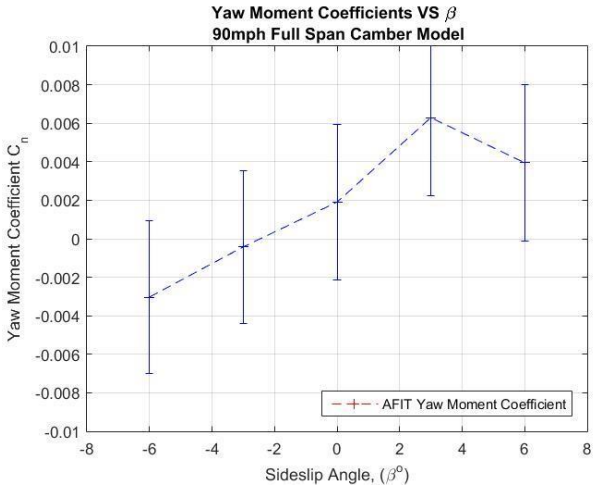
Yaw Moment Coefficients VS β
90mph Full Span Camber Model
Yaw Moment Coefficient C_n
Sideslip Angle, (β°)
AFIT Yaw Moment Coefficient

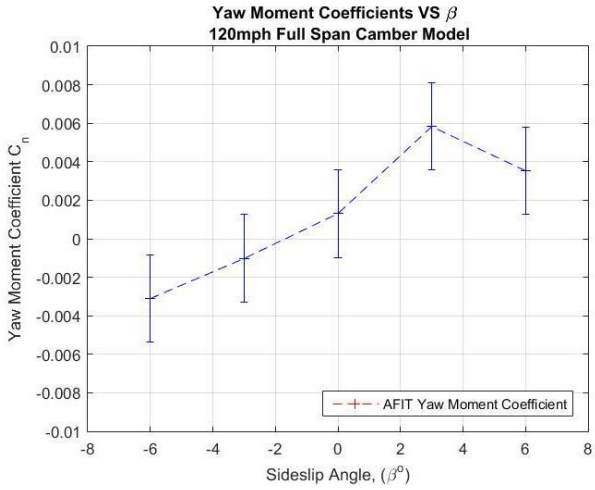
Yaw Moment Coefficients VS β
120mph Full Span Camber Model
Yaw Moment Coefficient C_n
Sideslip Angle, (β°)
AFIT Yaw Moment Coefficient

Bibliography

[1] Anderson, J. D., "Aerodynamics in the Age of Propeller-Driven Airplanes,"*A History of Aerodynamics and Its Impact on Flying Machines,* 1st ed., Cambridge, New York, 1997, pp. 364-365.

[2] Khot, N.S., Eastep, F.E., Kolonay, R.M., "Wing Twist and Camber for the Rolling Maneuver of a Flexible Wing Without Aileron," *AIAA-97-1268 Presented at 38th AIAA/ASME/ASCE/AHS/ Adaptive Structures Forum,* Kissimmee, Fl. April. 1997.

[3] Anderson, J. D., "Fundamentals of Aerodynamics," 4th ed., McGraw-Hill, New York, 2007.

[4] Wickenheiser, A. M., Garcia, E., "Aerodynamic Modeling of Morphing Wings Using an Extended Lifting-Line Analysis," *Journal of Aircraft,* Vol. 44, No. 1, January-February 2007, pp. 10-16.

[5] Powers, S. G., Webb, L. D., Friend, E. L., Lokos, W. A., "Flight Test Results From a Supercritical Mission Adaptive Wing with Smooth Variable Camber," Memorandum 4415, National Aeronautics and Space Administration Technical Memorandum, 1992.

[6] Sanders, B., Eastep, F.E., and Forster, E., "Aerodynamic and Aeroelastic Characteristics of Wings with Conformal Control Surfaces for Morphing Aircraft," *Journal of Aircraft,* Vol. 40, No. 1, January-February 2003, pp. 94-99.

[7] Gano, S.E., and Renaud, J.E., "Optimized Unmanned Aerial Vehicle with Wing Morphing for Extended Range and Endurance," *Ninth Symposium on Multidisciplinary Analysis and Optimization,* AIAA/ISSMO, Atlanta, GA, 2002.

[8] Previtali, F., Arrieta, A. F., Ermanni, P., "Performance of a Three-Dimensional Morphing Wing and Comparison with a Conventional Wing," *AIAA Journal,* Vol. 52, No. 10, 2014, pp. 2101-2113.

[9] Parker, H.F., "The Parker Variable Camber Wing," National Advisory Committee for Aeronautics, Report No. 77, 1920.

[10] Kota, S., Osborn, R., Ervin, G., Maric, D., Flick, P., Paul, D., "Mission Adaptive Compliant Wing – Design, Fabrication and Flight Test," *RTO Applied Vehicle Technology Panel (AVT) Symposium, RTO MP-AVT-168,* Evora, Portugal, 20-24 April 2009.

[11] Gilbert, W.W., "Mission Adaptive Wing System for Tactical Aircraft," *Journal of Aircraft,* Vol. 18, No. 7, July 1981, pp. 597-602.

[12] Kudva, J.N., Appa, K., Martin, C.A., Jardine, A.P., Sendeckyj, G., Harris, T., McGowan, A., Lake, R., "Design, Fabrication, and Testing of the DARPA / Wright Lab "Smart Wing" Wind Tunnel Model," AIAA.

[13] Kudva, J. N., Martin, C. A., Scherer, L. B., Jardine, A. P., McGowan, A. R., Lake, R. C., Sendeckyj, G., Sanders, B., "Overview of the DARPA/AFRL/NASA Smart Wing Program," *SPIE Conference on Industrial and Commercial Applications of Smart Structures Technologies*, Newport Beach, California, March 1999.

[14] Hetrick, J. A., Osborn, R. F., Kota, S., Flick, P. M., Paul, D. B., "Flight Testing of Mission Adaptive Compliant Wing," *48th AIAA/ASME/ASCE/AHS/ASC Structures, Structural Dynamics, and Materials Conference*, Honolulu, Hawaii, 2007.

[15] Tsang, K., "Long-Sought Seamless Wing Technology Introduced at AIAA SciTech 2014 Show | flexsys",http://www.flxsys.com/blog/2014/12/19/flexfoil-variable-geometry-control-surface-youtube-video-january-2014-flexsys-update-long-sought-seamless-wing-technology-introduced-at-aiaa-scitech-2014-show [retrieved 20 January 2016].

[16] Bowman, J., Sanders, B., Cannon, B., Kudva, J., Joshi, S., Weisshaar, T., "Development of Next Generation Morphing Aircraft Structures," *48th AIAA/ASME/ASCE/AHS/ASC Structures, Structural Dynamics, and Materials Conference*, Honolulu, Hawaii, 2007.

[17] Flanganl, J. S., Strutzenberg, R. C., Myers, R. B., Rodrian, J. E., "Development and Flight Testing of a Morphing Aircraft, the NextGen MFX-1," *48th AIAA/ASME/ASCE/AHS/ASC Structures, Structural Dynamics, and Materials Conference*, Honolulu, Hawaii, 2007.

[18] Marks, C. R., Zientarski, L., Culler, A., Hagen B., Smyers, B., Joo, J. J., "Variable Camber Compliant Wing – Wind Tunnel Testing," *23rd AIAA/ASME/AHS Adaptive Structures Conference*, AIAA Scietech 2015, Kissimmee, FL, 5-9 January 2015.

[19] Joo, J. J., Marks, C. R., Zientarski, L., Culler, A., "Variable Camber Compliant Wing – Design," *23rd AIAA/ASME/AHS Adaptive Structures Conference*, AIAA Scietech 2015, Kissimmee, FL, 5-9 January 2015.

[20] Perkins, C. D., Hage, R. E., "Airplane Performance Stability and Control," 11th ed., Wiley, New York, 1967.

[21] Etkin, B., "Dynamics of Flight Stability and Control," 2nd ed., Wiley, New York, 1982.

[22] Yechout, T. R., Morris, S. L., Bossert, D. E., Hallgren, W. F., "Introduction to Aircraft Flight Mechanics Performance, Static Stability, Dynamic Stability, and Classical Feedback Control," 1st ed., AIAA, Virginia, 2003.

[23] Hodges, D. H., Pierce, G. A., "Introduction to Structural Dynamics and Aeroelasticity," 2nd ed., Cambridge, New York, 2011.

[24] Martindale, T., Law, C., and Pedro, J., "A Vortex Lattice Aerodynamic Model for Active Camber Controlled Wings," *Seventh South African Conference on Computational and Applied Mechanics*, Pretoria, South Africa, 2010

[25] Previtali, F., and Ermanni, P., "Performance of a Non-Tapered 3D Morphing Wing with Integrated Compliant Ribs," Smart Matierals and Structures Paper 0964-1726, Apr. 2012.

[26] Lockheed Martin Skunkworks, "X-56A | Lockheed Martin," http://www.lockheedmartin.com/us/products/x-56.html [retrieved 13 December 2015].

[27] Reed, J., "Meet the Air Force's Newest X-Plane | defensetech," http://www.defensetech.org/2012/02/02/meet-the-air-forces-newest-x-plane/ [retrieved 17 September 2015].

[28] CompositesWorld, "Lockheed Martin/NASA UAS to test advanced wing design | CompositesWorld," http://www.compositesworld.com/news/lockheed-martinnasa-uas-to-test-advanced-wing-design [retrieved 29 January 2016].

[29] Military Factory, "The Lockheed X-56A unmanned experimental air vehicle is being used to further research active flutter control | MilitaryFactory," http://www.militaryfactory.com/aircraft/detail.asp?aircraft_id=1115 [retrieved 14 October 2015].

[30] Suh, P. M., Chin, A. W., Marvis, D. N., "Virtual Deformation Control of the X-56A Model with Simulated Fiber Optic Sensors," National Aeronautics and Space Administration Technical Memorandum, 2014.

[31] Simons, M., "Model Aircraft Aerodynamics," 2nd ed., Argus, England, 1983.

[32] Anderson, J. D., "Introduction to Flight," 5th ed., McGraw-Hill, New York, 2005.

[33] Mueller, T. J., "Aerodynamic Measurements at Low Reynolds Numbers for Fixed Wing Micro-Air-Vehicles," *RTO AVT course on,* "*Development and Operation of UAV's for Military and Civil Applications*", VKI Belgium, 13-17 September 2009.

[34] Melin, T. "A Vortex Lattice MATLAB Implementation for Linear Aerodynamic Wing Applications," Master Thesis, Dept. of Aeronautics, Royal Institute of Technology (KTH), Stockholm, Sweden, 2003.

[35] Kuethe, A. M., Chow, C., "Foundations of Aerodynamics, Bases of Aerodynamic Design," 4th ed., Wiley, New York, 1986.

[36] Melin, T., "User's Guide and Reference Manual for Tornado," User's Manual, Dept. of Aeronautics, Royal Institute of Technology (KTH), Stockholm, Sweden, 2000-2012.

[37] DeLuca, A. M., "Experimental Investigation Into the Aerodynamic Performance of Both Rigid and Flexible Wing Structured Micro-Air-Vehicles," Master Thesis, Dept. of Aeronautics and Astronautics, Air Force Institute of Technology, Wright-Patterson AFB OH, 2004.

[38] Barlow, J. B., Rae, W. H., Pope, A., "Low-Speed Wind Tunnel testing," 3rd ed., New York, NY, 1999.

[39] Nelson, R. C., "Flight Stability and Automatic Control," 2nd ed., McGraw-Hill, New York, 1998.

[40] Hays, A. P., "Oswald Span Efficiency Method | Aircraft Design and Consulting (ADAC)," http://www.adac.aero/linked/12.6_drag_due_to_lift.pdf [retrieved 1 Feb 2016].

REPORT DOCUMENTATION PAGE

Form Approved
OMB No. 0704–0188

1. REPORT DATE (DD–MM–YYYY)	2. REPORT TYPE	3. DATES COVERED *(From — To)*
24-03-2016	Master's Thesis	Sept 2014 – March 2016

4. TITLE AND SUBTITLE
Investigation into Active Spanwise Camber Deformation on the Lateral Stability and Roll Control of the X-56A Compared to Conventional Ailerons

5a. CONTRACT NUMBER
5b. GRANT NUMBER
5c. PROGRAM ELEMENT NUMBER

6. AUTHOR(S)
Yerly, Eric T, Capt

5d. PROJECT NUMBER
5e. TASK NUMBER
5f. WORK UNIT NUMBER

7. PERFORMING ORGANIZATION NAME(S) AND ADDRESS(ES)
Air Force Institute of Technology
Graduate School of
2950 Hobson Way
WPAFB OH 45433-7765

8. PERFORMING ORGANIZATION REPORT NUMBER
AFIT-ENY-MS-16-M-249

9. SPONSORING / MONITORING AGENCY NAME(S) AND ADDRESS(ES)
Design and Analysis Branch AFRL/RQVC
Dr. James J. Joo
2210 8th St.
Wright-Patterson AFB, OH 45433
312-713-7137
James.Joo.1@us.af.mil

10. SPONSOR/MONITOR'S ACRONYM(S)
AFRL

11. SPONSOR/MONITOR'S REPORT NUMBER(S)

12. DISTRIBUTION / AVAILABILITY STATEMENT
Distribution Statement A. Approved for Public Release; Distribution is Unlimited

13. SUPPLEMENTARY NOTES

14. ABSTRACT

This research compares the stability and roll characteristics of an X-56A using AFRL's Variable Camber Complaint wing technology to actively change wing camber compared to conventional ailerons deflected at set angles. An analysis of the stability and roll characteristics was modeled using a 3-D vortex lattice theory simulation, and that data was compared to wind tunnel testing to verify and validate the model results. Wind tunnel data was collected using 19 inch 3-D printed scale models with wings fabricated with a pre-determined percentage of camber deformation, as well as models with fixed aileron deflections.

Wind tunnel testing was performed at a Reynolds number range from 30,000 to 150,000. Testing indicated at high speeds and low angles of attack, the camber deformed wings produced a roll moment and roll rate equivalent to, or greater than conventional ailerons. Because of early onset stall, the camber deformed wing had a lower lift coefficient with increased drag. The camber deformed models did not result in aerodynamic moment instability; however, they did demonstrate a decrease in roll and pitch stability. The 3-D model predicted accurate trends in roll and stability, but could not model viscous effects due to the inviscid nature of the simulation.

15. SUBJECT TERMS
Roll Camber Deformation X-56A Aileron

16. SECURITY CLASSIFICATION OF:			17. LIMITATION OF ABSTRACT	18. NUMBER OF PAGES	19a. NAME OF RESPONSIBLE PERSON
a. REPORT	b. ABSTRACT	c. THIS PAGE			Lt. Col. Anthony M. DeLuca, AFIT/ENY
U	U	U	UU	178	19b. TELEPHONE NUMBER (Include Area Code) (937) (937)785-6565x4537 anthony.deluca@afit.edu

Standard Form 298 (Rev. 8–98)
Prescribed by ANSI Std. Z39.18